Title
Understanding Orientation-dependent Dielectric and Ferroelectric Properties in Ferroelectric Thin Films

Author
Xu, Ruijuan

Publication Date
2018

Peer reviewed|Thesis/dissertation

Understanding Orientation-dependent Dielectric and Ferroelectric Properties in Ferroelectric Thin Films

By

Ruijuan Xu

A thesis submitted in partial satisfaction of the

requirements for the degree of

Doctor of Philosophy

in

Engineering - Materials Science and Engineering

in the

Graduate Division

of the

University of California, Berkeley

Committee in charge:

Professor Lane W. Martin, Chair
Professor Mark Asta
Professor Sayeef Salahuddin

Spring 2018

Understanding Orientation-dependent Dielectric and Ferroelectric Properties in Ferroelectric Thin Films

Abstract

Understanding Orientation-dependent Dielectric and Ferroelectric Properties in Ferroelectric Thin Films

by

Ruijuan Xu

Doctor of Philosophy in Materials Science and Engineering

University of California, Berkeley

Professor Lane W. Martin, Chair

Complex oxide materials, which exhibit a wide range of structures and functionalities such as superconductivities, magnetic and multiferroic properties, have driven considerable research in materials science and condensed matter physics over past decades. As one important variant of oxide materials, ferroelectric materials which possess an electrically-addressable polarization hold great promise for next-generation non-volatile, low-power nanoelectronics. Leveraging the polarization and the coupled dielectric, piezoelectric, and pyroelectric properties, ferroelectric materials have been integrated into the state-of-the-art devices such as memories, logics, sensors/actuators, etc. My work is focused on developing new routes to engineering ferroelectric domain structures for enhanced dielectric response and controllable polarization switching in ferroelectric thin films that allow for new functionalities in device applications. In particular, I studied the evolution of domain structures, dielectric, and ferroelectric properties in $PbZr_{0.2}Ti_{0.8}O_3$ thin films via the control of film orientation. First, using a combination of Ginzburg-Landau-Devonshire thermodynamic model and epitaxial thin film growth and characterization, I probed the domain structure and dielectric susceptibility in (001)-, (101)-, and (111)-oriented $PbZr_{0.2}Ti_{0.8}O_3$ thin films. In this work, I observe that (111)-oriented films, in which the extrinsic contributions from domain wall motion are frozen out, exhibit enhanced dielectric permittivity due to the stationary domain wall contribution from high densities of 90° domain walls. After exploring the enhanced dielectric response in (111)-oriented films, I studied how the polarization switching proceeds in films with different orientations. Differences are demonstrated between (001)-/(101)- and (111)-oriented films, with the latter exhibiting complex, nanotwinned ferroelectric domain structures with high densities of 90° domain walls and considerably broadened switching characteristics. Molecular-dynamics simulations predict both 180° (for (001)-/(101)-oriented films) and 90° multi-step switching (for (111)-oriented films) and these processes are subsequently observed in stroboscopic piezoresponse force microscopy. These results have implications for our understanding of ferroelectric switching and offer opportunities to change domain reversal speed.

Furthermore, I demonstrated multi-state polarization switching in (111)-oriented $PbZr_{0.2}Ti_{0.8}O_3$ thin films, wherein the polarization can be deterministically written into a number of non-volatile and stable states in any order by varying the driving voltage. Such switching phenomena are driven by kinetic control over the volume fraction of two geometrically different domain structures generated by two distinct switching pathways: one direct, bi-polar-like switching process and another multi-step process with the formation of a thermodynamically-stable intermediate twinning structure. This work provides new insights into the control of ferroelectric switching and demonstrates a candidate material with multi-state functionality for memory devices and adaptive neuromorphic electronics. Last, I explored the scaling potential of ferroelectric thin films for low-voltage operation and low-power consumption. In this work, it is noted that (111)-oriented $PbZr_{0.2}Ti_{0.8}O_3$ films exhibit a deviation from JKD scaling with a smaller scaling exponent for the evolution of coercive field in films of thickness $\lesssim 165$ nm. A combination of detailed X-ray structural analysis and first-principles calculations suggest a transition from tetragonal to monoclinic symmetry in films of thickness $\lesssim 165$ nm contributes to the deviation from the expected scaling as the monoclinic phase has a lower energy barrier for switching. In addition, the reduced tetragonality in (111)-oriented heterostructures also drives a reduction of the remanent polarization and, therefore, a reduction of the overall energy barrier to switching which further exacerbates the deviation from the expected scaling. This work demonstrates a route towards reducing coercive fields in ferroelectric thin films and provides a possible mechanism to understand the deviation from JKD scaling. Overall, my work presented in this dissertation provides new insights into understanding fundamental mechanisms of emergent dielectric and ferroelectric properties in ferroelectric films and demonstrates a new route to engineering domain structures for enhanced dielectric response and controllable polarization switching in ferroelectric thin films that allow for new functionalities in device applications.

To my family and all my friends

TABLE OF CONTENTS

ACKNOWLEDGEMENTS

I would like to express my gratitude to those people who have helped me in the past six years. Without their help and support, I wouldn't have completed my Ph.D. journey.

First and foremost, I would like to express my gratitude to my advisor, Prof. Lane Martin for bringing me into this exciting field. Lane, thank you for your support and trust to allow me to explore so many exciting research topics and your guidance to help me develop my own research philosophy. I learned a lot from your mentorship which benefit me not just for now but also for my future career.

I would also like to thank my qualifying exam and thesis committee members: Prof. Mark Asta, Prof. Ramamoorthy Ramesh, Prof. Sayeef Salahuddin, and Prof. Oscar Dubon, who provide lots of insightful advice that helps me to complete this dissertation.

I am also honored and grateful to have chances to work with many excellent theorists: Dr. Shi Liu, Prof. Ilya Grinberg, Prof. Andrew Rappe, Dr. Sebastian Lillo, Prof. Jeffrey Neaton, Dr. Jianjun Wang, Dr. Zijian Hong, and Prof. Longqing Chen. Their theoretical insights and support have helped me to gain better understandings of various experimental phenomena. I could not have completed this dissertation work without their theoretical support.

It has also been a great honor for me to work with so many excellent and nice people from the Martin group. I am especially grateful to Ran and Sahar for their generous help in my work and life. I would also like to extend my sincere gratitude to all the past and present Martin group members including Anoop, Karthik, Sungki, Eric, Brent, Vengadesh, Josh A, Christoph, Zuhuang, Jarret, Liv, Zach, Jialan, Shishir, Jieun, Arvind, Gabe, Eduardo, Anirban, Josh M, Lei, and Abel, who create such a diverse and collaborative culture that helps me learn and grow. I also particularly enjoy the process to mentor many excellent undergraduates including Hongling and Aileen.

I would also like to thank the members from Prof. Ramash and Prof. Salahuddin' group who constitute such a wonderful and collaborative working environment. Particularly I am grateful to Prof. Julia Mundy, Dr. Christopher Nelson, Shang-lin Hsu for their generous and kind help when I worked at NCEM.

I also gratefully acknowledge the financial support from National Science Foundation and Lam Research fellowship which enable me to perform my work.

Finally, I would like to sincerely thank my parents for their love and support. Particularly I would like to thank my husband Yin for always being there to support me. Without him I would not have completed this degree.

CHAPTER 1

Introduction

In this Chapter, I give an overview of the basic principles of ferroelectricity and the technical background of ferroelectric thin films. In particular, I review the crystallographic signature of ferroelectricity in perovskite oxide materials and discuss the origins of ferroelectricity in the view of coordination chemistry and phonon theory. I further introduce the background of ferroelectric thin films wherein I discuss domain structure formation and possible pathways to controlling these structures in thin films. Next, I discuss how these domain structures influence ferroelectric properties including both dielectric susceptibility and polarization switching, and how to utilize these properties in modern electronic applications. At the end, I introduce the central question which motivates our work, and the organization of my thesis.

1.1 Introduction to Ferroelectricity

Ferroelectricity refers to the property of materials wherein spontaneous polarization can be reversed by applying an electric field. Such a material property, which was first discovered in 1920 by Valasek in Rochelle salt [1], is named with a prefix "ferro" in analogy of ferromagnetism although usually without the presence of iron. The switchable polarization in ferroelectrics not only leads to bistable states which are promising for non-volatile memories [2,3] and low-power logics [4,5], but also makes such materials applicable in a wide range of modern electronics such as capacitors, piezoelectric sensors/actuators [6], and pyroelectric devices for energy harvesting [7], *etc*. due to the coupled dielectric, piezoelectric, and pyroelectric properties. In order to engineer ferroelectric materials for enhanced material properties and performance, it is essential to study and understand the origin of spontaneous polarization in such materials. Thus, in this Section, I discuss the crystallographic signature and physical origins of ferroelectricity from aspects of crystal symmetry, coordination chemistry, and phonon theory.

1.1.1 Crystallographic Signature

Although ferroelectricity was first discovered in hydrogen-bonded materials, the later discovery of non-hydrogen-bonded ferroelectric oxide $BaTiO_3$ pushed forward the understanding of ferroelectric physics dramatically. $BaTiO_3$ is one example of a perovskite oxide, also the most extensity studied structural variant in ferroelectrics. Such oxides are usually represented using the chemical formula ABO_3, where each unit cell contains a corner-linked network of oxygen octahedra with the *A*-site cation occupying interstices and the *B*-site cation occupying the center of octahedral cage (Fig. 1.1). Ferroelectricity, however, is only present in a subgroup of perovskite oxides. For instance, no spontaneous polarization is observed in paraelectric $SrTiO_3$ at room temperature. The question then, is what determines the presence of ferroelectricity in materials? The simplest consideration is to examine the material symmetry. Among the 32 possible point groups, 20 do not possess an inversion center and thus exhibit piezoelectricity wherein external stresses are applied which gives rise to changes in polarization. Among these piezoelectric material classes, 10 possess a unique polar axis (have a spontaneous polarization) and exhibit pyroelectric response wherein a temperature change leads to a change in polarization. Ferroelectricity originates only from a subgroup of the pyroelectric material classes (Fig. 1.2) when the polarization is switchable with an applied electric field. This symmetry restriction not only indicates that materials such as cubic $SrTiO_3$ (point group $m\bar{3}m$) is not ferroelectric but also suggests that ferroelectric materials exhibit piezoelectricity and

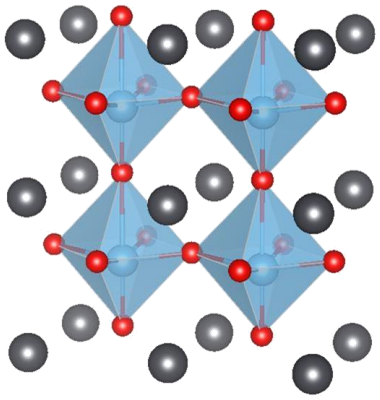

Fig. 1.1: The schematic of atomic structure of perovskite oxide.

pyroelectricity simultaneously in nature. The crystal symmetry of ferroelectric materials also varies with increasing temperature. Most ferroelectric materials go through a phase transition from a ferroelectric phase to a non-polar paraelectric phase at the Curie temperature. These phase transitions can be continuous second-order or discontinuous first-order in nature, which are usually studied in the treatment of phenomenological Landau-Ginzburg-Devonshire model (The details of this method are provided in Chapter 2).

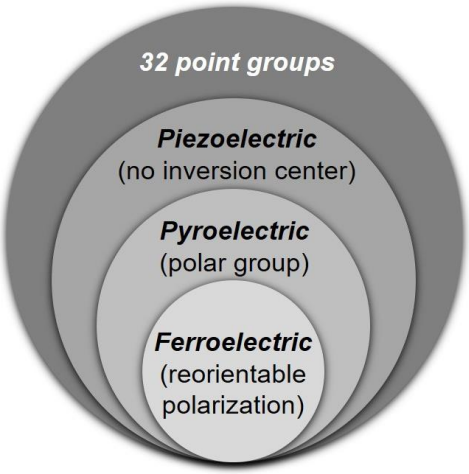

Fig. 1.2: Classification of the crystallographic groups by their electrical properties.

Additionally, another empirical criterion to determine the stability of ferroelectricity in perovskite oxides is using the Goldschmidt tolerance factor [8], defined as $t = \frac{r_A + r_O}{\sqrt{2}(r_B + r_O)}$, where r_A, r_B, and r_O represent the ionic radii of *A*, *B*, and O ions, respectively. For $t > 1$ when the *B*-site cation is small, a polar distortion is developed in the perovskite structure (*e.g.*, $BaTiO_3$ and $PbTiO_3$). On the other hand, for $t < 1$ when the *A*-site cation is small which cannot effectively bond with *O* ions, oxygen octahedra rotations are favored while the polar distortion is suppressed (*e.g.*, $SrTiO_3$ and $CaTiO_3$) (Fig. 1.3).

1.1.2 Origins of Ferroelectricity

In this Section I discuss the origin of ferroelectricity as to how the ionic off-centering is developed in perovskite oxides. From the atomic level, ferroelectricity results from the competition between the short-range repulsion which favors a centrosymmetric non-ferroelectric structure and the long-range Coulomb force which favors a distorted ferroelectric structure. Ultimately this distorted structure can be stabilized through a change in the chemical bonding. Such a phenomenon

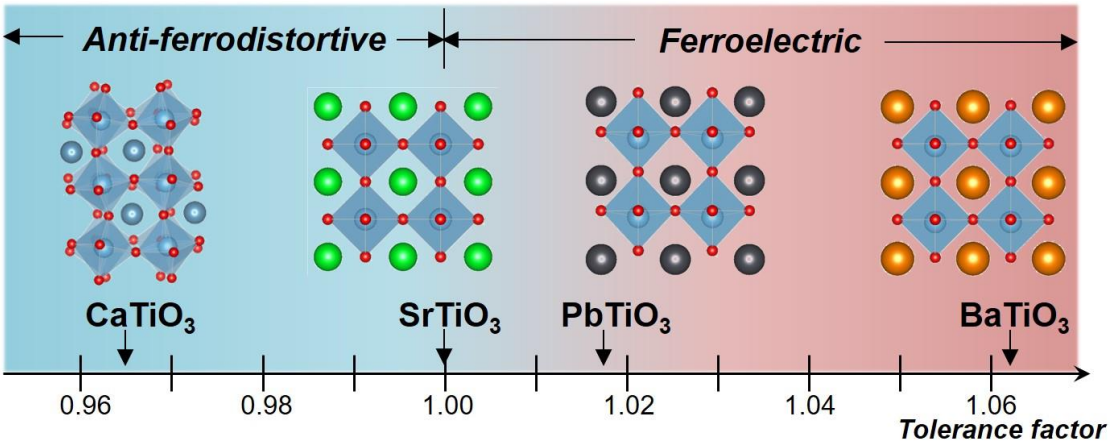

Fig. 1.3: The relation between the tolerance factor and the material structure of perovskite oxide.

is referred to as a *second-order Jahn-Teller* effect [9,10,11], which usually leads to two different stabilization mechanisms. For instance, in $BaTiO_3$, the $3d^0$ titanium mixes with oxygen $2p$ character which results in a displacement of the titanium ion towards an oxygen ion and thus the formation of a polarization. On the other hand, in materials such as $PbTiO_3$, the second-order Jahn-Teller effect can also be driven by the stereochemical activity of lead $6s^2$ electron "lone pairs" which mix in some cation and anion *p* character and therefore lose the center of symmetry.

The origin of ferroelectricity can also be understood in the frame of soft-mode theory [12]. In the case of non-primitive lattices such as perovskite oxides, there are two types of phonon modes: acoustic and optical phonons. The acoustic phonon refers to the coherent movement of atoms while the optic phonon refers to the out-of-phase movement of atoms. At the transition temperature, the phonon softening occurs such that the frequency of transverse optical phonon becomes zero at the center of first Brillouin zone. This physical picture translated into the real space, indicates that a spontaneous polarization is developed at the phase transition, since the softening of optical phonon mode at the zone center ($k = 0$) corresponds to an off-centering displacement in an infinite region ($\lambda \rightarrow \propto$) of real space lattice. This soft-mode theory, again, provides another explanation for the origin of ferroelectricity in materials.

1.2 Ferroelectric Thin Films

Thin-film epitaxy can dramatically impact the structure and property of ferroelectric materials. Novel structures and intriguing properties can be induced in ferroelectric thin films through the control of epitaxial strain, film chemistry, and other factors. Details of thin-film growth techniques are provided in Chapter 2. In this section, I review the formation of ferroelectric domain structures and pathways to controlling these domain structures in ferroelectric thin films.

1.2.1 Domain Formation in Thin Films

Domains in ferroelectrics refer to homogeneously polarized regions. In ferroelectric thin films, the polarization *P* of a homogeneously polarized domain changes abruptly at the surface which contributes to a surface charge density σ ($\sigma = P \cdot \hat{n}$, where $\hat{n}$ is the vector perpendicular to the film surface). The surface bound charge can generate an electric field to increase the system energy (Fig. 1.4a). In order to eliminate the surface charge, the system introduces polydomain

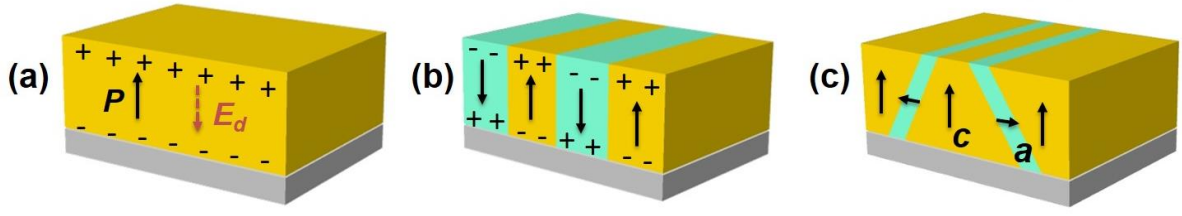

Fig. 1.4: Schematics of (a) single-domain structures, (b) ferroelectric domain structures with 180° domain walls, and (c) ferroelastic domain structures with ferroelastic 90° domain walls.

structures with domain walls to separate adjacent differently-oriented domains, including: 1) 180° domain walls separating regions with anti-parallel polarizations (Fig. 1.4b); 2) non-180° ferroelastic domain walls bisecting the angle between two domains pointing head-to-tail at the wall (Fig. 1.4c). In addition, non-180° domain walls which separate domains in different strain states also minimizes the elastic energy of the system. Also note that the presence of domain walls introduces extra domain-wall energy by itself. Clearly, the formation of polydomain structure is a result to minimize the overall energy [8].

1.2.2 Pathways to Controlling Domain Structures

In ferroelectric thin films, there are a number of routes to control and engineer domain and domain-wall structures. In this Section, I focus on introducing two strategies that have been studied extensively, including: 1) strain engineering of and 2) size effects on domain structures.

First, thin-film epitaxy allows one to manipulate the thin-film-strain state through the use of a range of available single-crystal substrates. Similar to the effect of pressure on phase evolution in bulk materials, biaxial strain applied to thin films also manipulates the phase and domain structure of ferroelectric thin films. For instance, $PbZr_{1-x}Ti_xO_3$, one of the most widely studied piezoelectric and ferroelectric materials, exhibits a rich phase diagram encompassing a variety of structural phases as a function of titanium composition [13] (Fig. 1.5). The ferroelectric phase adopts a tetragonal structure for titanium-rich compositions, and a rhombohedral structure for zirconium-rich compositions. For endpoint compound $PbZrO_3$, the structure adopts an orthorhombic antiferroelectric phase. Near 50% titanium compositions (also referred to as morphotropic phase boundary, MPB), a mixture of tetragonal, rhombohedral, and even monoclinic structures is present in the ferroelectric phase. Further imposing biaxial strain, for instance, to titanium-rich phases such as $PbTiO_3$, a variety of domain structures are observed: out-of-plane polarized *c* domains are favored in the compressive strain regime, *c*/*a* domain structures with a mixture of out-of-plane and in-plane polarizations are favored in the intermediate strain regime, and a_1/a_2 domain structures with orthogonally in-plane polarized a_1 and a_2 domains are favored in tensile strain regimes [14] (Fig. 1.6). Additionally, recent work suggests that a mixed-domain region occurs near the *c*/*a* and a_1/a_2 domain boundary exhibiting intriguing hierarchical superdomain structures. Such strain effects are used to control domain structures in a variety of ferroelectric thin films such as $BiFeO_3$, $BaTiO_3$, *etc*. Note that these different substrates not only provide tunable lattice constants for films

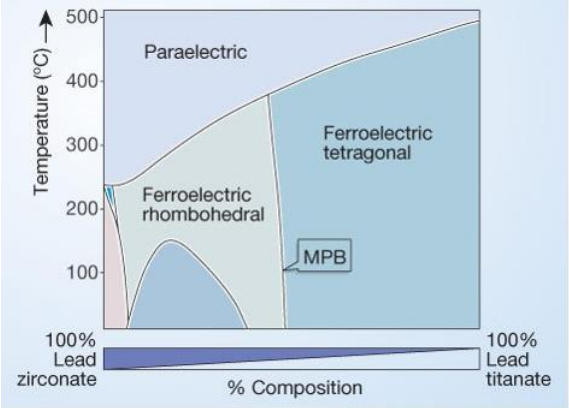

Fig. 1.5: Temperature-composition phase diagram of $PbZr_{1-x}Ti_xO_3$ [13].

to reach a desired strain state but can also provide different miscut angles to engineer domain structures.

Another route to controlling domain structures is using ferroelectric size effects, which refer to the change of structures and properties with reducing physical dimension in ferroelectric materials. For ferroelectric epitaxial thin films, size effects are primarily driven by reducing film thickness, which can possibly originate from either intrinsic or extrinsic mechanisms. For instance, reducing film thickness below a certain critical value intrinsically modifies the balance between the short-range repulsion and long-range attraction, and thus destabilize the spontaneous polarization. On the other hand, the suppressed ferroelectricity in thinner films might be driven extrinsically by the growth-induced non-switchable interfacial "dead layer" [15,16]. In addition, thickness change also leads to the evolution of domain size in ferroelectric films. Kittel's law [17] which describes the relation between domain size and film thickness (*i.e.*, $w = \sqrt{(\sigma/U)d}$, where w is the domain size, σ and U are the energy density of the domain and domain wall, and d is the film thickness) reveals that domain size increases with increasing film thickness. On the other hand, when the thickness change is coupled with the strain-state change, namely, from a fully strained to a partially strained state with film thickness, the thickness-dependent domain evolution, in this case, is essentially driven by the change in strain. For instance, in $PbTiO_3$ thin films, a coherently strained *c* domain only remains up to a critical thickness, above which the domain relaxes into *c/a* domain structure to release the strain energy. Size effects also include the evolution of coercive field with film thickness, which is usually referred to as the coercive-field scaling law or the Janovec-Kay-Dunn (JKD) law [18,19], $E_c \propto d^{-2/3}$, where E_c and d represent the coercive field and film thickness, respectively. More details about this scaling law can be found in Chapter 7, where I introduce my work about how to reduce coercive-field scaling by engineering film orientation.

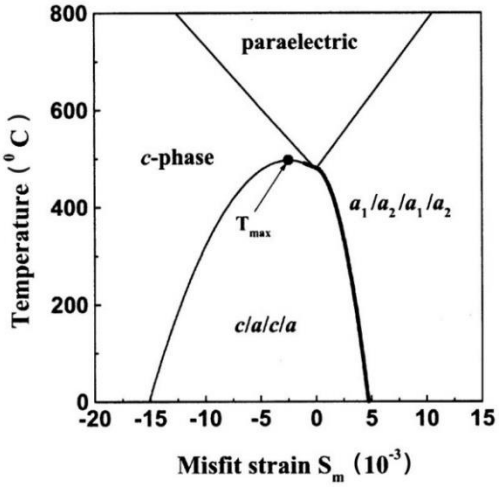

Fig. 1.6: Temperature-strain phase diagram of $PbZr_{1-x}Ti_xO_3$ [14].

1.3 Ferroelectric Properties and Applications

As is mentioned at the beginning of this Chapter, ferroelectric materials are used in a wide range of modern electronic applications due to their switchable spontaneous polarization and the coupled dielectric, piezoelectric, and pyroelectric properties. In this Section, I review these properties and applications of ferroelectrics with a particular focus on the relationship between structure and properties.

1.3.1 Dielectric Susceptibilities

Material properties inherent to ferroelectrics include dielectric susceptibility, piezoelectricity, and pyroelectricity, *etc.* These properties are the linear relationships between electrical, mechanical, thermal variables as described in the Heckmann Diagram [20,21] (Fig. 1.7).. These material properties follow Neumann's Principle, wherein the symmetry elements of any physical property of a crystal must include the symmetry elements of the point group of the crystal [20]. The best way to represent such a relationship between material structure and properties is to treat these properties as tensors. Thus, materials properties, also called tensor properties, are usually represented using vectors or matrices which can change with coordinate system and material symmetry [21]. Imposing symmetry operations to tensor properties can significantly reduce the number of independent components and thus directly reveal the property anisotropy.

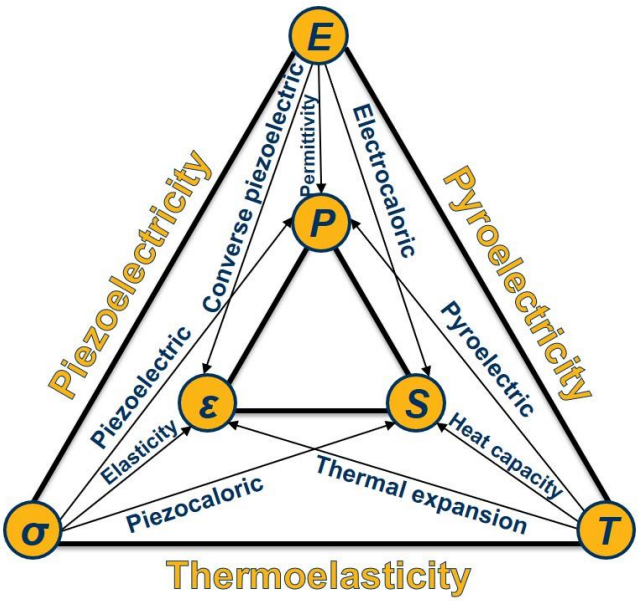

Fig. 1.7: Heckman diagram describing the linear relationships between electrical, mechanical, and thermal variables.

For instance, dielectric permittivity is a second rank tensor which describes the linear relation between electric displacement *D* and electric field *E*. In a three-dimensional case, such a relation is expressed as follows:

$$\begin{bmatrix} D_x \\ D_y \\ D_z \end{bmatrix} = \begin{bmatrix} \varepsilon_{xx} & \varepsilon_{xy} & \varepsilon_{xz} \\ \varepsilon_{yx} & \varepsilon_{yy} & \varepsilon_{yz} \\ \varepsilon_{zx} & \varepsilon_{zy} & \varepsilon_{zz} \end{bmatrix} \begin{bmatrix} E_x \\ E_y \\ E_z \end{bmatrix}$$

Introducing symmetry elements such as a four-fold axis in a tetragonal crystal, the dielectric permittivity tensor can be reduced into three non-zero diagonal terms, with two of which equal to each other. This tensor treatment reduces 9 components into 2 independent components which significantly simplify the process to understand material properties.

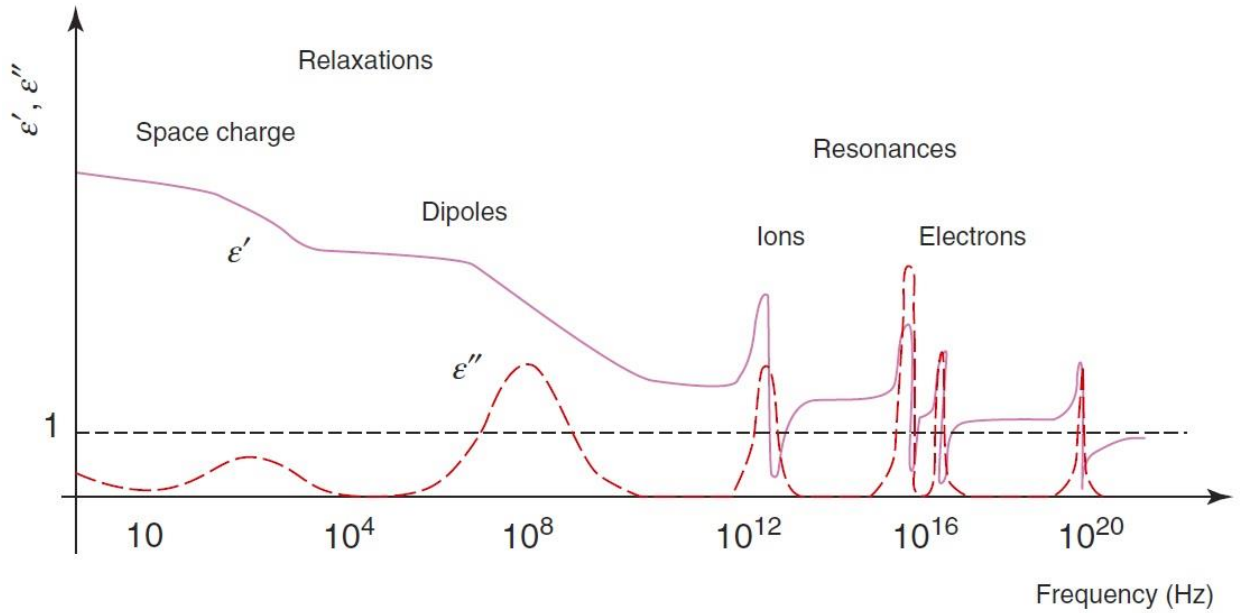

Fig. 1.8: Frequency dependence of polarization dispersion [22].

After reviewing this powerful mathematical method, I will introduce dielectric susceptibility in the rest of this Section with a focus on how domain structures affect dielectric property of ferroelectric materials. First, according to Gauss's flux theorem, dielectric permittivity refers to the amount of charge needed to generate one unit of electric flux in a particular medium. That said, dielectric response is not a unique property of ferroelectrics but a common property in most materials. For instance, the permittivity of metals is usually negative below their plasmon resonance frequency (also called plasma frequency which is near optical frequencies approaching 10^{15} Hz), but becomes positive above this frequency as a result of frequency-dependent electron oscillations. Insulators, on the other hand, usually exhibit positive dielectric permittivity below optical frequencies due to large ionic contributions. Such insulators are also called dielectric materials. Among the dielectric material family, ferroelectric materials exhibit high dielectric constants which hold great promise for capacitor applications, high-k gate materials, and high permittivity dynamic random-access memory (DRAM), *etc*. In ferroelectrics, there are a number of mechanisms contributing to the dielectric response including both intrinsic electronic, ionic contributions, extrinsic space charge, dipolar contributions. These different dielectric mechanisms are strongly dependent on the probed frequency range [12,22] (Fig. 1.8). Starting from high frequencies, the electronic contribution which originates from electron oscillations dominates in the optical range (10^{15} Hz). The ionic contribution which originates from the displacement of ions dominates in the terahertz range (10^{12} Hz). The orientation contribution which originates from the polar molecules to reorient themselves dominate the radio frequency range. The space charge contribution which originates from the diffusion of ions often occurs in the audio frequency range (10^{3} Hz). In addition, strong dielectric-loss peaks usually occur near the relaxation or resonance frequency of each dielectric contribution.

In the study of ferroelectric thin films, space charge and orientation contributions are usually neglected for high-quality films which have low defect concentrations and low leakage currents. The permittivity, in this case, usually consists of two major contributions. The first one is the intrinsic contribution arising from the change in the polarization to an applied stimulus within the bulk of the domains (*i.e.*, the aforementioned ionic and electronic contribution). The second one is the extrinsic contribution which refers to the contribution that arises due to the motion of domain walls under an applied stimulus [23-26]. Beyond the motional extrinsic contribution from domain walls, another domain-wall response called stationary or frozen contribution arises from the response of the volume of the ferroelectric material within the finite width of the domain walls to an applied stimulus, irrespective of any lateral displacements or deformations of the wall. Early studies of dielectric permittivity in $BaTiO_3$ revealed what was suspected to be a large domain-wall contribution to permittivity even at excitation fields where the lateral displacement of domain walls was unlikely [27]. Subsequent theoretical studies probed the possibility of the weak measurement fields inducing nuclei on the existing domain walls and thus promoting protuberance-type oscillation but revealed that these could only account for a small fraction of the observed permittivity change [28]. Soon after this it was conjectured that the material within the domain walls themselves could possess significantly enhanced dielectric permittivity [29,30]. Such models suggested that 180° domain walls in $BaTiO_3$ could possess permittivity almost an order of magnitude larger than the bulk of the domains. More recently, advanced Ginzburg-Landau-Devonshire (GLD) models have probed the role of polarization gradients near 90° domain walls in $BaTiO_3$ to suggest that such domain walls could give rise to an enhancement of susceptibilities between 1.1 to 1000-times larger than the bulk [31]. Despite these predictions as to the potential importance of such stationary contributions, it has proven difficult to quantitatively measure and isolate the stationary contribution (possibly because of the small relative volume associated with domain walls in most samples). In Chapter 4, I introduce my work of using a combination of theoretical and experimental approaches to investigate the effect of 90° domain walls on the dielectric permittivity in $PbZr_{0.2}Ti_{0.8}O_3$ thin films and probe the stationary domain wall contribution in (111)-oriented films.

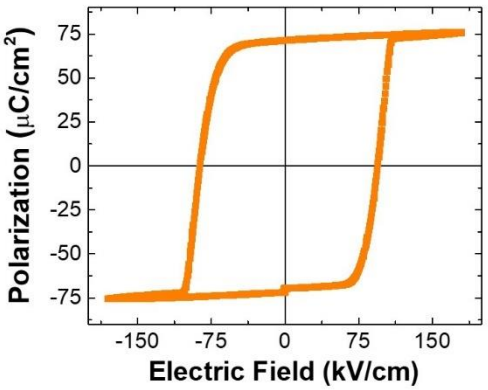

Fig. 1.9: The schematic of polarization-electric field hysteresis loop.

1.3.2 Ferroelectric Polarization Switching

As is mentioned earlier in this Chapter, the most fundamental characteristic of a ferroelectric material is the presence of an electrically switchable polarization, which leads to a polarization-electric field (P-E) hysteresis loop (Fig. 1.9). Compared with volatile memory

technologies such as static random-access memory (SRAM) and DRAM, ferroelectric random-access memory (FeRAM) use the P-E characteristic to hold data in a non-volatile state [32] (Table 1.1). Compared with other non-volatile memory technologies such as flash memories, FeRAM possess lower write voltages, shorter write time, and a greater write endurance [32] (Table 1.1). FeRAM are currently used in a wide variety of device applications including electricity meters, automotive, business machines, medical equipment, *etc*. In particular, a recently developed product based on embedded FeRAM is the RF-operated smart card used in public transportation, electronic banking, and sales, *etc*. Despite these applications, FeRAM still remains a relatively small part of the overall semiconductor market mostly due to their lower storage density caused by the growth limitation and integration difficulty of high-quality films on silicon. Recent strategies to increase the storage density of FeRAM include improving processing and fabrication technologies such as developing vertical capacitor structures. These vertical devices with reduced cell sizes, however, usually lead to weak signals that are hard to detect [33]. Apparently, new routes to increasing the storage density of FeRAM are needed. Thus, in the study of ferroelectric thin films, it is imperative to achieve controllable polarization switching that can be applied in next-generation high-storage, low-power memory applications. In order to engineer polarization switching for these advanced applications, one needs to understand the switching process in ferroelectric thin films. The rest of this Section reviews aspects of ferroelectric switching and basic methodologies to study these switching behaviors.

Table 1.1: Comparison of different memory technologies [32].

Property	***SRAM***	***eFlash***	***eDRAM***	***eFeRAM***
Min. Voltage	> 0.5 V	> 12 V	> 1 V	> 1 V
Write Time	< 10 ns	100 μs – 1 s	< 20 ns	< 20 ns
Write Endurance	$> 10^{15}$	$< 10^{5}$	$> 10^{15}$	$> 10^{15}$
Read Time	< 10 ns	20 ns	< 20 ns	< 20 ns
Read Endurance	$> 10^{15}$	$> 10^{15}$	$> 10^{15}$	$> 10^{15}$
Non-volatility	No	Yes	No	Yes
Cell Size (F=half metal pitch)	~ 80 F^2	~ 8 F^2	~ 8 F^2	~ 15 F^2

The most commonly observed switching process in ferroelectric thin films is shown in Fig. 1.10, which include the following three stages [34,35]: 1) the nucleation of reversed domains; 2) the forward growth of domains; 3) the sideway propagation of domains. First, in the nucleation process, the homogenous nucleation is less likely to occur due to the high energy barrier which is insurmountable by thermal energy even in the presence of electric field (Fig. 1.11). This fact is

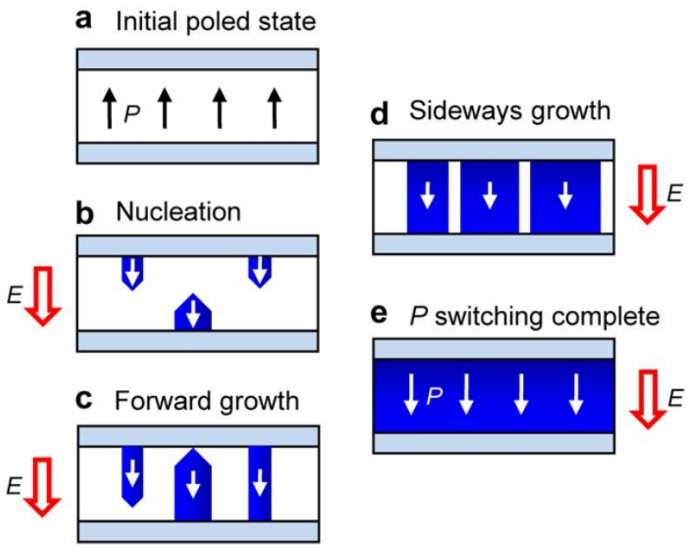

Fig. 1.10: The schematic of switching process in ferroelectric thin films including (a) the initial poled state, (b) the nucleation of domains, (c) the forward growth of domains, (d) the sideway growth of domains, and (e) the fully poled state [35].

also known as Landauer's paradox [36], namely, at room temperature the barrier will be around 10^8 kT under the electric field of 1 kV/cm and 10^3 kT under the electric field of 100 kV/cm. Thus, it is more likely for the system to go through an inhomogeneous process at defect sites which allow for a lower energy barrier. The nucleation time is typically 1 ns for oxide films with a critical size around 1-10 nm. Next, these needle-like nuclei grow parallel or antiparallel to the electric field from the anode to the cathode. This forward growth speed is usually limited by the speed of sound, which proceeds with an estimated time $t_{fg} = d/v$, where d is the film thickness and v is the speed of sound. For instance, assuming a 100-nm-thick thin film with a speed of sound a few (km/s), the forward growth is ~0.1 ns. After completing the forward growth, these domains propagate sideways to fill the unswitched region. This sideways growth is usually the rate-limiting step, which can be slow ranging from a few (ns) to (μs), as a result of defect-pinning. Such a defect-domain-wall interaction leads to a non-linear behavior of domain-wall motion with applied electric field [37]. When electric field $E < E_0$, where E_0 is the threshold value of switching, domain walls are pinned, and can only proceed in a "creep" hopping manner with the assistance of thermal energy. This process is usually temperature dependent with a domain-wall velocity of $v \sim \exp[-(U/k_BT)(E_0/E)^{\mu}]$, where U is an energy barrier, μ is a dynamical exponent, and T is temperature. When $E \geq E_0$, domain walls experience a pinning-depinning transition with a domain-wall velocity of $v \sim (E - E_0)^{\theta}$, where θ is the velocity exponent. When $E \gg E_0$, domain walls are de-pinned completely, and can move in a temperature-independent "flow" manner with a velocity $v \sim E$.

Such switching behaviors can be analyzed both macroscopically and microscopically. In the macroscale studies, switching behaviors are characterized on capacitor structures using P-E loops, switching kinetics measurements, *etc*. P-E loops measure the films' capability to switch the

polarization (measured as coercive field E_c) and the capability to retain the polarization (measured as remanent polarization P_r). On the other hand, switching kinetics measurements study how fast domain walls can move under the electrical field. The early work studying switching kinetics, also referred to as Merz's law, found that the domain-wall speed is proportional to $\exp(-E_a/E)$, where E_a is the activation field and E is the applied field [38]. Additionally, the commonly accepted approach to study the switching kinetics in ferroelectrics is the kinetics KAI model developed by Ishibashi, Kolmogorov, and Avrami, based on the classical statistical theory of nucleation and unrestricted domain growth during phase transformation [39-41]. More recently, Tagantsev, *et al.* [42] developed a nucleation-limited-switching (NLS) model to describe the switching behavior in polycrystalline films which consist of many areas with independent switching kinetics. These kinetics studies are usually performed via pulsed-switching measurements, details of which can be found in Chapter 2. Switching behaviors can also be analyzed microscopically using scanning probe microscopy (SPM) and transmission electron microscopy (TEM). Applying a DC bias through conductive scanning probe tips enables the study of local domain switching events (see Chapter 2 for more details). TEM, on the other hand, allows for probing the *in situ* switching process [43-46], which can directly reveal the process of domain nucleation, forward and sideway growth, *etc*. In Chapters 5-7, I introduce my work of using a combination of macroscale and microscale switching characterizations to understand and manipulate the polarization switching in $PbZr_{0.2}Ti_{0.8}O_3$ films.

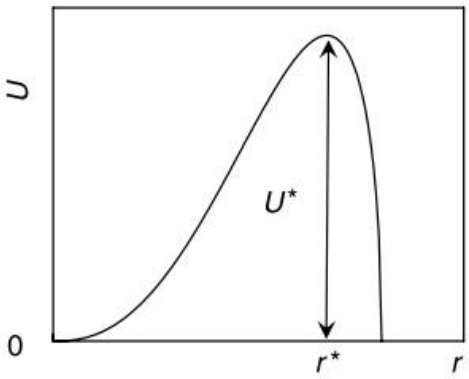

Fig. 1.11: The schematic of nucleation energy barrier as a function of nucleus radius [199].

1.4 Central Question and Organization of the Dissertation

The central question I focus on in this thesis is how to develop new routes to engineering domain structures in ferroelectric thin films for enhanced dielectric response and controllable polarization switching that allow for new functionalities in ferroelectric device applications. As is mentioned in this Chapter, commonly-used strategies to manipulate domain structures include strain engineering and size effects, *etc*. Here, I study the effects of film orientation on dielectric and ferroelectric properties of ferroelectric thin films. In the scope of this overarching theme, I focus on following questions in this thesis, summarized as follows:

1. Is it possible to induce different domain structures and achieve enhanced dielectric response by engineering film orientation? To address this question, in Chapter 3, a phenomenological Ginzburg-Landau-Devonshire model was used to theoretically study the evolution of structure and dielectric response as a function of film orientation in

$PbZr_{0.2}Ti_{0.8}O_3$ thin films, while in Chapter 4, the enhanced dielectric response and its structural origin was experimentally investigated in (111)-oriented $PbZr_{0.2}Ti_{0.8}O_3$ films.

2. Can one control polarization switching by engineering film orientation such that they can be operated into multiple states to increase the storage capacity? To address this question, in Chapters 5 and 6, both local switching events and macroscale switching behaviors were studied in $PbZr_{0.2}Ti_{0.8}O_3$ films using a combination of macroscale and microscale switching characterizations. In particular, I observed and studied the intriguing 90° mediated polarization reversal and tunable, multi-state polarization switching in (111)-oriented films.
3. Can one achieve reduced coercive-field scaling by engineering film orientation such that they can be used for low-power/voltage operation in devices with reduced dimensions? To address this question, in Chapter 7, I studied size effects of ferroelectric thin films with different film orientations. In particular, I observed smaller coercive field that deviates from JKD scaling while reducing the film thickness of (111)-oriented $PbZr_{0.2}Ti_{0.8}O_3$ films and studied the structural origin for this phenomenon.

In addition, the basic methodology used in the study of ferroelectric thin films is discussed in Chapter 2. The summary of each chapter and possible follow-up work are provided in Chapter 8.

CHAPTER 2

Synthesis and Characterization of Ferroelectric Thin Films

In this Chapter, I describe the basic methodology used in the study of ferroelectric thin films including thin-film synthesis, structural characterization, electrical measurements, and phenomenological calculations. First, I introduce epitaxial thin-film growth and discuss the technique of pulsed-laser deposition, which is the primary growth method used in the work to synthesize ferroelectric films. This is followed by a discussion of structural characterization methods including X-ray diffraction and scanning-probe microscopy. I also introduce electrical measurements which are used to characterize the dielectric and ferroelectric property of the materials. Lastly, I review the basic methodology of phenomenological thermodynamic modeling, so-called Ginzburg-Landau-Devonshire models, and discuss how to modify and apply this model to a variety of material systems.

2.1 Synthesis of Ferroelectric Thin Films

Advances in the growth of oxide thin films have enabled the elegant design and precise control of thin-film structures for a range of desired functionalities. In particular, recent developments in epitaxial growth have brought in thin-film growth techniques such as pulsed-laser deposition which allows for the growth of high-quality epitaxial ferroelectric thin films with novel structures and intriguing properties. In this Section, I give a short introduction of thin-film epitaxy and discuss the basic principles of pulsed-laser deposition.

2.1.1 Overview of Thin Film Epitaxy

Epitaxial growth refers to the deposition of a single-crystal film on a crystalline substrate. There are two types of epitaxial growth, *homoepitaxy* which refers to the growth of a film on a substrate of the same material, and *heteroepitaxy* which refers to the growth of a film on a substrate of a different material [47,48]. In particular, in the case of heteroepitaxy, two major parameters, namely the surface energy and the lattice mismatch dominate the growth. For instance, the different surface energy between film and substrate leads to three different growth modes, which can affect the film morphology: 1) layer-by-layer or Frank-Van der Merwe growth; 2) island or Volmer-Weber growth; or 3) Stranski-Krastanov growth wherein the growth mode changes from layer-by-layer growth to island growth after a few monolayers. On the other hand, the lattice mismatch between film and substrate also plays an important role in epitaxial growth. When the film is chemically bonded to the substrate, the lattice of the film can be strained to fit the in-plane lattice parameter of the substrate and result in the so-called commensurate growth. The strain energy stored per unit area of the coherently-strained film scales with the film thickness [49]. Beyond a certain critical thickness, the strain relaxation occurs to relieve the increasing strain energy. In ferroelectric thin films, strain relaxation usually proceeds via two mechanisms: the formation of misfit dislocations and/or the formation of polydomain structures [50-52].

Table 2.1: Basic characteristics of various thin film growth methods [53]

	MBE	**PLD**	**Sputtering**	**CVD**
Mechanism	Thermal energy	Thermal energy	Momentum transfer	Chemical reaction
Energy of deposited species	0.1 - 0.5 eV	1 – 100 eV	1 - 100 eV	0.1 – 0.5 eV; can be high with plasma-aid

2.1.2 Pulsed-Laser Deposition

A wide spectrum of growth techniques including molecular-beam epitaxy (MBE), pulsed-laser deposition (PLD), sputtering, and chemical vapor deposition (CVD) are used to produce high-quality epitaxial ferroelectric thin films. Table 2.1 summarizes basic characteristics of these

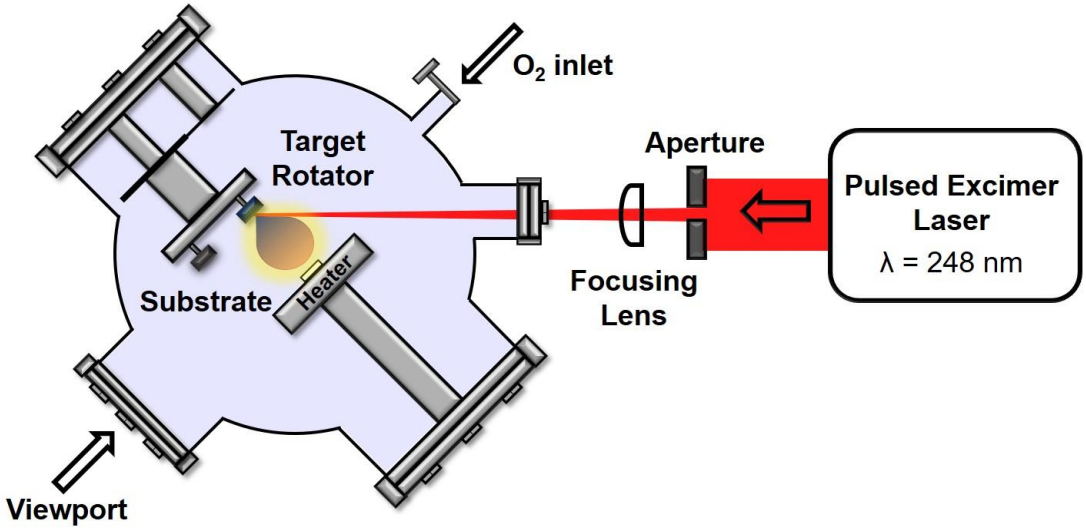

Fig. 2.1: The schematic of the experimental set-up of pulsed-laser deposition.

different methods. Here, I focus on PLD, which is the primary synthesis method used in this work. In PLD growth, a nanosecond pulsed excimer laser (in this case, a KrF excimer laser with 248 nm wavelength) is focused on a ceramic target, which immediately leads to the formation of a plasma due to the high fluence (usually 1-5 J/cm^2) on the target surface [54] (Fig. 2.1). The plasma, which contains neutral atoms, ions, electrons, molecules, and even some particulates and molten globules, is formed as a result of a series of complex laser-material interactions including photon absorption, target-surface melting, material evaporation, and plasma excitation [55] (Fig. 2.2). The generated plasma deposits materials from the target to the heated single-crystalline substrate that allows for the production of thin films with the preserved stoichiometry similar to substrates. This process occurs in high or ultra-high vacuum in the presence of background gas such as oxygen. PLD provides a variety of tunable parameters such as temperature, laser fluence, pressure, frequency, etc., which allows the control of growth mode and growth rate of epitaxial thin films. In this work, I used PLD to grow (001)-, (101)-, and (111)-oriented $PbZr_{0.2}Ti_{0.8}O_3/SrTiO_3$ heterostructures with $SrRuO_3$ or $La_{0.7}Sr_{0.3}MnO_3$ as the bottom electrode buffer layer. The growth of all film layers was

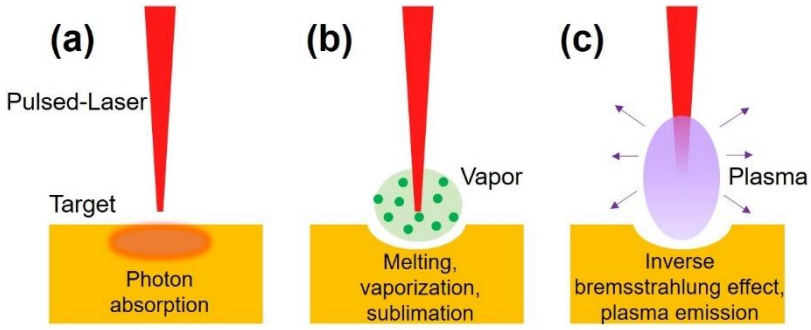

Fig. 2.2: The laser-target interaction process. (a) The absorption of laser radiation in the ceramic target. (b) Melt front propagates into the target and vaporization continues. (c) The plasma forms as a result of ionization and the heating of the plasma continues via the inverse-Bremsstrahlung effect.

carried out in a dynamic oxygen pressure of 200 mTorr, at a growth temperature of 650°C, and a laser fluence and repetition rate of 1.0 J/cm^2 and 3 Hz, respectively. Following growth, the samples were cooled to room temperature at a cooling rate of 5°C/min. under at a static oxygen pressure of 760 Torr.

2.2 Characterization of Ferroelectric Thin Films

In the study of materials science, materials characterization plays a central role in understanding the interrelationship among material's structure, properties, processing, and performance. Likewise, thin-film characterization focuses on understanding the aspects of material structure and property and their interrelationships. In this Section, I introduce basic principles of typical characterization methods that are used in the study of ferroelectric thin films, including both structural characterization and property measurement.

2.2.1 X-ray Diffraction

X-ray diffraction is a non-destructive elastic scattering technique that has been widely used to characterize the macroscale crystal structure, lattice mismatch, and crystalline quality of ferroelectric thin films. One of the most commonly used X-ray diffraction methods for thin-film studies is the θ-2θ scan which measures the Bragg diffraction of thin-film heterostructures [56] (Fig. 2.3a). During the scan process, the angle θ of the incoming and scattering beam varies continuously, but remains equal. Film peaks occur when θ satisfies Bragg's law:

$$2dsin\theta = \lambda,$$

where d is the out-of-plane lattice spacing, and λ is the X-ray wavelength (in this work, λ = 1.54 Å which corresponds to the Cu K_α radiation). This measurement allows for the examination of phase, structure, and strain condition of the films, wherein the in-plane misfit strain can impact the out-of-plane spacing d through Poisson's ratio and thus cause a shift in the peak position.

Another X-ray diffraction technique that is used extensively in thin-film studies is the rocking-curve measurement, or the so-called ω scan. In this measurement, the 2θ angle of the

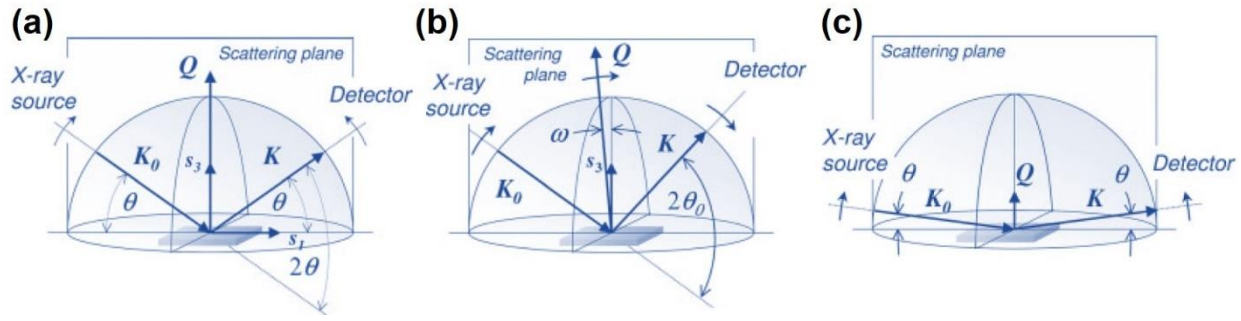

Fig. 2.3: The schematic of experimental set-up of X-ray (a) θ-2θ, (b) Rocking curves, (c) reciprocal space mapping measurements [56].

detector is fixed while the sample is "rocked" in the vicinity of the Bragg angle θ_0 [56] (Fig. 2.3b). Rocking curves are usually used to determine the crystalline quality of thin films since crystal imperfections such as dislocations and the crystal mosaicity can lead to the broadening of the rocking-curve peak.

The X-ray diffraction technique that provides the most complete structural information in thin-film studies is the reciprocal space map (RSM), which is performed such that the Bragg diffraction is mapped in a confined area of reciprocal space. This measurement collects a number of ω-2θ coupled scans, wherein each coupled scan is measured with a slightly different ω tilt such that $2\theta = 2\omega$ + tilt. RSMs are usually categorized into symmetric scans (or on-axis scans) which probe the diffraction from planes parallel to the film surface, and asymmetric scans (or off-axis scans) which probe the diffraction from planes tilted from the film surface. In the study of ferroelectric thin films, symmetric RSMs are usually used to separate domain structures with different lattice tilts (*e.g.*, *c* and *a* domains in $PbZr_{0.2}Ti_{0.8}O_3$ which have different lattice tilt) while asymmetric RSMs are usually used to analyze the lattice parameter and thus provide information about the strain condition and crystal structure of films. In Chapter 7, I will discuss, in detail, how to apply both symmetric and asymmetric RSM measurements to understand the crystal structure and strain condition of $PbZr_{0.2}Ti_{0.8}O_3$ films.

In addition, X-ray reflectivity (XRR) is another X-ray technique which is commonly used in the study of thin films. This measurement does not probe the Bragg diffraction, instead it uses a grazing incidence configuration to measure the interference from reflections at the film/substrate interface and the film top surface [56] (Fig. 2.3c). Typical XRR measurements generate a series of oscillation peaks, or the so-called Kiessig fringes, wherein the distance between oscillation peaks can be used to analyze the film thickness while the intensity of these peaks can be used to analyze the interface and surface roughness. In Chapter 7, we discuss how to apply this technique to analyze the thickness of $PbZr_{0.2}Ti_{0.8}O_3$ films.

2.2.2 Scanning-Probe Microscopy

Different from the X-ray techniques which probe the macroscale material structure, the scanning-probe microscopy (SPM) focuses on the microscale surface structure and properties. Since its discovery in the 1980s, SPM has developed rapidly over the past three decades, becoming a versatile platform with capabilities to probe a wide variety of functional materials [57,58]. In particular, in the study ferroelectric thin films, the most-widely

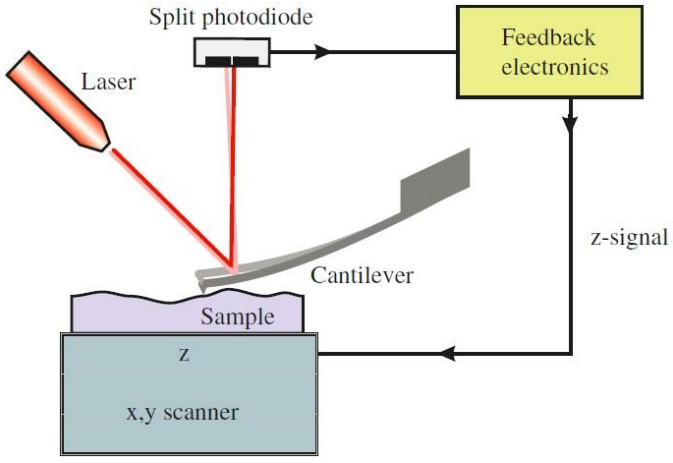

Fig. 2.4: The schematic of experimental set-up of atomic force microscope [57].

used SPM technique is atomic force microscopy (AFM) and piezoresponse force microscopy (PFM).

AFM probes the tip-sample force in which the feedback loop maintains a constant force by changing the z-position of the tip when scanning on a surface [57] (Fig. 2.4). As a result, topographical information such as the surface morphology and the film roughness can be extracted from the corresponding z-position change. AFM is usually operated in static contact mode or dynamic tapping mode. In contact mode, the tip-sample force is represented as the change of the cantilever bending, while in tapping mode, the tip-sample force is represented as the amplitude change of the cantilever oscillation.

PFM, on the other hand, is used to probe and manipulate the domain structure of ferroelectric thin films. In this measurement, application of an AC electric field through a conductive AFM tip results in a sample surface oscillation due to the converse piezoelectric effect [59] (Fig. 2.5). The cantilever displacement can be detected by the photodiode which is further processed by the lock-in-amplifier to retrieve the phase and amplitude information of the surface oscillation. The phase and amplitude of the surface oscillation are coupled with the direction and magnitude of polarizations in different domain regions. By mapping out PFM phase and amplitude signals, the ferroelectric-domain structure can be reconstructed through PFM contrast analysis. Typical PFM imaging provides information of both out-of-plane and in-plane polarization components which allow one to understand the three-dimensional polarization configuration in each domain. In addition, PFM can also be used to manipulate the polarization by applying a local DC bias which can induce local polarization switching. This method is also called PFM lithography which is used to create a desired domain pattern by selectively switching certain areas

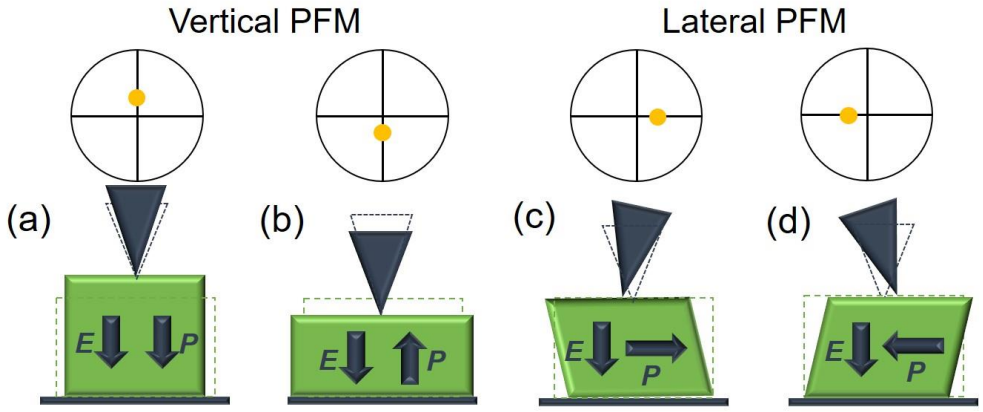

Fig. 2.5: The basic principle of piezoresponse force microscopy. (a) (b) The vertical PFM probes the polarization component which is parallel or anti-parallel to the applied electric field which leads to the lifting or contraction of the cantilever via the d_{33} effect. (c) (d) The lateral PFM probes the horizontal polarization component which leads to a shear movement of the sample and thus a torsion deformation of the cantilever via the d_{15} effect.

of ferroelectric films. In this work, PFM has been used extensively to characterize and manipulate the domain structure of $PbZr_{0.2}Ti_{0.8}O_3$ films, details of which can be found in Chapter 4, 5, and 6.

2.2.3 Electrical Measurements

In this Section I focus on basic electrical characterization of ferroelectrics including both the dielectric and ferroelectric property measurements. First, all these electrical measurements are measured on capacitor structures. The details of how to fabricate capacitor structures with conductive oxide electrodes are provided in Chapter 6.

In dielectric measurements, the complex dielectric permittivity of ferroelectrics is usually measured using either the impedance analyzer or the LCR meter which can probe dielectric properties in the frequency range of 10 Hz – 10^8 Hz. In these techniques, both the real and imaginary impedance parameters are measured as a function of frequency with an applied AC excitation, which can generate both the dielectric capacitance and loss tangent simultaneously. Furthermore, by varying the AC excitation magnitude, both the linear and the non-linear dielectric response (*i.e.* the linear and nonlinear relationship between polarization and electric field) are probed. Such a measurement or the so-called Rayleigh measurement is usually used to probe the reversible and irreversible domain-wall contributions to the dielectric permittivity [60] (see Appendix C for details of this measurement).

In the study of ferroelectric properties, typical characterization methods include hysteresis loop, leakage, and pulse measurements [61]. All these ferroelectric characterizations can be performed using a ferroelectric tester with a Sawyer-Tower, Shunt, or Virtual Ground set-up which measure the charge change of the capacitor. Hysteresis-loop measurements probe polarization switching parameters such as the saturated polarization P_s, remanent polarization P_r, and coercive field E_c. The leakage measurement, on the other hand, probes the flow of current through the sample. Pulse measurements including retention, fatigue, and switching-kinetics measurements, probe the potential of robust ferroelectricity for ferroelectric memories in terms of polarization stability, endurance, and switching speed. In Chapter 6 and Appendix A, I discuss in detail about how I perform these measurements in $PbZr_{0.2}Ti_{0.8}O_3$ thin films.

2.3 Ginzburg-Landau-Devonshire Theory of Ferroelectric Thin Films

Phenomenological Ginzburg-Landau-Devonshire (GLD) models, which describe the equilibrium behavior of ferroelectric systems near a phase transition, have been widely used in the study of ferroelectrics to understand their equilibrium domain structure and properties. In such phenomenological models, the free energy of the system near a phase transition can be expanded into a power series of the order parameter (*i.e.*, polarization *P*) with expansion coefficients from experiment or first-principles calculations [62,63]. Minimizing the free energy with respect to *P* begets the equilibrium state of the system that allows the understanding of the symmetry and properties of ferroelectrics. Although the GLD model only predicts macroscopic properties, the

versatility of this method allows one to study the effect of temperature, strain, and other macroscopic parameters on the structure and properties of ferroelectrics, which makes it particularly useful in the study of ferroelectric thin films. In this Section, I discuss the methodology of how to modify the GLD model such that it can be applied to the study of equilibrium domain structures and dielectric properties in ferroelectric $PbZr_{1-x}Ti_xO_3$ films with different crystallographic orientations. In particular, I discuss the treatment within the framework of both monodomain and polydomain structures.

2.3.1 Thermodynamic Analysis of Monodomain Models

Here, I consider the case of single-crystal, epitaxial thin films of the ferroelectric $PbZr_{1-x}Ti_xO_3$ grown in the cubic paraelectric state on semi-infinite, cubic (001)-, (110)-, and (111)-oriented substrates. During cooling from the growth temperature the paraelectric-to-ferroelectric transition takes place, resulting in the formation of a monodomain ferroelectric state at lower temperatures. Although monodomain models are usually applied to ultra-thin films where the interfacial polarization gradient and depolarization field will be considered to ensure a more accurate simulation, a monodomain model is usually used to develop a foundation for the polydomain model and, more specifically, to develop a picture of the basic monodomain phases that are possible in the composition-strain phase diagram. Thus to simplify the analysis I will ignore the effects of interfacial polarization gradient and depolarization field and only consider the case of homogeneous polarization and strains throughout the thickness of the ferroelectric film.

Here, I utilize the sixth-order Helmholtz free-energy formalism applicable to strained ferroelectric thin films to calculate the stable polarization states and dielectric susceptibilities as a function of substrate orientation, film composition, and misfit strain. The Helmholtz free energy per unit volume F is derived from the Legendre transformation of the Gibbs free energy G via $F = G + \sum_{n=1}^{6} \sigma_n S_n$. In the crystallographic reference frame $X(x_1, x_2, x_3)$ with x_1, x_2, and x_3 along [100], [010], and [001], respectively, the modified Helmholtz free energy density $\tilde{F}$, which allows for the presence of electric field E_i (i = 1, 2, 3), can be written in terms of the polarization P_i (i = 1, 2, 3) and stresses σ_n (n = 1, 2, 3, … 6) as [62,63]

$$\tilde{F} = \alpha_1(P_1^2 + P_2^2 + P_3^2) + \alpha_{11}(P_1^4 + P_2^4 + P_3^4) + \alpha_{12}(P_1^2P_2^2 + P_2^2P_3^2 + P_1^2P_3^2) + \alpha_{111}(P_1^6 + P_2^6 + P_3^6) + \alpha_{112}[P_1^4(P_2^2 + P_3^2) + P_2^4(P_3^2 + P_1^2) + P_3^4(P_1^2 + P_2^2)] + \alpha_{123}P_1^2P_2^2P_3^2 + \frac{1}{2}s_{11}(\sigma_1^2 + \sigma_2^2 + \sigma_3^2) + s_{12}(\sigma_1\sigma_2 + \sigma_2\sigma_3 + \sigma_1\sigma_3) + \frac{1}{2}s_{44}\left(\sigma_4^2 + \sigma_5^2 + \sigma_6^2\right) - \frac{1}{2}\varepsilon_0(E_1^2 + E_2^2 + E_3^2) - E_1P_1 - E_2P_2 - E_3P_3 \quad (1)$$

where α_1 is the primary stiffness coefficient given by the Curie-Weiss law as $\frac{T-T_c}{2\varepsilon_0 C}$, α_{ij} and α_{ijk} are the higher order dielectric stiffness coefficients at constant stress, s_{mn} are the elastic compliances at constant polarization, E_i are the components of external electric field in the film, C is the Curie constant, T_c is the ferroelectric Curie temperature, and ε_0 is the permittivity of free space. The values of the above coefficients are provided in Table I of the main text [64].

In order to apply the proper mechanical boundary conditions and to simplify the analyses for (101)- and (111)-orientations, I introduce new crystallographic reference frames for both cases. For (101)-oriented films, I use the crystallographic reference frame X' (x_1', x_2', x_3') where x_1', x_2', and x_3' correspond to the $[\bar{1}01]$, $[0\bar{1}0]$, and [101] of reference frame X. Likewise for (111)-oriented films I define reference frame X'' (x_1'', x_2'', x_3'') where x_1'', x_2'', and x_3'' correspond to the $[1\bar{1}0]$, $[11\bar{2}]$, and [111] of reference frame X. In both the X' and X'' reference frames x_3' (x_3'') are defined to be perpendicular to the plane of the film and $x_1'(x_2')$ and $x_1''(x_2'')$ are aligned in the plane of the film. Using the following transformation matrices t_{ij}' and t_{ij}'', respectively:

$$t_{ij}' = \begin{bmatrix} -\frac{1}{\sqrt{2}} & 0 & \frac{1}{\sqrt{2}} \\ 0 & -1 & 0 \\ \frac{1}{\sqrt{2}} & 0 & \frac{1}{\sqrt{2}} \end{bmatrix}, \qquad (2) \qquad t_{ij}'' = \begin{bmatrix} \frac{1}{\sqrt{2}} & -\frac{1}{\sqrt{2}} & 0 \\ \frac{1}{\sqrt{6}} & \frac{1}{\sqrt{6}} & -\frac{2}{\sqrt{6}} \\ \frac{1}{\sqrt{3}} & \frac{1}{\sqrt{3}} & \frac{1}{\sqrt{3}} \end{bmatrix}, \qquad (3)$$

P_i and σ_n in the reference frame X can be expressed in terms of P_i', σ_n' and P_i'', σ_n'' in the reference frames X' and X'', respectively, via the relation $\mathbf{P} = \left(t_{ij}'\right)^{-1}\mathbf{P}'$, $\mathbf{K} = \left(t_{ij}'\right)^{-1} \cdot \mathbf{K}' \cdot t_{ij}'$ and $\mathbf{P} = \left(t_{ij}''\right)^{-1}\mathbf{P}''$, $\mathbf{K} = \left(t_{ij}''\right)^{-1} \cdot \mathbf{K}'' \cdot t_{ij}''$, where $\mathbf{P}$, $\mathbf{P}'$, and $\mathbf{P}''$ are polarization and $\mathbf{K}$, $\mathbf{K}'$, and $\mathbf{K}''$ are stress tensor matrices in the reference frames X, X', and X'', respectively. Thus the free energy $\tilde{F}$ can be transformed to free energy $\tilde{F}'$ and $\tilde{F}''$ in terms of P_i', σ_n' and P_i'', σ_n'' in the reference frames X' and X'', where P_1', P_2', and P_3' and P_1'', P_2'', and P_3'' are along x_1', x_2', and x_3' and x_1'', x_2'', and x_3'' in reference frames X' and X'', respectively. The explicit formalism of $\tilde{F}'$ and $\tilde{F}''$ are rather complex and long and thus for brevity I provide those in simplified in equations (4) and (5) using $\widetilde{\mathbf{P}}'$, $\widetilde{\mathbf{K}}'$ and $\widetilde{\mathbf{P}}''$, $\widetilde{\mathbf{K}}''$ to represent the matrices $\left(t_{ij}'\right)^{-1}\mathbf{P}'$, $\left(t_{ij}'\right)^{-1} \cdot \mathbf{K}' \cdot t_{ij}'$ and $\left(t_{ij}''\right)^{-1}\mathbf{P}''$, $\left(t_{ij}''\right)^{-1} \cdot \mathbf{K}'' \cdot t_{ij}''$, respectively:

$$\begin{aligned}\tilde{F}' = {} & \alpha_1\left(\widetilde{\mathbf{P}}'^2_{1,1} + \widetilde{\mathbf{P}}'^2_{2,1} + \widetilde{\mathbf{P}}'^2_{3,1}\right) + \alpha_{11}\left(\widetilde{\mathbf{P}}'^4_{1,1} + \widetilde{\mathbf{P}}'^4_{2,1} + \widetilde{\mathbf{P}}'^4_{3,1}\right) + \alpha_{12}\left(\widetilde{\mathbf{P}}'^2_{1,1}\widetilde{\mathbf{P}}'^2_{2,1} + \widetilde{\mathbf{P}}'^2_{2,1}\widetilde{\mathbf{P}}'^2_{3,1} + \widetilde{\mathbf{P}}'^2_{1,1}\widetilde{\mathbf{P}}'^2_{3,1}\right) + \\ & \alpha_{111}\left(\widetilde{\mathbf{P}}'^6_{1,1} + \widetilde{\mathbf{P}}'^6_{2,1} + \widetilde{\mathbf{P}}'^6_{3,1}\right) + \alpha_{112}\left[\widetilde{\mathbf{P}}'^4_{1,1}\left(\widetilde{\mathbf{P}}'^2_{2,1} + \widetilde{\mathbf{P}}'^2_{3,1}\right) + \widetilde{\mathbf{P}}'^4_{2,1}\left(\widetilde{\mathbf{P}}'^2_{3,1} + \widetilde{\mathbf{P}}'^2_{1,1}\right) + \widetilde{\mathbf{P}}'^4_{3,1}\left(\widetilde{\mathbf{P}}'^2_{1,1} + \widetilde{\mathbf{P}}'^2_{2,1}\right)\right] + \\ & \alpha_{123}\widetilde{\mathbf{P}}'^2_{1,1}\widetilde{\mathbf{P}}'^2_{2,1}\widetilde{\mathbf{P}}'^2_{3,1} + \frac{1}{2}s_{11}\left(\widetilde{\mathbf{K}}'^2_{1,1} + \widetilde{\mathbf{K}}'^2_{2,2} + \widetilde{\mathbf{K}}'^2_{3,3}\right) + s_{12}\left(\widetilde{\mathbf{K}}'_{1,1}\widetilde{\mathbf{K}}'_{2,2} + \widetilde{\mathbf{K}}'_{2,2}\widetilde{\mathbf{K}}'_{3,3} + \widetilde{\mathbf{K}}'_{1,1}\widetilde{\mathbf{K}}'_{3,3}\right) + \\ & \frac{1}{2}s_{44}\left(\widetilde{\mathbf{K}}'^2_{2,3} + \widetilde{\mathbf{K}}'^2_{1,3} + \widetilde{\mathbf{K}}'^2_{1,2}\right) - \frac{1}{2}\varepsilon_0(E'^2_1 + E'^2_2 + E'^2_3) - E_1'P_1' - E_2'P_2' - E_3'P_3' \end{aligned} \qquad (4)$$

$$\begin{aligned}\tilde{F}'' = {} & \alpha_1\left(\widetilde{\mathbf{P}}''^2_{1,1} + \widetilde{\mathbf{P}}''^2_{2,1} + \widetilde{\mathbf{P}}''^2_{3,1}\right) + \alpha_{11}\left(\widetilde{\mathbf{P}}''^4_{1,1} + \widetilde{\mathbf{P}}''^4_{2,1} + \widetilde{\mathbf{P}}''^4_{3,1}\right) + \alpha_{12}\left(\widetilde{\mathbf{P}}''^2_{1,1}\widetilde{\mathbf{P}}''^2_{2,1} + \widetilde{\mathbf{P}}''^2_{2,1}\widetilde{\mathbf{P}}''^2_{3,1} + \right. \\ & \left.\widetilde{\mathbf{P}}''^2_{1,1}\widetilde{\mathbf{P}}''^2_{3,1}\right) + \alpha_{111}\left(\widetilde{\mathbf{P}}''^6_{1,1} + \widetilde{\mathbf{P}}''^6_{2,1} + \widetilde{\mathbf{P}}''^6_{3,1}\right) + \alpha_{112}\left[\widetilde{\mathbf{P}}''^4_{1,1}\left(\widetilde{\mathbf{P}}''^2_{2,1} + \widetilde{\mathbf{P}}''^2_{3,1}\right) + \widetilde{\mathbf{P}}''^4_{2,1}\left(\widetilde{\mathbf{P}}''^2_{3,1} + \widetilde{\mathbf{P}}''^2_{1,1}\right) + \right. \\ & \left.\widetilde{\mathbf{P}}''^4_{3,1}\left(\widetilde{\mathbf{P}}''^2_{1,1} + \widetilde{\mathbf{P}}''^2_{2,1}\right)\right] + \alpha_{123}\widetilde{\mathbf{P}}''^2_{1,1}\widetilde{\mathbf{P}}''^2_{2,1}\widetilde{\mathbf{P}}''^2_{3,1} + \frac{1}{2}s_{11}\left(\widetilde{\mathbf{K}}''^2_{1,1} + \widetilde{\mathbf{K}}''^2_{2,2} + \widetilde{\mathbf{K}}''^2_{3,3}\right) + s_{12}\left(\widetilde{\mathbf{K}}''_{1,1}\widetilde{\mathbf{K}}''_{2,2} + \right. \\ & \left.\widetilde{\mathbf{K}}''_{2,2}\widetilde{\mathbf{K}}''_{3,3} + \widetilde{\mathbf{K}}''_{1,1}\widetilde{\mathbf{K}}''_{3,3}\right) + \frac{1}{2}s_{44}\left(\widetilde{\mathbf{K}}''^2_{2,3} + \widetilde{\mathbf{K}}''^2_{1,3} + \widetilde{\mathbf{K}}''^2_{1,2}\right) - \frac{1}{2}\varepsilon_0(E''^2_1 + E''^2_2 + E''^2_3) - E''_1P''_1 - \\ & E''_2P''_2 - E''_3P''_3 \end{aligned} \qquad (5)$$

where E_i' and E_i'' are components of external electric field in the reference frames X' and X''. Thus it is possible to eliminate all the stress σ_n (σ_n' or σ_n'') from the $\tilde{F}$ ($\tilde{F}'$or $\tilde{F}''$) using the following mechanical boundary conditions:

(001)-oriented films:

$$S_1 = S_2 = u_m, \quad S_6 = 0, \tag{6}$$

$$\sigma_3 = \sigma_4 = \sigma_5 = 0, \tag{7}$$

(101)-oriented films:

$$S_1' = S_2' = u_m', \quad S_6' = 0, \tag{8}$$

$$\sigma_3' = \sigma_4' = \sigma_5' = 0, \tag{9}$$

(111)-oriented films:

$$S_1'' = S_2'' = u_m'', \quad S_6'' = 0, \tag{10}$$

$$\sigma_3'' = \sigma_4'' = \sigma_5'' = 0, \tag{11}$$

where S_n, S_n', and S_n'' refer to strain components in the reference frames X, X', and X'' for (001)-, (101)-, and (111)-oriented systems, respectively, and u_m, u_m', and u_m'' refer to the in-plane misfit strain from the substrate with respect to the growth plane in (001)-, (101)-, and (111)-oriented films, respectively. Performing the minimization of $\tilde{F}$ ($\tilde{F}'$or $\tilde{F}''$) in terms of P_i (P_i' or P_i'') in the absence of electric field, I can find the equilibrium polarizations states as a function of misfit strain and film compositions for each film orientation, which allows for the generation of orientation-dependent, composition-strain phase diagrams.

2.3.2 Thermodynamic Analysis of Polydomain Models

In the framework of the polydomain models, I consider epitaxial thin films of the ferroelectric $PbZr_{1-x}Ti_xO_3$, which are grown in the cubic, paraelectric state on semi-infinite, cubic (001)-, (110)-, and (111)-oriented substrates, with a thickness greater than the critical thickness for domain formation. During cooling from the growth temperature (T_g) the paraelectric-to-ferroelectric phase transition takes place, resulting in the formation of either a single-domain or a polydomain state at lower temperatures. Here, to simplify the analysis, I neglect the strain accommodation by the generation of misfit dislocations and domain wall self-energy due to the rather small width of the domain-wall structures as opposed to the film thickness (consistent to prior work on similar models) [14,63,51]. Additionally, in the case of the thick films considered in such models, I also neglect polarization gradient effects near the substrate interface or film surface and, instead, assume homogeneous polarization and strains throughout the thickness of the film (again consistent with prior work in the field that assumes that the thickness of the interfacial layers is relatively small as compared to the total film thickness). Additionally, I impose a short-circuit boundary condition to the system as would be present in a capacitor structure with high-carrier-density metal contacts, thereby negating the depolarization fields in the film.

For our formalism I utilize the Helmholtz free energy applicable to ferroelectric films with dense domain structures [14,63] to calculate the domain structures and dielectric susceptibilities as

a function of substrate orientation and mismatch strain. The Helmholtz free energy F is derived from the Legendre transformation of the Gibbs free energy G via $F = G + \sum_{n=1}^{6} \sigma_n S_n$. In the crystallographic reference frame X (x_1, x_2, x_3) with x_1, x_2, and x_3 along [100], [010], and [001], respectively, the modified Helmholtz free energy density $\tilde{F}$ can be written in terms of the polarization P_i and stresses σ_n as [62,14]

$$\tilde{F} = \alpha_1(P_1^2 + P_2^2 + P_3^2) + \alpha_{11}(P_1^4 + P_2^4 + P_3^4) + \alpha_{12}(P_1^2P_2^2 + P_2^2P_3^2 + P_1^2P_3^2) + \alpha_{111}(P_1^6 + P_2^6 + P_3^6) + \alpha_{112}[P_1^4(P_2^2 + P_3^2) + P_2^4(P_3^2 + P_1^2) + P_3^4(P_1^2 + P_2^2)] + \alpha_{123}P_1^2P_2^2P_3^2 + \frac{1}{2}s_{11}(\sigma_1^2 + \sigma_2^2 + \sigma_3^2) + s_{12}(\sigma_1\sigma_2 + \sigma_2\sigma_3 + \sigma_1\sigma_3) + \frac{1}{2}s_{44}(\sigma_4^2 + \sigma_5^2 + \sigma_6^2) - \frac{1}{2}\varepsilon_0(E_1^2 + E_2^2 + E_3^2) - E_1P_1 - E_2P_2 - E_3P_3 \quad (12)$$

where α_1, α_{ij}, and α_{ijk} are the dielectric stiffnesses at constant stress, s_{mn} are the elastic compliances at constant polarization, Q_{ij} are the electrostrictive constants of the paraelectric phase, and E_i are the components of external electric field in the film. The values of the above coefficients are provided in Table 2.2 [64]:

Table 2.2. Values of thermodynamic coefficients for $PbZr_{1-x}Ti_xO_3$ (x = 1.0, 0.9, 0.8, 0.7 ,0.6, 0.5) used in the Ginzburg-Landau-Devonshire modeling at T = 300 K.

Parameters	**1.0**	**0.9**	**0.8**	**0.7**	**0.6**	**0.5**
$a_1(10^8\ C^{-2}\cdot m^2\cdot N)$	-1.75	-1.64	-1.49	-1.24	-0.83	-0.49
$a_{11}(10^7\ C^{-4}\cdot m^6\cdot N)$	-7.25	-5.85	-3.05	0.65	3.61	4.76
$a_{12}(10^8\ C^{-4}\cdot m^6\cdot N)$	7.50	7.06	6.32	5.11	3.23	1.74
$a_{111}(10^8\ C^{-6}\cdot m^{10}\cdot N)$	2.6	2.52	2.48	2.35	1.86	1.34
$a_{112}(10^8\ C^{-6}\cdot m^{10}\cdot N)$	6.1	8.10	9.68	10.25	8.50	6.13
$a_{123}(10^9\ C^{-6}\cdot m^{10}\cdot N)$	-3.66	-4.36	-4.90	-5.00	-4.06	-2.89
$s_{11}(10^{-12}\ m^2\cdot N^{-1})$	8.0	8.1	8.2	8.4	8.6	10.5
$s_{12}(10^{-12}\ m^2\cdot N^{-1})$	-2.5	-2.5	-2.6	-2.7	-2.8	-3.7
$s_{44}(10^{-12}\ m^2\cdot N^{-1})$	9.00	12.0	14.4	17.5	21.2	28.7

Similar to the monodomain models, in order to apply the proper mechanical boundary conditions and to simplify the analyses for (101)- and (111)-orientations, I introduce new crystallographic reference frames for both cases. For (101)-oriented films, I use the crystallographic reference frame X' (x_1', x_2', x_3') where x_1', x_2', and x_3' correspond to the $[\bar{1}01]$, $[0\bar{1}0]$, and [101] of reference frame X. Likewise for (111)-oriented films I define reference frame

$X''(x_1'', x_2'', x_3'')$ where x_1'', x_2'', and x_3'' correspond to the $[1\bar{1}0]$, $[11\bar{2}]$, and [111] of reference frame X. In both the X' and X'' reference frames x_3', x_3'' are defined to be perpendicular to the plane of the film and $x_1'(x_2')$, $x_1''(x_2'')$ are aligned in the plane of the film. Thus the free energy (G and $\tilde{F}$) can be rewritten as G' and $\tilde{F}'$ or G'' and $\tilde{F}''$ in terms of P_i', σ_n' and P_i'', σ_n'' in the reference frame X' and X'' using the following transformation matrices t_{ij}' and t_{ij}'', respectively [65,66]:

$$t_{ij}' = \begin{bmatrix} -\frac{1}{\sqrt{2}} & 0 & \frac{1}{\sqrt{2}} \\ 0 & -1 & 0 \\ \frac{1}{\sqrt{2}} & 0 & \frac{1}{\sqrt{2}} \end{bmatrix}, \qquad (13) \qquad t_{ij}'' = \begin{bmatrix} \frac{1}{\sqrt{2}} & -\frac{1}{\sqrt{2}} & 0 \\ \frac{1}{\sqrt{6}} & \frac{1}{\sqrt{6}} & -\frac{2}{\sqrt{6}} \\ \frac{1}{\sqrt{3}} & \frac{1}{\sqrt{3}} & \frac{1}{\sqrt{3}} \end{bmatrix}. \qquad (14)$$

The explicit expressions of G' and $\tilde{F}'$ or G'' and $\tilde{F}''$ are cumbersome and thus here I only list the formalisms after applying the numerical values of the thermodynamic coefficients:

$$G' = -1.5\times10^8(P_1'^2 + P_2'^2 + P_3'^2) + 1.4\times10^8(P_1'^4 - 0.2P_2'^4 + P_3'^4) + 6.3\times10^8(P_1'^2P_2'^2 + P_2'^2P_3'^2 - 0.65P_1'^2P_3'^2) + 3.0\times10^8(P_1'^6 + 0.83P_2'^6 + P_3'^6) - 7.4\times10^8P_1'^4(P_2'^2 - 0.93P_3'^2) + 9.7\times10^8P_2'^4(P_1'^2 + P_3'^2) - 7.4\times10^8P_3'^4(P_2'^2 - 0.93P_1'^2) + 5.4\times10^9P_1'^2P_2'^2P_3'^2 - 3.2\times10^{-12}(\sigma_1'^2 + 1.3\sigma_2'^2 + \sigma_3'^2) - 7.2\times10^{-12}\left(\sigma_4'^2 + 1.5\sigma_5'^2 + \sigma_6'^2\right) + 2.6\times10^{-12}(\sigma_1'\sigma_2' + 3.0\sigma_1'\sigma_3' + \sigma_2'\sigma_3') - 0.045\sigma_1'(P_1'^2 - 0.53P_2'^2 + 0.27P_3'^2) + 0.024\sigma_2'(P_1'^2 - 3.38P_2'^2 + P_3'^2) - 0.012\sigma_3'(P_1'^2 - 2P_2'^2 + 3.75P_3'^2) - 0.064\ (\sigma_4'P_2'P_3' + 3.28\sigma_5'P_1'P_3' + \sigma_6'P_1'P_2') \qquad (15)$$

$$\tilde{F}' = -1.5\times10^8(P_1'^2 + P_2'^2 + P_3'^2) + 1.4\times10^8(P_1'^4 - 0.2P_2'^4 + P_3'^4) + 3.0\times10^8(P_1'^6 + 0.83P_2'^6 + P_3'^6) + 6.3\times10^8(P_1'^2P_2'^2 + P_2'^2P_3'^2 - 0.65P_1'^2P_3'^2) - 7.4\times10^8P_1'^4(P_2'^2 - 0.93P_3'^2) + 9.7\times10^8P_2'^4(P_1'^2 + P_3'^2) - 7.4\times10^8P_3'^4(P_2'^2 - 0.93P_1'^2) + 5.4\times10^9P_1'^2P_2'^2P_3'^2 + 3.2\times10^{-12}(\sigma_1'^2 + 1.3\sigma_2'^2 + \sigma_3'^2) + 7.2\times10^{-12}\left(\sigma_4'^2 + 1.5\sigma_5'^2 + \sigma_6'^2\right) - 2.6\times10^{-12}(\sigma_1'\sigma_2' + 3.0\sigma_1'\sigma_3' + \sigma_2'\sigma_3') - 4.4\times10^{-12}(E_1'^2 + E_2'^2 + E_3'^2) - (P_1'E_1' + P_2'E_2' + P_3'E_3') \qquad (16)$$

$$G'' = -1.5\times10^8(P_1''^2 + P_2''^2 + P_3''^2) + 1.4\times10^8(P_1''^4 + P_2''^4 + 0.2P_3''^4) + 3.0\times10^8(P_1''^6 + 0.57P_2''^6 + 2P_3''^6) - 6.1\times10^8(P_1''^2P_3''^2 + P_2''^2P_3''^2 - 0.48P_1''^2P_2''^2) + 0.016P_2''P_3''^3 + 3.0\times10^8P_2''^3P_3'' - 3.0\times10^8P_1''^2P_2''P_3'' - 2.7\times10^8P_1''^4(P_2''^2 - 0.78P_3''^2) + 2.1\times10^8P_2''^4(P_3''^2 + 0.81P_1''^2) + 1.6\times10^9P_3''^4(P_1''^2 + P_2''^2) + 0.031P_1''P_2''P_3''^4 + 1.3\times10^9P_1''^4P_2''P_3'' + 9.0\times10^8P_1''^2(P_2''^3P_3''^1 - 1.56P_2''^3P_3''^1) + 0.062P_1''P_2''^2P_3''^3 + 0.062P_2''P_3''^5 - 4.5\times10^8P_2''^5P_3'' + 0.094P_1''P_3''^5 + 48\times10^8P_2''^3P_3''^3 + 4.2\times10^8P_1''^2P_2''^2P_3''^2 - 3.2\times10^{-12}(\sigma_1''^2 + \sigma_2''^2 - 0.9\sigma_3''^2) - 9.6\times10^{-12}\left(\sigma_4''^2 + \sigma_5''^2 + 0.875\sigma_6''^2\right) + 2.0\times10^{-12}(\sigma_1''\sigma_2'' + 0.7\sigma_1''\sigma_3'' + 0.7\sigma_2''\sigma_3'' - 0.85\sigma_1''\sigma_4'' + 0.85\sigma_2''\sigma_4'' - 1.7\sigma_5''\sigma_6'') - 0.045\sigma_1''(P_1''^2 - 0.27P_2''^2 - 0.035P_2''P_3'') + 0.012\sigma_2''(P_1''^2 - 3.75P_2''^2 + 2.9P_2''P_3'') - 1.4\times10^{-4}\sigma_3''(P_1''^2 + P_2''^2 + 228P_3''^2) - 0.035\sigma_4''(P_1''^2 - P_2''^2 + 4.6P_2''P_3'') - 0.07\sigma_5''(P_1''P_2'' + 2.29P_1''P_3'') - 0.11\sigma_6''(P_1''P_2'' + 0.63P_1''P_3'') \qquad (17)$$

$$\tilde{F}'' = -1.5\times10^{8}(P_1''^2+P_2''^2+P_3''^2)+1.4\times10^{8}(P_1''^4+P_2''^4+0.2P_3''^4)+3.0\times10^{8}(P_1''^6+0.57P_2''^6+2P_3''^6)-6.1\times10^{8}(P_1''^2P_3''^2+P_2''^2P_3''^2-0.48P_1''^2P_2''^2)+0.016P_2''P_3''^3+3.0\times10^{8}P_2''^3P_3''-3.0\times10^{8}P_1''^2P_2''P_3''-2.7\times10^{8}P_1''^4(P_2''^2-0.78P_3''^2)+2.1\times10^{8}P_2''^4(P_3''^2+0.81P_1''^2)+1.6\times10^{9}P_3''^4(P_1''^2+P_2''^2)+0.031P_1''P_2''P_3''^4+1.3\times10^{9}P_1''^4P_2''P_3''+9.0\times10^{8}P_1''^2(P_2''^3P_3''^1-1.56P_2''^3P_3''^1)+0.062P_1''P_2''^2P_3''^3+0.062P_2''P_3''^5-4.5\times10^{8}P_2''^5P_3''+0.094P_1''P_3''^5+48\times10^{8}P_2''^3P_3''^3+4.2\times10^{8}P_1''^2P_2''^2P_3''^2+3.2\times10^{-12}(\sigma_1''^2+\sigma_2''^2-0.9\sigma_3''^2)+9.6\times10^{-12}\left(\sigma_4''^2+\sigma_5''^2+0.875\sigma_6''^2\right)-2.0\times10^{-12}(\sigma_1''\sigma_2''+0.7\sigma_1''\sigma_3''+0.7\sigma_2''\sigma_3''-0.85\sigma_1''\sigma_4''+0.85\sigma_2''\sigma_4''-1.7\sigma_5''\sigma_6'')-4.4\times10^{-12}(E_1''^2+E_2''^2+E_3''^2)-(P_1''E_1''+P_2''E_2''+P_3''E_3'') \quad (18)$$

For polydomain structures, the thermodynamic equilibrium state can be described by the average free-energy density $\langle\tilde{F}\rangle$ which can be written as $\langle\tilde{F}\rangle=\sum_{k=1}^{n}\phi_k F_k$, $\langle\tilde{F}'\rangle=\sum_{k=1}^{n}\phi_k' F_k'$, and $\langle\tilde{F}''\rangle=\sum_{k=1}^{n}\phi_k'' F_k''$ for the (001)-, (101)-, and (111)-oriented films, respectively. In these equations, ϕ_k (ϕ_k' or ϕ_k'') are the volume fraction of the k^{th} domain type and F_k (F_k' or F_k'') are the energy density within the k^{th} domain. It is possible to eliminate the stresses σ_n (σ_n' or σ_n'') from the $\langle\tilde{F}\rangle$ ($\langle\tilde{F}'\rangle$ or $\langle\tilde{F}''\rangle$) using the following mechanical boundary conditions:

For (001)-oriented films:

$$\langle S_1\rangle=\sum_{k=1}^{n}\phi_k S_1^k=u_m,\quad \langle S_2\rangle=\sum_{k=1}^{n}\phi_k S_2^k=u_m,\quad \langle S_6\rangle=\sum_{k=1}^{n}\phi_k S_6^k=0, \quad (19)$$

$$\langle\sigma_3\rangle=\langle\sigma_4\rangle=\langle\sigma_5\rangle=0, \quad (20)$$

For (101)-oriented films:

$$\langle S_1'\rangle=\sum_{k=1}^{n}\phi_k' S'^k_1=u_m',\quad \langle S_2'\rangle=\sum_{k=1}^{n}\phi_k' S'^k_2=u_m',\quad \langle S_6'\rangle=\sum_{k=1}^{n}\phi_k' S'^k_6=0, \quad (21)$$

$$\langle\sigma_3'\rangle=\langle\sigma_4'\rangle=\langle\sigma_5'\rangle=0, \quad (22)$$

For (111)-oriented films:

$$\langle S_1''\rangle=\sum_{k=1}^{n}\phi_k'' S''^k_1=u_m'',\quad \langle S_2''\rangle=\sum_{k=1}^{n}\phi_k'' S''^k_2=u_m'',\quad \langle S_6''\rangle=\sum_{k=1}^{n}\phi_k'' S''^k_6=0, \quad (23)$$

$$\langle\sigma_3''\rangle=\langle\sigma_4''\rangle=\langle\sigma_5''\rangle=0, \quad (24)$$

where S_n^k (S'^k_n and S''^k_n) refers to the strain components in the k^{th} domain which can be derived from $S_n=-\frac{\partial G}{\partial\sigma_n}$ ($S_n'=-\frac{\partial G'}{\partial\sigma_n'}$ or $S_n''=-\frac{\partial G''}{\partial\sigma_n''}$) and u_m (u_m' or u_m'') refers to the in-plane misfit strain with respect to the growth plane. In polydomain films, these macroscopic conditions must be supplemented by the microscopic boundary conditions related to the presence of the domain walls. To achieve this, I create a local reference frame Y (y_1, y_2, y_3) with y_3 perpendicular to the domain walls and thus the strain compatibility in the neighboring domains implies

$$S_{n'}^k=S_{n'}^{k+1}\ (S'^k_{n'}=S'^{k+1}_{n'}\text{ or }S''^k_{n'}=S''^{k+1}_{n'})\ (\text{n = 1, 2, 6}) \quad (25)$$

and the mechanical equilibrium of the domains implies that the stress components are related as

$$\sigma_{n'}^k=\sigma_{n'}^{k+1}\ (\sigma'^k_{n'}=\sigma'^{k+1}_{n'}\text{ or }\sigma''^k_{n'}=\sigma''^{k+1}_{n'})\ (\text{n = 3, 4, 5}). \quad (26)$$

In addition, I can set the average electric field $\langle E_i \rangle$ ($\langle E_i' \rangle$ or $\langle E_i'' \rangle$) to be zero in the case of the short-circuit boundary conditions and in the absence of a depolarization field. The microscopic electric field continuity equation thus yields the following boundary conditions:

$$E_{1'}^{k} = E_{1'}^{k+1} \; (E'^{k}_{1'} = E'^{k+1}_{1'} \text{or } E''^{k}_{1'} = E''^{k+1}_{1'}), \tag{27}$$

$$E_{2'}^{k} = E_{2'}^{k+1} \; (E'^{k}_{2'} = E'^{k+1}_{2'} \text{or } E''^{k}_{2'} = E''^{k+1}_{2'}), \tag{28}$$

$$\varepsilon_0 E_{3'}^{k} + P_{3'}^{k} = \varepsilon_0 E_{3'}^{k+1} + P_{3'}^{k+1} \; (\varepsilon_0 E'^{k}_{3'} + P'^{k}_{3'} = \varepsilon_0 E'^{k+1}_{3'} + P'^{k+1}_{3'} \text{ or}$$

$$\varepsilon_0 E''^{k}_{3'} + P''^{k}_{3'} = \varepsilon_0 E''^{k+1}_{3'} + P''^{k+1}_{3'}). \tag{29}$$

The above relations make it possible to rewrite the free-energy density for each film orientation in terms of polarization components P_i^k (P'^{k}_{i} or P''^{k}_{i}) and domain volume fractions ϕ_k (ϕ_k' or ϕ_k''). Performing the minimization of $\langle \tilde{F} \rangle$ ($\langle \tilde{F}' \rangle$ and $\langle \tilde{F}'' \rangle$), it can be found that the equilibrium polarizations and domain populations as a function of mismatch strain ($u_m = (b - a_p)/b$, where b is the lattice parameter of the substrate and a_p is the lattice parameter of the cubic paraelectric phase of the film) for the respective film orientations [51]. This thermodynamic theory also allows for the calculation of the out-of-plane dielectric permittivity ($\varepsilon_\perp$, $\varepsilon_\perp'$, $\varepsilon_\perp''$ for (001)-, (101)-, and (111)-oriented films, respectively) as the sum of the intrinsic (the first term) and the motional extrinsic (the second term) contributions as

$$\varepsilon_\perp = \sum_k \phi_k \cdot \frac{dP_3}{dE_3} + \sum_k P_3^k \cdot \frac{d\phi_k}{dE_3} \;, \tag{30}$$

$$\varepsilon_\perp' = \sum_k \phi_k' \cdot \frac{dP_3'}{dE_3'} + \sum_k P_3'^k \cdot \frac{d\phi_k'}{dE_3'} \,, \tag{31}$$

$$\varepsilon_\perp'' = \sum_k \phi_k'' \cdot \frac{dP_3''}{dE_3''} + \sum_k P_3''^k \cdot \frac{d\phi_k''}{dE_3''} \;. \tag{32}$$

Here the intrinsic dielectric susceptibility can be described as the reversible variation of polarization P_i (P_i' or P_i'') with varying electric field E_j (E_j' or E_j'') $\chi_{ij} = \frac{dP_i}{dE_j}$ ($\chi_{ij}' = \frac{dP_i'}{dE_j'}$ or $\chi_{ij}'' = \frac{dP_i''}{dE_j''}$). With the relation $E_i = \frac{d\tilde{F}}{dP_i}$ ($E_i' = \frac{d\tilde{F}'}{dP_i'}$ or $E_i'' = \frac{d\tilde{F}''}{dP_i''}$), I can further use differentiation of free energy to derive the expression for the dielectric susceptibility. Using the inversion of the reciprocal dielectric susceptibility matrix ($\boldsymbol{\Theta} = [\eta_{ij}]$, $\boldsymbol{\Theta}' = [\eta_{ij}']$, $\boldsymbol{\Theta}'' = [\eta_{ij}'']$ for (001)-, (101)-, and (111)-oriented films, respectively, where $\eta_{ij} = \frac{\partial^2 \tilde{F}}{\partial P_i \partial P_j}$ and $\eta_{ij}' = \frac{\partial^2 \tilde{F}'}{\partial P_i' \partial P_j'}$ and $\eta_{ij}'' = \frac{\partial^2 \tilde{F}''}{\partial P_i'' \partial P_j''}$), I find the dielectric susceptibility as $\chi_{ij} = \boldsymbol{\Theta}_{i,j}^{-1}$ ($\chi_{ij}' = \boldsymbol{\Theta}_{i,j}'^{-1}$ or $\chi_{ij}'' = \boldsymbol{\Theta}_{i,j}''^{-1}$) and thus the relative dielectric permittivity as $\varepsilon_{ij}^{int} = \chi_{ij} + 1$ ($\varepsilon_{ij}^{int\prime} = \chi_{ij}' + 1$ or $\varepsilon_{ij}^{int\prime\prime} = \chi_{ij}'' + 1$). For the film geometry considered in this work, I will only study the out-of-plane dielectric permittivity (ε_{33}^{int}, $\varepsilon_{33}^{int\prime}$, $\varepsilon_{33}^{int\prime\prime}$) using the explicit expression for dielectric permittivity obtained by performing

the inversion of the reciprocal dielectric susceptibility matrix ($\varepsilon_{33}^{int} = \frac{(\eta_{11}+\eta_{12})}{[\eta_{33}(\eta_{11}+\eta_{12})-2\eta_{13}^2]} + 1$, $\varepsilon_{33}^{int\prime} = \frac{(\eta'_{11}+\eta'_{12})}{[\eta'_{33}(\eta'_{11}+\eta'_{12})-2\eta'^2_{13}]} + 1$, $\varepsilon_{33}^{int\prime\prime} = \frac{(\eta''_{11}+\eta''_{12})}{[\eta''_{33}(\eta''_{11}+\eta''_{12})-2\eta''^2_{13}]} + 1$ for (001)-, (101)-, and (111)-oriented films, respectively). For (001)-oriented films, the second term can be expanded as $\sum_k P_3^k \cdot \frac{d\phi_k}{dE_3} = P_3^1 \cdot \frac{d\phi_1}{dE_3} + P_3^2 \cdot \frac{d\phi_2}{dE_3}$, where $k = 1$ represents the in-plane polarized *a* domains and $k = 2$ represents the out-of-plane polarized *c* domains. For *a* domains, the polarization along the [001] (P_3^1) is absent which can simplify $\sum_k P_3^k \cdot \frac{d\phi_k}{dE_3}$ to be $P_3^2 \cdot \frac{d\phi_2}{dE_3}$. In addition, ϕ_2 is known to be $1 - \frac{(s_{11}-s_{12})(u_{\mathrm{m}}-Q_{12}P_s^2)}{s_{11}(Q_{11}-Q_{12})P_s^2} + \frac{E_3(s_{11}^2-s_{12}^2)}{s_{11}(Q_{11}-Q_{12})^2P_s^3}$ by minimizing the total free energy, where $P_{\mathrm{s}} = P_3^2$. Thus, $P_3^2 \cdot \frac{d\phi_2}{dE_3}$ can be re-written as $\frac{(s_{11}^2-s_{12}^2)}{s_{11}(Q_{11}-Q_{12})^2P_s^2}$, which is the analytic formula for the motional, extrinsic contribution in (001)-oriented films. For (101)-oriented films, however, the formula of ϕ'_k is very cumbersome after performing the transformation matrix in the free energy of (101)-oriented system. Thus, I only obtained numerical solutions for $\frac{d\phi'_k}{dE'_3}$. For (111)-oriented films, ϕ''_k turns out to be independent on the electric field where $\frac{d\phi''_k}{dE''_3}$ is zero which indicates the absence of motional, extrinsic contributions in (111)-oriented films. Therefore, the intrinsic and the motional, extrinsic contributions to the dielectric permittivity can be calculated numerically in various strain regimes via such thermodynamic analyses. The details regarding the calculation and analysis for the phase diagrams and dielectric response will be discussed in Chapter 3.

CHAPTER 3

Orientation-dependent Structural Phase Diagrams and Dielectric Properties of Polydomain $PbZr_{1-x}Ti_xO_3$ Thin Films

In this Chapter, I investigate the orientation-dependent equilibrium ferroelectric domain structures and dielectric properties of polydomain $PbZr_{1-x}Ti_xO_3$ thin films using a phenomenological Ginzburg-Landau-Devonshire thermodynamic model. I develop and describe three-dimensional, polydomain models for (001)-, (101)-, and (111)-oriented films and explore the evolution of the structure and dielectric permittivity of the system as a function of epitaxial strain across the composition range $0.5 \leq x \leq 1.0$. Our studies reveal that the film orientation, epitaxial strain, and composition can be combined in unexpected ways to drive exotic phase stability and transformations which have intriguing implications for the properties. In particular, in (101)- and (111)-oriented films, the application of epitaxial strains along non-$\langle 001 \rangle$-type crystallographic directions significantly reduces the stability range of the parent tetragonal phase (which is dominant in (001)-oriented films) and results in a variety of new symmetries. I also observe that the film orientation can be used to tune the relative fraction of intrinsic (*i.e.*, within a domain) and extrinsic (*i.e.*, from domain-wall motion) contributions to the dielectric permittivity. Ultimately these studies reveal how composition, epitaxial strain, and film orientation provide for comprehensive control of the structure and properties of ferroelectrics.

3.1 Introduction

Advances in modern thin-film growth and characterization enable new modalities of strain control of ferroelectric materials that go beyond traditional lattice mismatch effects [67,48]. Recent experimental work has demonstrated that the control of film orientation is one promising and effective approach to manipulate ferroelectric domain structure and properties [68]. In studies of thin-film materials, such as the model ferroelectrics $PbZr_{1-x}Ti_xO_3$ and $BiFeO_3$, it has been noted that the variation of film orientation could result in exotic crystal and domain structures and give rise to enhanced ferroelectric susceptibilities [69-72]. In particular, recent work on (111)-oriented, tetragonal $PbZr_{0.2}Ti_{0.8}O_3$ films highlighted how domain-wall contributions to dielectric susceptibilities and ferroelectric switching characteristics can be dramatically tuned with film orientations [71,72]. In fact, varying the relative orientation of applied electric fields relative to the direction of polarization in ferroelectrics has been shown to give rise to enhanced dielectric and piezoelectric response and it has even been suggested that it could potentially give rise to frustrated poling [73-76].

The ultimate control of domain structure and properties, however, requires not only empirical observation, but the insights and understandings gleaned from theoretical simulations. To date the majority of theoretical models including Ginzburg-Landau-Devonshire theories and phase-field modeling have been developed to study the evolution of ferroelectric thin-film structures and properties that are tunable with strain, composition, temperature, and thickness. Most of these studies, however, have focused on (001)-oriented heterostructures manifested in either monodomain or polydomain states. In fact, few studies have focused on systems of different orientations [14,63,66,77-80]. For instance, thermodynamic calculations of (111)-oriented monodomain $PbTiO_3$ films have predicted the presence of a dielectric anomaly in the paraelectric state that can be tailored from standard Curie-Weiss to diffuse-type by tuning the misfit strain [81]. Furthermore, recent first-principles calculations have suggested that a complex phase transition process, tuned by epitaxial strain, can occur in (111)-oriented $PbTiO_3$ and $BaTiO_3$ films [82,83] and that an unexpected triclinic phase and three distinct monoclinic phases may be possible in (110)-oriented $BaTiO_3$ films [84]. At the same time, for (101)-oriented $PbZr_{1-x}Ti_xO_3$ films with compositions near the morphotropic phase boundary, phase-field simulations suggest that mobile two-domain configurations can enhance piezoelectricity [69]. Other phase-field simulations have also systematically studied the ferroelectric domain structures in (001)-, (101)-, and (111)-oriented $BiFeO_3$ films [65]. Despite these few examples, the vast majority of these studies focus on monodomain versions of materials which deviate from experimental (and practical) forms of these materials found in “thick” films (typically greater than just 25-50 nm) that exhibit a range of polydomain structures that result from a competition between elastic, electrostatic, domain wall, and other energies. In the prototypical ferroelectric $PbZr_{1-x}Ti_xO_3$ system, for instance, a comprehensive theoretical approach to understanding and systematically comparing the orientation-dependent domain structures, properties, and susceptibilities has not been undertaken.

In this Chapter, I develop three-dimensional, polydomain phenomenological Ginzburg-Landau-Devonshire (GLD) thermodynamic models to produce orientation-, composition-, and strain-dependent phase diagrams that explore the evolution of structure and properties for thin films of the widely studied and technologically important tetragonal portion of the $PbZr_{1-x}Ti_xO_3$ phase diagram [85]. In particular, I study (001)-, (101)-, and (111)-oriented films and focus on the case of complex, polydomain phases in films above the critical thickness for domain formation. This work is accomplished by modifying the free-energy formalism for (001)-oriented heterostructures to allow for the construction of orientation-dependent, composition-strain phase diagrams for both (101)- and (111)-oriented films. I explore both phase and property (*i.e.*, dielectric permittivity) evolution for each film orientation. My studies reveal that the film orientation, epitaxial strain, and composition can combine in unexpected ways to drive exotic phase stability and transformations which have intriguing implications for the properties of materials. The models suggest that the variation of film orientation can dramatically impact the energetics of the system and the application of epitaxial strains along non-$\langle 001 \rangle$-type crystallographic directions significantly reduces the stability range of the parent tetragonal phase (which is dominant in (001)-oriented films) and results in a variety of new symmetries. I also observe that the film orientation can be used to tune the relative fraction of intrinsic (*i.e.*, within a domain) and extrinsic (*i.e.*, from domain wall motion) contributions to permittivity. This work has implications for the experimental design of ferroelectric heterostructures and could ultimately aid in the optimization of material response via a combination of film orientation, composition, and misfit strain control.

3.2 Phase Diagrams of Monodomain and Polydomain $PbZr_{1-x}Ti_xO_3$ Thin Films

As noted in Chapter 1, few reports (either experimental or theoretical) have discussed the strain- and composition-dependence of polydomain structures in (101)- and (111)-oriented $PbZr_{1-x}Ti_xO_3$ ($0.5 \leq x \leq 1.0$) films. Thus, to aid the development of the polydomain phase diagrams from the limited resources, I first utilized a monodomain model, which has been described in Chapter 2, to provide insights into various phases and structures that can potentially be produced. Based on these equilibrium monodomain phases, the polydomain phases were hence evaluated numerically as the equilibrium states which possesses the minimum free energy at a given elastic strain condition and titanium content ($0.5 \leq x \leq 1.0$) using the polydomain model described in Chapter 2.

3.2.1 (001)-Oriented Heterostructures

In (001)-oriented heterostructures, three monodomain phases were found to be present across the range of strain and composition values explored herein: 1) a tetragonal *c* phase ($P_1 =$

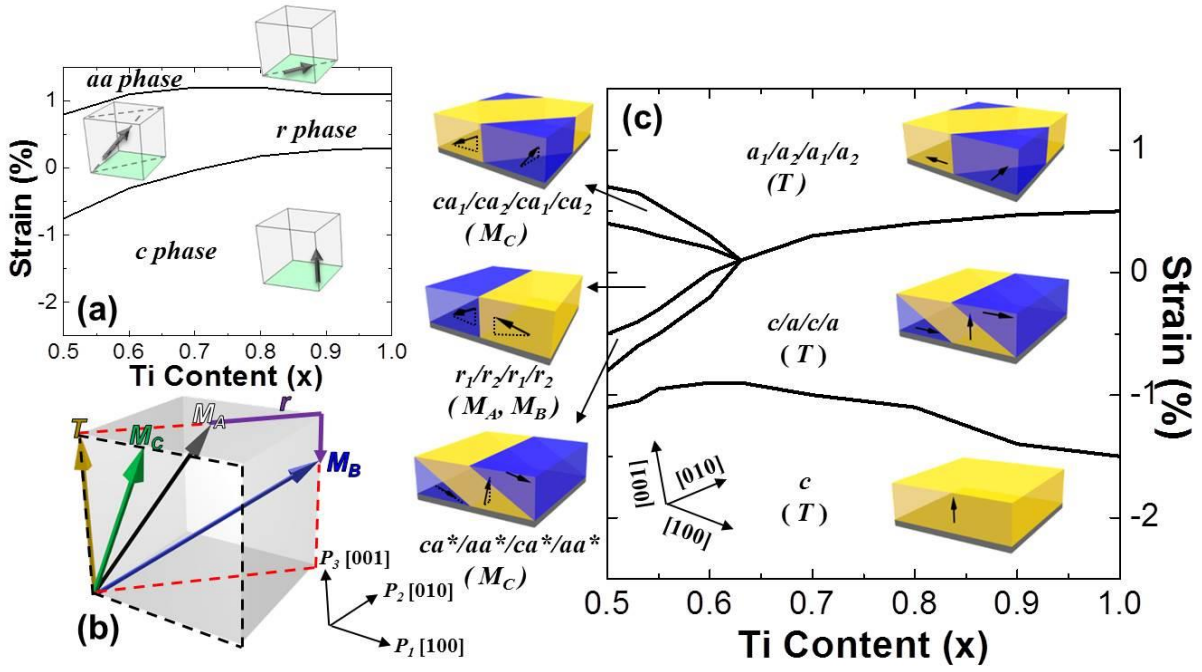

Fig. 3.1: (a) The composition-strain monodomain phase diagram, (b) the schematic illustration of possible monodomain components in the polydomain structure, and (c) The composition-strain polydomain phase diagram for (001)-oriented films.

$P_2 = 0, P_3 \neq 0$), 2) a monoclinic *r* phase ($P_1 = P_2 \neq 0, P_3 \neq 0$), and 3) an orthorhombic *aa* phase ($P_1 = P_2 \neq 0, P_3 = 0$) in the compressive-, intermediate-, and tensile-strain regimes, respectively, where P_1, P_2, and P_3 are along the crystallographic directions x_1, x_2, and x_3 in reference frame *X* (x_1, x_2, x_3) (See Chapter 2 for the detailed definition of reference frame *X*, Fig. 3.1a). Note that the *c* phase is energetically favored under large compressive strains since the strain stabilizes the out-of-plane P_3 component. Upon decreasing the compressive strain, the in-plane P_1 and P_2 components appear in the *r* phase and finally, under the influence of large tensile strains, the structure evolves into the *aa* phase with pure in-plane components.

Based on these monodomain results, I can further evaluate the polydomain structures. Performing the minimization of $\tilde{F}$ in terms of P_i and ϕ_k for (001)-oriented $PbZr_{1-x}Ti_xO_3$ films at $T = 300\ K$, I acquire results similar to the polydomain-phase diagram predicted in prior work [14]. To aid in the discussion, a table (Table 3.1) is provided that indicates the notation which will be used to refer to each phase in the polydomain structures as well as the polarization components and symmetry of that phase. In the polydomain, (001)-oriented heterostructures, seven different, uniquely identifiable phases are observed (here noted in the notation to be used throughout the rest of this manuscript with the corresponding letter in parentheses demarcating the traditional nomenclature used in prior literature as a reference): T_c *(c)*, T_a *(a)*, M_A *(r)*, M_B *(r)*, M_{C1} *(ca*)*, M_{C2} *(ca)*, M_{C3} *(aa*)*. Again, specific definition of the polarization components of each phase is provided (Table 3.1) and a schematic illustration of the various phases is provided (Fig. 3.1b, note

Table 3.1: The polarization component and the symmetry of all possible monodomain components in the polydomain structure for (001)-, (101)-, and (111)-oriented films.

(001)	$T(c)$	$P_1 = P_2 = 0, P_3 \neq 0$	Tetragonal
	$T(a)$	$P_2 = P_3 = 0, P_1 \neq 0$	Tetragonal
	$M_C(ca)$	$P_1 \neq 0, P_2 = 0, P_3 \neq 0$	Monoclinic
	$M_A(r)$	$P_1 = P_2 \neq 0 < P_3 \neq 0, 0.60 < P_1/P_3 < 1.0$	Monoclinic
	$M_B(r)$	$P_1 = P_2 \neq 0 > P_3 \neq 0, 1.0 < P_1/P_3 < 1.50$	Monoclinic
	$M_C(ca^*)$	$P_1 = 0, P_2 \neq 0, P_3 \neq 0$	Monoclinic
	$M_C(aa^*)$	$P_1 \neq 0, P_2 \neq 0, P_3 = 0$	Monoclinic
(101)	O	$P_1 = P_2 \neq 0, P_3 = 0$	Orthorhombic
	M_C	$P_1 \neq 0, P_2 = 0, P_3 \neq 0, 0.27 < P_1/P_3 < 0.79$	Monoclinic
	T-like M_C	$P_1 \neq 0, P_2 = 0, P_3 \neq 0, 0.001 < P_1/P_3 < 0.19$	Monoclinic
	M_A	$P_1 = P_2 \neq 0, P_3 \neq 0, 0.67 < P_1/P_3 < 0.95$	Monoclinic
(111)	R	$P_1 = P_2 = P_3 \neq 0$	Rhombohedral
	T-like M_A	$P_1 = P_2 \neq 0, P_3 \neq 0, 0.001 < P_1/P_3 < 0.19$	Monoclinic
	M_A	$P_1 = P_2 \neq 0, P_3 \neq 0, 0.67 < P_1/P_3 < 0.96$	Monoclinic

that this illustration schematically shows the orientation of polarization within the unit cell in reference frame *X*).

The nomenclature used herein is different from the traditionally applied nomenclature for two reasons. First, in the subsequent analysis of (101)- and (111)-oriented heterostructures, no prior nomenclature has been established and thus I provide a unified naming pattern to all systems. Second, the earlier nomenclature of the (001)-oriented heterostructures fails to accurately differentiate some of the subtle differences in structure that are observed. In this regard, I find two different tetragonal phases: one with the polarization along the out-of-plane [001] which I refer to as T_c (*c*) and one with the polarization in-the-plane along [100] or [010] which I refer to as T_a (*a*). There are, additionally, a number of phases with monoclinic symmetry (M_A, M_B, and M_{Ci}). The M_A and M_B phases possess polarizations only within {110} and the M_{Ci} phases possess polarizations only within {001}. The M_A and M_B phases make up what has traditionally been referred to as the *r* phase, as in polydomain $r_1/r_2/r_1/r_2$ structures. Our studies reveal that it is possible for the polarization to rotate continuously within the {110} from $0.6 < P_1/P_3 < 1.5$ across the strain range ($-2.5\% \leq \varepsilon \leq 2.5\%$) thus leading to two sub-phases M_A and M_B in the so-called $r_1/r_2/r_1/r_2$ structure. For this work, the M_A and M_B phases are differentiated by the magnitude of the ratio P_1/P_3 which is < 1.0 in the M_A phase but > 1.0 in the M_B phase. The M_{Ci} phases make up what has traditionally been referred to as the *ca**, *ca*, and *aa** phases and in all cases two of the polarization

components are non-zero and one is zero. Here the i = 1, 2, or 3 and it refers to the polarization component that is zero to differentiate the phases.

Based on these calculated phases, I have constructed the composition-strain polydomain phase diagrams for (001)-oriented films (Fig. 3.1c). In the polydomain system, a single domain T_c phase is present in the compressive-strain regime. At intermediate strains, across most of the composition space explored here, a polydomain T_c/T_a (*c/a/c/a*) domain structure is observed. Also at these intermediate strains, when the titanium content x < 0.6, a polydomain M_A *(*or M_B*)* ($r_1/r_2/r_1/r_2$) structure is observed. Furthermore, due to a P_2 instability near the morphotropic phase boundary, the polydomain T_c/T_a (*c/a/c/a*) domain structure evolves into a polydomain M_{C1}/M_{C3} (*ca*/aa*/ca*/aa**) structure. At larger tensile strains, a polydomain T_a ($a_1/a_2/a_1/a_2$) structure is stabilized. Similar to what occurred at intermediate-strain states, due to a P_3 instability near the morphotropic phase boundary, the polydomain T_a ($a_1/a_2/a_1/a_2$) structure evolves into a polydomain M_{C2}/M_{C1} ($ca_1/ca_2/ca_1/ca_2$) struture. Overall, across much of the composition and strain space studied herein, with the exception of compositions near the morphotropic phase boundary, a tetragonal symmetry is maintained. The tetragonal phases can give rise to polydomain structures which are further complicated by the formation of monoclinic structures near the morphotropic phase boundary.

3.2.2 (101)-Oriented Heterostructures

In (101)-oriented heterostructures, three monodomain phases were found to be present across the range of strain and composition values explored herein: 1) an orthorhombic *O* phase ($P_1 = P_2 \neq 0, P_3 = 0$), 2) a monoclinic M_{C2} phase ($P_1 \neq 0,\ P_2 = 0,\ P_3 \neq 0$), and 3) a monoclinic M_A phase ($P_1 = P_2 \neq 0, P_3 \neq 0$) in the compressive-, intermediate-, and tensile-strain regimes, respectively, where P_1, P_2, and P_3 are along the crystallographic directions x_1, x_2, and x_3 in reference frame *X* (See Chapter 2 for the detailed definition of reference frame *X*, Fig. 3.2a). Note that the *O* phase is energetically favored under large compressive strains since the strain stabilizes the out-of-plane polarization component. Upon decreasing the compressive strain, the in-plane polarization components appear in the M_{C2} phase and finally the structure evolves into the M_A phase with pure in-plane polarization components as a result of the application of tensile strain.

As I did before, I can leverage these monodomain results to further evaluate the polydomain structures. Performing the minimization of $\tilde{F}'$ in terms of P_i' for (101)-oriented $PbZr_{1-x}Ti_xO_3$ films at 300 K, I can generate a composition-strain phase diagram. To aid in the discussion, a table (Table 3.1) is provided that indicates the notation which will be used to refer to each phase in the polydomain structures as well as the polarization components and symmetry of that phase. In the polydomain, (101)-oriented heterostructures, five different, uniquely identifiable phases are observed: *O*, M_A, M_{C2}, *T-like* M_{C1}, and *T-like* M_{C2}. Again, specific definition of the polarization components of each phase is provided (Table 3.1) and a schematic illustration of the various phases

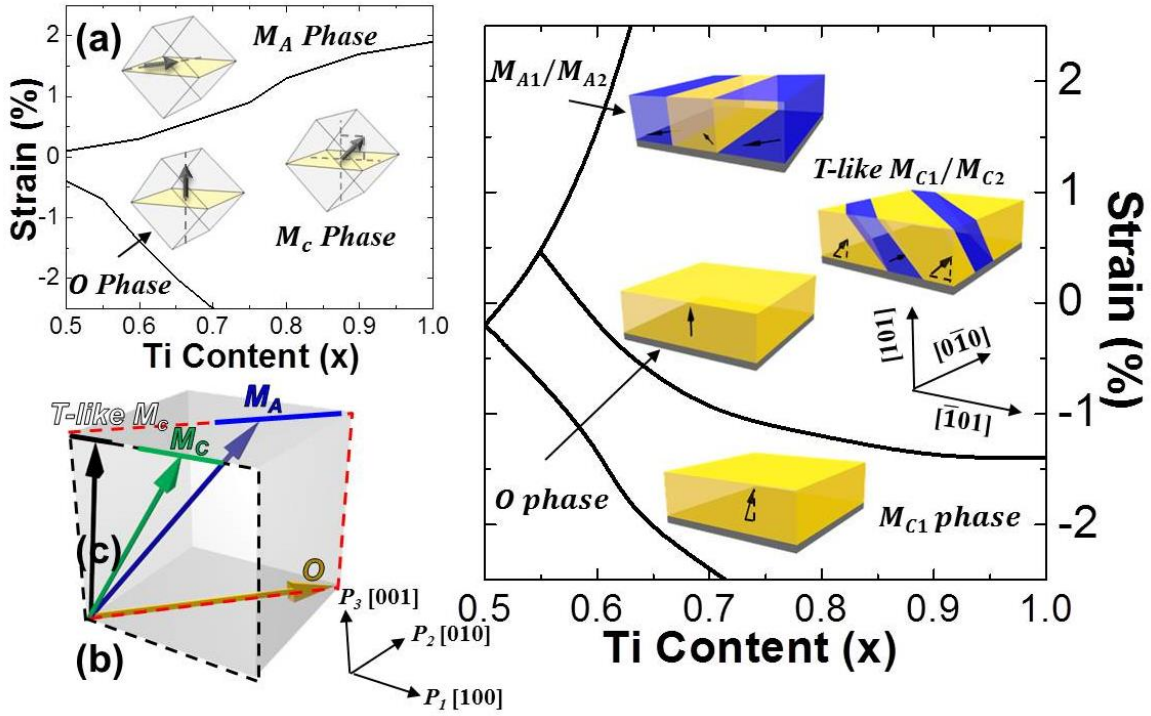

Fig 3.2: (a) The composition-strain monodomain phase diagram, (b) the schematic illustration of possible monodomain components in the polydomain structure, and (c) The composition-strain polydomain phase diagram for (101)-oriented films.

is provided (Fig. 3.2b, note that this illustration schematically shows the orientation of polarization within the unit cell in reference frame *X*).

In this case, the *O* phase is found to have non-zero polarization in both the [100] and [010]. Additionally, I differentiate three monoclinic structures. The M_A phase has $P_1 = P_2 \neq 0$, and $P_3 \neq 0$ where $0.67 < P_1/P_3 < 0.95$ and the polarization can only lie within the $\{110\}$. The M_{C2} phase has $P_1 \neq 0, P_2 = 0$, and $P_3 \neq 0$ where $0.27 < P_1/P_3 < 0.79$ and the polarization can only lie within the $\{100\}$. Finally, there are two *T*-like M_{Ci} phases: *T*-like M_{C1} ($P_1 \neq 0$, $P_2 \neq 0$, P_3=0) where $0.001 < P_1/P_2 < 0.19$ and *T*-like M_{C2} ($P_1 \neq 0$, P_2=0, $P_3 \neq 0$) where $0.001 < P_1/P_3 < 0.19$. The *T*-like M_{C2} phase is differentiated from the M_{C2} phase in that it can only exist with $0.001 < P_1/P_3 < 0.19$ in the considered strain range ($-2.5\% \leq \varepsilon \leq 2.5\%$). In general, the *T*-like M_{Ci} phases can be considered as a monoclinically-distorted, but nearly-tetragonal structures with polarization slightly deviating from the [010] and [001] for *i* = 1 and 2, respectively.

Based on these calculated structures, I have constructed the composition-strain polydomain phase diagram for (101)-oriented films (Fig. 3.2c). In the polydomain system, a monodomain, *O*-phase region is stabilized under compressive strains and relatively zirconium-rich portions of the composition range studied herein. Upon increasing the titanium content, the structure morphs to the M_{C2} phase and a monodomain structure is still maintained. Note that this monodomain M_{C2} phase persists all the way down to small strain regimes at x < 0.7. At small compressive and tensile

strains, at titanium content x ≳ 0.65, the monodomain M_{C2} phase is replaced by a polydomain *T*-like M_{C1}/*T*-like M_{C2} domain structure. In the same strain regime, as the composition nears the morphotropic phase boundary, the M_A phase is stabilized and a polydomain M_A structure is formed. Overall, the composition-strain phase diagram of (101)-oriented heterostructures is found to exhibit a fewer number and less variation of stable phases as compared to the (001)-oriented heterostructures within the range of strain and composition considered herein. Additionally, the observed phases in the (101)-oriented films tend to take on monoclinic distortions due to the fact that in-plane misfit strain is akin to a shear strain on the tetragonal $PbZr_{1-x}Ti_xO_3$ unit cell. This is consistent with previously reported experimental observations, where a number of x-ray studies have confirmed the presence of dominant monoclinic symmetry in (101)-oriented $PbZr_{1-x}Ti_xO_3$ films with compositions near morphotropic phase boundary [86,87].

3.2.3 (111)-Oriented Heterostructures

In the (111)-oriented heterostructures, three monodomain phases were found to be present across the range of strain and composition values explored herein: 1) a rhombohedral *R* phase ($P_1 = P_2 = P_3 \neq 0$), 2) a monoclinic *T*-like M_A phase ($P_1 = P_2 \neq 0,\ P_3 \neq 0$), and 3) a monoclinic M_A phase ($P_1 = P_2 \neq 0,\ P_3 \neq 0$) in the compressive-, intermediate-, and tensile-strain regimes, respectively, where P_1, P_2, and P_3 are along the crystallographic directions x_1, x_2, and x_3 in reference frame *X* (See Chapter 2 for the detailed definition of reference frame *X*, Fig. 3.3a). Note that the *R* phase is energetically favored under large compressive strains (for all compositions studied herein) since the strain stabilizes the out-of-plane polarization component. Upon transitioning to tensile strain, in-plane polarization components appear and in compositions with higher titanium content, a *T-like* M_A phase forms and in compositions with less titanium (or at large tensile strains and high titanium content) a M_A phase is observed.

Based on these monodomain results, I can further evaluate the polydomain structures. Performing minimization of $\tilde{F}''$ in terms of P_i'' at 300 K I can generate yet another composition-strain phase diagram to study the evolution of structure and phases in (111)-oriented films. To aid in the discussion, a table (Table 3.1) is provided that indicates the notation which will be used to refer to each phase in the polydomain structures as well as the polarization components and symmetry of that phase. In the polydomain, (111)-oriented heterostructures, seven different, uniquely identifiable phases are observed: *R*, M_{A1}, M_{A2}, M_{A3}, *T*-like M_{A1}, *T*-like M_{A2}, and *T*-like M_{A3}. Again, specific definition of the polarization components of each phase is provided (Table 3.1) and a schematic illustration of the various phases is provided (Fig. 3.3b, note that this illustration schematically shows the orientation of polarization within the unit cell in reference frame *X*).

In this case, the *R* phase is found to have non-zero polarization along [100], [010], and [001]. Additionally, although all the monoclinic phases possess polarizations only within {110}, I differentiate the monoclinic structures based on different P_1/P_3 ratios that are possible. In particular, there are three M_{Ai} phases (M_{A1} ($P_1 = P_2 \neq 0$ and $P_3 \neq 0$) where $0.67 < P_1/P_3 < 0.96$,

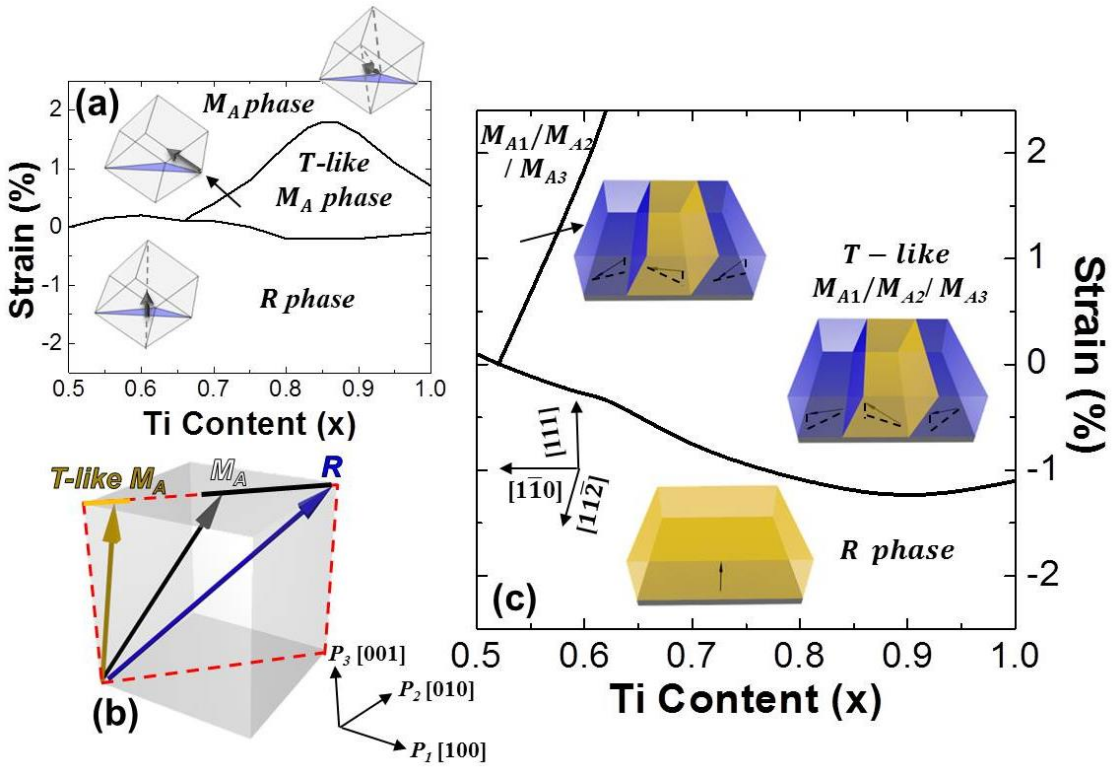

Fig. 3.3: (a) The composition-strain monodomain phase diagram, (b) the schematic illustration of possible monodomain components in the polydomain structure, and (c) The composition-strain polydomain phase diagram for (111)-oriented films.

M_{A2} ($P_1 = P_3 \neq 0$ and $P_2 \neq 0$) where $0.67 < P_1/P_2 < 0.96$, and M_{A3} ($P_2 = P_3 \neq 0$ and $P_1 \neq 0$) where $0.67 < P_2/P_1 < 0.96$) and three *T*-like M_{Ai} phases (*T*-like M_{A1} ($P_1 = P_2 \neq 0$ and $P_3 \neq 0$) where $0.001 < P_1/P_3 < 0.19$, *T*-like M_{A2} ($P_1 = P_3 \neq 0$ and $P_2 \neq 0$) where $0.001 < P_1/P_2 < 0.19$, and *T*-like M_{A3} ($P_2 = P_3 \neq 0$ and $P_1 \neq 0$) where $0.001 < P_2/P_1 < 0.19$) in the considered strain range ($-2.5\% \leq \varepsilon \leq 2.5\%$). In other words, the *T*-like M_{Ai} phase is akin to a monoclincially-distorted, tetragonal structure with polarization slightly deviating from [001], [010], and [100] for i = 1, 2, and 3 while the M_{Ai} phases possesses a higher distortion and a polarization that can rotate smoothly all the way to the *R* phase.

Based on these calculated structures, I have constructed the composition-strain polydomain phase diagrams for (111)-oriented films (Fig. 3.3c). In the polydomain system, a monodomain, *R*-phase region is stabilized across all compositions under large compressive strains. When x ≳ 0.6 and in both the low-compressive- and high-tensile-strain regimes, the *T*-like M_{Ai} phases are stabilized and a polydomain *T*-like M_{A1}/*T*-like M_{A2}/*T*-like M_{A3} domain structure is created. Under tensile strain and near the morphotropic phase boundary, the M_{Ai} phase is stabilized and a polydomain $M_{A1}/M_{A2}/M_{A3}$ structure is generated. In general, the phase diagram of (111)-oriented heterostructures exhibits the least number and variation of stable phases as compared to the (001)- and (101)-oriented heterostructures in the strain and composition range considered herein. Again, it is noted that although a two-domain configuration is directly derived based on the microscopic

boundary conditions with equal volume fraction of M_{Ai} (or T -like M_{Ai}) domains, in order to highlight the degenerate nature of all polarization variants, I represent this system as a three-domain configuration with equal volume fraction, which has been experimentally observed in our previous work [71,72]. Additionally, the observed phases in the (111)-oriented heterostructures tend to take on rhombohedral (or monoclinically-distorted versions of rhombohedral) symmetry due to the fact that in-plane misfit strain is akin to a shear strain on the tetragonal $PbZr_{1-x}Ti_xO_3$ unit cell. Again, this is consistent with the previously reported experimental observations, where a number of x-ray studies have also confirmed the presence of dominant rhombohedral symmetry in (111)-oriented $PbZr_{1-x}Ti_xO_3$ films with compositions near the morphotropic phase boundary [86,87].

3.3 Dielectric Properties of Polydomain $PbZr_{1-x}Ti_xO_3$ Thin Films

3.3.1 (001)-Oriented Heterostructures

Having studied the orientation-dependent, composition-strain phase diagrams in polydomain $PbZr_{1-x}Ti_xO_3$ heterostructures, I proceeded to explore the effects of strain, composition, and orientation on the dielectric response. First, I studied the composition-strain map for the intrinsic (Fig. 3.4a) and total dielectric response (intrinsic plus extrinsic contributions, Fig. 3.4b) in (001)-oriented heterostructures and obtained similar results to those reported previously [14,63,88]. The maximum intrinsic response is found near the boundary between the polydomain T_a and M_{C2}/M_{C1} structures as a result of the effect of anisotropic dielectric permittivity, where the permittivity measured along the non-polar axis is higher than that measured along the polar axis and thus the T_a structure, with pure in-plane polarization components, has the largest intrinsic response.

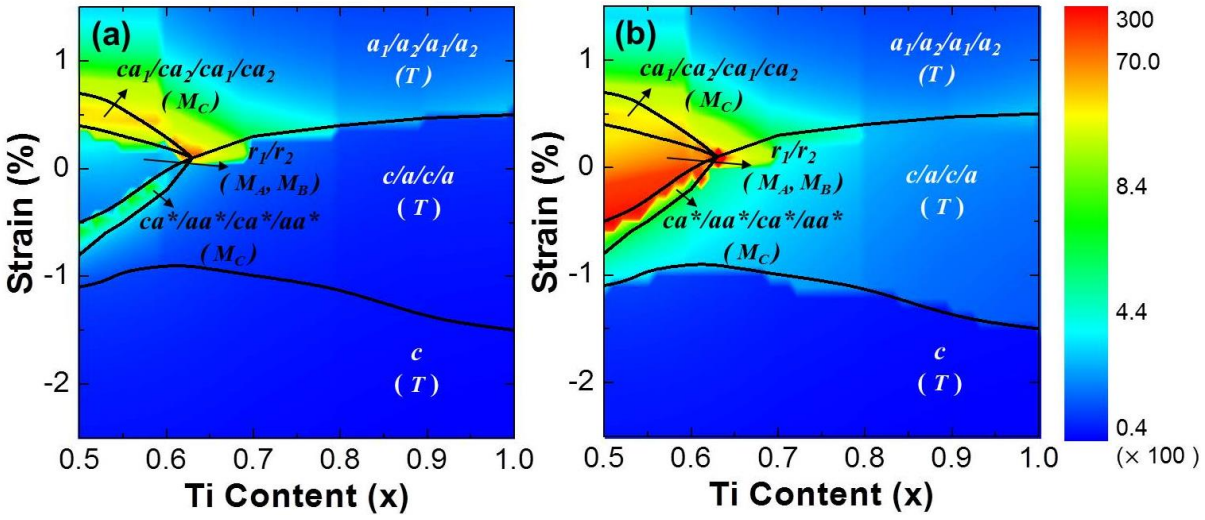

Fig. 3.4: The composition-strain map for (a) the intrinsic and (b) the total (intrinsic plus extrinsic contribution) dielectric permittivity (001)-oriented films.

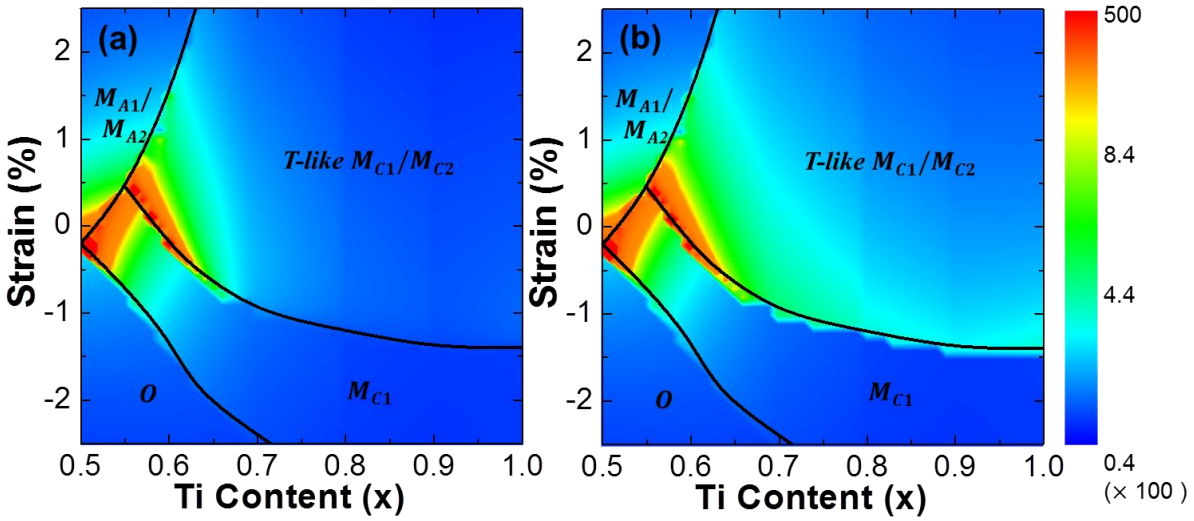

Fig. 3.5: The composition-strain map for (a) the intrinsic and (b) the total (intrinsic plus extrinsic contribution) dielectric permittivity in (101)-oriented films.

As compared to the intrinsic response, in the map of total dielectric response, enhanced effects can be observed in the T_c/T_a, polydomain M_A (or M_B), M_{C1}/M_{C3}, and M_{C2}/M_{C1} structures due to the contribution from extrinsic effects (*i.e.*, domain-wall motion). In particular, a large extrinsic contribution is observed in the polydomain M_A (or M_B) structure which leads to the maximum total dielectric permittivity near the multicritical point at the boundary between the five polydomain phases and extending along the boundary between polydomain M_A (or M_B) and M_{C1}/M_{C3} structures due to the presence of opposite signs of out-of-plane polarization in the variants of the polydomain M_A (or M_B) structure which, in turn, lead to larger field-driven effects at these domain walls. The total dielectric response in the T_c and polydomain T_a structures remains the same since there are no domain walls in the T_c region and because of the degenerate nature of the T_a domain variants with respect to the electric field leads to no volume faction change under the electric field.

3.3.2 (101)-Oriented Heterostructures

I also studied the composition-strain map of the intrinsic (Fig. 3.5a) and total dielectric response (intrinsic plus extrinsic contribution, Fig. 3.5b) for (101)-oriented heterostructures. Large intrinsic dielectric response is observed near the phase boundaries between the polydomain M_A, *T*-like M_{C1}/*T*-like M_{C2}, and M_{C2} structures, especially in films with lower titanium content and near zero strain, due to the structural instability near the morphotropic phase boundary. As compared to the intrinsic response map, the map of total dielectric response reveals enhanced response in the *T*-like M_{C1}/*T*-like M_{C2} structure due to the presence of additional extrinsic contributions from the domain walls. Such extrinsic contributions, however, are found to be less pronounced as the in the related T_c/T_a polydomain structure in the (001)-oriented heterostructures as a result of less preferential alignment of the electric field with a single polarization variant in the (101)-oriented heterostructures which provides less driving force for domain-wall motion. The total dielectric

response in the monodomain *O* and M_{C2} regimes remains the same as there are no domain walls present and in the polydomain M_A regime as the degenerate nature of variants in polydomain M_A with respect to the electric field which leads to no volume faction change under application of electric field.

3.3.3 (111)-Oriented Heterostructures

I also studied the composition-strain map for the total dielectric response (intrinsic plus extrinsic contribution, Fig. 3.6) in (111)-oriented films. Note that in the (111)-oriented heterostructures, the extrinsic contribution from domain-wall motion is not present due to the single-domain nature of the *R*-phase regime and the degenerate nature of polarization variants in the polydomain *T*-like M_{A1}/*T*-like M_{A2}/*T*-like M_{A3} and $M_{A1}/M_{A2}/M_{A3}$ structures where the structures are made up of equal volume fractions (*i.e.*, 1/3) of the different structural/polarization variants which results in the system having no electric-field-in domain-fraction change. This noted, large intrinsic dielectric response can be obtained at the phase boundaries between *T*-like M_{A1}/*T*-like M_{A2}/*T*-like M_{A3} and $M_{A1}/M_{A2}/M_{A3}$ phases due to the structural instability near the morphotropic phase boundary. It is also noted that the intrinsic response in the *T*-like M_{A1}/*T*-like M_{A2}/*T*-like M_{A3} regime in the (111)-oriented heterostructures is higher than the related structures in the other orientations (*i.e.*, T_c/T_a polydomain structure in (001)-oriented heterostructures and *T*-like M_{C1}/*T*-like M_{C2} polydomain structures in (101)-oriented heterostructures) due to the anisotropic dielectric response of $PbZr_{1-x}Ti_xO_3$ where the permittivity along the [100] is larger than that along the [001] and thus the intrinsic contribution to permittivity increases as the substrate normal is inclined more towards the [100].

Although the motional extrinsic response is not present in the (111)-oriented heterostructures, which leads to a lower overall response according to our calculation, recent experimental work [71] indicates that (111)-oriented $PbZr_{0.2}Ti_{0.8}O_3$ films can exhibit greatly enhanced dielectric response among (001)-, (101)-, and (111)-oriented versions due to other possible enhancement mechanisms such as stationary domain-wall contributions which have not been considered here. This added contribution arises from the fact that high domain-wall densities can be achieved in the (111)-oriented heterostructures, thereby adding a new (and still underdeveloped) contribution from the volume domain wall phase in the material. Recent Ginzburg-Landau-Devonshire (GLD) models in $BaTiO_3$, for instance, suggest that such domain walls could give rise to an enhancement of susceptibilities between 1.1 to 1000-times over the bulk [31] and the experimental work suggests that the domain wall phase has a permittivity 6-70 times than the bulk of the domain. Recent density functional theory and molecular dynamics simulations suggest that this enhanced low-field permittivity is a result of frustrated dipoles with the finite width of the domain walls, which can induce 100% enhancement of the dielectric susceptibility arising from the softer potential wells within them [89]. Addition of such effects into these models will require additional insights into the nature of this effects and would require more advanced

models that can provide realistic domain structures and densities to estimate the volume fraction of domain-wall phase.

Overall, I have compared the predicted evolution of dielectric permittivity as a function of strain and composition for (001)-, (101)-, and (111)-oriented polydomain $PbZr_{1-x}Ti_xO_3$ films and here I will highlight some key similarities and differences. First, as is expected, the ferroelectric instability usually results in an enhanced dielectric response and thus irrespective of the film orientation enhanced dielectric permittivity is always present near the phase transition boundary. Second, varying the film orientation can tune the relative fraction of the intrinsic and extrinsic contribution to the dielectric permittivity. For instance, in $PbZr_{0.2}Ti_{0.8}O_3$ films, if I compare the dielectric response of polydomain T_c/T_a structure in (001)-oriented films and its related counterparts, *T*-like M_{C1}/T-like M_{C2} structure in (101)-oriented films and *T*-like M_{A1}/ *T*-like M_{A2}/ *T*-like M_{A3} structure in (111)-oriented films, I can make a few observations. First at a given equivalent misfit strain, the highest intrinsic response is observed in (111)-oriented heterostructures (followed by (101)- and (001)-oriented heterostructures) as a result of the anisotropic dielectric response of $PbZr_{0.2}Ti_{0.8}O_3$ where the permittivity along the [100] is larger than that along the [001] and thus the intrinsic contribution to permittivity increases as the substrate normal is inclined more towards the [100]. This is similar to the monodomain case where the permittivity exhibits higher values along non-polar directions (*i.e.*, [111]) than polar directions (*i.e.*, [001]) in tetragonal ferroelectrics [90,91]. Second, the relative extrinsic contribution (from domain wall motion) to the permittivity decreases as I move from (001)- to (101)-oriented films (as a result of less preferential alignment of the electric field with a single polarization variant) and completely vanishes in (111)-oriented films due to the constant volume fraction of the three polarization variants which is independent of the electric field. Ultimately, the studies indicate that a judiciously chosen combination of elastic strain and film orientation can be used to access a wide variety of structural phase variants and correspondingly diverse dielectric response in ferroelectrics. This knowledge, in turn, can enable the response of a system like $PbZr_{1-x}Ti_xO_3$ to be optimized without relying simply on traditional chemical-routes (*i.e.*, being near to the morphotropic phase boundary).

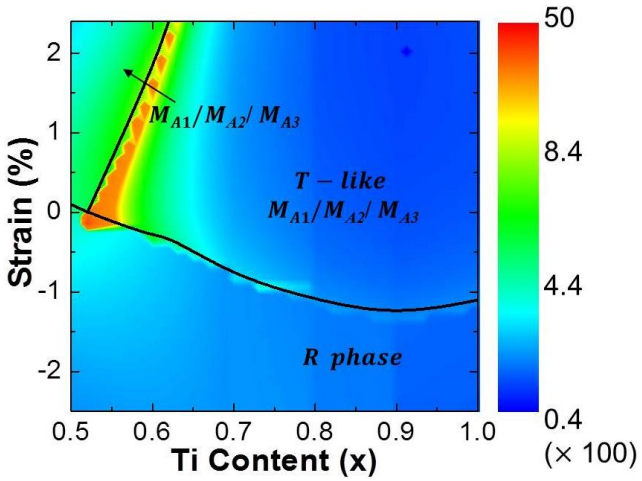

Fig. 3.6: The composition-strain map for the total (intrinsic plus extrinsic contribution) dielectric permittivity in (111)-oriented films.

3.4 Conclusions

In this Chapter, I have used a thermodynamic model to calculate the structural phase diagrams and dielectric response in polydomain (001)-, (101)-, and (111)-oriented $PbZr_{1-x}Ti_xO_3$ thin films. Our studies reveal that beyond simple chemistry and strain variations, the use of film orientation can enable dramatic changes in the energetics of the system and thus be used to tune the structure of the equilibrium phases. In particular, I observe that in (101)- and (111)-oriented films, the stability of the parent *T* phase is greatly reduced and tends to evolve into a distorted version. And I have observed monoclinic and rhombohedral phases present in the predicted phase diagram of (101)- and (111)-oriented films, respectively, which is consistent with the previously reported experimental observations. Additionally, our work provides a theoretical platform by which to systematically optimize the dielectric response in thin films as a function of composition, strain, and orientation. Large dielectric susceptibilities can be found near phase transition boundaries where the ferroelectric instability is induced in these films. At the same time, I also observed that the film orientation can be used to tune the relative fraction of contributions from domain and domain wall motion to the dielectric permittivity. Ultimately, the use of additional orientations of films – beyond the predominantly studied (001)-oriented versions in the literature – provide a rich and complex landscape in which I can potentially enhance and gain deterministic control over the properties of materials.

CHAPTER 4

Engineering Domain Structures for Enhanced Dielectric Susceptibility in $PbZr_{0.2}Ti_{0.8}O_3$ Thin Films

Domain walls play an important role in determining the response of ferroelectrics to applied stimuli. While contributions to ferroelectric properties from the intrinsic response of the polarization within a domain and so-called extrinsic contributions from the motion of domain walls have been studied, non-motional or stationary contributions from the material within the finite width of the domain wall itself have been particularly difficult to understand. In this Chapter, I probe the stationary-domain-wall contribution to dielectric susceptibility in nanodomained $PbZr_{0.2}Ti_{0.8}O_3$ thin films. Using a combination of phenomenological models, thin-film growth, and multi-scale characterization I have probed model versions of (001)-, (101)-, and (111)-oriented epitaxial films. In particular, I observe that (111)-oriented films, in which the extrinsic contributions from a high density of 90° domain walls are frozen out, exhibit permittivity values approximately 3-times larger than that expected from the intrinsic response alone. This discrepancy can only be accounted for by considering a stationary contribution to the permittivity from the domain-wall volume of the material that is 6-78-times larger than the bulk response and is consistent with recent predictions of the enhancement of susceptibilities within 90° domain walls.

4.1 Introduction

The search for ferroelectric materials with high electric field (dielectric), stress (piezoelectric), and thermal (pyroelectric) susceptibilities has garnered much attention in recent years as these materials serve as the foundation for modern memory [92,93], sensor and actuator [94,95], and thermal imaging and infrared detector systems [96]. To ultimately understand the nature of such responses, it is imperative to understand the various contributions to the susceptibility in these complex materials. As noted in Chapter 1, much work on polydomain ferroelectrics has neglected the stationary-domain-wall contribution to dielectric permittivity. Regardless, it is clear that in order to fully understand the response of a ferroelectric to an applied stimulus, one must consider not only the response of the bulk material within the domains but also the response of the domain walls to the applied stimuli. In this Chapter, I use a combination of theoretical and experimental approaches to investigate the effect of 90° domain walls on the dielectric permittivity of (001)-, (101)-, and (111)-oriented $PbZr_{0.2}Ti_{0.8}O_3$ thin films [71]. Using phenomenological GLD models I calculate the intrinsic and motional extrinsic contributions to permittivity for these different film orientations. Thin-film epitaxy is employed to synthesize highly-controlled model versions of these films. The choice of these three orientations enables us to tune the density of domain walls and thus the relative magnitude of the stationary domain wall contribution to permittivity. In particular, I observe that in (111)-oriented films high-density, nanotwinned domain structures made entirely of 90° domain walls can be produced. Subsequent comparison of the measured dielectric permittivity and the GLD models reveals a large enhancement of the permittivity that is consistent with a large stationary domain wall contribution. From these measurements it is noted that the magnitude of the stationary domain wall response is 6-77.5-times larger than the intrinsic response within a domain.

4.2 Ginzburg-Landau-Devonshire Model of Dielectric Permittivity in $PbZr_{0.2}Ti_{0.8}O_3$ Films

In order to study the intrinsic and motional extrinsic contributions to the dielectric permittivity, I considered thin films of the tetragonal ferroelectric $PbZr_{0.2}Ti_{0.8}O_3$ grown epitaxially on (001)-, (101)-, and (111)-oriented cubic substrates. The Helmholtz free energy formalism applicable to ferroelectric films with dense domain structures was used to calculate the domain structures and dielectric susceptibilities as a function of substrate orientation and epitaxial strain [14-97]. Consistent with prior approaches, homogeneous strain fields within the domains were assumed and the domain wall self-energies and inter-domain electrostatic interactions were neglected. Applying short-circuit electrical boundary conditions, the free energy of the system was minimized as a function of the in-plane strain imposed by the substrate so that I can calculate the equilibrium polarizations (P_1, P_2, P_3) and domain fractions. Using these models, I can then calculate explicitly the out-of-plane permittivity ($\varepsilon_\perp$) as the sum of the intrinsic (the first term) and the motional extrinsic (the second term) contributions [14,63,81,88,97] as

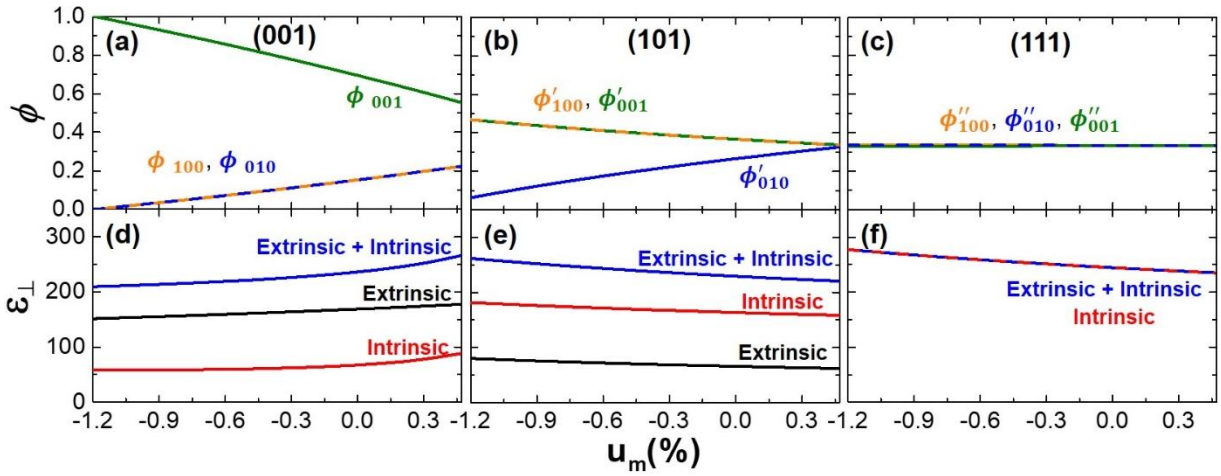

Fig. 4.1: Domain and permittivity evolution in $PbZr_{0.2}Ti_{0.8}O_3$ thin films. Using Ginzburg-Landau-Devonshire models, the volume fraction of polarization variants (ϕ) and out-of-plane, room temperature dielectric permittivity ($\varepsilon_\perp$) are predicted as a function of mismatch strain (u_m). The evolution of ϕ is provided for (a) (001)-, (b) (101)-, and (c) (111)-oriented films including the relative fraction of different polarization variants (referenced to the cardinal directions of the lattice, [100], [010], and [001]). The evolution of the intrinsic (red), extrinsic (black), and total (blue) $\varepsilon_\perp$ is provided for (d) (001)-, (e) (101)-, and (f) (111)-oriented films.

$$\varepsilon_\perp = \sum_i \phi_i \cdot \left(\frac{d^2F}{d\left(P_i^\perp\right)^2}\right)^{-1} + \sum_i P_i^\perp \cdot \frac{d\phi_i}{dE} \quad (1)$$

where i = 1, 2, 3 corresponding to domains with polarization P_i, ϕ_i is the fraction of domains with polarization P_i, F is the free energy formalism, $P_i^\perp$ is the out-of-plane polarization component of P_i, and E is the electric field along the substrate normal. Note that these models exclude stationary-domain-wall contributions from the portion of the material contained within the finite width of the domain walls.

The domain volume fraction (ϕ) and dielectric permittivity ($\varepsilon_\perp$) have been calculated numerically for all three orientation variants as a function of misfit strain (Fig. 4.1). For comparison, the strain regime that was explored was chosen to correspond to theoretically predicted epitaxial strains that give rise to *c/a/c/a* polydomain structures in (001)-oriented films [14,98]. Schematic illustrations of the expected domain structures in each film orientation are provided (Fig. 4.2). In (001)-oriented films, the volume fraction of *c* domains (ϕ_{001}) is observed to decrease with increasing tensile strain, while the volume fraction of *a* domains (ϕ_{100} and ϕ_{010}) increases as a result of the tensile strain that favors in-plane oriented polarization (Fig. 4.1a). A similar competitive trend is observed in (101)-oriented films where the population of the in-plane polarized domains (ϕ'_{010}) increases and the fraction of out-of-plane polarized domains (ϕ'_{100} and ϕ'_{001}) deceases with increasing strain (Fig. 4.1b). This is not the case for the (111)-oriented films, however, which due to symmetry, possess three energetically degenerate domain types and thus an equal volume fraction ($\phi''_{100} = \phi''_{010} = \phi''_{001} = 1/3$) of each domain separated by 90° domain walls at all values of misfit strain considered (Fig. 4.1c). Correspondingly, the impact of changing

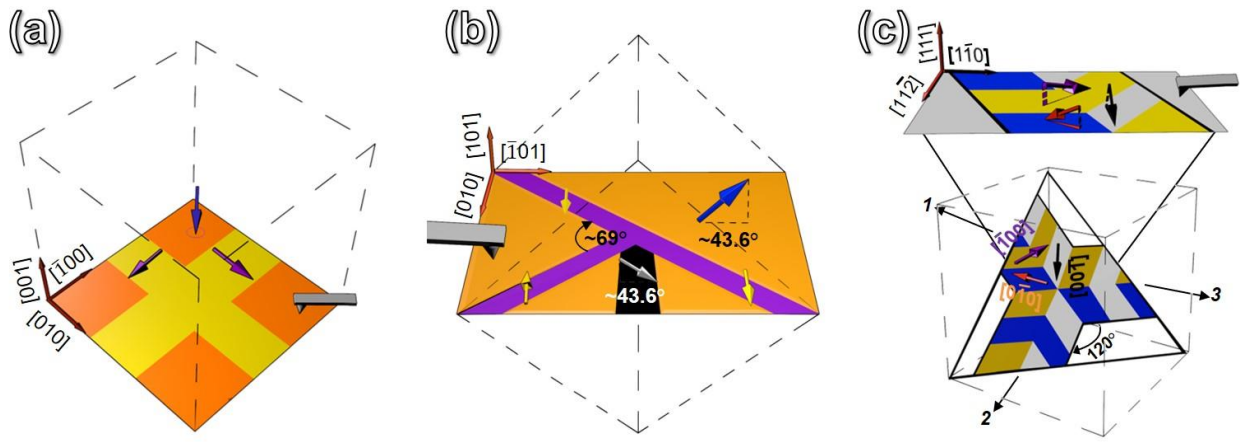

Fig. 4.2: Schematic illustrations of $PbZr_{0.2}Ti_{0.8}O_3$ domain structures. Expected domain structures for (a) (001)-, (b) (101)-, and (c) (111)-oriented $PbZr_{0.2}Ti_{0.8}O_3$ thin films. The minority domain represents domains with polarizations along the [100] and [010]/[0$\bar{1}$0] in (001)- and (101)-oriented films, respectively. In (111)-oriented films, any of the polarization variants can be selected as the minority domain due to the symmetry.

film orientation on $\varepsilon_\perp$ can be observed (Figs. 4.1d-f). In general, the intrinsic contribution to permittivity increases as the substrate normal is inclined more towards the [100] which is similar to the monodomain case where the permittivity exhibits higher values along non-polar directions (*i.e.*, [111]) than polar directions (*i.e.*, [001]) in tetragonal ferroelectrics [90,91]. This is due to the anisotropic dielectric response of $PbZr_{0.2}Ti_{0.8}O_3$ where the permittivity along the [100] is larger than that along the [001] [90]. Thus, the enhanced intrinsic response in (101)- and (111)-oriented films arises from the fact that additional intrinsic contributions are activated. It is also noted that the increasing tensile strain results in an increasing intrinsic response in the (001)-oriented films, which behaves in an opposite trend as compared to the (101)- and (111)-oriented films due to the fact that the intrinsic response of each polarization variant in (001)-oriented films increases while this component in (101)- and (111)-oriented films decreases with increasing tensile strain. At the same time, the relative contribution from the motional extrinsic response decreases as I move from (001)- to (101)-oriented films (as a result of less preferential alignment of the electric field with a single polarization variant) and completely vanishes in (111)-oriented films due to the constant volume fraction of the three polarization variants which is independent of the electric field. Similar to $BaTiO_3$ single crystals poled along [111] [99,100], the extrinsic contribution from domain-wall motion will be "frozen out" in (111)-oriented $PbZr_{0.2}Ti_{0.8}O_3$ films. In addition, the motional extrinsic contribution $\left(\frac{d\phi_i}{dE}\right)$ for (001)- and (101)-oriented films behaves differently with increasing strain, leading to an increasing and decreasing extrinsic contribution in (001)- and (101)-oriented films, respectively. Despite these differences, across the entire strain regime studied here and for all three film orientations, the overall predicted $\varepsilon_\perp$ is found to exist in a rather narrow range between 220-290.

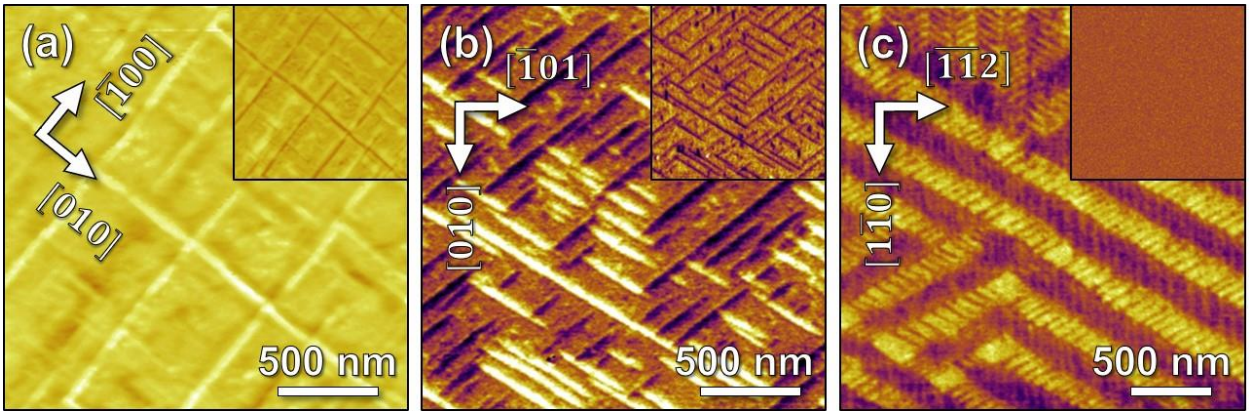

Fig. 4.3: Domain structure characterization of $PbZr_{0.2}Ti_{0.8}O_3$ films. Piezoresponse force microscopy images showing lateral (mixed phase (θ) and amplitude (A), A·cosθ) and vertical (mixed phase (θ) and amplitude (A), A·cosθ, inset) contrast for equilibrium domain structures of (a) (001)-, (b) (101)-, and (c) (111)-oriented $PbZr_{0.2}Ti_{0.8}O_3$ thin films.

4.3 Domain Structures in $PbZr_{0.2}Ti_{0.8}O_3$ Films

I proceed to examine model ferroelectric thin films of different orientations experimentally. I focus on 150 nm $PbZr_{0.2}Ti_{0.8}O_3$ / 10 nm $SrRuO_3$ or $La_{0.7}Sr_{0.3}MnO_3$ / $SrTiO_3$ (001), (110), and (111) heterostructures grown via pulsed-laser deposition. The domain structure of the films was probed via piezoresponse force microscopy (PFM). In (001)-oriented $PbZr_{0.2}Ti_{0.8}O_3$ thin films, I observe *c/a/c/a* domain structures that are commonly seen in tetragonal ferroelectric thin films and consist of majority out-of-plane polarized *c* and minority in-plane polarized *a* domains separated by 90° domain walls (Fig. 4.3a) [101,102]. The density of 90° domain walls is known to increase with increasing tensile strain which corresponds to an enhancement of the motional extrinsic contribution to the low-field permittivity in (001)-oriented films [14,63,88]. Considerably less work in this vein, however, has been undertaken for (101)- and (111)-oriented films [69].

Thus, here I provide detailed studies of domain structures and permittivity in (101)- and (111)-oriented films. In the (101)-oriented films the PFM images reveal a mixed-domain pattern where the majority of the sample is made up of domains with polarization along the [001] which is oriented at an angle of ~43.6° from the plane of the film, while the remaining structure consists of stripe-like domains possessing only in-plane polarization components pointing along the [010] or [0$\bar{1}$0] (Fig. 4.3b). In (111)-oriented films, a complex metastable domain structure was observed in the as-grown state (Fig. 4.4) and in order to probe the equilibrium domain structure the samples were poled with a series of +/- 6 V biases applied locally to a PFM tip to switch a 2.5 μm × 2.5 μm region (samples were switched between 2-6 times). Following such poling a complex, ordered nanotwinned domain pattern with a high density of uncharged 90° domain walls was observed (Fig. 4.3c). The observed domain structure is the result of the tiling of three types of domain bands, separated by 120° with average domain-band widths of ~300 nm. Within each domain band, the domain structure consists of a mixture of all three degenerate polarization variants (pointing along the [0$\bar{1}$0], [00$\bar{1}$], and [$\bar{1}$00], which are oriented at an equal angle of ~33.9° from the plane of the

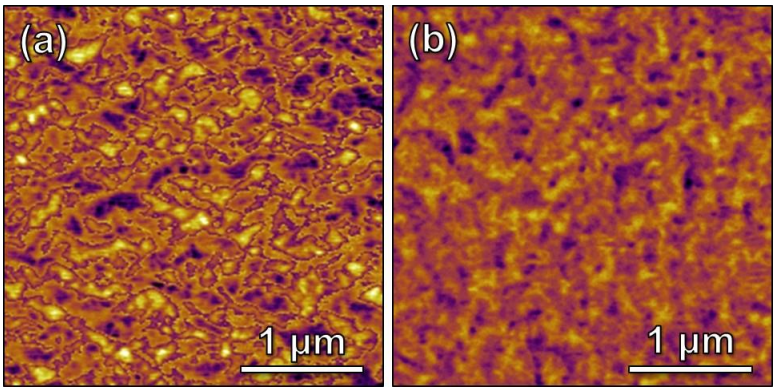

Fig. 4.4: Piezoresponse force microscopy images of as-grown (111)-oriented films. (a) Vertical and (b) lateral (mixed phase (θ) and amplitude (A), A·cosθ) images showing complex, nanoscale, metastable domain patterns.

film) distributed into two sub-bands, with each sub-band being made-up of only two of the polarization variants, consistent with prior predictions [103]. Reciprocal space mapping studies confirm the above polydomain structures for the various film orientations (Fig. 4.5). Regardless of the film orientation, the PFM studies indicate no 180° domain walls present as a result of the preferential out-of-plane direction of the polarization which is induced by the asymmetric electrical boundary conditions (*i.e.*, the presence of a bottom electrode). Thus, in comparison to traditional bulk ceramic samples, these films provide a well-characterized, model system exhibiting controllable domain structures possessing only a single type of domain walls (*i.e.*, 90°).

The PFM analysis further allows for the direct quantification of the domain structures – in particular the determination of the domain-wall density (λ, defined as the total length of domain walls in a given area) and the volume fraction of minority domains ($\phi_{\min}$, defined as the volume fraction of the domain type which possesses the smallest population among all polarization variants in the case of a poled film). Definition and schematic illustrations of these minority domains are provided (Fig. 4.2). In (001)- and (101)-oriented films, the minority domain represents the domain with the polarization pointing in the plane-of-the-film (along the [100], [010] and [010], [$0\bar{1}0$], respectively). Due to symmetry in (111)-oriented films, however, one can select any of the three polarization variants as the minority domain as they all form an equal angle with the normal direction of the substrate and occur in equal fractions. Details of the analysis are provided in Appendix B, but briefly, image analysis of the PFM domain structure images allows for the selection and measurement of the perimeter and area of all domain types and hence direct measurement of λ and the area fraction of the domains. To estimate $\phi_{\min}$, I have assumed a uniform width of the domains throughout the thickness of the film [104-107]. It should be noted that this assumption matches the assumptions of the GLD models (or, in other words, matches the ideal domain structure that would be predicted from such models), but might slightly overestimate the

Table 4.1: Line density of 90° domain walls (λ) and volume fraction of minority domains (ϕ_{min}) measured for (001)-, (101)-, and (111)-oriented films.

Orientation	λ (μm^{-1})	ϕ_{min} (%)
(001)	8.91	15.3
(101)	16.3	19.9
(111)	48.9	33.3

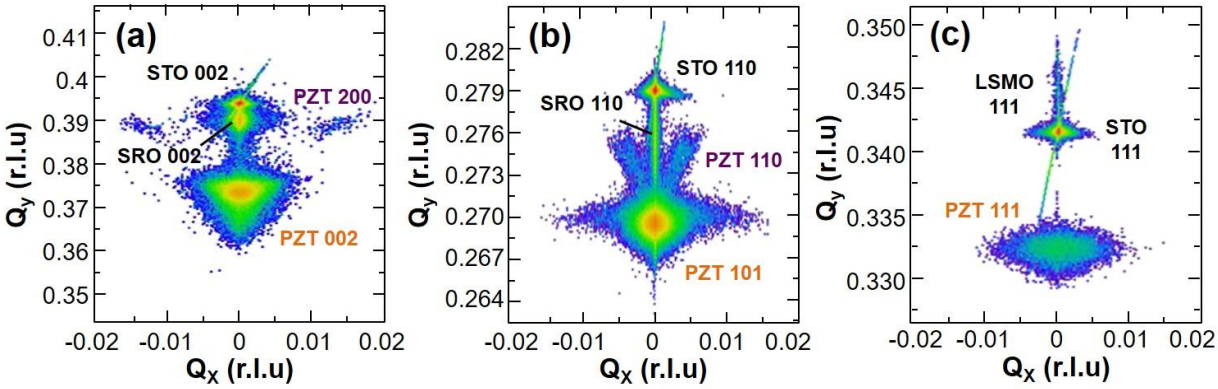

Fig. 4.5: X-ray reciprocal space mapping studies of $PbZr_{0.2}Ti_{0.8}O_3$ films. On-axis reciprocal space maps measured about the $SrTiO_3$ 002-, 110-, and 111-diffraction conditions for (a) (001)-oriented heterostructures with a majority peak corresponding to the 002-diffraction condition and a minority peak corresponding to the 200-diffraction condition of the $PbZr_{0.2}Ti_{0.8}O_3$ which represent *c* and *a* domains, respectively; (b) (101)-oriented heterostructures with diffraction peaks corresponding to the 101- and 110-diffraction conditions which represent the majority and minority domains of $PbZr_{0.2}Ti_{0.8}O_3$, respectively; (c) (111)-oriented heterostructures with only one broad diffraction peak which confirms the degeneracy of various polarization variants in this orientation that possess uniform out-of-plane lattice spacing.

volume density if the domains are more wedge-shaped [108]. Regardless, this potential slight discrepancy has little to no impact on the overall conclusion of the data below. The values of λ and $\phi_{\min}$ are provided (Table 4.1). From this analysis, it is clear that the (111)-oriented films possess domain-wall densities that are at least 3-5.5-times the values for (001)- and (101)-oriented films and that the experimentally observed $\phi_{\min}$value is consistent with the degeneracy of the three polarization variants in (111)-oriented films calculated from the GLD models.

This work reveals that in addition to the use of epitaxial strain [67], film thickness [101], and film composition [13] to manipulate domain structures in ferroelectrics, film orientation is another effective route by which to control the domain structure and domain wall density. In fact, (111)-oriented films enable the study of domain structures and densities not possible in other orientations at these film thicknesses. This enhanced density of domain walls will boost the contribution of such features to the overall response to applied stimuli. Furthermore, due to the degeneracy of the different domain variants the extrinsic contribution from the domain walls is expected to be solely due to the stationary-domain-wall contributions (not motional extrinsic contributions), which presents a unique opportunity to study the stationary response of domain walls to external stimuli quantitatively.

4.4 Dielectric Properties of $PbZr_{0.2}Ti_{0.8}O_3$ Films

Detailed dielectric characterization of the various orientations of films was performed on symmetric capacitor structures using $SrRuO_3$ or $La_{0.7}Sr_{0.3}MnO_3$ top and bottom electrodes. For all measurements reported herein, the capacitor structures were subjected to current-voltage and ferroelectric characterization first, including multiple switching processes to assess the nature of

the hysteresis loops and to assure measurements of poled capacitors only. Only capacitors showing symmetric current-voltage response, well-saturated, symmetric, and imprint-free hysteresis loops across the frequency range 1 Hz – 10 kHz were probed (Fig. 4.6). The quality of the films and the accuracy of the measurements of domain wall density and domain fraction are confirmed using the procedure of Ref. [109]. The estimated values of polarization along the [001] are found to be approximately constant across the different orientations. Subsequently, the room temperature low-field dielectric permittivity ($\varepsilon_\perp$) was measured with an AC excitation field with an amplitude of 50 mV (in the frequency range from 0.1 kHz to 10 kHz). The amplitude of the applied field was confirmed to be in the reversible regime via Rayleigh studies (Appendix C). The (001)- and (101)-oriented films show values within the range $\varepsilon_\perp$= 185 – 267, while the (111)-oriented films exhibit significantly enhanced $\varepsilon_\perp$ = 654-691 across this same frequency range (Fig. 4.7).

A comparison of these measured values with the calculated permittivity from the GLD models was made by extracting the data point from Fig. 4.1 at the experimentally measured $\phi_{\min}$ given in Table 4.1. The calculated $\varepsilon_\perp$ (including both intrinsic and extrinsic contributions) for all three orientations shows small differences (all orientations are predicted to have values between 220–250), which agrees well with the experimental results for (001)- and (101)-oriented films. The (111)-oriented films, however, show a significant discrepancy between the experimentally measured and theoretically predicted values. As is noted in the discussion of the GLD model for

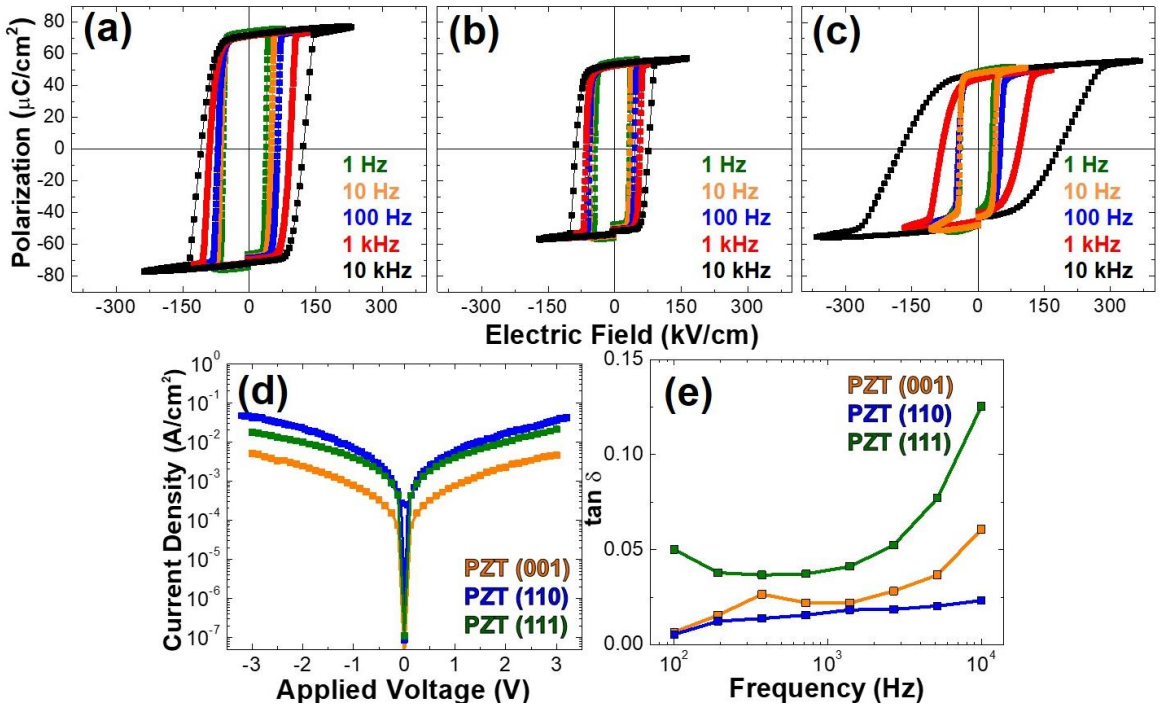

Fig. 4.6: Electronic, dielectric, and ferroelectric properties. Frequency dependent polarization-electric field hysteresis loops measured in (a) (001)-, (b) (101)-, and (c) (111)-oriented $PbZr_{0.2}Ti_{0.8}O_3$ films in the frequency range of 1 Hz to 10 kHz. (d) Leakage current – voltage and (e) loss tangents measured in the frequency range of 0.1 kHz – 10 kHz for (001)-, (101), and (111)-oriented $PbZr_{0.2}Ti_{0.8}O_3$ films.

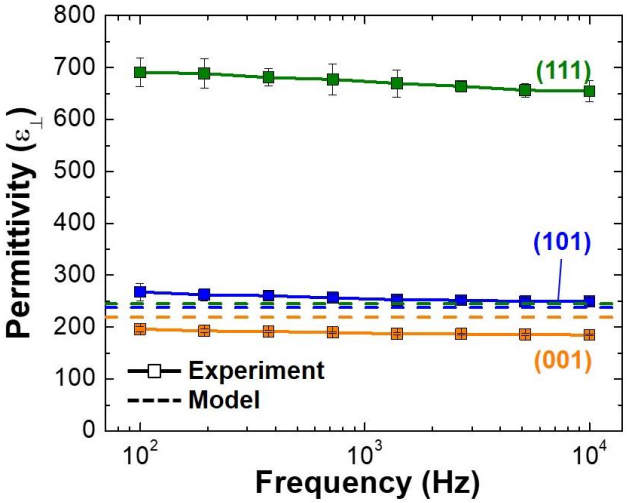

Fig. 4.7: Frequency dependence of permittivity ($\varepsilon_\perp$) in $PbZr_{0.2}Ti_{0.8}O_3$ thin films. The solid symbol line shows $\varepsilon_\perp$ measured at an AC excitation of 50 mV for (001)-, (101)-, and (111)-oriented $PbZr_{0.2}Ti_{0.8}O_3$ thin films. The dashed lines show the predicted $\varepsilon_\perp$ (including intrinsic and extrinsic contributions) from the Ginzburg-Landau-Devonshire models.

the (111)-oriented films, all three degenerate polarization variants are present in equal volume fractions and these fractions will not vary with application of an electric field thus leading to an absence of a motional extrinsic contribution. The experimental results, however, imply that $\varepsilon_\perp$ for (111)-oriented films is greatly enhanced with increasing domain-wall density (or decreasing average domain width). This enhancement suggests that the high density of domain walls in the (111)-oriented films could potentially give rise to a stationary-domain-wall contribution that can enhance the permittivity.

To further quantify this stationary-domain-wall contribution, I utilized an equivalent electrical circuit model to calculate the effective domain-wall permittivity. Previous studies [103] suggest that the 90° domain walls present in the (111)-oriented heterostructures, by symmetry and to avoid charged domain boundaries, should be inclined from the plane of the film at an angle of ~33.9°. When applying electric field along the normal direction of the film, the electric field lines should proceed straight along the normal direction within the domains, but will be deflected from the vertical direction within the domain walls according to Maxwell's equations (Fig. 4.8). Thus, an appropriate model of an equivalent circuit for this system requires that I treat the domain and domain walls as capacitors in series where the effective thickness of each capacitor is geometrically calculated based on the path-length of the field within that element. Using the experimentally measured average domain width (~40 nm), the experimentally measured $\varepsilon_\perp$ (~670), the calculated intrinsic dielectric permittivity (~245), and by assuming the domain-wall width to be (conservatively) 1-10 nm [104-107,110] one can estimate $\varepsilon_{\mathrm{dw}}$ to be 1,500-19,000, which is 6-78 times larger than the expected intrinsic response within a domain. As noted above, recent theoretical work using a decoupling approximation and GLD modeling suggests the possibility of up to a thousand-fold enhancement of the dielectric susceptibility and piezoelectric response across 90° domains walls in tetragonal ferroelectrics (like those found in our samples) due to structural and polarization inhomogeneities within the domain-wall region [31]. In addition, recent density functional theory and molecular dynamics simulations suggest that this enhanced low-field permittivity is a result of frustrated dipoles with the finite width of the domain walls, which can induce 100% enhancement of the dielectric susceptibility arising from the softer potential wells within them [89]. Our work, in turn, experimentally

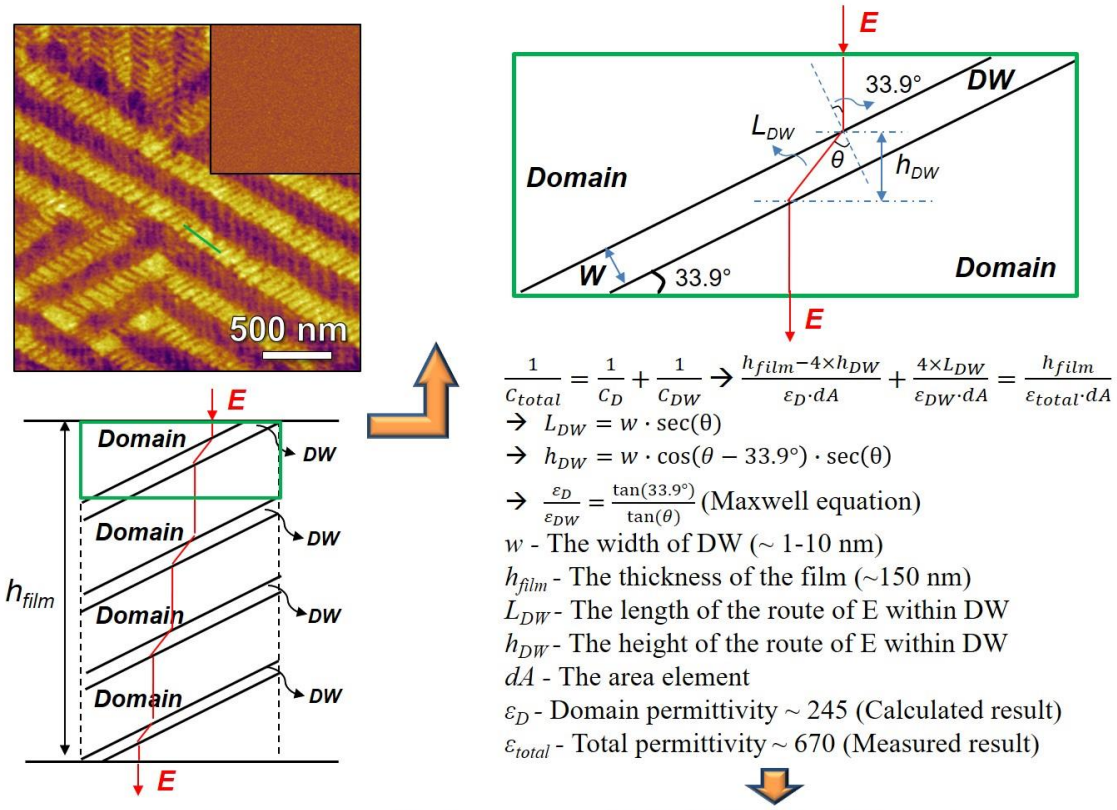

Fig. 4.8: Quantification of the stationary-domain-wall permittivity. Detailed process of the extraction of the effective domain wall permittivity using an equivalent circuit approach.

demonstrates that high density, stationary 90° domain walls could provide significantly enhanced dielectric response in the epitaxial thin films, particularly at large domain-wall densities.

The above results show that the application of electric field along certain non-polar directions in tetragonal ferroelectrics can be used to effectively "freeze out" the domain-wall motion and thus enables us to probe the stationary-domain-wall contribution to susceptibility. This is aided by the fact that growth of (111)-oriented films produces a configuration of numerous degenerate polarization variants, enables the application of electric fields along non-polar directions, and produces domain-wall densities high enough to promote the stationary-domain-wall contribution to be comparable in magnitude to the intrinsic response from the bulk of the domains. These observations, made possible by the simplicity of the engineered domain structure in the epitaxial thin films and our ability to directly probe the type, density, and response of these domain wall structures in different orientations produces a complimentary approach to the study ferroelectric single crystals with fields applied along different crystallographic directions and provides an opportunity to re-examine the importance of domain structure in controlling field-induced response.

4.5 Conclusions

The studies in this Chapter suggest that the stationary-domain-wall contribution to ferroelectric susceptibility should be given additional attention for its potential to enhance overall material performance. To date the understanding of intrinsic and motional extrinsic responses in these materials has led researchers to decrease the average domain size to enhance susceptibilities. The observed increase in performance, although likely partially enhanced by extra motional extrinsic contributions, could also be strengthened by simultaneous turn-on of stationary-domain-wall contributions. In one extreme case one could imagine that in systems controlled to have extremely fine domain structures, domain wall-domain wall interactions could lessen the extent of motional extrinsic contributions while still exhibiting enhancements in susceptibility from the stationary-domain-wall contribution. The failure to consider such stationary-domain-wall contributions, in turn, could result in the attribution of performance enhancements to the wrong feature in the material. Our work suggests that motional extrinsic contributions to permittivity are (at best) a factor of 2-times larger than the intrinsic response while stationary-domain-wall contributions could be as large as 6-78 times larger than the intrinsic response [111,112]. This work provides a new intellectual framework in which to consider ferroelectric susceptibilities and to explain observations in a range of samples. Our observations provide new insights into the microscopic structural origin of enhanced ferroelectric susceptibilities and a new approach to optimize the properties of epitaxial thin films.

CHAPTER 5

Ferroelectric Polarization Reversal via Successive Ferroelastic Transitions

Switchable polarization makes ferroelectrics a critical component in memories, actuators, and electro-optic devices and potential candidates for nanoelectronics. Although many studies of ferroelectric switching have been undertaken, much remains to be understood about switching in complex domain structures and in devices. In this Chapter, a combination of thin-film epitaxy, macro- and nanoscale property and switching characterization, and molecular-dynamics simulations are used to elucidate the nature of switching in $PbZr_{0.2}Ti_{0.8}O_3$ thin films. Differences are demonstrated between (001)-/(101)- and (111)-oriented films, with the latter exhibiting complex, nanotwinned ferroelectric domain structures with high densities of 90° domain walls and considerably broadened switching characteristics. Molecular-dynamics simulations predict both 180° (for (001)-/(101)-oriented films) and 90° multi-step switching (for (111)-oriented films) and these processes are subsequently observed in stroboscopic piezoresponse force microscopy. These results have implications for our understanding of ferroelectric switching and offer opportunities to change domain reversal speed.

5.1 Introduction

Ferroelectric materials are increasingly being considered as critical components in next generation logic [93], non-volatile memories [113,95], actuators and sensors [95], and electro-optic elements for waveguide devices. Such applications require a deep understanding of the susceptibilities (especially to electric fields) and routes to control and manipulate the order parameters in these materials. Recent advances in thin-film synthesis have enabled the manipulation of structure and properties of ferroelectric thin films [114,48]. For example, in the tetragonal ferroelectric $PbZr_{0.2}Ti_{0.8}O_3$ both the domain structure [101,115] and properties (*i.e.*, dielectric [88,116,117], piezoelectric [117,118], and pyroelectric [119,97]) can be dramatically tuned by varying epitaxial strain, film thickness, electrical boundary conditions, and other parameters. To date, the majority of work on such films has focused on (001)-oriented heterostructures, where the possible domain structures have been theoretically predicted [97,77] and observed [97,102]. How these domain structures evolve in other film orientations, however, has not been widely probed [109,120,71]. Studies of single-crystal ferroelectrics, however, where it is possible to apply the stimulus field along different crystallographic directions, have demonstrated that a poling field that is not purely along the bulk polarization direction produces increased domain-wall density and enhanced dielectric [74] and piezoelectric [73] responses. Similar studies on thin-film samples have not been completed.

Breakthrough applications of these materials require knowledge of both the static structure and the dynamics of field-dependent responses. Real-time studies of polarization dynamics including (for example) X-ray scattering [121-123], piezoresponse force microscopy (PFM) [124-126], and transmission electron microscopy [127-129] have shed new light on switching processes. Despite these advances, it remains difficult to explore some aspects of switching that take place on very short time scales. Advances in molecular-dynamics (MD) simulations now provide an unprecedented look at the dynamics of complex nanoscale events, and interatomic potentials derived from *ab initio* calculations can be applied to study finite-temperature properties [130-132] in a variety of environments [133,134]. These studies provide insights into the coupling of polarization, strain, electric field, stress, temperature, and local structure; however, there are still very few MD simulations of domain wall motion [129] and growth rates [135], and the dynamics of 90° domain walls has not been investigated previously.

In this Chapter, I develop a comprehensive picture of the interrelationships between thin-film epitaxy, nanoscale domain structures, and electric-field switching in $PbZr_{0.2}Ti_{0.8}O_3$ [72]. Clear differences are demonstrated between (001)-/(101)- and (111)-oriented films with the latter exhibiting complex, nanotwinned ferroelectric domain structures with high densities of 90° domain walls, considerably broadened ferroelectric switching characteristics, and lower threshold fields for the onset of non-linearity in Rayleigh studies. MD simulations reveal the presence of both 180° switching and multi-step 90° switching domain reversal processes. Subsequent stroboscopic PFM studies confirm the presence of intermediate, 90° switching events in (111)-

oriented films and 180° switching events in (001)- and (101)-oriented films. The varying effects of domain sizes (or volume fractions) and electric field on the different film orientations give rise to the difference in switching mechanism. These results have implications for our fundamental understanding of ferroelectric switching and provide avenues to accelerate domain reversal in these materials for next-generation applications.

5.2 Domain Structures in $PbZr_{0.2}Ti_{0.8}O_3$ Thin Films

I focus on 150 nm $PbZr_{0.2}Ti_{0.8}O_3$ / 10 nm $SrRuO_3$ or $La_{0.7}Sr_{0.3}MnO_3$ / $SrTiO_3$ (001), (110), and (111) heterostructures grown via pulsed-laser deposition. X-ray diffraction studies show that the films are epitaxial and single-phase (Fig. 5.1). The ferroelectric domain structure was probed using PFM. It is noted that the detailed domain structure characterization and analysis of (001), (110), and (111)-oriented heterostructures has been discussed in Chapter 4. In this Chapter I will briefly recap the domain structures using the following terminology to describe the polarization variants in the samples: for tetragonal $PbZr_{0.2}Ti_{0.8}O_3$, domains with polarization along the positive and negative [100], [010], and [001] axes will be referred to as $P_1^{+/-}$, $P_2^{+/-}$, and $P_3^{+/-}$, respectively. In (001)-oriented heterostructures, a typical polydomain structure with majority P_3^- domains and minority P_1^+ and P_2^- domains is observed (Figs. 5.2a, b). In (101)-oriented heterostructures, three different domain types are found (Figs. 5.2c, d), with majority P_3^+ domains (in which the polarization is oriented at an angle of ≈43.6° from the plane of the film) and the remainder primarily composed of in-plane polarized stripe-like P_2^+ and P_2^- domains and small fractions of P_1^- domains (also oriented ≈43.6° from the plane of the film). The as-grown domain structure of the (001)- and (101)-oriented films, as probed by PFM studies which enable exact determination of the polarization directions, represents the equilibrium domain structure predicted for these film orientations [136,69] and does not change with electric field cycling (Fig. 5.3).

Analysis of the (111)-oriented heterostructures reveals a dramatically different picture. The as-grown domain structure has a complex, metastable nanoscale domain pattern. A domain structure consistent with that predicted to the equilibrium domain structure is obtained after a series of ± 6 V dc voltages were applied to the PFM tip to switch a 1.5 μm × 1.5 μm region of the film a

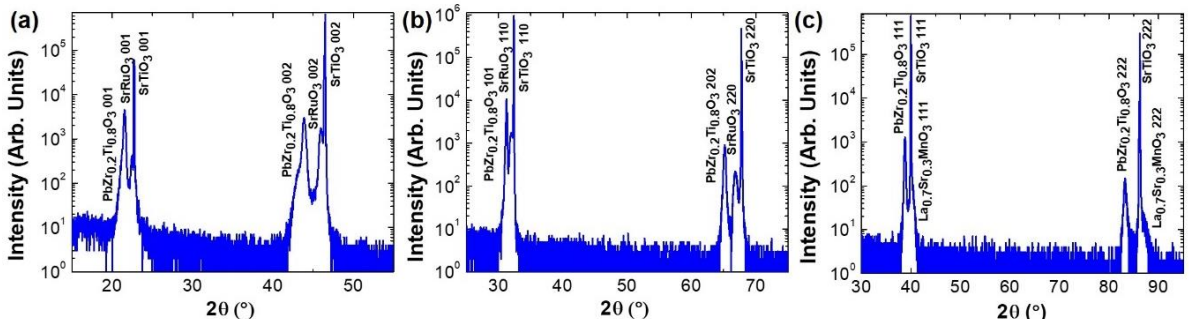

Fig. 5.1: Crystal structure analysis. X-ray diffraction θ-2θ scans of (a) (001)-, (b) (101)-, and (c) (111)-oriented $PbZr_{0.2}Ti_{0.8}O_3$ films.

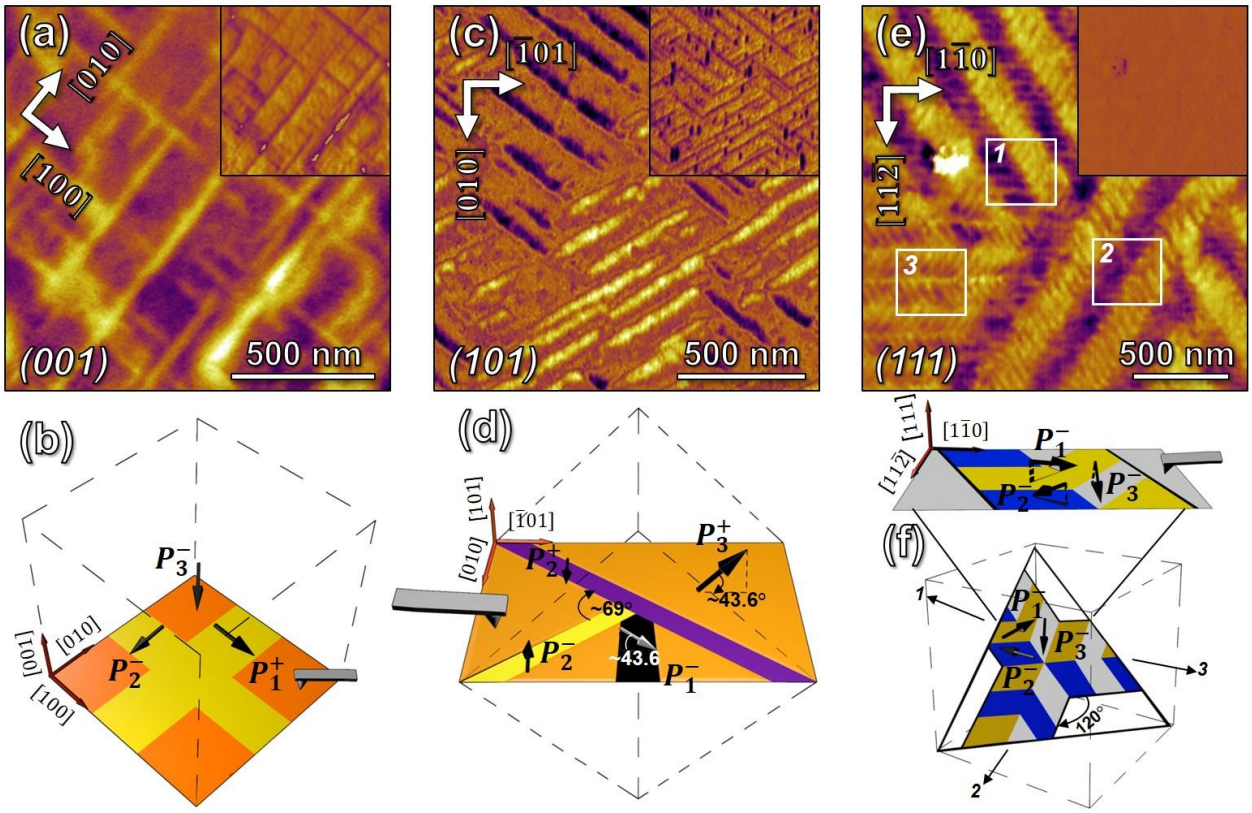

Fig. 5.2: Piezoresponse force microscopy studies of $PbZr_{0.2}Ti_{0.8}O_3$ thin films. Lateral ($A\cos\theta$, combining phase θ and amplitude A) and vertical ($A\cos\theta$, inset) piezoresponse force microscopy images for equilibrium domain structures and corresponding illustrations of those domain structures for (a), (b) (001)-oriented heterostructures with majority P_3^- domains (orange domains) and minority P_1^+ and P_2^- domains (yellow domains); (c), (d) (101)-oriented heterostructures with majority P_3^+ domains (with polarization oriented at ≈43.6° from the plane-of-the-film, orange domains) and minority domains including stripe-like P_2^+ and P_2^- domains (in-plane polarized, purple domains) and small fractions of P_1^- domains (with polarization oriented at ≈43.6° from the plane-of-the-film, black domains); (e), (f) (111)-oriented heterostructures with complex nanotwinned domain structures wherein there are three degenerate polarization variants P_1^-, P_2^-, and P_3^- oriented at an angle of ≈33.9° from the plane of the film (represented by yellow, blue, and grey domains, respectively) which are tiled to produce three degenerate domain bands separated by 120° as labeled in the open squares (1), (2), and (3).

total of 2-6 times. The domain pattern consists of a high density of nanotwinned domains (Fig. 5.2e). The observed domain structure is the result of the tiling of three types of domain bands, separated by 120° (noted as areas 1, 2, and 3, Fig. 5.2e) with average domain-band widths of ≈300 nm. Within each domain band, the domain structure consists of a mixture of all three degenerate polarization variants (P_1^-, P_2^-, and P_3^-, each possessing a polarization direction that is oriented at an angle of ≈33.9° form the plane of the film) distributed into two sub-bands, with each sub-band composed of only two of the polarization variants. The average domain size within the domain sub-bands is ≈40 nm. The geometry of such domain structures is shown in a schematic illustration (Fig. 5.2f). Prior theoretical treatments predicted such equilibrium domain structures [103].

5.3 Macroscale Switching Studies of $PbZr_{0.2}Ti_{0.8}O_3$ Thin Films

Having established the difference in domain structures for the various heterostructure orientations, I probed their dielectric and ferroelectric properties using symmetric metal-oxide capacitor structures [137]. All heterostructures, regardless of orientation, were found to exhibit symmetric, well-saturated polarization-electric field hysteresis loops (Fig. 5.4a) that are maintained down to at least 1 Hz. As expected, the saturation polarization scales with the film orientation, with (001)- and (111)-oriented films having the largest and smallest values, respectively. In addition, although all films possess high remnant polarization, the (001)- and (101)-oriented films show nearly square hysteresis loops with sharp electric-field switching, while (111)-oriented films exhibit more slanted hysteresis loops regardless of frequency, indicative of switching at a broader range of fields (Fig. 5.5).

The dielectric permittivity was then measured as a function of increasing ac electric field excitation. Since I focus here on switching behavior, the fields were extended to higher values than typically applied in Rayleigh studies for this work (Appendix C) [60]. These studies reveal that (111)-oriented heterostructures exhibit a lower threshold field (8.2 kV/cm) for the onset of non-linearity (or polarization switching) as compared to (001)- and (101)-oriented films (46.3 kV/cm and 22.5 kV/cm, respectively) (Fig. 5.4b). Additionally, the field dependence of the dielectric response of the (111)-oriented heterostructures shows a gradual increase (and, therefore, ferroelectric switching) over a much larger range of fields, relative to the (001)- and (101)-oriented films, consistent with the polarization-electric field hysteresis loops (Fig. 5.4a).

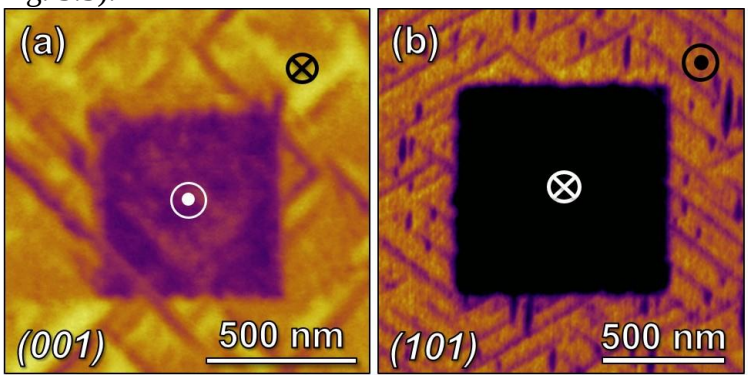

Fig. 5.3: Domain structure characterization. Vertical ($A\cos\theta$, combining phase θ and amplitude A) piezoresponse force microscopy images of $PbZr_{0.2}Ti_{0.8}O_3$ of (a) (001)-oriented films after applying a negative tip bias of -5 V in PFM to locally switch a central square region, which indicates the as-grown down-poled domain structure, (b) (101)-oriented films after applying a positive tip bias of 4 V in PFM to locally switch a central square region, which indicates the as-grown up-poled domain structure.

5.4 Molecular-Dynamics Simulations of Switching in $PbZr_{0.2}Ti_{0.8}O_3$ Thin Films

To understand what gives rise to these different electric field responses, MD simulations were applied to examine the evolution of domain switching under differently oriented electric fields. These studies, done by Dr. Shi Liu and Prof. Andrew Rappe, probed the evolution of domain

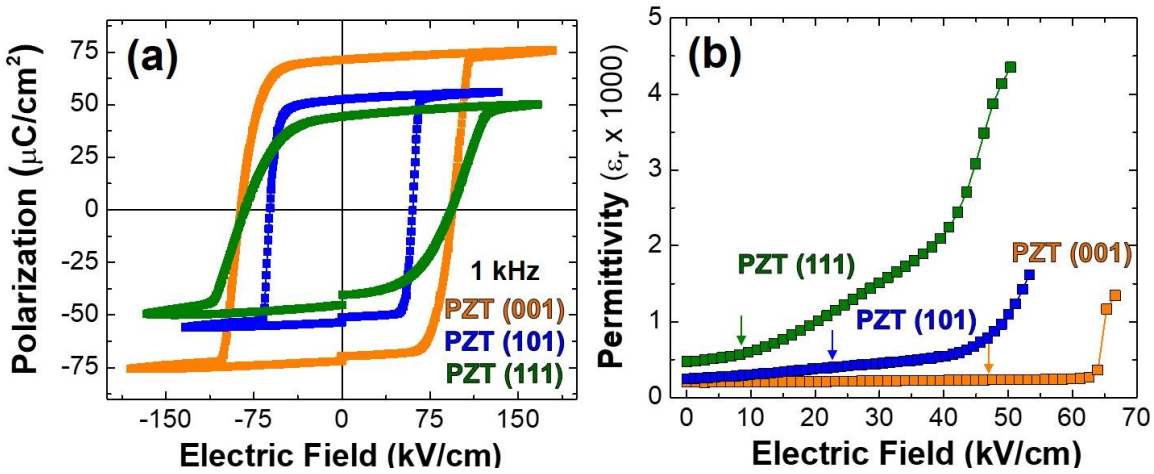

Fig. 5.4: Electrical characterization of $PbZr_{0.2}Ti_{0.8}O_3$ films. (a) Polarization - electric field hysteresis loops measured at 1 kHz and (b) permittivity as a function of ac electric field measured at 1 kHz for (001)-, (101)-, and (111)-oriented $PbZr_{0.2}Ti_{0.8}O_3$ thin films. The arrows demarcate the location of the onset of non-linearity from the Rayleigh studies.

structures resembling those experimentally observed in (001)-, (101)- and (111)-oriented films possessing 90° domain walls under electric fields applied along the film normal directions $[00\bar{1}]$, $[\bar{1}0\bar{1}]$ (Fig. 5.6a), and $[\bar{1}\bar{1}\bar{1}]$ (Fig. 5.6b), respectively. The volume fraction of the minority domains used in the simulations was based on experimental observations. The MD simulations provide a time-resolved view of the evolution of the domain structure including specific polarization variants (Fig. 5.7).

For brevity, I discuss here only the detailed MD studies of (101)-oriented films, but detailed studies of (001)-oriented films, which show similar results, are also provided (Fig. 5.8). In the case of (101)-oriented films, in the initial state (0.0 ps) a domain configuration with 20% minority P_2^+ domains (green, Fig. 5.6a) and 80% majority P_1^+ domains (red, Fig. 5.6a) with the electric field applied along the $[\bar{1}0\bar{1}]$ (yellow arrow, Fig. 5.6a) is simulated. This results in a series of complicated changes (Fig. 5.6a). At 3 ps, it is observed that the volume fraction of P_2^+ domains increases as they widen via changes of the type $P_1^+ \rightarrow P_2^+$ at the domain boundary due to the $[\bar{1}00]$-component of the electric field. In addition, a significant number of P_1^+ dipoles close to domain boundaries are switched by 180° to P_1^- dipoles (cyan). Further application of electric field facilitates the growth of the P_1^- domains via the 180° switching process of $P_1^+ \rightarrow P_1^-$ (see 5 and 7 ps images, Fig. 5.6a). At 10 ps, the whole supercell reaches a nearly single-domain state. Subsequent relaxation of the structure (after the field is turned off) for another 30 ps results in the reemergence of domain structures similar to that in the initial state (albeit poled in the opposite direction) due to strain accommodation. The lateral shift of the domain boundary is likely due to the application of large electric field to achieve picosecond switching in MD simulations.

In the case of (111)-oriented films, in the initial state (0.0 ps) a domain configuration with 50% P_1^+ domains (red, Fig. 5.6b) and 50% P_2^+ domains (green, Fig. 5.6b) was simulated with the

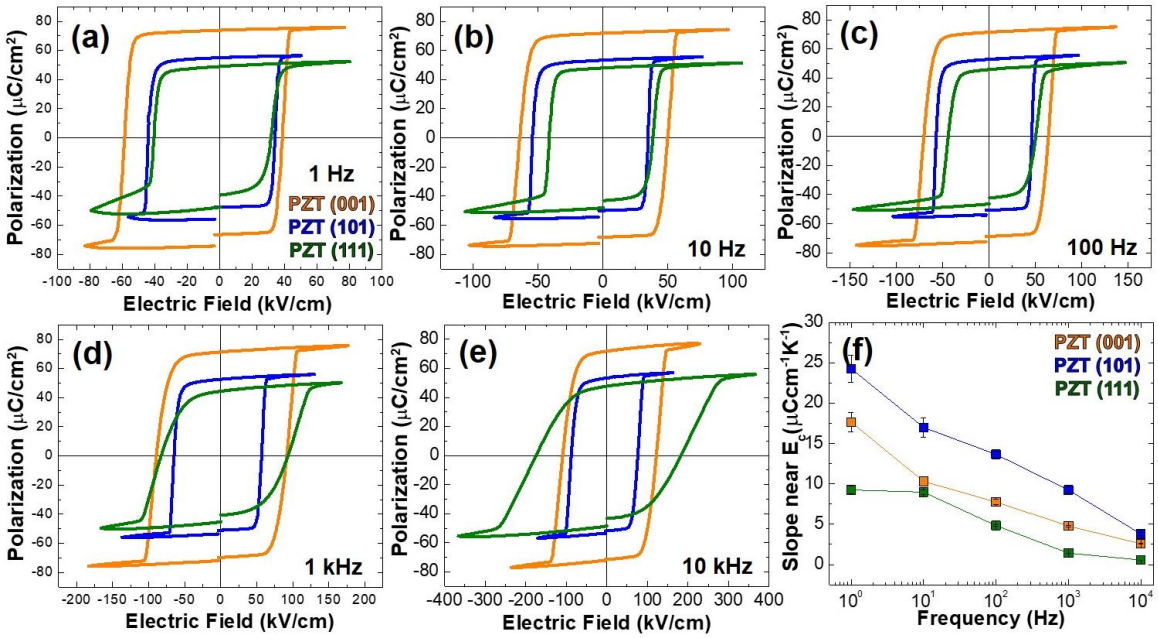

Fig. 5.5: Frequency dependent ferroelectric hysteresis loops. Ferroelectric hysteresis loops for (001)-, (101)-, and (111)-oriented $PbZr_{0.2}Ti_{0.8}O_3$ heterostructures measured at (a) 1 Hz, (b) 10 Hz, (c) 100 Hz, (d) 1,000 Hz, and (e) 10,000 Hz. (f) The frequency dependence of the slope of the loops near the coercive field is used to quantify the slant of each loop.

electric field applied along the $[\bar{1}\bar{1}\bar{1}]$ (yellow arrow, Fig. 5.6b). This process results in a fundamentally different domain-switching evolution (Fig. 5.6b). First, I observe that there is no significant domain-wall motion. Although decidedly different from the behavior in (101)-oriented heterostructures, this is expected since all polarization directions are energetically equivalent with respect to the applied field. Additionally, at 5 ps, new domains perpendicular to their parent domains appear via two types of 90° switching processes: $P_1^+ \rightarrow P_2^-$ and $P_2^+ \rightarrow P_1^-$, respectively. By 8 ps, the new domains spread quickly across their parent domains and dipole frustration at domain boundaries, leading to transient charged-domain walls, are also observed (Fig. 5.9) [75]. This switching process continues, until the final configuration of P_1^- and P_2^- domains is achieved by 10 ps. The strain-driven structural relaxation for another 10 ps in the absence of electric field leads to a slight change in the positions of domain walls, but overall the reemergence of domain structures similar to that in the initial state (albeit poled in the opposite direction).

5.5 Mesoscale Switching Studies of $PbZr_{0.2}Ti_{0.8}O_3$ Thin Film

What these MD simulations reveal, is that if one only considers the starting and final states, the domain structures could potentially lead one to assume only 180° switching has taken place on the macroscale. These time-dependent models, however, reveal a more nuanced evolution with clear differences between (001)-/(101)- and (111)-oriented films with the latter revealing a multi-step, 90° switching domain-reversal process. To further explore these proposed switching

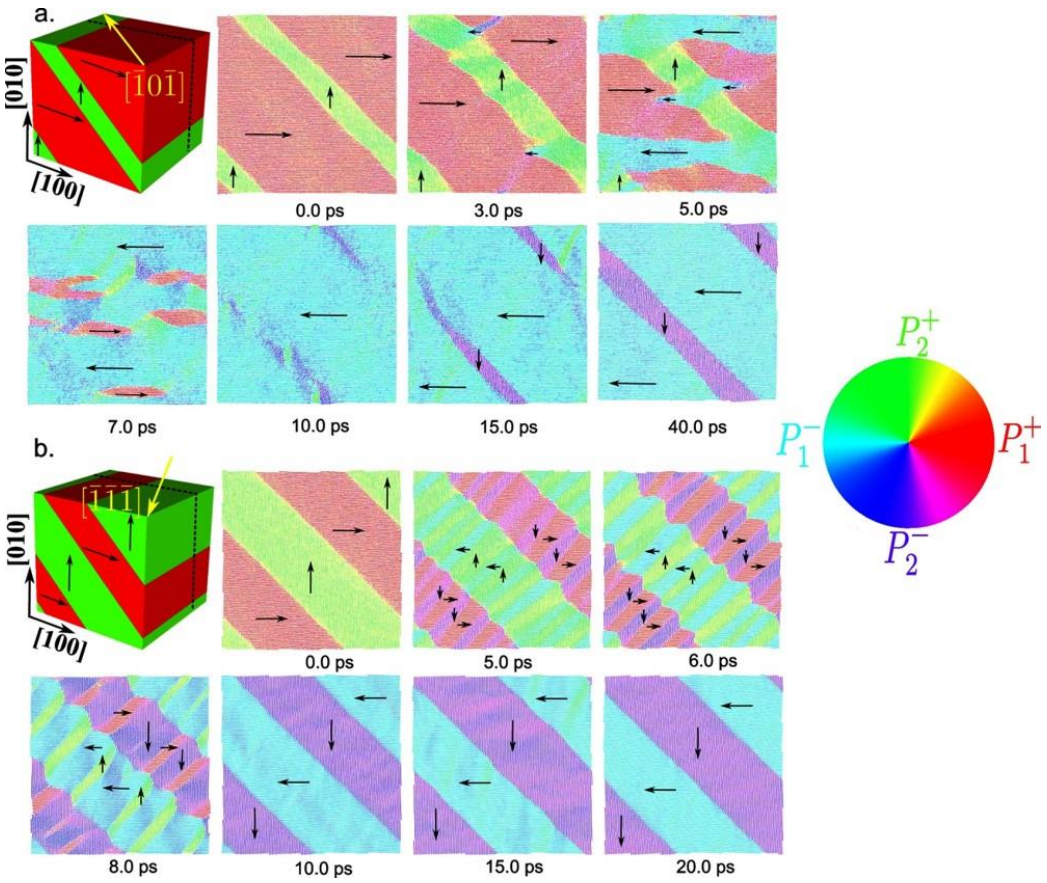

Fig. 5.6: Molecular dynamics simulations of switching in domain structures possessing 90° domain walls. These images show the evolution of domain structures under applied field. In both cases, the electric field is turn-on at 0.0 ps and off at 10 ps and allowed to relax at zero applied field from that point. The colors in the domain maps correspond to the polarization wheel shown at the right. (a) This simulation focuses on a domain structure that would be found in a (101)-oriented film. The domain structure consists of 20 volume % of minority (green, P_2^+) domains with polarization along [010] and 80 volume % of majority (red, P_1^+) domains with polarization along [100]. The electric field is applied along the $[\bar{1}0\bar{1}]$ (yellow arrow) to the initial domain structure. As the domains evolve, direct 180º reversal is observed ($P_2^+ \rightarrow P_2^-$ and $P_1^+ \rightarrow P_1^-$). (b) This simulation focuses on a domain structure that would be found in a (111)-oriented film. The domain structure consists of 50 volume % domains (green, P_2^+) with polarization along [010] and 50 volume % of domains (red, P_1^+) with polarization along [100]. The electric field is applied along the $[\bar{1}\bar{1}\bar{1}]$ (yellow arrow) to the initial domain structure. During the application of the field, 90º switching events ($P_2^+ \rightarrow P_1^-$ and $P_1^+ \rightarrow P_2^-$) are observed. The local polarization within each unit cell is represented with an arrow that is colored based on the angle formed with [100] axis.

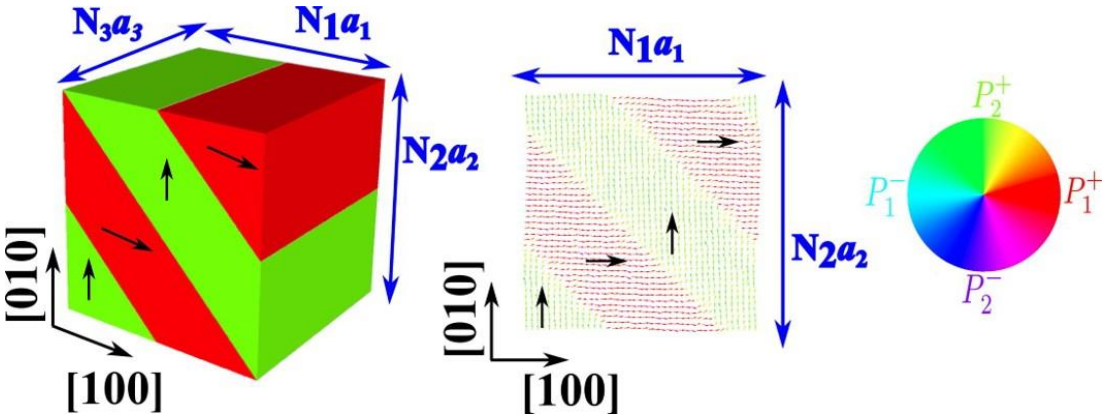

Fig. 5.7: Molecular dynamics simulations. (a) Domain structures possessing 90° domain walls constructed with a 40×40×40 supercell, (b) zig-zag domain patterns in {001} plane. $\gamma = 0.5$.

pathways and their implications for material properties, I completed local-scale PFM switching studies where a time series of images was produced while incrementally increasing the applied tip bias. Focusing first on switching in the (001)- and (101)-oriented films, similarly abrupt switching processes occurring in a narrow field range have been observed, consistent with the macroscale property studies. For brevity, I discuss here only the detailed switching studies of (101)-oriented films (Fig. 5.10). The (101)-oriented films show no obvious contrast change in either the lateral or vertical PFM images (Figs. 5.10a, b) when applying biases from 0-3.0 V to locally switch a 1 μm × 1 μm square region in the center of the scanned area. A schematic of this domain structure before switching is provided (Fig. 5.10c). Upon increasing the applied tip bias further, to 3.5 V, domains in the film start to switch, resulting in a contrast change in both the lateral and vertical PFM images (Fig. 5.10d). Further increasing the bias to 4.0 V results in complete switching of the central square region (Fig. 5.10e). Based on the PFM images, the final switched domain structure is interpreted such that both domains initially possessing polarization P_3^+(orange regions, Fig. 5.10c) and in-plane oriented stripe domains P_2^- and P_2^+ (black and grey regions, Fig. 5.10c) are switched by 180° (Fig. 5.10f). These observations are consistent with the abrupt switching that occurs in a narrow field range in the polarization hysteresis loops and with the abrupt increase of dielectric response in the Rayleigh analysis. These results indicate that 180° switching reversal occurs in (101)-oriented films, in agreement with MD prediction.

Similar studies of (111)-oriented films, however, reveal decidedly different responses with a complex evolution of domain structures involving four characteristic steps in the switching (Figs. 5.11a-d). Detailed static domain-structure characterization of the (111)-oriented films has been discussed above, and here I focus on an area possessing fully down-poled nanotwinned domain bands of a single type for simplicity (Fig. 5.11a). When applying a tip bias of –2.5 V to locally switch a 1 μm × 1 μm square region, only a small fraction of the domains switch (inset, Fig. 5.11b). Examination of the lateral PFM contrast reveals that the orientation of the long axes of the domains that were switched rotates by 90° in-the-plane of the film, resulting in a new domain configuration with a characteristic angle of 60° between the domain sub-bands (Fig. 5.11b). Upon further

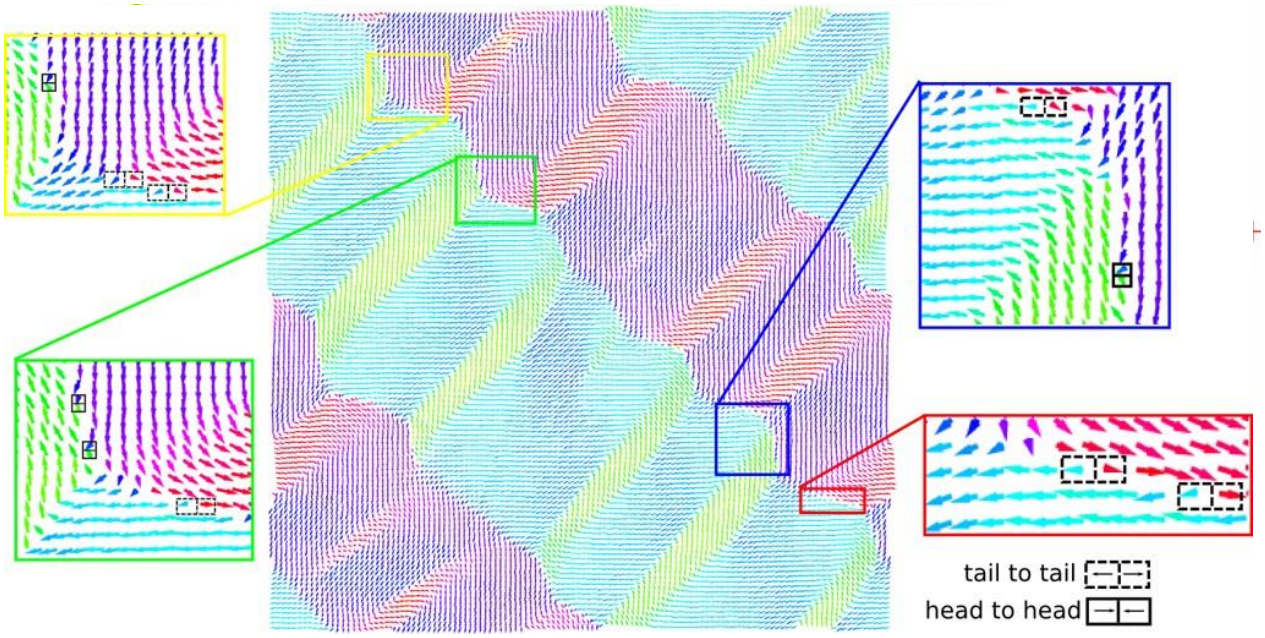

Fig. 5.9: Simulating domain structures with volume fraction of minority domain of 0.15 under $[00\bar{1}]$ electric field. The electric field is turned off at 10 ps. The local polarization within each unit cell is represented with an arrow that is colored based on the angle formed with [001] axis. The yellow arrow represents the direction of electric field and the black dashed line represents the 2D plane that is extracted to observe the dynamics in the other panels.

increasing the bias to –3.5 V, the majority of the square region subjected to the bias has been switched in the out-of-plane direction (inset, Fig. 5.11c) with the contrast changing accordingly in the lateral PFM images to reveal a characteristic angle of 60° between all domain sub-bands in the switched region (Fig. 5.11c). The domain structure does not exhibit further evolution until the applied tip bias exceeds –6 V. At this point, all domains in the square region subjected to the bias have been fully up-poled (inset, Fig. 5.11d). The nanotwinned-domain pattern is observed to return to the initial orientation and reestablishes the characteristic angle of 120° between the long axes of the domains (Fig. 5.11d). Although a similar nanotwinned-domain structure has been achieved, the in-plane contrast in the nanotwinned array has changed as compared to the initial state (*i.e.*, sub-bands with dark PFM contrast become light and vice versa, Fig. 5.11d) suggesting that full switching is accompanied by an orientation change of the in-plane component of polarization.

This multi-step switching process is intriguing, and here it is systematically analyzed. Schematic illustrations of the geometry of the sample including the crystallographic axes (Fig. 5.11e), the six possible polarization variants (Fig. 5.11(f)), and the twelve possible (six distinct) 90° domain boundaries (*i.e.*, those between $P_1^+ - P_2^+$ $(P_1^- - P_2^-)$, $P_1^+ - P_3^+$ $(P_1^- - P_3^-)$, $P_2^+ - P_3^+$ $(P_2^- - P_3^-)$, $P_1^+ - P_2^-$ $(P_1^- - P_2^+)$, $P_1^+ - P_3^-$ $(P_1^- - P_3^+)$, $P_2^+ - P_3^-$ $(P_2^- - P_3^+)$; each given a unique color in the figure) (Fig. 5.11(g)) projected on the (111) of the PFM image are provided. Additional details about the geometry of the domain boundaries are provided (Fig. 5.12). To aid the discussion, schematic illustrations of the domain structures (Figs. 5.11h-o) in each distinct

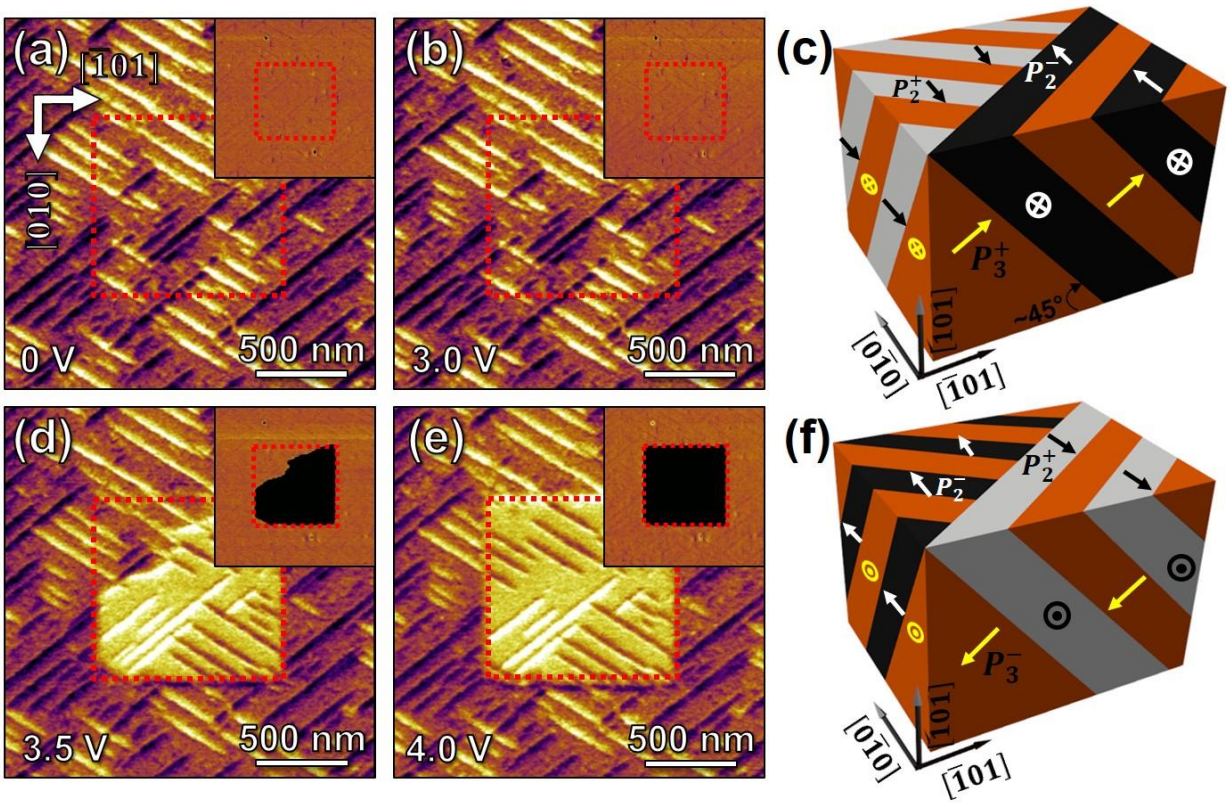

Fig. 5.10: Piezoresponse force microscopy switching studies of $PbZr_{0.2}Ti_{0.8}O_3$ (101) thin films. Lateral (Acosθ, combining phase θ and amplitude A) and vertical (phase θ, inset) piezoresponse force microscopy images of field-dependent domain structure evolution in (101)-oriented $PbZr_{0.2}Ti_{0.8}O_3$ in the (a) as-grown state and (b) after applying a tip bias of 3.0 V in the central square region. (c) Schematic illustration of the observed, unswitched domain structure with the majority P_3^+ (orange domains, oriented at an angle of 43.6° from the plane of the film) and the stripe-like P_2^- (black domains) and P_2^+ (white domains) domains (in-plane polarized). Upon increasing the applied tip bias to (d) 3.5 V and (e) 4.0 V, abrupt switching is observed. (f) Schematic illustration of the switched domain structure in (d) and (e) with the majority P_3^- (orange domains), P_2^- (black domains), and P_2^+ (white domains) after the 180° switching.

domain sub-band type for the four PFM images (Figs. 5.11a-d) are also provided. Three different colors (orange, blue, and grey) are used to represent the three different polarization variants with solid and dashed lines corresponding to down- and up-poled versions, respectively. In the initial state (Fig. 5.11a), all domains are down-poled, and the dark (Fig. 5.11h) and light (Fig. 5.11i) domain sub-bands consist of alternating P_1^-/P_2^- and P_1^-/P_3^- domains, respectively. Upon application of the –2.5 V applied bias (Fig. 5.11b), the orientation of the domain boundaries in both the dark (Fig. 5.11j) and light (Fig. 5.11k) domain sub-bands are found to rotate by 90° in-the-plane of the film. Such a change in the domain boundary orientation can only be achieved by a complex switching process which includes three different switching events including 90° switching that maintains the vertical component of the polarization ($P_1^- \rightarrow P_2^-$, area 1; Fig. 5.11j), 180° switching ($P_1^- \rightarrow P_1^+$, area 2; Fig. 5.11j), and 90° switching that changes the vertical component of the polarization ($P_2^- \rightarrow P_1^+$, area 3; Fig. 5.11j) as well as regions that experience no

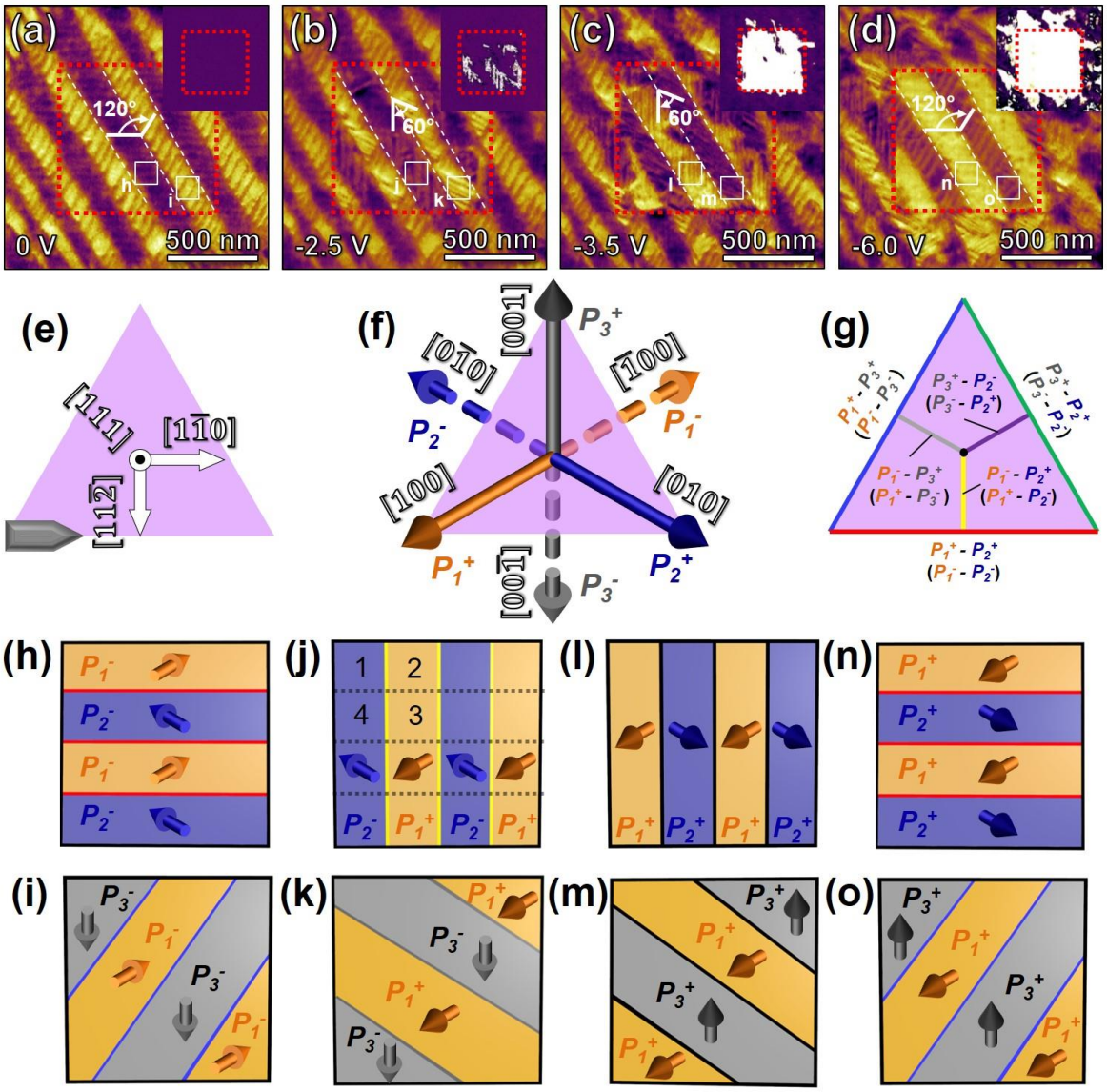

Fig. 5.11: Piezoresponse force microscopy switching studies of $PbZr_{0.2}Ti_{0.8}O_3$ (111) thin films. Lateral (Acosθ, combining phase θ and amplitude A) and vertical (phase θ, inset) piezoresponse force microscopy images of field dependent domain structure evolution in (111)-oriented $PbZr_{0.2}Ti_{0.8}O_3$ in the (a) initial down-poled state, after applying a tip bias of (b) -2.5 V to achieve partial switching, (c) -3.5 V to achieve complete out-of-plane switching, but incomplete in-plane switching, and (d) -6.0 V to achieve complete out-of-plane and in-plane switching. Schematic illustrations of the geometry of the sample are provided including (e) the projection of the crystallographic axes, (f) the six possible polarization variants (solid pointing out of the plane and dashed pointing into the plane of the film), and (g) the six possible distinct 90° domain boundaries (each given a unique color that is carried throughout the remaining panels). Additional illustrations of the proposed switching process for dark and light domain bands, respectively, for the (h) and (i) initial state, (j) and (k) a majority down-poled intermediate state, (l) and (m) an up-poled intermediate, and (n) and (o) the final, fully switched state.

switching ($P_2^- \rightarrow P_2^-$, area 4; Fig. 5.11j). Similar complex switching occurs in the light domain sub-bands as well (Fig. 5.11k). Upon further increasing the bias to –3.5 V (Fig. 5.11c), the orientation of the domain boundaries remains the same, but all domains are now up-poled (Figs.

5.11l, m) with a change of the in-plane contrast from light to dark (and vice versa) for the different domain sub-band types. This switching process includes 90° switching that maintains the vertical component of the polarization ($P_1^+ \rightarrow P_2^+$, Fig. 5.11l) and 90° switching that changes it ($P_2^- \rightarrow P_1^+$, Fig. 5.11l). Similar 90° switching events occur in the other domain sub-bands (Fig. 5.11m). Based on the PFM analysis, this up-poled domain structure should likely possess charged domain walls; however, it is not changed until the applied bias is further increased to –6 V (Fig. 5.11d). At this point, the domain boundaries are again rotated in-the-plane of the film by 90° and the domain structure is returned to a configuration consistent with the initial state (Figs. 5.11n, o), but with a change of the in-plane contrast in the PFM from light to dark (and vice versa) for the different domain sub-band types. Again, the domain walls in the final state are uncharged. This process is again accomplished by two types of 90° switching events that maintain the vertical component of the polarization ($P_1^+ \rightarrow P_2^+$ and $P_2^+ \rightarrow P_1^+$, Fig. 5.11n). Again, similar 90° switching events are observed for both domain sub-band types (Fig. 5.11o). In the end, regardless of how the switching is probed and acknowledging potential differences in the fine-scale nature of excitation and final domain structure produced by the different methodologies, the mechanisms underlying the switching events are innate to the materials. Thus, the combination of macroscopic capacitor, scanning-probe, and MD studies provides a detailed, multiple length- and time-scale look at the switching in these materials. From these studies, I observe that (001)-/(101)-oriented films switch via 180° switching processes while (111)-oriented films undergo domain reorientation via 90° switching mediated processes.

Although the nucleation and growth process for 180° switching events is fairly well understood, little evidence for 90° switching mediated domain reversal has been presented. It has been suggested that broadened (or double) current peaks during reverse switching of previously poled $PbZr_{0.415}Ti_{0.585}O_3$ ceramics could be the result of non-180° domain switching as a result of the residual stresses developed during forward poling [138] and that in single-crystals of [111]-oriented 95.5% $PbZn_{1/3}Nb_{2/3}O_3$ – 4.5% $PbTiO_3$, polarization reversal through intermediate polarization rotations of 71° and 109° can occur [139,140]. Despite these observations, the mechanisms underlying such behavior are not entirely clear [141] and no direct measurements and examples of 90° switching mediated domain reversal have been reported in the literature. This is particularly the case for thin films where there are no reports in this regard. In thin films, the 90° domain switching process, due to the elastic clamping of the substrate, is thought to be so energetically costly that it does not typically occur. Enhanced 90° domain switching can be realized in thin films if the effect of clamping can be compensated by engineering specific film or domain structures such as in patterned ferroelectric layers [142] or through a layered structure where the top layer is anchored on an underneath layer of a secondary ferroelectric phase [143]. Here I have achieved the 90° switching mediated domain reversal process in thin films by utilizing (111)-oriented domain structures where the energetics are such that it permits these events to take place.

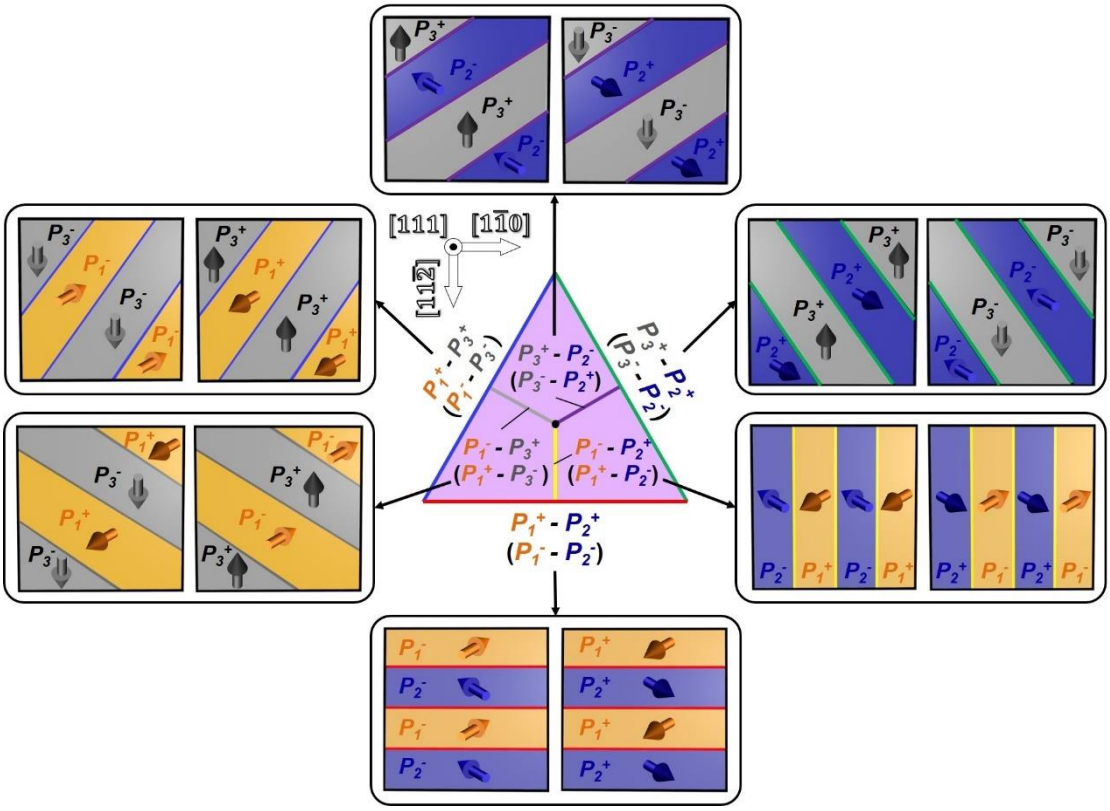

Fig. 5.12: The geometry of domain boundaries in (111)-oriented $PbZr_{0.2}Ti_{0.8}O_3$ thin films: The projection of six distinct uncharged neutral domain boundaries in (111)-oriented films which are arranged in the central triangle including three "sides" and three "normal lines". The schematic figures in the open boxes indicate the domain configuration corresponding to each type of domain boundaries.

The preference for a 90° or 180° switching process in different films is ultimately controlled by the clamping of the ferroelectric film (and the resulting domain size). In both (001)-/(101)-oriented heterostructures, the elastic constraints from the substrate lead to dramatic differences in the fraction of in-plane and out-of-plane polarized domains (in particular, minimizing the fraction of in-plane polarized domains). Although 90° domain walls have lower domain-wall energy than 180° domain walls [144], the 90° ferroelastic switching in thin films is generally unfavorable as compared to 180° ferroelectric switching (as I observed for (001)-/(101)-oriented films in our simulations) under moderate electric fields because of the large energy penalty associated with the change of volume fractions of in-plane and out-of-plane polarized domains that must occur to accommodate such switching events [43]. Said another way, the free energy change (Δf) for a ferroelastic 90° switching event is dominated by the contributions from the stress (σ^2) and the stress-polarization coupling (σP^2) terms. These energy terms are high in the (001)-/(101)-oriented films due to the elastic constraints of the substrate and the drastically different stress states for an in-plane or out-of-plane polarized domain. On the other hand, the (111)-oriented films possess three energetically-degenerate polarization variants (in a fully-poled state) all possessing in-plane and out-of-plane polarization components that are the same and, in

effect, renders the elastic energy costs associated with a ferroelastic 90° switching event greatly reduced. Additionally, our MD simulations reveal that coordinated 90° switching events (*i.e.*, $P_1^+ \rightarrow P_2^-$ and $P_2^+ \rightarrow P_1^-$) occur in essentially equal proportions across the entire domain width to accommodate (and maintain) both the elastic and electrostatic energy state of the system. As a result, the coordinated, multi-step 90° switching process will not incur a large elastic energy cost in agreement with the arguments above. Ultimately the preference of the 90° switching over the 180° switching in the (111)-oriented films is due to the lower kinetic barrier for 90° polarization rotation indicated by the lower energy of the 90° domain wall compared to that of the 180° domain wall.

The observation of such 90° switching mediated domain reversal, in turn, has important implications for our overall understanding of ferroelectric materials and their utilization in devices. First, the presence of active intermediate switching states can be correlated to the differences observed in the dielectric and ferroelectric response of the various orientations of films. Although all films possess high remnant polarization, the (001)-/(101)-oriented films show nearly square hysteresis loops with sharp electric field switching (consistent with 180° switching events), while (111)-oriented films exhibit more slanted hysteresis loops with larger coercive fields, indicative of switching at a broader range of fields and a multi-step switching process. Furthermore, it is likely that the availability of low-field intermediate switching can account for the observation of lower threshold fields for the nucleation of switching events in the Rayleigh studies of the (111)-oriented films. The domain reversal process is significantly impacted by changing the orientation of the epitaxial film and by allowing all possible switching types to be active in the material. Ultimately, if one can create pathways similar to those demonstrated in the stroboscopic PFM studies by which to deterministically stabilize or incrementally step the switched polarization from one state, through a number of intermediate states, before reaching the oppositely poled state, the possibility for creating new modalities of low-power, multi-state memory or logic are possible. At the same time, if one can determine ways to promote the 90° switching mediated domain reversal process, this could further accelerate the domain reversal and reduce the timescale of ferroelectrics thereby increasing their potential for use in advanced nanoelectronics.

5.6 Conclusions

In this Chapter, I have discussed both 180° and multi-step 90° switching domain reversal processes in $PbZr_{0.2}Ti_{0.8}O_3$ thin films. Using a combination of epitaxial thin-film growth, macro- and nano-scale characterization, and MD simulations, I have been able to manipulate the domain structure through the control of film orientations and explore the coupling between the domain structures and properties. Specifically, stark differences between (001)-/(101)- and (111)-oriented films were observed, with the latter exhibiting complex, nanotwinned ferroelectric domain structures with high densities of 90° domain walls, considerably broadened ferroelectric switching characteristics, and lower threshold fields for the onset of non-linearity during Rayleigh studies.

Subsequent MD simulations and PFM studies reveal both types of switching mechanisms are possible, but that the switching process that ultimately occurs is determined by a combination of factors including domain wall energy, elastic strain, and domain size. These observations provide insight into a previously unexplored aspect of ferroelectric switching and highlight the complexity of these materials. Such studies are crucial for developing precise control of nanoscale ferroelectric materials and can potentially lead to interesting multi-state devices and accelerated switching in ferroelectrics.

CHAPTER 6

Tunable, Multi-State Switching in Ferroelectric Thin Films

Deterministic creation of multiple polarization states in ferroelectrics remains challenging due to the inherent bi-stability of ferroelectric switching. In this Chapter, I demonstrate multi-state polarization switching in (111)-oriented $PbZr_{0.2}Ti_{0.8}O_3$ thin films, wherein the polarization can be deterministically written into a number of non-volatile and stable states in any order by varying the driving voltage. Such switching phenomena are driven by kinetic control over the volume fraction of two geometrically different domain structures generated by two distinct switching pathways: one direct, bi-polar-like switching process and another multi-step process with the formation of a thermodynamically-stable intermediate twinning structure. This work provides new insights into the control of ferroelectric switching and demonstrates a candidate material with multi-state functionality for memory devices and adaptive neuromorphic electronics.

6.1 Introduction

Ferroelectric materials, with electrically-addressable polarization, hold great promise for non-volatile and low-power device operation [145,146]. Leveraging reversible bi-polar switching in ferroelectrics, numerous devices including non-volatile memories [3], low-power logic [4,5], and nanoscale sensors and actuators [94,6] have been demonstrated. With increasing requirements for computational density in modern electronics, it is essential to create multiple polarization states in ferroelectric materials beyond the inherent bi-stability to increase the storage density of ferroelectric memories [147,148]. On the other hand, these multiple polarization states can be integrated into adaptive computational systems to emulate adjustable neural synaptic weights in neuromorphic devices, which hold promise to overcome fundamental limitations of CMOS scaling with increased computational density, complexity, and power efficiency [149-151].

Due to the inherent bi-stability of ferroelectric switching, deterministic creation of multiple stable states with distinct polarization values (henceforth multi-state polarization), however, remains a hallmark challenge. Efforts in this regard, which rely on controlling the fraction of switched domains to access multi-state polarization, fail to precisely and repeatedly achieve the same fraction of switching, due to the stochastic nature of inhomogeneous nucleation in ferroelectric switching; a point that is further exacerbated in small material volumes, preventing device downscaling. Recent work has introduced external factors such as defects and non-switchable interfacial layers to gain some control over the nucleation process [152-154], but does so at the cost of degrading ferroelectric properties including worsening fatigue [155-157] and imprint [158,15] properties. In addition, other approaches to generate multi-state polarization include controlling the number of switched ferroelectric layers in multi-layer heterostructures [159,160] or controlling sequential polarization switching in films with multiple coexisting structural instabilities [161-164]. These efforts, however, lead to a limited number of switching states that are confined by the number of film layers or available structural phases. Thus far, an alternative approach that transcends the inherent bi-stability of ferroelectrics to create non-volatile, deterministic, and repeatedly obtainable multi-state polarization without compromising other important properties, has not been achieved.

In this Chapter, I demonstrate deterministic multi-state and non-volatile function, via kinetic control of two distinct switching pathways in (111)-oriented ferroelectric $PbZr_{0.2}Ti_{0.8}O_3$ films. Combining thin-film growth, capacitor-based pulse-switching studies, molecular dynamics (MD) simulations (collaborated with Dr. Shi Liu and Prof. Andrew Rappe from University of Pennsylvania), phase-field modeling (collaborated with Dr. Jianjun Wang, Dr. Zijian Hong, and Prof. Longqing Chen from Pennsylvania State University), and piezoresponse force microscopy (PFM), the mechanism underlying the realization of multi-state polarization is revealed to be a previously unobserved process, wherein the different polarization states are associated with variations in the volume fraction of two geometrically different domain twinning structures

generated by the competition of two distinct switching pathways. The resulting domain structures provide repeatable, deterministic, and stable multi-state polarization beyond that observed to date.

6.2 Pulsed-Switching Measurements in (001)- and (111)-Oriented Heterostructures

This study focuses on epitaxial and single-phase (001)- and (111)-oriented 80 nm $La_{0.7}Sr_{0.3}MnO_3$/100 nm $PbZr_{0.2}Ti_{0.8}O_3$/20 nm $La_{0.7}Sr_{0.3}MnO_3$ heterostructures [71,72] wherein the circular top electrodes (12.5 μm) were fabricated using a wet etching method (Figs. 6.1a-c). The switching behavior, studied using a modified positive-up-negative-down (PUND) test (Appendix A), is dramatically different in (001)- (Fig. 6.2a) and (111)-oriented (Fig. 6.3a) heterostructures. The (001)-oriented heterostructures exhibit typical bi-polar switching from the down- to up-poled state, where switching occurs at shorter pulse widths for higher pulse voltages [165-168] (Fig. 6.2a). (111)-oriented heterostructures, however, exhibit multi-state polarization between the 50% and fully up-poled states with increasing pulse voltages (10 intermediate, 12 overall states shown; Fig. 6.3a). The stability of the various states in the (001)- (Fig. 6.2b) and (111)-oriented (Fig. 6.3b) heterostructures was probed using a retention pulse sequence (Appendix A). In (001)-oriented heterostructures, the fully down- and up-poled states are the only stable states; all others decay

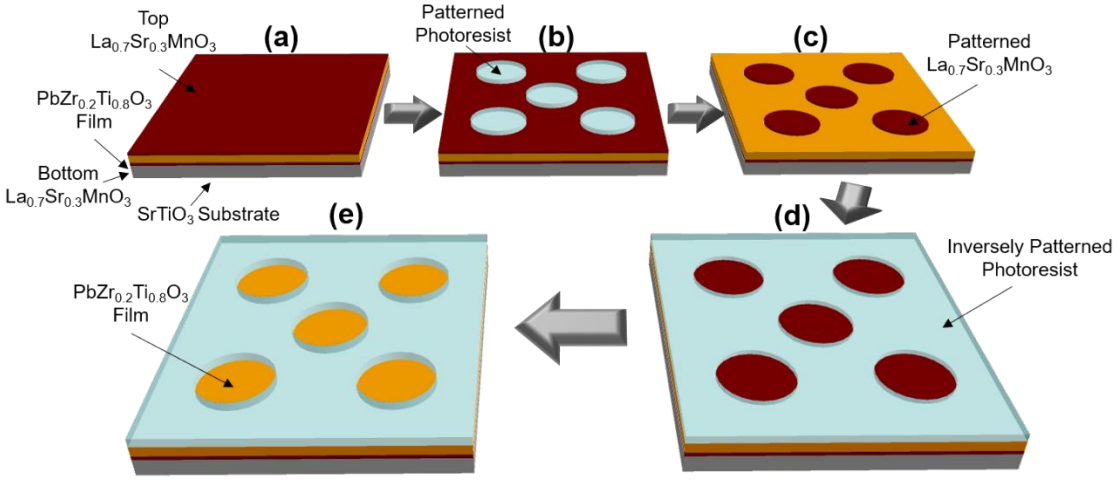

Fig. 6.1: Schematic of the fabrication process to enable domain-structure characterization in switched (111)-oriented heterostructures. (a) The as-grown heterostructure before patterning. (b) A layer of photoresist is patterned onto the as-grown heterostructures using photolithography which only covers the circular electrode regions only. (c) Using a dilute H_3PO_4 acid (dilution ratio 1 part acid : 5 parts water) the uncovered $La_{0.7}Sr_{0.3}MnO_3$ was etched away within 30 seconds leaving circular $La_{0.7}Sr_{0.3}MnO_3$ covered by photoresist. Subsequently, the photoresist was removed by acetone. (d) Multiple capacitors were pre-poled into different polarization states and then a layer of inversely patterned photoresist was coated by photolithography that only covers the exposed $PbZr_{0.2}Ti_{0.8}O_3$ regions. (e) The uncovered top $La_{0.7}Sr_{0.3}MnO_3$ electrodes were then etched away using dilute H_3PO_4 acid as noted previously. The inversely-patterned photoresist was left on the film serving as a marker that aids the accurate location and imaging of regions that were under the pre-poled capacitors.

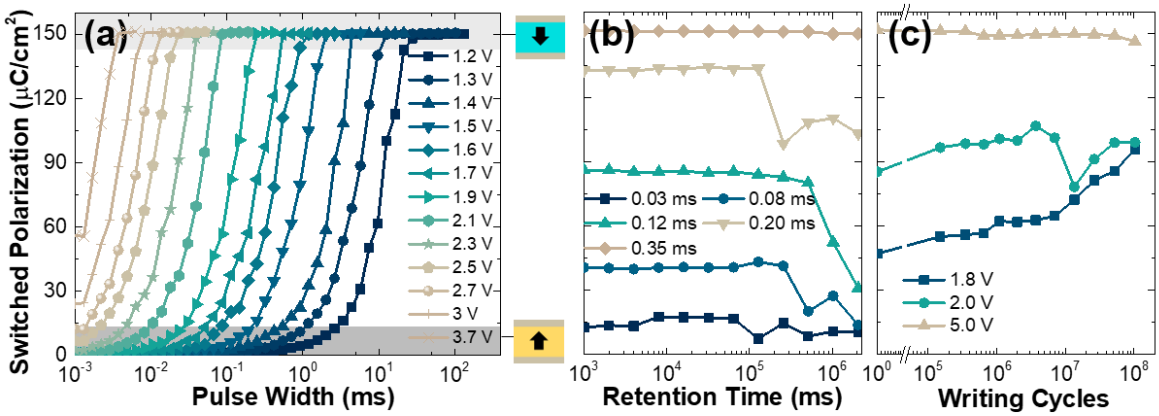

Fig. 6.2: Pulse-switching measurements in (001)-oriented $La_{0.7}Sr_{0.3}MnO_3$ / $PbZr_{0.2}Ti_{0.8}O_3$ / $La_{0.7}Sr_{0.3}MnO_3$ heterostructures. (a) The switched polarization measured as a function of pulse width for different pulse voltages at a pulse delay of 1 ms. (b) Retention measurement to measure the time stability of various partially-switched polarization states. (c) Endurance measurements to measure the switched polarization as a function of writing cycles.

with time (Fig. 6.2b). All states in (111)-oriented heterostructures are stable, showing < 5% polarization loss even after ≈ 8 hours (Fig. 6.3b). In terms of deterministic repeatability of reaching a given state, the (001)- and (111)-oriented heterostructures also show remarkable differences. Taking the average of ten pulse measurements, the (001)-oriented heterostructures exhibit poor repeatability, with error bars in the partially-switched regime > 50% of the switched polarization value, due to the stochastic nature of switching (Fig. 6.4a). The (111)-oriented heterostructures reveal deterministic accessibility, with all polarization states specific to within < 5% polarization variation (Fig. 6.3c and Fig. 6.4b). The endurance of each polarization state was also explored (Appendix A). The (001)-oriented heterostructures exhibit poor fatigue properties, as different partially-switched states converge to a similar value and provide diminished distinguishability after repeated cycling (Fig. 6.2c). By contrast, each of the polarization states in the (111)-oriented heterostructures exhibit robust distinguishability even after 10^8 writing cycles (Fig. 6.3d).

Clearly, the (111)-oriented heterostructures exhibit a number of features that are important for robust multi-state operation, including deterministic stimuli-driven access to precisely defined and distinguishable states, non-volatility and retention of those states, and endurance of those states to repeated modification without loss of distinguishability. I also studied how to control these polarization states such that they can be deterministically placed into the desired value in an on-demand fashion. Here I achieved such a control of polarization switching in the (111)-oriented heterostructures by simultaneously controlling the pulse voltage and width (Figs. 6.3e, f). In addition, I can also accomplish such control of polarization switching via cumulative pulse-switching measurements (Figs. 6.3g-i). By varying the number of identical pulses, it is possible to tune the polarization states to vary in an ascending or descending manner (Figs. 6.3g, h). Furthermore, by applying a series of identical pulses with varying polarities to the (111)-oriented heterostructures, different polarization states can be selected deterministically (Fig. 6.3i). Note that

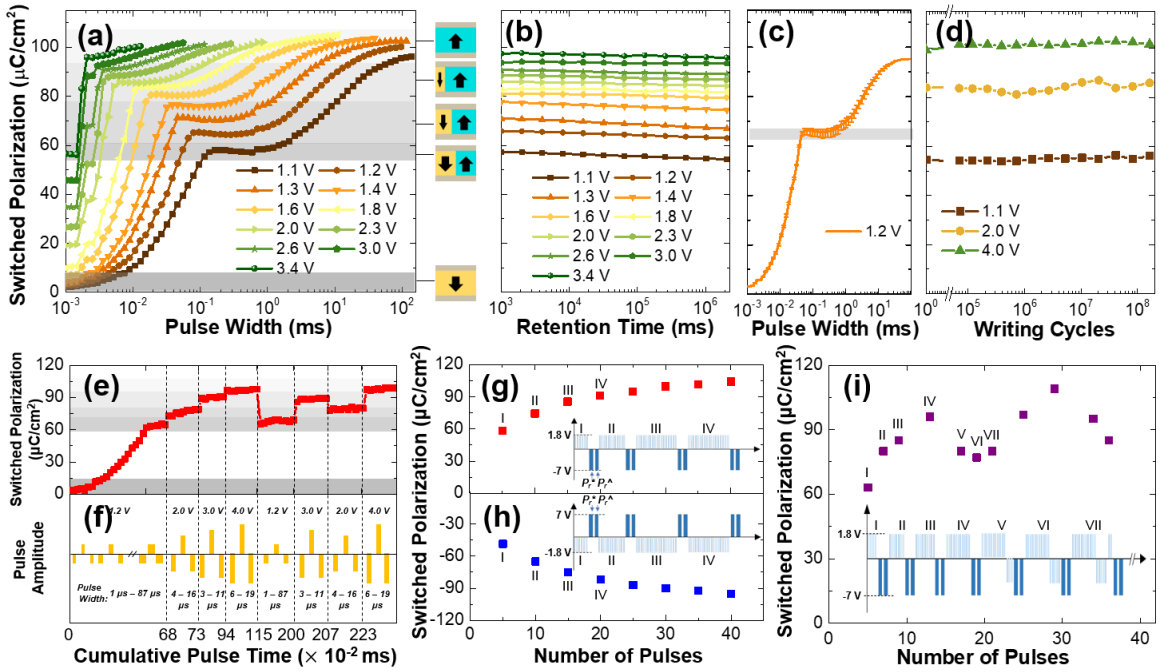

Fig. 6.3: Pulse-switching measurements in (111)-oriented $La_{0.7}Sr_{0.3}MnO_3$ / $PbZr_{0.2}Ti_{0.8}O_3$ / $La_{0.7}Sr_{0.3}MnO_3$ / $SrTiO_3$ heterostructures. (a) Switched polarization measured as a function of pulse width for different pulse voltages at a pulse delay of 1 ms. (b) Retention measurements probing the time stability of intermediate-polarization states. (c) Repeatability measurements in wherein the error bars were generated after repeating each pulse-switching measurement 10 times. (d) Endurance measurements of the switched polarization as a function of writing cycles. (e) The demonstration of switching ability including ascending and arbitrary access to any desired polarization state by simultaneously controlling the pulse duration and amplitude. (f) The schematic illustration of pulse series used in (e). Cumulative pulse-switching measurements to select the polarization state in an ascending manner by varying the number of identical (g) positive and (h) negative switching pulses. (i) Cumulative pulse-switching measurements to tune the polarization states in an arbitrary manner by varying the polarity of identical pulses.

such tunability by varying the number of repeated pulses of the same amplitude and width is particularly useful for accomplishing the spike-time dependent plasticity (STDP)-like function [2,169] in neuromorphic devices, which produces different synaptic weights with changing the relative spike timing of pre- and post-spike pulses. Ultimately, these results suggest that using classical bi-stable switching (*e.g.*, in (001)-oriented heterostructures) to achieve the desired function is difficult, and one

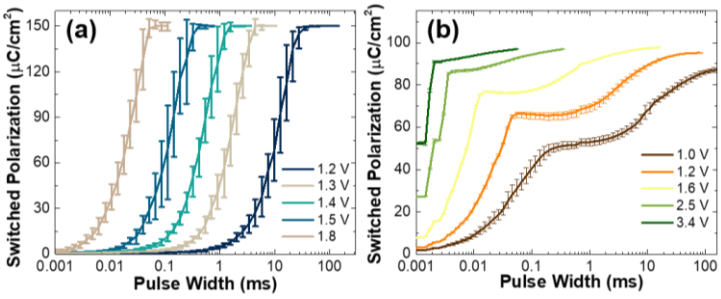

Fig. 6.4: Repeatability measurements in $La_{0.7}Sr_{0.3}MnO_3$ / $PbZr_{0.2}Ti_{0.8}O_3$ / $La_{0.7}Sr_{0.3}MnO_3$ / $SrTiO_3$ (001) and (111) heterostructures. Repeatability measurements in (a) (001)- and (b) (111)-oriented heterostructures. Error bars were generated after repeating each pulse switching measurement 10 times.

must introduce additional factors to realize deterministic, tunable multi-state polarizations and the other critical functions required for potential neuromorphic applications. Below, I elucidate the origin of this type of response in the (111)-oriented heterostructures.

6.3 Molecular-Dynamics Simulations of Field-Strength-Dependent Switching in (111)-Oriented Heterostructures

MD simulations, completed by Dr. Shi Liu and Prof. Andrew Rappe of the University of Pennsylvania, were used to examine the switching process under varying electric fields applied along the [111] direction of a $PbTiO_3$ supercell. The MD simulations were performed on a (111)-oriented $28\sqrt{6}\times50\sqrt{2}\times16\sqrt{3}$ supercell of $PbTiO_3$ (672,000 atoms, Fig. 6.5) with periodic boundary conditions and a bond-valence-based interatomic potential parameterized from first-principles [131]. The supercell has the Cartesian axes aligned along crystallographic axes $[11\bar{2}]$, $[1\bar{1}0]$, and $[111]$, respectively. First the supercell is equilibrated by running constant-pressure, constant-temperature simulations using a time step of 1 fs. The temperature is controlled via the Nosé-Hoover thermostat, and the pressure is maintained at 1 atm via the Parrinello-Rahman barostat implemented in LAMMPS. Once equilibrium is reached, a stable configuration is used as a starting point for runs in the presence of external electric fields. To capture the mechanical clamping effect in epitaxial thin-film experiments, the supercell dimensions along $[11\bar{2}]$ and $[1\bar{1}0]$ are fixed when applying the [111] electric field, while the [111] dimension is free to relax. We expect that the domain switching mechanisms simulated with $PbTiO_3$ are comparable to those in $PbZr_{0.2}Ti_{0.8}O_3$ given the structural similarity between these two ferroelectrics.

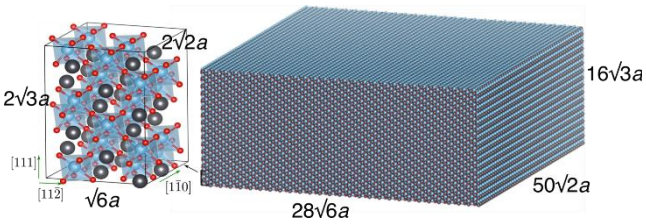

Fig. 6.5: Schematic of the supercell used for the molecular dynamics simulations. The molecular dynamics simulations were performed on a (111)-oriented $28\sqrt{6}\times50\sqrt{2}\times16\sqrt{3}$ supercell of $PbTiO_3$ (672,000 atoms) with periodic boundary conditions (PBCs) and a bond-valence-based interatomic potential parameterized from first-principles. The supercell has the Cartesian axes aligned along crystallographic axes $[11\bar{2}]$, $[1\bar{1}0]$, and [111], respectively.

Consistent with the experiments, a bi-polar-like switching at high fields and a multi-step switching characterized by a polarization plateau at low fields are observed (Fig. 6.6a). The domain structure evolution was also studied and is mapped in a spherical coordinate-based color scheme (Figs. 6.6b, c). For the case of bi-polar-like switching at high fields (E_5, Figs. 6.6d-i), the domain structure (Fig. 6.6d, called *Type-I* twinning) undergoes a series of coordinated (nearly simultaneous) 90° switching events including $P_3^- \rightarrow P_2^+$, $P_1^- \rightarrow P_3^+$, $P_2^- \rightarrow P_3^+$, and $P_3^- \rightarrow P_1^+$ (Figs. 6.6g, h) without substantial change in the overall twining structure orientation (albeit local polar vectors are rotated by 90°). In the case of multi-step switching at low fields (E_1, Figs. 6.6d, i, j-m), the polarization plateau (Fig. 6.6a) corresponds to the formation of a new domain

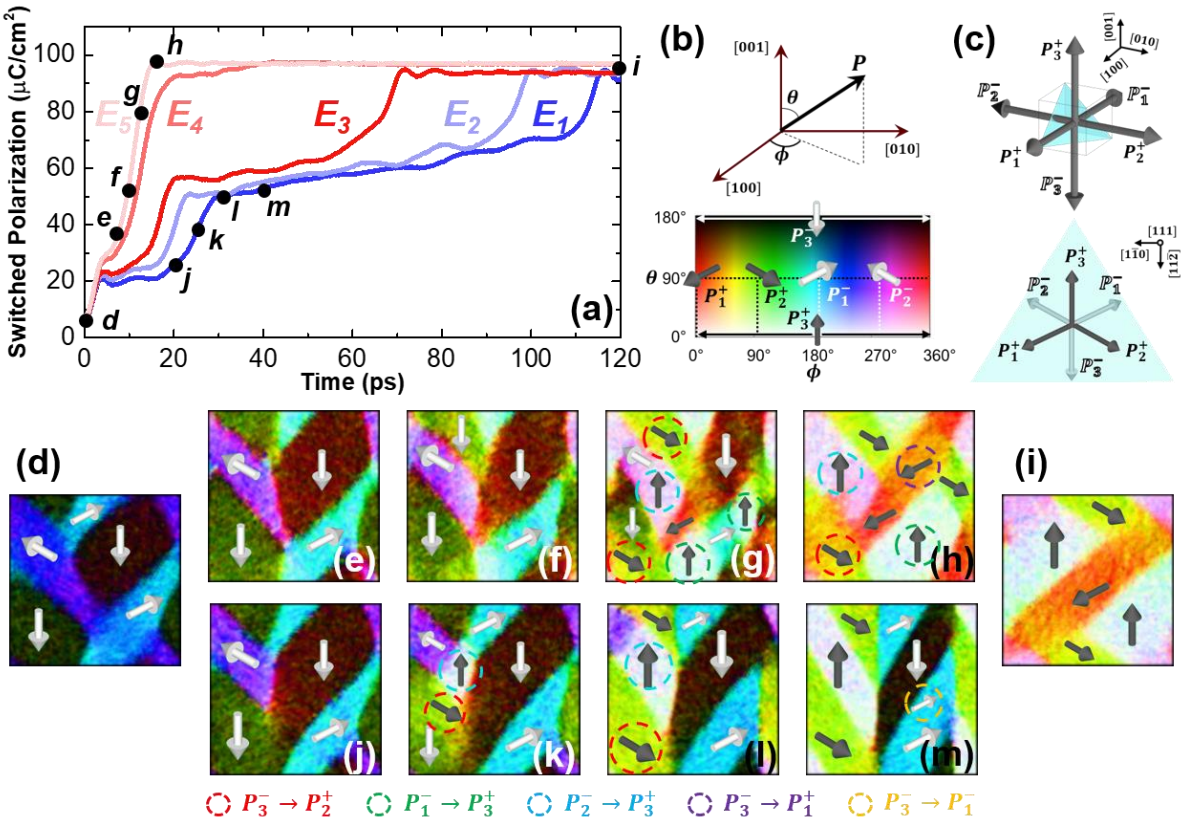

Fig. 6.6: Molecular dynamics simulations of field-strength-dependent switching in (111)-oriented heterostructures. (a) Evolution of switched polarization in response to electric field applied along the [111] for different field magnitudes ($E_1 < E_2 < E_3 < E_4 < E_5$). (b) Spherical coordinate-based color scheme used to represent the polarization variants. (c) Schematics of the six possible polarization variants in (111)-oriented tetragonal ferroelectrics and their corresponding projections on the (111). To guild the visualization, the polarization vectors with positive [111] components are colored in black and those with negative [111] components are colored in white. Simulated domain evolution under (d)-(i), high ($E = E_5$) and (d), (j)-(m), (i), low ($E = E_1$) fields revealing two distinct switching pathways. Under low field, the domains experience substantial changes in the twinning structures, characterized by an intermediate state with partially-switched polarization (k-m). Under high fields, three coordinated 90° switching events (g) enable rapid ferroelectric switching without significant change in twinning structure orientation.

configuration (Fig. 6.6m; called *Type-II* twinning) with one up-poled band (P_2^+/P_3^+) and one down-poled band (P_1^-/P_3^-) (with 50% reversal of the out-of-plane polarization) resulting from three 90° switching events: $P_3^- \rightarrow P_2^+$ and $P_2^- \rightarrow P_3^+$ (Figs. 6.6k, l) wherein the out-of-plane component of polarization is reversed and $P_3^- \rightarrow P_1^-$ (Fig. 6.6m) wherein the out-of-plane component of polarization is unchanged. The significance of these two types of 90° switching events will be discussed later. The volume fraction of the down-poled band in the *Type-II* twinning is further gradually reduced with continued application of field and eventually transforms to a fully up-poled *Type-I* twinning structure (Fig. 6.6i).

The MD simulations provide insights into the mechanism underlying the realization of this multi-state polarization, including: 1) Consistent with prior work [159,170], 90° switching is

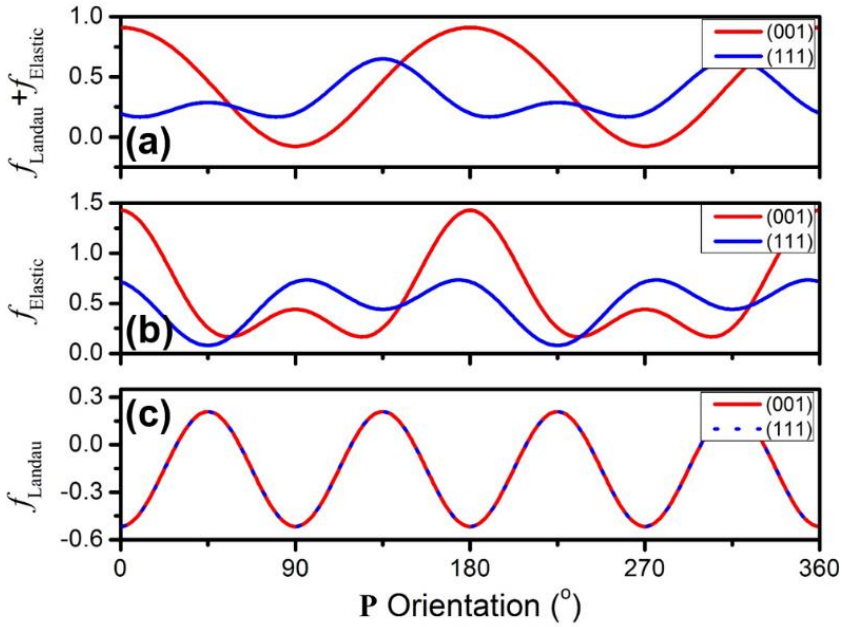

Fig. 6.7: Phase-field modeling energy landscape for polarization switching in (001)- and (111)-oriented heterostructures. (a) Total, (b) elastic, and (c) Landau energies calculated as a function of polarization orientation. Regardless of film orientation, the Landau energy exhibits local minima at polarization orientations along 0°, 90°, 180°, and 270° due to the tetragonal symmetry of the $PbZr_{0.2}Ti_{0.8}O_3$ films. The elastic energy varies significantly and, therefore, the total energy, which is a sum of the Landau and elastic energies, differs for (001)- and (111)-oriented heterostructures. The angle between the two total energy minima is 180° and ~90° for (001)- and (111)-oriented heterostructures, respectively, which suggests 180° switching is favored in (001)-oriented films, while 90° switching is favored in (111)-oriented films.

favored in (111)-oriented heterostructures regardless of field strength due to a lower-energy barrier; which is further verified by phase-field modeling (Fig. 6.7, see methods in Appendix D). 2) (111)-oriented heterostructures possess two switching pathways, including direct bi-polar-like switching at high fields (transiting from down-poled *Type-I* → up-poled *Type-I* through coordinated single-step 90° switching events) and multi-step 90° switching at low fields (transiting from down-poled *Type-I* → half down-poled *Type-II* → up-poled *Type-I*). This multi-step 90° switching pathway is enabled by the presence of a manifold degeneracy of mesoscale twinning-structure variants (*i.e.*, *Type-I* and *-II* domain configurations) in (111)-oriented heterostructures predicted by phase-field models (Fig. 6.8, see methods in Appendix D). 3) The tunable and stable intermediate polarization states are created by varying the proportion of the two switching pathways. Specifically, at low fields, only multi-step 90° switching is active, giving rise to a 50% poled twinning structure (fully *Type-II*). At intermediate fields, both switching pathways are active simultaneously and the kinetic equilibrium of these two switching pathways leads to a series of intermediate polarization states with different volume fractions of *Type-I* and *Type-II* structures. At high fields, bi-polar-like, direct 90° switching is active giving rise to the fully up-poled state (fully *Type-I*).

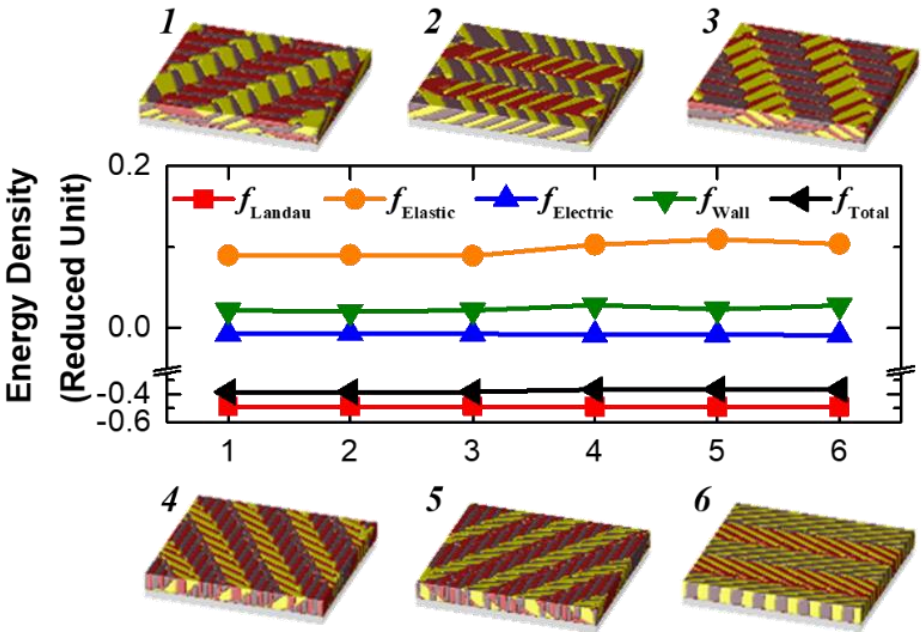

Fig. 6.8: Energy density of degenerate domain structure variants in (111)-oriented heterostructures. The calculated Landau, elastic, electric, domain wall, and total (a sum of all noted energies) energies for six domain structure variants in (111)-oriented films discovered by phase-field modeling. The calculated total energy for these six domain structure variants is essentially the same suggesting they are energetically-degenerate domain ground states. These degenerate domain structure variants can be grouped into two categories, fully up- or down-poled *Type-I* twinning (labeled as 1, 2, 3) and half up- or half-down-poled *Type-II* twinning structures (labeled as 4, 5, 6); consistent with experimental observations.

6.4 Visualizing Domain Structures for Intermediate Polarization States in (111)-Oriented Heterostructures.

The coexistence of and ability to manipulate the fraction of two distinct twinning structures was experimentally confirmed in capacitor-based structures which were pre-poled into different states including: fully down-poled [(e) in Fig. 6.9a], two intermediate [(f), (g) in Fig. 6.9a], and fully up-poled [(h) in Fig. 6.9a] states. In order to image the domain structure under the pre-poled capacitors, first multiple capacitors were pre-poled into different polarization states and then coated a layer of inversely patterned photoresist using photolithography that only covers the $PbZr_{0.2}Ti_{0.8}O_3$ film region (Fig. 6.1d). The uncovered top $La_{0.7}Sr_{0.3}MnO_3$ electrodes could be readily etched away using dilute H_3PO_4 acid (dilution ratio 1 part acid : 5 parts water) (Fig. 6.1e). The inversely patterned photoresist was left on the film surface serving as a marker that aids the accurate location and imaging for regions that were under the pre-poled capacitors.

PFM analysis reveals the presence of two distinct domain configurations, as suggested by the phase-field and MD simulations, namely, *Type-I* and *-II* twinning structures (Fig. 6.9b). To better illustrate this coexistence of two twinning structures, the regions of *Type-I* (yellow-orange, Figs. 6.9e-h) and *Type-II* (blue, Figs. 6.9e-h) structures were mapped in the PFM images. The initial state exhibits fully down-poled *Type-I* twinning structures with uniform contrast in vertical

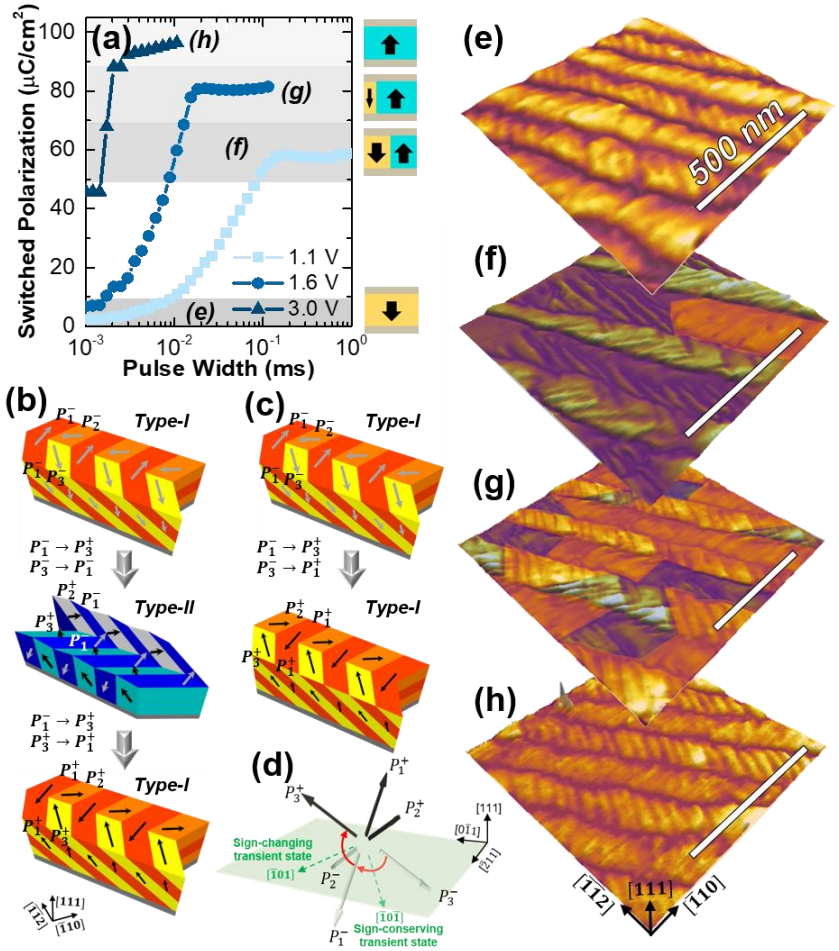

Fig. 6.9: Visualizing domain structures for intermediate polarization states in (111)-oriented heterostructures. (a) Multiple polarization states were pre-poled at pulse voltages of 1.1, 1.6, and 3 V. Schematics of the (b) multi-step switching pathway at low fields which transitions from fully down-poled *Type-I* structures to half down-poled *Type-II* structures to fully up-poled *Type-I* structures and (c) direct bi-polar-like switching pathway at high fields which transitions from fully down-poled *Type-I* structures to fully up-poled *Type-I* structures. (d) Schematic of the transient states for *sign-conserving* and *sign-changing* 90° switching events. Corresponding domain structures and the evolution in the volume fraction of the two types of twinning structures in polarization states for the (e) initial, fully up-poled state, the intermediate states poled at (f) 1.1 V and (g) 1.6 V, as well as the (h) final, fully down-poled state poled at 3.0 V. In these figures, the *Type-I* twinning structures are shaded yellow-orange and the *Type-II* twinning structures are shaded blue.

PFM images (Fig. 6.9e and Fig. 6.10a). *Type-II* twinning appears in the first intermediate state resulting in an almost 50% reversed contrast in vertical PFM (Fig. 6.9f and Fig. 6.10b). Furthermore, a mixture of *Type-I* and *-II* twinning was observed in the second intermediate state with *Type-I* twinning becoming fully up-poled, leading to a reversal of vertical contrast (Fig. 6.9g and Fig. 6.10c). Finally, the system transforms to fully up-poled *Type-I* twinning, exhibiting a uniformly reversed vertical contrast (Fig. 6.9h and Fig. 6.10d). These observations verify the mechanism responsible for the multi-state polarization suggested by the MD simulations, where

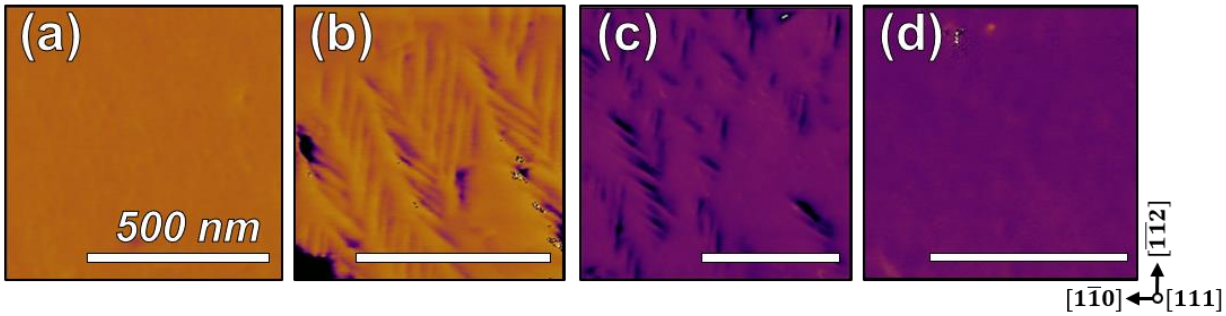

Fig. 6.10: Piezoresponse force microscopy characterization of domain structures (detailed scans). Vertical phase (bottom row) PFM images for the (a) initial fully-up-poled state, (b) intermediate state poled at 1.1 V, (c) intermediate state poled at 1.6 V, and (d) final fully-down-poled state poled at 3.0 V.

the voltage-based control of two competing switching pathways (Figs. 6.9b, c) enables the manipulation of the volume fraction of *Type-I* and -*II* structures.

The combined PFM and MD results provide a complete understanding of the switching mechanisms active in the (111)-oriented heterostructures. First, for multi-step switching, two types of 90° switching events are identified: 1) *sign-changing* switching wherein there is a change in the out-of-plane component of polarization (*e.g.*, $P_1^- \rightarrow P_3^+$, Fig. 6.9b) and 2) *sign-conserving* switching wherein there is no change in the out-of-plane component of polarization ($P_3^- \rightarrow P_1^-$ and $P_3^+ \rightarrow P_1^+$, Fig. 6.9b). For bi-polar-like switching, only *sign-changing* switching occurs ($P_1^- \rightarrow P_3^+$ and $P_3^- \rightarrow P_1^+$, Fig. 6.9c). Energetically, *sign-changing* switching is favored thermodynamically by an electrostatic energy gain $-EP$, but is associated with an elastic energy barrier ΔE_e^1, while sign-conserving switching is associated only with an elastic energy barrier ΔE_e^2. Moreover, $\Delta E_e^1 >> \Delta E_e^2$ because the transient state of *sign-changing* switching is fully within the (111) and thus subject to stronger clamping effects, whereas the transient state of *sign-conserving* switching has a smaller in-plane component of polarization (Fig. 6.9d). Thus, at low fields (where the elastic energy dominates), as a *sign-changing* switching occurs first in one domain (*e.g.*, $P_1^- \rightarrow P_3^+$) the neighboring domain compensates the strain via a *sign-conserving* switching event (*e.g.*, $P_3^- \rightarrow P_1^-$), which is much more rapid *kinetically* due to the lower elastic-energy barrier. This rationalizes the formation of the 50% poled *Type-II* twinning structure with half of the domains up-poled (resulting from the *sign-changing* switching) and half of the domains down-polled (resulting from the *sign-conserving* switching). The net-zero out-of-plane polarization of the *Type-II* twinning structure also explains its stability due to the absence of depolarization field. At high fields (where the electrostatic energy dominates), the system *thermodynamically* prefers to proceed through more *sign-changing* switching events that have a larger electrostatic energy gain. This explains the bi-polar-like switching pathway accomplished through coordinated single-step, *sign-changing* switching without substantial changes in the twinning structures. When the electric field is intermediate, such that the electrostatic energy *EP* is comparable to $\Delta E_e^1 - \Delta E_e^2$ (Bell-Evans-Polanyi principle [171,172]), both switching pathways are comparably fast,

producing a mixture of Type-I and -II twinning structures and different intermediate polarization states.

6.5 Conclusions

In this Chapter, I demonstrate an approach to move beyond the inherent bi-stability of ferroelectrics and provide a candidate material for neuromorphic applications that offers non-volatile, deterministic, and repeatedly obtainable multi-state polarization without compromising other important properties. This work also explores the capability of a ferroelectric to transition through multiple switching pathways, beyond a single bi-polar-like switching route, to produce a number of tunable intermediate polarization states. This phenomenon, which is fundamentally distinct from the bi-polar switching in conventional ferroelectrics, reveals a picture of an energy landscape where multiple thermodynamically-stable, degenerate ground states coexist, thus providing the structural and energetic foundation for multi-state switching. As a result, it is possible to create tunable intermediate states in ferroelectrics without relying on defect-induced pinning, while addressing the requirements of deterministic and repeatable production of multi-state polarization. The effects noted herein are well suited to application in various device architectures, including ferroelectric-gated field-effect transistors (FeFETs) [93] and ferroelectric tunnel junctions (FTJ) [173,174] – both of which have the potential for utilization in neuromorphic applications, are highly scalable, and provide for non-volatile and non-destructive reading. Although FeFETs have often been limited by retention issues [175], the combination of the extraordinary ability to create multiple polarization states on demand, in a deterministic and repeatable manner, and considerably improved retention and endurance properties herein suggests this could be promising for improving the performance of such devices.

CHAPTER 7

Reducing Coercive-Field Scaling in Ferroelectric Thin Films *via* Orientation Control

The desire for low-power/voltage operation of devices is driving renewed interest in understanding scaling effects in ferroelectric thin films. As the dimensions of ferroelectrics are reduced, the properties can vary dramatically, including the robust scaling relationship between coercive field (E_c) and thickness (d), also referred to as the Janovec-Kay-Dunn (JKD) law wherein $E_c \propto d^{-2/3}$. In this Chapter, I report while (001)-oriented heterostructures follow JKD scaling across the thicknesses range of 20-330 nm, (111)-oriented heterostructures of the canonical tetragonal ferroelectric $PbZr_{0.2}Ti_{0.8}O_3$ exhibit a deviation from JKD scaling wherein a smaller scaling exponent for the evolution of E_c is observed in films of thickness $\lesssim 165$ nm. X-ray diffraction reveals that, while (001)-oriented heterostructures remain tetragonal for all thicknesses, (111)-oriented heterostructures exhibit a transition from tetragonal to monoclinic symmetry in films of thickness $\lesssim 165$ nm. First-principles calculations suggest that this symmetry change contributes to the deviation from the expected scaling as the monoclinic phase has a lower energy barrier for switching. This structural evolution also gives rise to changes in the *c/a* lattice parameter ratio, wherein this ratio increases and decreases in (001)- and (111)-oriented heterostructures, respectively, as the films are made thinner. In (111)-oriented heterostructures, this reduced tetragonality drives a reduction of the remanent polarization and, therefore, a reduction of the domain-wall energy and overall energy barrier to switching which further exacerbates the deviation from the expected scaling. Overall, this work demonstrates a route towards reducing coercive fields in ferroelectric thin films and provides a possible mechanism to understand the deviation from JKD scaling.

7.1 Introduction

Ferroelectric thin films, which possess an electrically-switchable spontaneous polarization, have garnered increasing attention for applications in modern nanoelectronics. Such materials have been utilized as critical components in non-volatile memories [146,113] and logic devices [176,4], exhibiting improved performance [177,178] such as high-speed write operation, long-term endurance, low-voltage operation, *etc*. With the increasing requirement for storage density and power efficiency in these devices, it is essential to investigate the scaling potential of ferroelectric thin films for low-voltage operation and low-power consumption. In particular, it is possible to accomplish low-voltage operation in ferroelectrics simply by reducing film thickness. Such a variation of coercive field with thickness pertains to ferroelectric size effects, or the change in properties with decreasing physical dimension, which have been widely observed in ferroelectric ceramics [179], single crystals [19,18], and thin films [180-184]. While early work on thin and ultra-thin versions of these materials was susceptible to extrinsic size effects, such as interfacial "dead layers" which lead to suppressed ferroelectricity [185-187], recent advances in contact materials as well as material synthesis [47,48], has produced increasingly high-quality ferroelectric thin films that beget the study of intrinsic size effects.

One of the foremost intrinsic size-effect phenomena is the scaling relationship between coercive field (E_c) and film thickness (d), or the so-called Janovec-Kay-Dunn (JKD) law, wherein $E_c \propto d^{-2/3}$. This semi-empirical relation derived in the 1960s from studies of ferroelectric single crystals was later found to be applicable to thin films from 100 μm to 100 nm thick [19,18,188]. Despite the vast majority of materials explored to date following this scaling law, occasional studies have found deviations [189-191]. For example, work on ultrathin films of poly(vinylidene fluoride-trifluoroethylene) reported a deviation from JKD scaling wherein the measured E_c was independent of thickness in films of thickness < 15 nm [189,190]. Later work, however, found that such deviations could be accounted for by considering depolarization fields arising from incomplete screening from electrodes which leads to a difference between the measured and true E_c in ultrathin films [192]. Despite the seeming universality of JKD scaling, its semi-empirical nature leaves the door open to the identification of systems that deviate from this behavior and thus provide even better low-voltage operation. How to engineer materials to achieve such reduced E_c scaling remains a challenge.

In this Chapter, I describe the study of the effect of film orientation on E_c scaling in tetragonal $PbZr_{0.2}Ti_{0.8}O_3$ thin films using a combination of advanced thin-film epitaxy, X-ray diffraction, and first-principles calculations. Here, I report that while (001)-oriented heterostructures follow JKD scaling across the thicknesses range of 20-330 nm, (111)-oriented heterostructures exhibit a deviation from JKD scaling wherein a reduced scaling exponent for the evolution of E_c is observed in films of thickness $\lesssim 165$ nm. X-ray diffraction reveals that, while (001)-oriented heterostructures remain tetragonal for all thicknesses, (111)-oriented heterostructures exhibit a transition from tetragonal to monoclinic symmetry in films of thickness

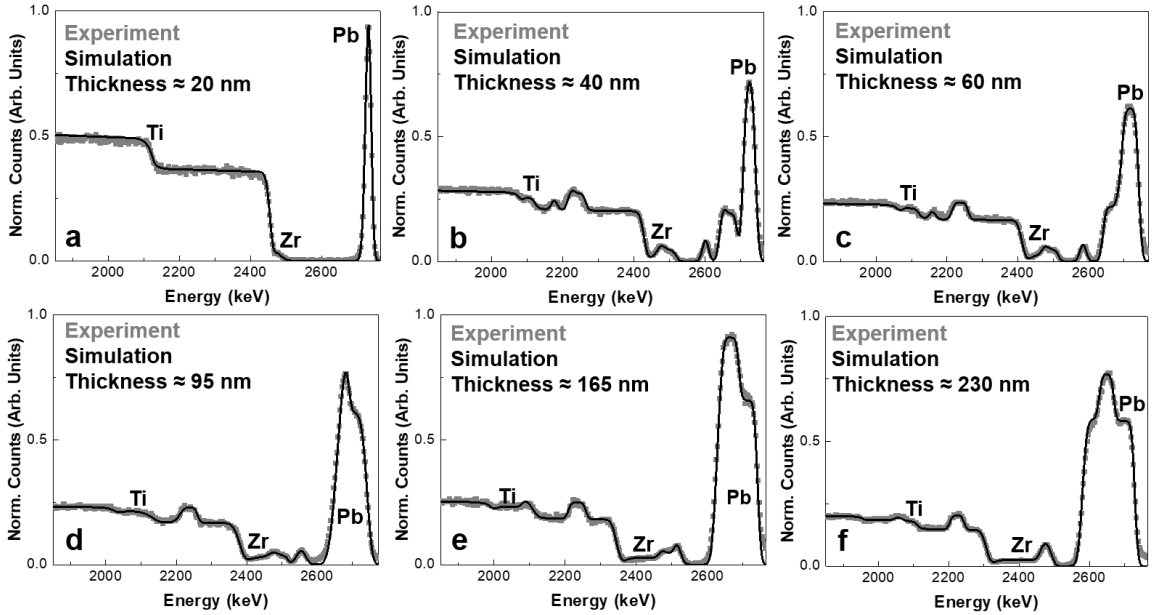

Fig. 7.1: RBS measurements performed for $PbZr_{0.2}Ti_{0.8}O_3$ films of (a) 20 nm, (b) 40 nm, (c) 60 nm, (d) 95 nm, (e) 165 nm, (f) 230 nm thickness in the (001) and (111)-oriented $La_{0.7}Sr_{0.3}MnO_3$ / $PbZr_{0.2}Ti_{0.8}O_3$ / $La_{0.7}Sr_{0.3}MnO_3$ / $SrTiO_3$ heterostructures.

$\lesssim$ 165 nm as a result of the compressive strain. First-principles calculations suggest that this symmetry change contributes to the deviation from the expected scaling as the monoclinic phase has a lower energy barrier for switching. This structural evolution also gives rise to changes in the *c/a* lattice parameter ratio, wherein this ratio increases and decreases in (001)- and (111)-oriented heterostructures, respectively, as the films are made thinner. In (111)-oriented heterostructures, this reduced tetragonality drives a reduction of the remanent polarization and, therefore, a reduction of the domain-wall energy and overall energy barrier to switching which further exacerbates the deviation from the expected scaling. Overall, this work demonstrates a route towards reducing E_c in ferroelectric thin films and provides a possible mechanism to understand the deviation from JKD scaling.

7.2 Electrical Measurements of $PbZr_{0.2}Ti_{0.8}O_3$ Thin Films

80 nm $La_{0.7}Sr_{0.3}MnO_3$ / 20-330 nm $PbZr_{0.2}Ti_{0.8}O_3$ / 20 nm $La_{0.7}Sr_{0.3}MnO_3$ / $SrTiO_3$ (001) and (111) heterostructures were grown *via* pulsed-laser deposition using established procedures [71,72]. All film thicknesses were measured using both X-ray reflectivity and Rutherford backscattering spectrometry (Figs. 7.1 and 7.2). Following growth, the top $La_{0.7}Sr_{0.3}MnO_3$ layer was further patterned into 25 μm (diameter) circular electrodes using a wet-etching method. Ferroelectric hysteresis loop measurements were performed as a function of frequency on all heterostructures (for simplicity, only loops measured at 1 kHz are shown here for (001)- (Fig. 7.3a) and (111)-oriented (Fig. 7.3b) heterostructures). Regardless of the film thickness and orientation,

well-saturated hysteresis loops can be measured down to 1 Hz indicating the films are highly insulating (Figs. 7.4 and 7.5). The E_C, defined as $(E_c^+ - E_c^-)/2$ (where E_c^+ and E_c^- are the positive and negative E_c values, respectively) is plotted as a function of thickness for all the (001)- and (111)-oriented heterostructures (Fig. 7.3c). A number of key observations can be made. First, for all film thicknesses, the (111)-oriented heterostructures exhibit lower E_c than (001)-oriented heterostructures. This could be related to different local-switching events in these differently oriented films as prior studies [72] have found that direct 180° switching is favored in (001)-oriented heterostructures whereas multi-step, 90° switching is favored in (111)-oriented heterostructures. These 90° switching events, which have a lower energy barrier, could contribute to a lower E_c in the (111)-oriented heterostructures. Second, clear differences are observed in the E_c scaling for the two film orientations. In (001)-oriented heterostructures, $E_c \propto d^{-0.55\pm0.032}$ across the entire thickness regime studied herein, which is close to the expected JKD scaling. In the (111)-oriented heterostructures, $E_c \propto d^{-0.51\pm0.013}$ for films of thickness >165 nm and $E_c \propto d^{-0.28\pm0.019}$ for films of thickness <165 nm. In addition, the remanent polarization P_r, defined as $(P_r^+ - P_r^-)/2$ (where P_r^+ and P_r^- are the positive and

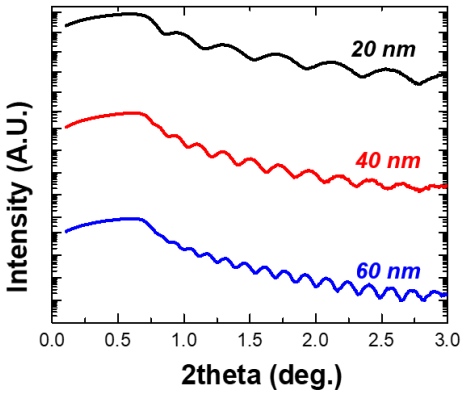

Fig. 7.2: XRR studies performed for various $PbZr_{0.2}Ti_{0.8}O_3$ films.

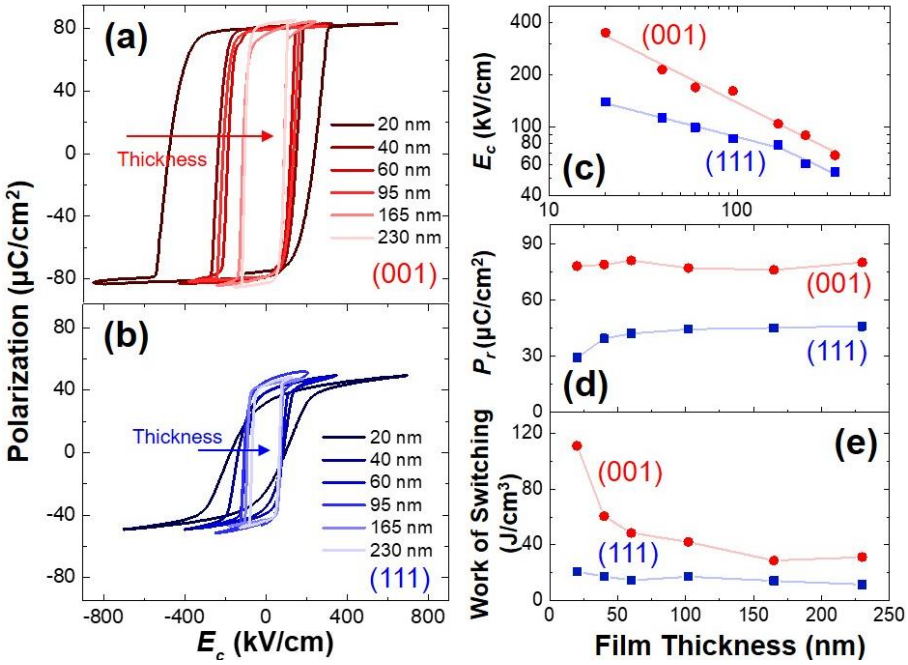

Fig. 7.3: Ferroelectric hysteresis loops measured at 1 kHz for (a) (001)- and (b) (111)-oriented heterostructures as a function of film thickness. The (c) coercive field (E_C), (d) remanent polarization (P_r), and (e) work of switching plotted as a function of film thickness for (001)- and (111)-oriented heterostructures.

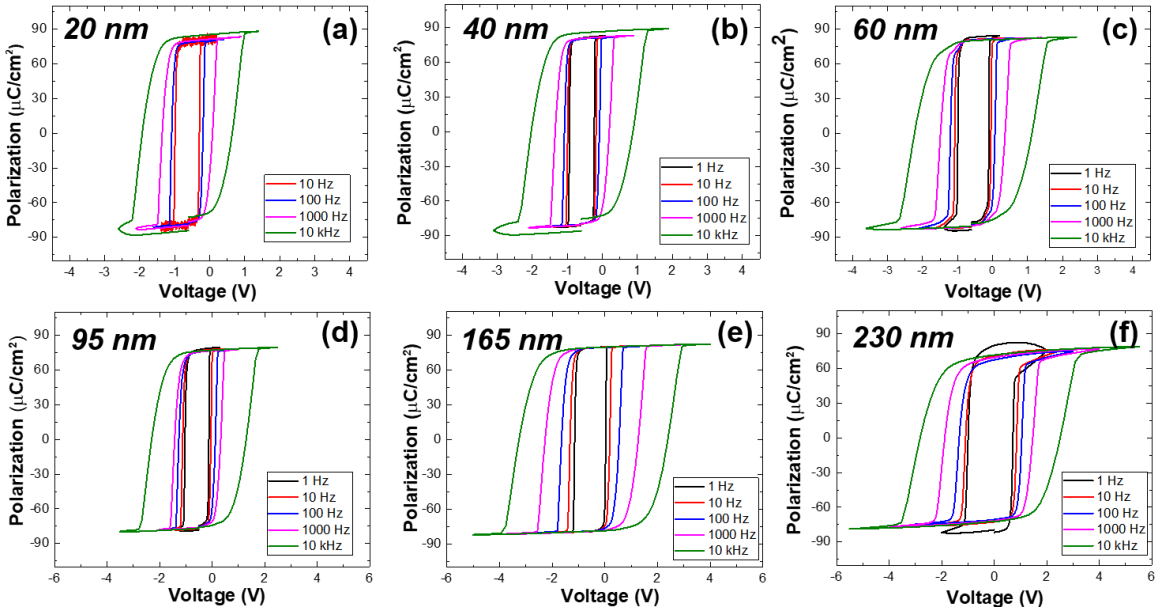

Fig. 7.4: Ferroelectric hysteresis loop measurements performed on (001)-oriented $PbZr_{0.2}Ti_{0.8}O_3$ heterostructures of thickness (a) 20 nm, (b) 40 nm, (c) 60 nm, (d) 95 nm, (e) 165 nm, and (f) 230 nm.

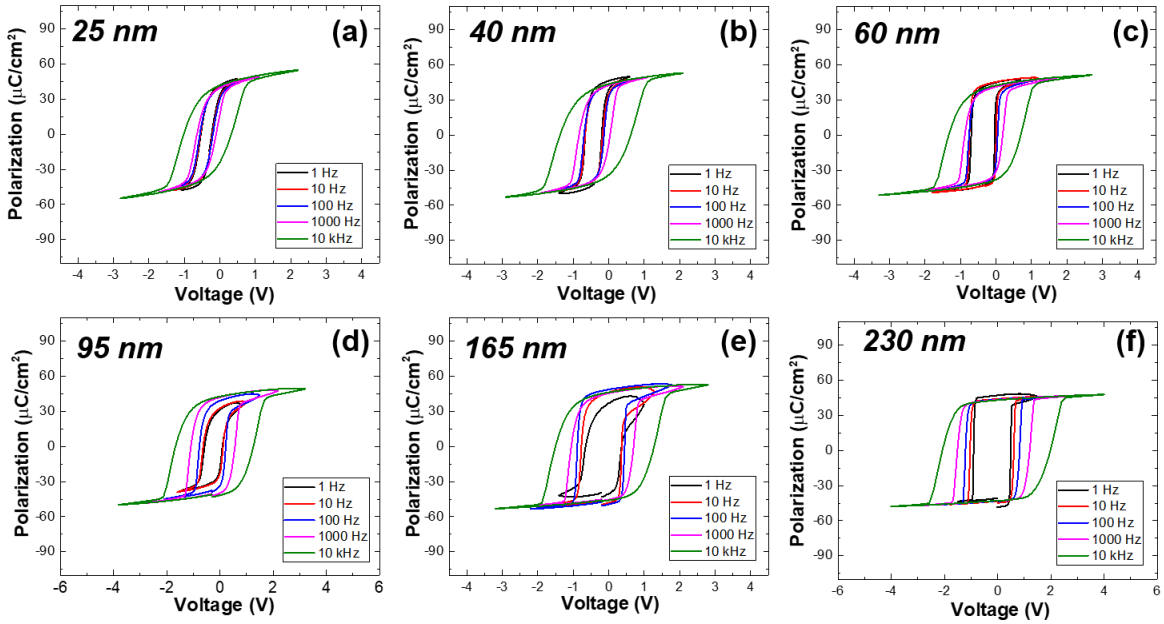

Fig. 7.5: Ferroelectric hysteresis loop measurements performed on (111)-oriented $PbZr_{0.2}Ti_{0.8}O_3$ heterostructures of thickness (a) 20 nm, (b) 40 nm, (c) 60 nm, (d) 95 nm, (e) 165 nm, (f) 230 nm thickness in the (111)-oriented heterostructures.

negative P_r values, respectively), remains essentially unchanged in (001)-oriented heterostructures, but decreases in (111)-oriented heterostructures as the film thickness is reduced (Fig. 7.3d). The work of switching, as defined as the area inside the hysteresis loop and a direct measure of the energy loss during switching (Fig. 7.3e), increases rapidly as the films are made thinner for the (001)-oriented heterostructures, but remains essentially unchanged for the (111)-oriented

heterostructures. The difference in the work of switching is particularly large in the thinnest films, where, in (111)-oriented heterostructures, the greatly reduced E_C and P_r dominate the response. Ultimately, what this data suggests is that the E_C scaling for (111)-oriented heterostructures deviates from the expected JKD scaling and this, in turn, manifests itself as a dramatic reduction of the work of switching in the thinnest films. This observation is particularly important from an engineering standpoint, but begs the question as to what causes this deviation in the scaling relation in (111)-oriented heterostructures?

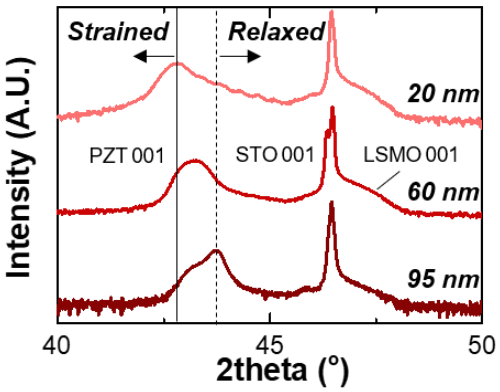

Fig. 7.7: X-ray θ-2θ scans performed on the (001)-oriented heterostructures.

7.3 Structural Analysis of $PbZr_{0.2}Ti_{0.8}O_3$ Thin Films

Before this deviation can be attributed to an intrinsic feature of the material, one must explore the possibility that this deviation is caused by extrinsic factors. Possible extrinsic factors such as interfacial "dead layers" and incomplete screening from electrodes, however, are excluded for the following reasons: In the case of an interfacial "dead layer," an extra voltage drop can be observed which leads to an increase in E_C and a larger exponent in E_C scaling ($E_c \propto d^{-1}$) [187,191]. Additionally, the $La_{0.7}Sr_{0.3}MnO_3$ electrodes were controlled to be of sufficient thickness to provide sufficient carriers to screen the polarization, were produced *in situ* during the same growth process as the ferroelectric layer, and were created using identical conditions to purposely make them as identical as possible. Thus, it is unlikely that the observed deviation is caused by the incomplete screening from electrodes that occurs only in the (111)-oriented heterostructures. Having ruled out such extrinsic factors, I focus on investigating possible intrinsic factors that could lead to the observed deviation. First, I performed X-ray rocking curve measurements to study whether the observed deviation could be related to variations in the film crystalline quality (Fig. 7.6). It is noted that the full-width-at-half-maximum (FWHM) of the rocking curves, which is indicative of the crystalline quality, evolves in a similar manner with film thickness for both film orientations, such that 20-nm-thick films of both orientations show small and similar FWHM (< 0.05°). Recall, however, that the largest deviation from the expected JKD scaling occurs in 20-nm-thick (111)-oriented heterostructures, not the (001)-oriented heterostructure; suggesting that the crystalline quality is not the cause for the observed deviation from JKD scaling.

In an attempt to better understand the driving force for this deviation from JKD scaling, X-ray diffraction experiments were completed to explore a further potential structural origin. First, for (001)-oriented heterostructures, analysis of the 001-diffraction conditions for the $PbZr_{0.2}Ti_{0.8}O_3$ films reveal that as the film thickness is reduced, the out-of-plane lattice parameter elongates (as expected for a compressively-strained film that is coherently strained only in the thinnest films;

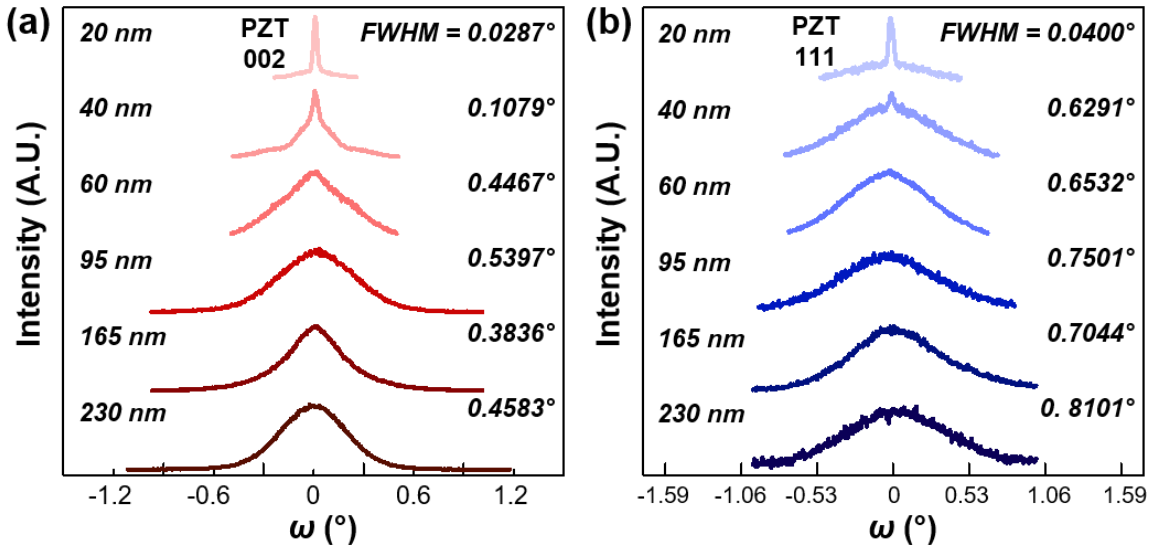

Fig. 7.6: X-ray rocking curves as a function of thickness for (a) (001)- and (b) (111)-oriented heterostructures.

Fig. 7.7). Reciprocal space mapping (RSM) studies were used to examine the evolution of both the in-plane and out-of-plane lattice parameters for the (001)-oriented heterostructures and, for brevity, only RSMs about the 103-diffraction conditions of the films and substrate for films of thickness of 40 nm (Fig. 7.8a) and 165 nm (Fig. 7.8b) are shown (RSMs for all thicknesses are provided in Appendix E). For the $PbZr_{0.2}Ti_{0.8}O_3$ films of thickness $\lesssim$ 60 nm, the 103-diffraction peaks arising from the $PbZr_{0.2}Ti_{0.8}O_3$ and $SrTiO_3$ exhibit the same in-plane values, confirming the films are coherently strained. For the $PbZr_{0.2}Ti_{0.8}O_3$ films of thickness $\gtrsim$ 60 nm, the 103-diffraction peak for the $PbZr_{0.2}Ti_{0.8}O_3$ is found to shift toward smaller Q_x values, indicating that the films are relaxing. A summary of the evolution of the lattice with film thickness, namely the evolution of the in-plane (*a*, *b*) and out-of-plane (*c*) lattice parameters as well as the lattice angle (α, β, and γ, the interaxial angles) (Fig. 7.8c) and the *c*/*a* lattice parameter ratio (Fig. 7.8d), are provided. It is found that, as the film thickness decreases, *c* increases and *a* (or *b*, *a* = *b*) decreases resulting in an increasing *c*/*a* ratio, while $\alpha, \beta, \gamma \approx 90°$ implying that the structure remains tetragonal. Using the measured and bulk lattice parameter values, I can calculate the effective self-strain (*i.e.*, the distortion of the lattice relative to bulk) as a function of thickness ($\varepsilon = \frac{a_{measured} - a_{bulk}}{a_{bulk}}$). It is noted that the effective compressive strain in the film increases with reducing film thickness (Fig. 7.8e).

Similar studies were performed for the (111)-oriented heterostructures. Analysis of the 111-diffraction conditions shows no obvious trend and thus provides limited insights into any structural changes (Fig. 7.9). RSM studies about the 312- and 330-diffraction conditions of the $PbZr_{0.2}Ti_{0.8}O_3$ films were completed to probe the lattice evolution along the (orthogonal) in-plane $[1\bar{1}0]$ and $[11\bar{2}]$, respectively. Again, for brevity, only RSMs about the 312-diffraction condition

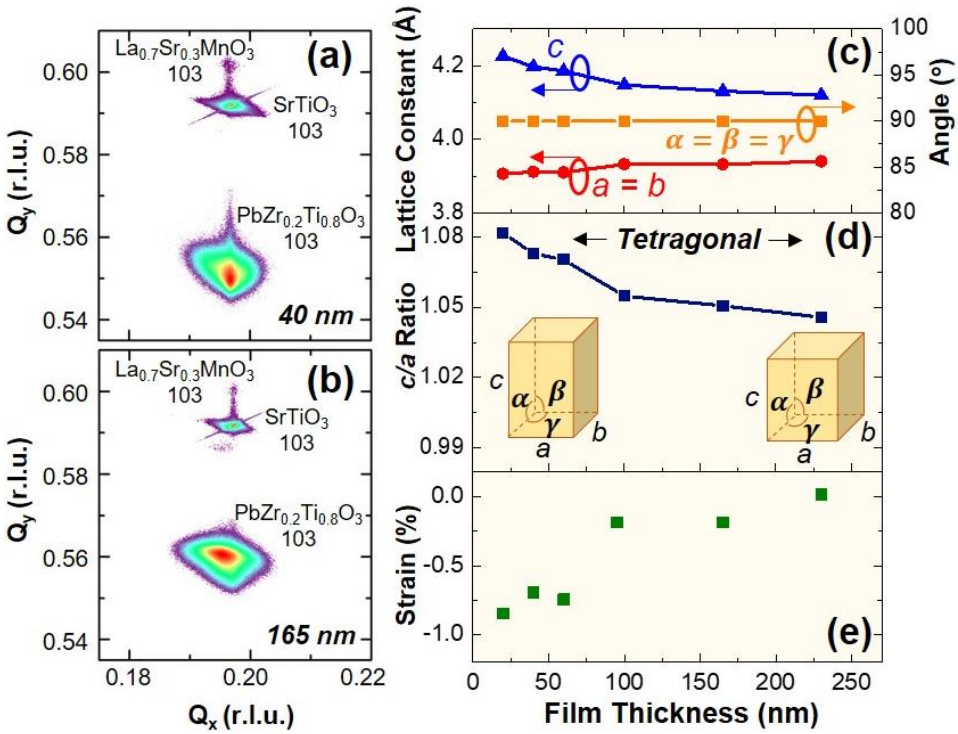

Fig. 7.8: X-ray reciprocal space mapping studies about the 103-diffraction conditions of films and substrates for (001)-oriented $PbZr_{0.2}Ti_{0.8}O_3$ heterostructures of thickness (a) 40 nm and (b) 165 nm. Thickness dependence of (c) lattice constants and interaxial angles, (d) *c/a* ratio, and e) self-strain in (001)-oriented heterostructures.

of the films of thickness of 40 nm (Fig. 7.10a) and 165 nm (Fig. 7.10b) are shown (RSMs about the 312- and 330-diffraction conditions for all thicknesses are provided in Appendix E). Complex diffraction patterns were observed about the 312-diffraction condition wherein the $PbZr_{0.2}Ti_{0.8}O_3$ peak splits into three peaks in films of thickness $\lesssim$ 60 nm and six peaks in films of thickness $\gtrsim$ 60 nm. It should be noted, that for (111)-oriented versions of tetragonal $PbZr_{0.2}Ti_{0.8}O_3$, three structural variants are present with the polar axis (*c* lattice parameter) aligned along the [100], [010], and [001], which could contribute to the splitting of the 312-diffraction peaks into three peaks which are indexed as the 312-, 231-, and 123-diffraction conditions (Figs. 7.10a and b). This mechanism, however, can only account for the splitting into three peaks in films of thickness $\lesssim$ 60 nm. In order to understand the additional peak splitting in thicker films, three-dimensional RSM studies were completed about the 222-diffraction condition. For brevity, only three-dimensional RSMs for films of thickness of 40 nm (Fig. 7.10c) and 165 nm (Fig. 7.10d) are shown (three-dimensional RSMs for all thicknesses about the 222-diffraction conditions are provided in Appendix

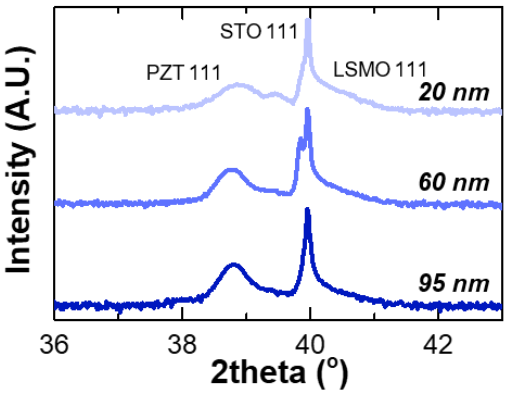

Fig. 7.9: X-ray θ-2θ scans performed on (111)-oriented heterostructures.

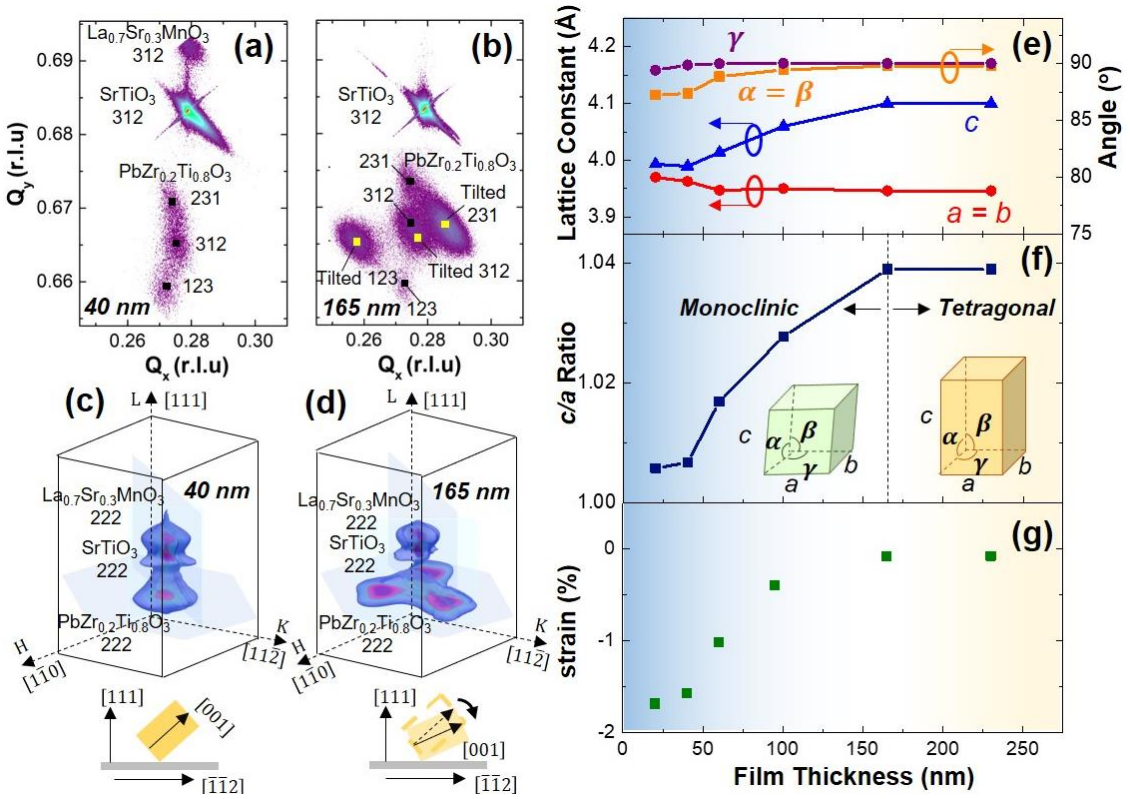

Fig. 7.10: X-ray reciprocal space mapping studies about the 312-diffraction conditions of films and substrates for (111)-oriented $PbZr_{0.2}Ti_{0.8}O_3$ heterostructures of thickness (a) 40 nm and (b) 165 nm. Three-dimensional reciprocal space mapping studies about the 222-diffraction conditions of films and substrates for (111)-oriented $PbZr_{0.2}Ti_{0.8}O_3$ heterostructures of thickness (c) 40 nm and (d) 165 nm. Thickness dependence of (e) lattice constants and interaxial angles, (f) *c/a* ratio, and g) self-strain in (111)-oriented heterostructures.

E). In such RSMs, clear three-fold splitting of the $PbZr_{0.2}Ti_{0.8}O_3$ 222-diffraction peaks was observed in the *HK* mapping for films of thickness $\gtrsim$ 60 nm (Appendix E). The three structural variants in the $PbZr_{0.2}Ti_{0.8}O_3$ films are indistinguishable under the on-axis 222-diffraction condition due to the fact that they have the same lattice projections along the [222], such that the on-axis peak splitting can only be explained by a unit-cell tilt wherein the unit cells are inclined towards the $\langle 11\bar{2} \rangle$ with three-fold symmetry within the plane (schematics, Figs. 7.10c, d). The tilting angles can be further analyzed from the *KL* mapping which shows increasing tilting with increasing film thickness (Fig. 7.11). In turn, a comprehensive picture of the structure of the films with thickness $\gtrsim$ 60 nm is produced wherein they include three structural variants and three tilted versions of those variants. Similar analysis is also applicable to RSM results measured about the $PbZr_{0.2}Ti_{0.8}O_3$ 330-diffraction condition (Appendix E). These fully indexed diffraction results allow for the extraction of a similar summary of the evolution of the lattice with film thickness, namely the evolution of *a*, *b*, and *c* as well as the interaxial angles α, β, and γ (Fig. 7.10e) and the *c/a* lattice parameter ratio (Fig. 7.10f). Here, *c* decreases while *a* (or *b*, *a* = *b*) increases resulting in a decreasing *c/a* ratio with reducing film thickness (the opposite trend to that observed the (001)-

oriented heterostructures). The lattice angles also evolve differently, wherein the α (or β, $\alpha = \beta$) and γ angles deviate from 90° upon reducing the film thickness, which leads to a tetragonal to monoclinic structural transition below ≈165 nm. The α and γ angles decrease further with reducing film thickness implying the monoclinic structure trends towards a rhombohedral structure. Using the measured and bulk lattice parameters, the effective self-strain (*i.e.*, the distortion of the lattice relative to bulk), can be extracted as a function of film thickness. Since the in-plane strain applied in the (111)-oriented heterostructures is not isotropic, I analyzed the average in-plane self-strain using the average lattice parameter along the ⟨110⟩ (Appendix E). Similar to the (001)-oriented heterostructures, it is noted that the compressive self-strain increases with reducing film thickness (Fig. 7.10g). All told, these structural analyses reveal that the structure of the (001)- and (111)-oriented heterostructures evolves differently in two major ways: 1) Upon reducing the film thickness, the (001)-oriented heterostructures remain tetragonal whereas the (111)-oriented heterostructures undergo a tetragonal-to-monoclinic structural evolution. 2) The *c/a* ratio evolves in an opposite trend wherein an increasing and a decreasing *c/a* ratio are observed as the thickness is reduced in (001)- and (111)-oriented heterostructures, respectively.

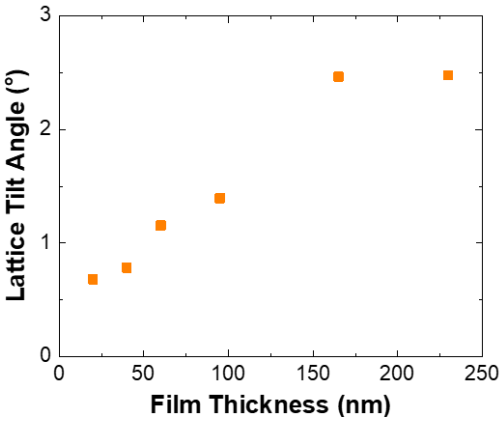

Fig. 7.11: The extracted tilting angle as a function of film thickness.

7.4 First-Principles Density Functional Calculations

Collaborated with Dr. Sebastian Lillo and Prof. Jeffrey Neaton from Department of Physics at University of California, Berkeley, we studied whether and how these two structural observations are related to the observed deviation from JKD scaling. First-principles density functional theory (DFT) calculations were performed to reveal the correlation between the structural changes and the evolution of the switching properties (see methods in Appendix F). Our DFT calculations captured the effects of strain on $PbTiO_3$ *via* a compressive strain within the (001) and (111) (referred to as (001)-strain and (111)-strain, respectively) to simulate (001)- and (111)-oriented heterostructures, respectively. For (001)-strain, *c* is computed to increase while *a* (or *b*, *a* = *b*) decreases resulting in an increasing *c/a* ratio with increasing compressive strain (Fig. 7.12a). At the same time, $\alpha = \beta = \gamma = 90°$ irrespective of the magnitude of the strain; thus, the ground state structure remains the tetragonal *P*4*mm* phase (Fig. 7.12b) for all compressive strains considered, consistent with the experimental observations (Fig. 7.8a). For (111)-strain, even at zero strain, due to the substrate clamping effect, the symmetry is lowered to monoclinic *Cm* - structure wherein α (or β, $\alpha = \beta$) and γ deviate slightly from 90° (*i.e.*, a monoclinically-distorted *P*4*mm* structure is produced at zero strain) (Figs. 7.12c, d). Upon increasing the magnitude of the

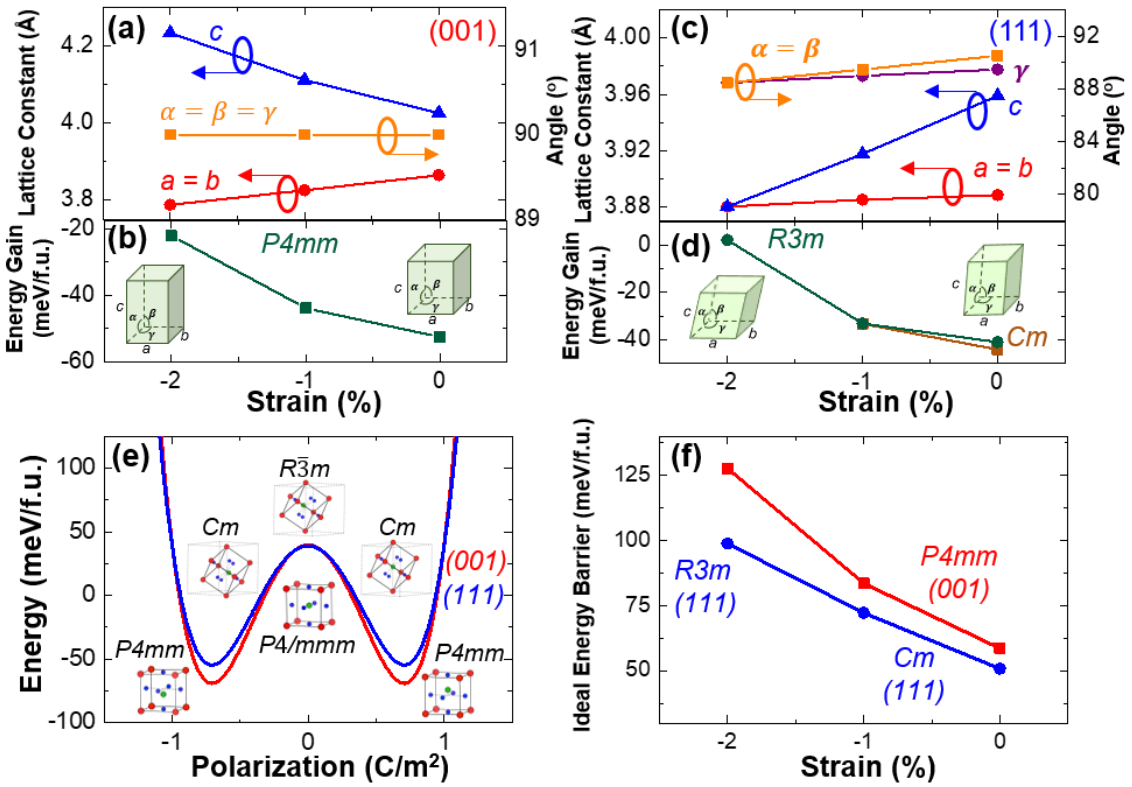

Fig. 7.12: DFT calculations of lattice constants and stable structures, respectively, in (a), (b) (001)- and (c), (d) (111)-oriented heterostructures as a function of strain. (e) The ideal energy barrier for (001)- and (111)-oriented heterostructures. (f) The calculated energy barrier as a function strain in the (001)- and (111)-oriented heterostructures.

compressive strain (simulating reduced film thickness), both *c* and *a* (or *b*, *a* = *b*) are computed to decrease (with *c* decreasing at a faster rate, thus resulting in a decreasing *c/a* ratio) and finally converge to the same value at ~ - 2% strain wherein the monoclinic *Cm* structure transforms to a rhombohedral *R*3*m* structure. At the same time, α and γ also decrease in magnitude and converge to the same value with increasing compressive strain (or reduced film thickness). The overall structural evolution predicted by the DFT calculations is consistent with our experiments on (111)-oriented heterostructures, wherein the ground state adopts a monoclinic structure and trends towards a rhombohedral structure when subjected to a (111)-strain. Furthermore, from the DFT calculations, it is possible to estimate the energy barrier for switching (as extracted from the double-well energy curve, defined as the energy difference between the local ferroelectric minima and the paraelectric saddle-point configurations, *i.e.*, *P*4/*mmm* and $R\bar{3}m$, respectively) for the *P*4*mm* and *Cm* structures (Fig. 7.12e). Plotting the ideal energy barrier as a function of strain, it is noted that the *Cm* structure not only exhibits lower energy barriers at all strains, but also increases with increasing compressive strain at a lower rate than does the energy barrier for the *P*4*mm* structure (Fig. 7.12f). In turn, a lower energy barrier for switching would translate to a lower E_C

and, thus, this could potentially play a role in the observed deviation from JKD scaling in the (111)-oriented heterostructures.

7.5 The Modified Scaling Relation

I note, however, that this simple explanation ignores a number of effects known to impact switching in ferroelectrics (*e.g.*, differences in interfacial "dead layer" effects, incomplete screening from electrodes, defect densities, crystalline quality, *etc.*); many of which I have already addressed and have shown to be unlikely explanations for the observations. Ultimately, for the (111)-oriented heterostructures of thickness ≳ 165 nm, the film adopts a relaxed tetragonal structure and exhibits a similar scaling behavior as the (001)-oriented heterostructures that follow JKD scaling. Upon reducing the film thickness, due to the effects of epitaxial strain, the film transforms to a monoclinic structure and gradually trends towards a rhombohedral structure (wherein the lattice tilt angles deviate more from 90°) with strain. Such a structural transition leads to the change in the fundamental energy barrier for switching that could potentially contribute to the observed scaling behavior. In addition to the observed structural transition contributing to the scaling deviation, the thickness dependent evolution of the *c/a* ratio also likely impacts the scaling relation. Recall that in the (001)-oriented heterostructures the *c/a* ratio increases with decreasing film thickness, but does not significantly affect P_r due to the large ionic displacement in (001)-oriented $PbZr_{0.2}Ti_{0.8}O_3$ films that is insensitive to such structural changes [182]. On the other hand, in the (111)-oriented heterostructures, the *c/a* ratio decreases with decreasing film thickness and this reduction in tetragonality drives a reduction in P_r. This reduction of P_r could also be exacerbated by the presence of a flexoelectric effect which arises from the partial relaxation of strain in the thin (111)-oriented heterostructures [193]. It has been shown that the thermodynamic E_C scales directly with P_r because changes in P_r can drive corresponding changes in the domain-wall energy. Thus, lowering the P_r would decrease the domain-wall energy and, in turn, the energy barrier for switching [184,168]. With this in mind, if one includes the effects of P_r variation in an adapted version of JKD scaling by multiplying $d^{-2/3}$ by a pre-factor P_{mea}/P_{max}, wherein P_{mea} refers to the measured P_r and P_{max} refers to the measured maximum polarization (*i.e.*, P_r measured for a 230 nm thick film). Note that P_{mea}/P_{max} also scales with thickness since both the *c/a* ratio evolution and the strain gradient depend on the film thickness. The modified scaling relation matches closely the observed E_C evolution in (111)-oriented heterostructures (Fig. 7.13). Thus, our work suggests that the decreasing P_r can potentially contribute to the reduced E_C in

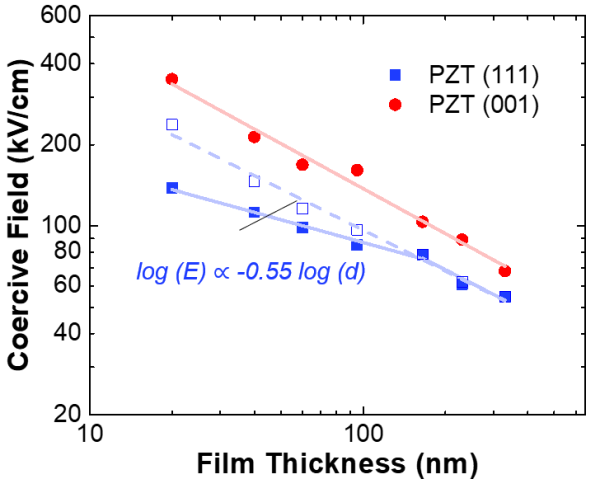

Fig. 7.13: Modified scaling relation in (111)-oriented $PbZr_{0.2}Ti_{0.8}O_3$ thin films. The dashed line represents the classical JKD scaling, open squares are the adjusted E_C values.

(111)-oriented heterostructures. Although this approach can be simply accomplished in ultra-thin films wherein a large depolarization field can destabilize and reduce P_r, such ultra-thin films are usually difficult to measure due to the large leakage currents and extrinsic interface effects. That said, our work suggests a method to achieve the desired reduced E_C for ferroelectrics outside of this ultra-thin limit by engineering the film orientation to induce both a structural transition and P_r reduction that can be combined to affect E_C dramatically.

7.6 Conclusions

In this Chapter, I studied the effects of film orientation on coercive-field scaling in tetragonal $PbZr_{0.2}Ti_{0.8}O_3$ thin films. I observed that while (001)-oriented heterostructures follow JKD scaling across the thicknesses range of 20-330 nm, (111)-oriented heterostructures of the canonical tetragonal ferroelectric $PbZr_{0.2}Ti_{0.8}O_3$ exhibit a deviation from JKD scaling wherein a smaller scaling exponent for the evolution of E_c is observed in films of thickness $\lesssim 165$ nm. X-ray diffraction reveals that, while (001)-oriented heterostructures remain tetragonal for all thicknesses, (111)-oriented heterostructures exhibit a transition from tetragonal to monoclinic symmetry in films of thickness $\lesssim 165$ nm as a result of compressive strain. First-principles calculations suggest that this symmetry change contributes to the deviation from the expected scaling as the monoclinic phase has a lower energy barrier for switching. This structural evolution also gives rise to changes in the *c/a* lattice parameter ratio, wherein this ratio increases and decreases in (001)- and (111)-oriented heterostructures, respectively, as the films are made thinner. In (111)-oriented heterostructures, this reduced tetragonality drives a reduction of the remanent polarization and, therefore, a reduction of the domain-wall energy and overall energy barrier to switching which further exacerbates the deviation from the expected scaling. Overall, this work demonstrates a route towards reducing coercive fields in ferroelectric thin films and provides a possible mechanism to understand this the deviation from JKD scaling.

CHAPTER 8

Summary and Suggestions for Future Work

8.1 Summary of Findings

In this dissertation, I studied orientation-dependent domain structures and the dielectric and ferroelectric properties in $PbZr_{0.2}Ti_{0.8}O_3$ thin films. In Chapter 3, I investigated the orientation-dependent equilibrium ferroelectric domain structures and dielectric properties of polydomain $PbZr_{1-x}Ti_xO_3$ thin films using a phenomenological Ginzburg-Landau-Devonshire thermodynamic model. In this work, I developed and described three-dimensional, polydomain models for (001)-, (101)-, and (111)-oriented films and explored the evolution of the structure and dielectric permittivity of the system as a function of epitaxial strain across the composition range $0.5 \leq x \leq 1.0$. This work revealed that the film orientation, epitaxial strain, and composition can be combined in unexpected ways to drive exotic phase stability and transformations which have intriguing implications for the properties. In Chapter 4, I further experimentally probed the domain structure and dielectric susceptibility in (001)-, (101)-, and (111)-oriented $PbZr_{0.2}Ti_{0.8}O_3$ thin films. In this work, I observed that (111)-oriented films, in which the extrinsic contributions from a high density of 90° domain walls are frozen out, exhibit permittivity values approximately 3-times larger than that expected from the intrinsic response alone. This discrepancy can only be accounted for by considering a stationary contribution to the permittivity from the domain-wall volume of the material that is 6-78-times larger than the bulk response and is consistent with recent predictions of the enhancement of susceptibilities within 90° domain walls.

After exploring the enhanced dielectric response in (111)-oriented films, I studied how the polarization switching proceeds in films with different orientations. Leveraging collaborations with Dr. Shi Liu and Prof. Andrew Rappe from University of Pennsylvania who performed molecular-dynamics simulations to provide theoretical insights, I studied both the local and macroscale switching behaviors in $PbZr_{0.2}Ti_{0.8}O_3$ thin films. First, in Chapter 5, differences were demonstrated between (001)-/(101)- and (111)-oriented films, with the latter exhibiting complex, nanotwinned ferroelectric domain structures with high densities of 90° domain walls and considerably broadened switching characteristics. Molecular-dynamics simulations predicted both 180° (for (001)-/(101)-oriented films) and 90° multi-step switching (for (111)-oriented films) and these processes were subsequently observed in stroboscopic piezoresponse force microscopy. These results have implications for our understanding of ferroelectric switching and offer opportunities to change domain reversal speed. In Chapter 6, I demonstrated multi-state polarization switching in (111)-oriented $PbZr_{0.2}Ti_{0.8}O_3$ thin films, wherein the polarization can be deterministically written into a number of non-volatile and stable states in any order by varying the driving voltage. Such switching phenomena are driven by kinetic control over the volume

fraction of two geometrically different domain structures generated by two distinct switching pathways: one direct, bi-polar-like switching process and another multi-step process with the formation of a thermodynamically-stable intermediate twinning structure. This work provides new insights into the control of ferroelectric switching and demonstrates a candidate material with multi-state functionality for memory devices and adaptive neuromorphic electronics.

Last, leveraging collaborations with Dr. Sebastian Lillo and Prof. Jeffrey Neaton from Department of Physics at University of California, Berkeley, I explored the scaling potential of ferroelectric thin films for low-voltage operation and low-power consumption. In this work it was noted that while (001)-oriented heterostructures follow JKD scaling across the thicknesses range of 20-330 nm, (111)-oriented heterostructures of the canonical tetragonal ferroelectric $PbZr_{0.2}Ti_{0.8}O_3$ exhibit a deviation from JKD scaling wherein a smaller scaling exponent for the evolution of E_c is observed in films of thickness $\lesssim 165$ nm. X-ray diffraction revealed that, while (001)-oriented heterostructures remain tetragonal for all thicknesses, (111)-oriented heterostructures exhibit a transition from tetragonal to monoclinic symmetry in films of thickness $\lesssim 165$ nm. First-principles calculations suggested that this symmetry change contributes to deviation from the expected scaling as the monoclinic phase has a lower energy barrier for switching. This structural evolution also gives rise to changes in the *c/a*-lattice-parameter ratio, wherein this ratio increases and decreases in (001)- and (111)-oriented heterostructures, respectively, as the films are made thinner. In (111)-oriented heterostructures, this reduced tetragonality drives a reduction of the remanent polarization and, therefore, a reduction of the domain-wall energy and overall energy barrier to switching which further exacerbates the deviation from the expected scaling. This work demonstrates a route towards reducing coercive fields in ferroelectric thin films and provides a possible mechanism to understand the deviation from JKD scaling.

Overall, my work presented in this dissertation provides new insights into understanding fundamental mechanisms of emergent dielectric and ferroelectric properties in ferroelectric films and demonstrates a new route to engineering domain structures for enhanced dielectric response and controllable polarization switching in ferroelectric thin films that allow for new functionalities in device applications.

8.2 Suggestions for Future Work

In this Section, I suggest a few directions which are worth investigating in the future as follow-up work for this dissertation:

1. ***Studying the effects of strain in films with different orientations***

In Chapter 3, I calculated the orientation-dependent strain-composition phase diagram of polydomain $PbZr_{1-x}Ti_xO_3$ films, which revealed that the strain and film orientation can be combined in unexpected ways to drive the exotic phase stability and dielectric properties. The

work presented in Chapter 7 also suggests that upon reducing the thickness, epitaxial strain plays a dominant role in the structural transformation and reduced coercivity of (111)-oriented films. Most of the other experimental work introduced in Chapters 4-6, however, focuses on relaxed (111)-oriented $PbZr_{0.2}Ti_{0.8}O_3$ films. Thus, one possible future direction is to investigate strain effects on the evolution of structures, dielectric response, and switching properties of (111)-oriented $PbZr_{0.2}Ti_{0.8}O_3$ films. It is possible to grow these films on $(101)_O$- or $(011)_O$- (akin to (111)-oriented pseudo-cubic substrates) oriented rare-earth scandate substrates which can provide a range of mismatch strain to tune material structures. Note that due to the symmetry difference between $PbZr_{0.2}Ti_{0.8}O_3$ films and scandate substrates, the applied strain becomes uniaxial within planes of (111). For instance, for the growth of $PbZr_{0.2}Ti_{0.8}O_3$ thin films on $(011)_O$-oriented $NdScO_3$ substrates, the applied uniaxial strain is not equivalent to all three polarization variants and thus can break the degeneracy of these variants to selectively control the polarization variants and their morphology. Thus, using a combination of strain and orientation effects, one can control the domain and domain wall structures that can further affect the material property.

2. Studying orientation-dependent structure and properties in films with phase coexistence

The work herein focused on studying the structure and property evolution in titanium-rich tetragonal $PbZr_{1-x}Ti_xO_3$ films. Very little work is focused on how film orientations affect $PbZr_{1-x}Ti_xO_3$ films with phase coexistence near the morphotropic-phase boundary (MPB) composition. Thus, another possible future direction would be to investigate how strain and orientation affects the structure and properties of (101)- and (111)-oriented $PbZr_{0.52}Ti_{0.48}O_3$ films. In particular, following topics are worth investigating: how does uniaxial or biaxial strain affect the free energy landscape of (101)- and (111)-oriented $PbZr_{0.52}Ti_{0.48}O_3$ films? How do they affect domain structure, dielectric, piezoelectric, and switching properties? Is that possible to induce novel structural phases? Note that $PbZr_{1-x}Ti_xO_3$ near the MPB composition usually exhibit an isotropic composition related flattening of the free energy profile. For instance, the application of uniaxial strain by growing $PbZr_{0.52}Ti_{0.48}O_3$ on $SmScO_3$ (110) substrates can break the isotropy of free energy profile and thus affect the domain morphology. Recent phenomenological calculations suggest that breaking the isotropy of free energy profile in MPB $PbZr_{1-x}Ti_xO_3$ can generate a large, polarization rotation related to enhancement of the piezoelectric effect [194]. Thus, it is worth further experimentally investigating the relation between the uniaxial strain and their induced effects to domain structures and susceptibilities of $PbZr_{1-x}Ti_xO_3$ near the MPB composition.

3. Studying orientation-dependent domain structures, dielectric, and switching properties in $BaTiO_3$ films

The work herein focused on orientation effects in Pb-based ferroelectric like $PbZr_{0.2}Ti_{0.8}O_3$ films in which the ferroelectric phase remains stable within a wide temperature range. Another possible future direction is to investigate how film orientations affect the structural instability of

$BaTiO_3$ films which have a complex temperature-dependent phase evolution. In particular, the following topics are worth investigating: how does the film orientation affect phase-transition temperature in (101)- and (111)-oriented $BaTiO_3$ films? Is that possible to obtain the phase transition at room temperature and thus achieve enhanced susceptibilities using the biaxial or uniaxial strain applied within these film orientations? For instance, growing $BaTiO_3$ films on $(110)_O$-oriented $NdScO_3$ substrates, one can expect a uniaxial compressive strain along [110] pseudo-cubic lattice direction that can distort the lattice to favor the orthorhombic phase. As a result, such strain effects can possibly cause a shift of the orthorhombic-to-tetragonal phase transition in $BaTiO_3$ from 278 K to a higher temperature. Thus, it is possible to induce enhanced dielectric and piezoelectric susceptibilities at room temperature which are accompanied with this phase transition.

Appendix A

Pulsed Measurements

A.1 Pulse-Switching Measurements

In the work introduced in Chapter 6, I performed pulse-switching measurements using a modified PUND pulse sequence on the symmetric capacitor structures using a Precision Multiferroic Tester (Radiant Technologies, Inc.). In a conventional PUND measurement, the ferroelectric capacitor is subjected to the pulse sequence including one preset pulse and four reading pulses (Fig. A1a). The first preset pulse is used to pre-pole the capacitor to the -V direction; no measurement will be performed as a result of this pulse. The second pulse switches the capacitor

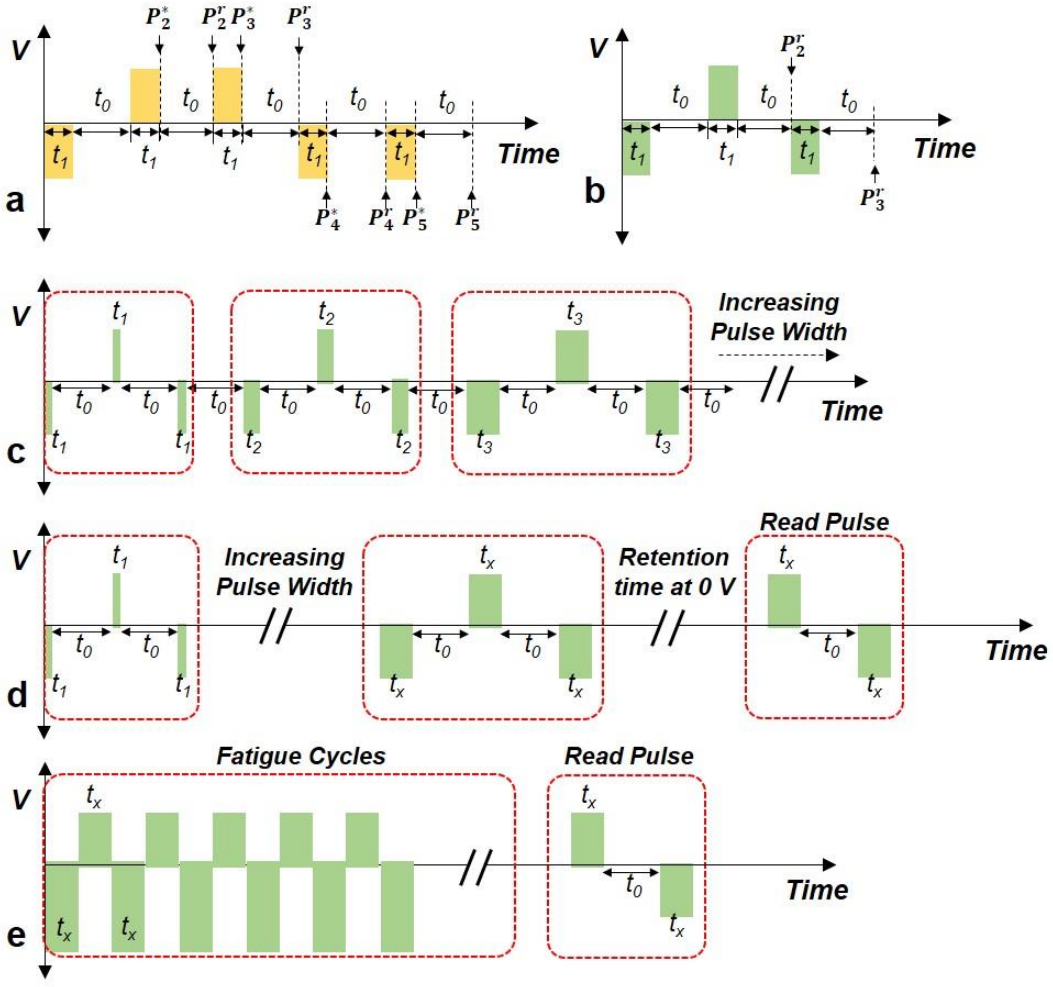

Fig. A1: Schematics of the pulse sequences used in the pulse-switching measurements. a, The pulse sequence used in conventional positive-up-negative-down (PUND) measurements. b, The modified PUND pulse sequence used in our measurements. c, The modified PUND measured as a function of pulse width for constant pulse voltages. d, The pulse sequence used in the retention measurement.

to the +V direction and measures the amount of switched polarization. The third pulse is a twin pulse of the second, which is used to read the non-remnant part of polarization that dissipates during the delay time after the second pulse. The fourth and fifth pulses mirror the second and third, and are used to switch the capacitor to the -V direction and read both the switched and non-switched polarization, respectively. There are eight measured parameters generated by the PUND measurement, namely P_i* and P_i^r (i = 2, 3, 4, 5), where P_i* is measured at the end of each reading pulse when the voltage is on, and P_i^r is measured after a certain amount of delay time when the voltage is off. These eight parameters can be measured as a function of pulse time and voltage by varying certain pulse parameters of the basic waveform.

Since I focused on the measurement of switched remnant polarization P_i^r read by the second and the fourth pulse instead of non-switched polarizations read by the third and the fifth pulse, I used a modified PUND pulse sequence wherein the third and fifth pulses are removed from the original PUND waveform (Fig. A1b). The pulse-switching measurement was performed as a function of pulse width for a certain pulse voltage (Fig. A1c). Each measurement cycle consists of three pulses with equal time widths. The pulse voltage is kept constant while the pulse width is varied incrementally for different cycles. For simplicity, only the positive remnant switched polarization is shown (Fig. 6.3a), which is measured at 0 V after a delay of t_0 from the fall of the positive reading pulse. The full switching profile is provided where both the positive and negative

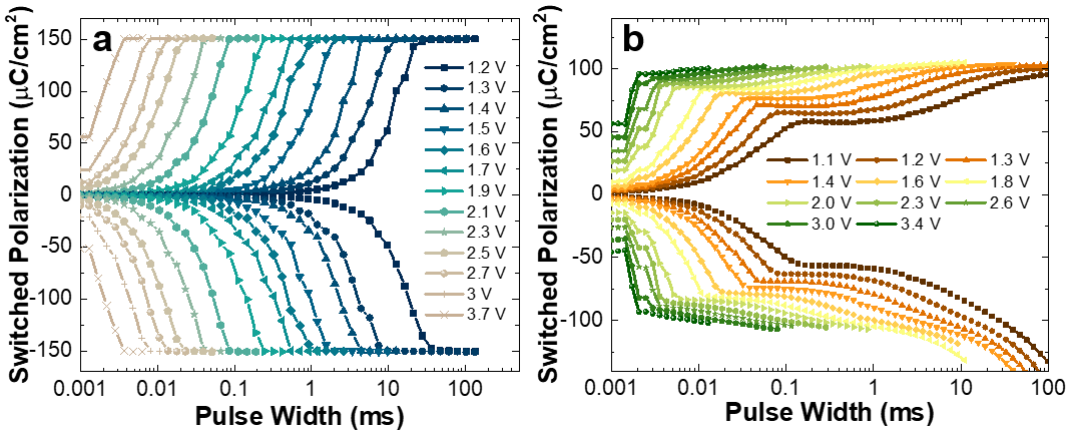

Fig. A2: Pulse-switching measurements – full data. The switched positive and negative polarization P_i^r measured as a function of pulse width for different pulse voltages in **a**, (001)- and **b**, (111)-oriented heterostructures

P_i^r (i = 2, 3) are shown here for (001)- and (111)-oriented films, respectively (Fig. A2).

A.2 Retention Measurements

The retention measurement pulse sequence is provided (Fig. A1d). In this measurement, the material is first switched into a certain polarization state (*e.g.*, partially-switched states and intermediate states in (001)- and (111)-oriented heterostructures, respectively) and then the system is held at 0 V for a certain amount of retention time. After this waiting period, a pair of reading

pulses is applied to read the variation in both the positive and negative switched polarization. Furthermore, the retention time can be varied to allow the measurement of polarization variations as a function of retention time.

A.3 Fatigue Measurements

The adapted fatigue measurement pulse sequence is provided (Fig. A1e). In this measurement, the fatigue cycles were applied to the capacitor to switch the capacitor multiple as many as 1.64×10^8 cycles. In order to reproduce the writing of various multi-state polarization values, the fatigue cycles were set to include a high negative voltage pulse which switches the capacitor into a fully up-poled state followed by a smaller positive voltage pulse which switches the capacitor from the fully up-poled state into one of many multi-state polarization values. The negative pulse voltage was 5.0 V and 4.0 V for (001)- and (111)-oriented heterostructures, respectively, and the positive pulse voltage varies from 1.8-5.0 V and 1.1-4.0 V for the (001)- and (111)-oriented heterostructures, respectively. The pulse width used in these studies was set to be 0.005 ms. The fatigue cycles were interrupted regularly by a pair of read pulses which monitors the variation of remanent polarization as a function of writing cycles.

Appendix B

Quantification of the Domain Structures

In this Appendix, I introduce how I quantify the domain wall density (λ, defined as the total length of domain walls in a given area) and the volume fraction of minority domains ($\phi_{\min}$, defined as the volume fraction of the domain type which possesses the smallest population among all polarization variants in the case of a poled film) for the different film orientations. This is achieved by directly measuring the total length of domain walls per unit area. Using the Igor Software for the Asylum Cypher system used to complete the PFM studies, it is possible to transform the domain structure images to a grey scale and then using the Particle Analysis software package, it is possible to select and highlight all areas of the image possessing similar color levels. For instance, for the (001)-oriented heterostructures (Fig. B1a) two contrasts in grey scale are observed: light color corresponding to the *c* domains and dark color corresponding to the *a* domains. Using the software it is possible to highlight and measure both the perimeter and area of the selected domains (in this case, the minority *a* domains). The same approach has hence forth been used on the (101)- (Fig. B1b, c) and (111)- (Fig. B1d) oriented heterostructures. In all images, the domain walls are highlighted in red. This analysis has produced the values of domain wall density λ and the area fraction of the domains. To estimate the volume fraction ($\phi_{\min}$), I have

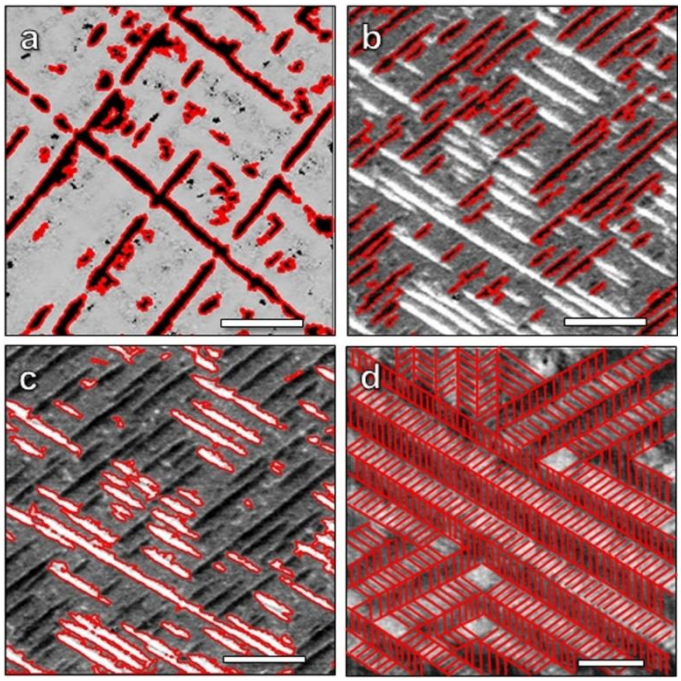

Fig. B1: Quantifications of domain structures. Extraction of domain area and domain wall lengths as achieved via Asylum Igor software for (a) (001)-, (b),(c) (101)-, and (d) (111)-oriented $PbZr_{0.2}Ti_{0.8}O_3$ films. Scale bar: 500 nm.

assumed a uniform width of the domains throughout the thickness of the film. It should be noted that this assumption matches the assumptions of the GLD models (or, in other words, matches the ideal domain structure that would be predicted from such models), but might slightly overestimate the volume density if the domains are more wedge-shaped as has been observed in some cross-section TEM studies [108]. Regardless, this potential slight discrepancy has little to no impact on the overall conclusion of the data. The values of λ and $\phi_{\min}$ are provided in Table 4.1.

Appendix C

Rayleigh Measurements

Dielectric Rayleigh analyses were conducted on the capacitor structures of (001)- and (101)- and (111)-oriented $PbZr_{0.2}Ti_{0.8}O_3$ films. Rayleigh studies measure the dielectric permittivity as a function of the AC excitation field and probe the reversible and irreversible domain wall (extrinsic) contribution to the dielectric response [60] (Fig. C1a). Note that the field dependent dielectric response can usually be separated into three different field regimes [26]: 1) Low Field Regime – where the reversible domain wall contribution is dominant and thus leads to a field independent constant permittivity; 2) Rayleigh Regime – where the permittivity increases linearly as a result of the irreversible domain wall contribution; 3) High Field Regime – where switching occurs, giving rise to a sub- or super- linear dielectric response to which the Rayleigh law no longer applies. Here the Rayleigh analyses were carried out prior to the standard low-field permittivity characterization to ensure the selection of an applied field in the permittivity measurement that activates reversible domain wall motion only. In order to confirm the valid electric field range of the Rayleigh region and therefore probe the low field dielectric response, I correlate the nonlinear

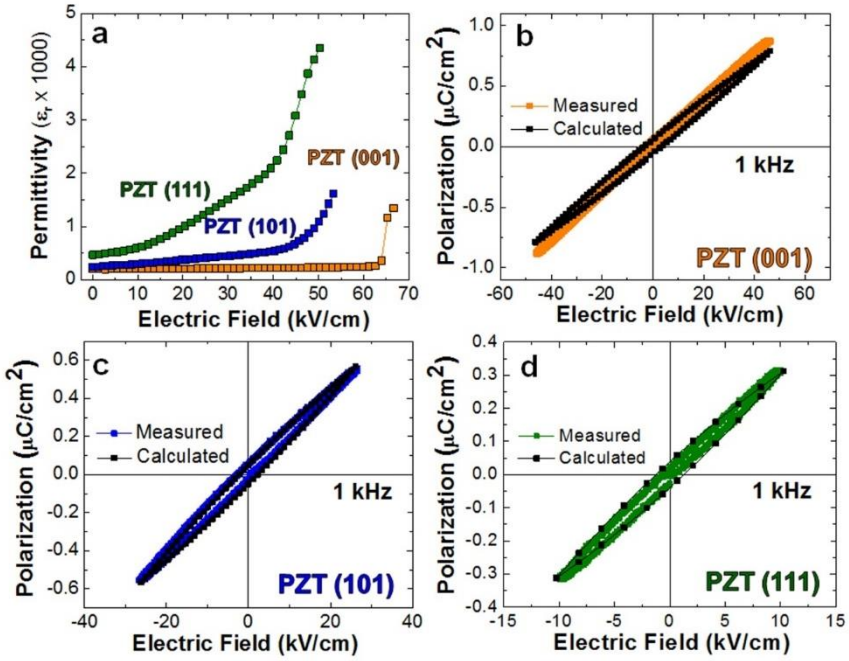

Fig. C1: Rayleigh studies of various film orientations. (a) Dielectric Rayleigh studies which measure the dielectric permittivity as a function of AC electric field at 1 kHz. Polarization-electric field hysteresis loops measured at 1 kHz for (b) E_0= 46.27 kV cm^{-1} in (001)-oriented films (orange), (c) E_0= 22.5 kV cm^{-1} in (101)-oriented films (blue), and (d) E_0= 8.22 kV cm^{-1} in (111)-oriented films (green). Black curves in (b), (c), and (d) are the corresponding calculated results using Eq. (1).

dielectric response with the polarization-electric field hysteresis loops at the sub-switching field by calculating the polarization response using the relation [60,74]:

$$P = (\varepsilon'_{\text{ini}} + \alpha' E_0)^{\pm}_{-} \frac{\alpha'}{2}(E_0^2 - E^2) \quad (1)$$

$$E = E_0 \sin(\omega t) \quad (2)$$

where $\varepsilon'_{\text{ini}}$ is the reversible Rayleigh parameter that is the result of the intrinsic lattice and reversible extrinsic (domain wall) contributions, α' is the Rayleigh coefficient (which is related to the irreversible domain wall contribution), E_0 is the amplitude of the applied AC field, and + is used for decreasing fields and – for increasing fields. These calculated polarization-electric field hysteresis loops in the various film variants are compared to the hysteresis loops measured at the same field range. All the calculated results fit well with the measured loops in the Rayleigh region (Fig. C1b-d). With the information acquired from such Rayleigh studies, I selected a relatively low voltage of 50 mV (~3.33 kV cm^{-1} for 150 nm films) as the AC driving amplitude in the subsequent permittivity measurements for all orientations which allows me to be confident that I am only probing the intrinsic response and reversible domain wall motion.

Appendix D

Phase-Field Modeling

Details of phase-field modeling are provided in this Appendix. This work is performed in collaboration with Dr. Jianjun Wang, Dr. Zijian Hong, and Prof. Longqing Chen from the Pennsylvania State University. Here, phase-field modeling was performed to study local switching events and domain structure variants in (001)- and (111)-oriented heterostructures. Two coordinate systems are used including $\boldsymbol{x}$ (x_1, x_2, x_3) with x_1, x_2, and x_3 along [100], [010], and [001] and $\boldsymbol{x'}$ (x_1', x_2', x_3') with x_1', x_2', and x_3' along $[01\bar{1}]$, $[\bar{2}11]$, and $[111]$ for the (001)- and (111)-oriented heterostructures, respectively. The polarization P' in the $\boldsymbol{x'}$ coordinate system can be related to the total free energy F through time-dependent Landau-Ginzburg (TDGL) equation [195,65],

$$\frac{\partial P_i'(\mathbf{r},t)}{\partial t} = -L\frac{\delta F}{\delta P_i'(\mathbf{r},t)}, \tag{1}$$

where L is the kinetic coefficient. The total free energy F includes bulk, elastic, electric, and gradient energies,

$$F = \iiint_V \left(f_{\text{bulk}} + f_{\text{elastic}} + f_{\text{electric}} + f_{\text{grad}} \right) dV, \tag{2}$$

where V represents the volume of ferroelectric thin films. The bulk free energy density for $PbZr_{0.2}Ti_{0.8}O_3$ is described by a sixth-order Landau-Devonshire polynomial [196],

$$\begin{aligned} f_{\text{bulk}} &= \alpha_1\left(P_1^2+P_2^2+P_3^2\right)+\alpha_{11}\left(P_1^4+P_2^4+P_3^4\right)+\alpha_{12}\left(P_1^2P_2^2+P_1^2P_3^2+P_2^2P_3^2\right) \\ &+\alpha_{112}\left[P_1^4\left(P_2^2+P_3^2\right)+P_2^4\left(P_1^2+P_3^2\right)+P_3^4\left(P_1^2+P_2^2\right)\right] \\ &+\alpha_{111}\left(P_1^6+P_2^6+P_3^6\right)+\alpha_{123}P_1^2P_2^2P_3^2, \end{aligned} \tag{3}$$

where all of the coefficients are independent of temperature except α_1. The elastic energy density is given by

$$f_{\text{elastic}} = \frac{1}{2}c_{ijkl}e_{ij}(\mathbf{r})e_{kl}(\mathbf{r}) = \frac{1}{2}c_{ijkl}\left(\varepsilon_{ij}(\mathbf{r})-\varepsilon_{ij}^0(\mathbf{r})\right)\left(\varepsilon_{kl}(\mathbf{r})-\varepsilon_{kl}^0(\mathbf{r})\right), \tag{4}$$

where c_{ijkl}, $e_{ij}(\mathbf{r})$, $\varepsilon_{ij}(\mathbf{r})$, $\varepsilon_{ij}^0(\mathbf{r})$ are the elastic stiffness tensor, elastic strain, total strain, and spontaneous strain, respectively. The spontaneous strain $\varepsilon_{ij}^0(\mathbf{r})$ can be expressed using electrostrictive coefficients and polarizations, *i.e.*, $\varepsilon_{ij}^0(\mathbf{r}) = Q_{ijkl}P_k(\mathbf{r})P_l(\mathbf{r})$, $i,j,k,l = 1,2,3$, where the summation convention for the repeated indices is employed. The total strain $\varepsilon_{ij}(\mathbf{r})$ can be expressed as a sum of the homogeneous and heterogeneous strain, *i.e.*, $\varepsilon_{ij}(\mathbf{r}) = \bar{\varepsilon}_{ij} + \delta\varepsilon_{ij}(\mathbf{r})$, based on Khachaturyan's elastic theory [197]. The homogeneous strain is defined in such a way so that

$\int \delta\varepsilon_{ij}(\mathbf{r})dV = 0$, which represents the macroscopic shape change of a system generated due to the formation of domain structures and can be determined from the mismatch between thin films and substrates. The heterogeneous strain does not change the macroscopic shape of a system and can be calculated from $\delta\varepsilon_{ij}(\mathbf{r}) = \frac{1}{2}\left[\partial u_i(\mathbf{r})/\partial r_j + \partial u_j(\mathbf{r})/\partial r_i\right]$, where $u_i(\mathbf{r})$ is the position-dependent displacement. The equilibrium elastic strain $e_{ij}(\mathbf{r})$ can be obtained by solving the mechanical equilibrium equation $\sigma_{ij,j} = 0$.

The electrostatic energy density of given domain structures can be calculated by

$$\begin{aligned} f_{\text{electric}} &= -\int_0^{\mathbf{E}} \mathbf{D}(\mathbf{r},\mathbf{E})\cdot d\mathbf{E} = -\mathbf{P}(\mathbf{r})\cdot\mathbf{E} - \frac{1}{2}\varepsilon_0\boldsymbol{\kappa}^{\mathrm{b}}\mathbf{E}^2 \\ &= -P_i(\mathbf{r})E_i(\mathbf{r}) - \frac{1}{2}\varepsilon_0\kappa_{ij}^{\mathrm{b}}E_i(\mathbf{r})E_j(\mathbf{r}) \ , \end{aligned} \tag{5}$$

where κ_{ij}^{b} is the background dielectric constant tensor. The gradient energy density in an anisotropic system can be expressed as

$$f_{\text{grad}} = \frac{1}{2}G_{ijkl}P_{i,j}P_{k,l} \ , \tag{6}$$

where G_{ijkl} is the gradient energy coefficient and $P_{i,j} = \partial P_i/\partial r_j$. For an isotropic system, equation (6) reduces to [198]:

$$f_{\text{grad}} = \frac{1}{2}G_{11}\left(P_{1,1}^2 + P_{2,2}^2 + P_{3,3}^2 + P_{1,2}^2 + P_{2,1}^2 + P_{1,3}^2 + P_{3,1}^2 + P_{2,3}^2 + P_{3,2}^2\right), \tag{7}$$

where G_{ij} is related to G_{ijkl} by the Voigt's notation, and $G_{12} = 0, G_{11} = 2G_{44} = 2G_{44}^{'}$ in an isotropic system.

In addition, the polarization components P_j in coordinate system $\boldsymbol{x}$ can be transformed to P_i' in coordinate system $\boldsymbol{x'}$ using transformation matrix T_{ij} via following relations:

$$P_i^{'} = T_{ij}P_j \ , \tag{8}$$

where the transformation matrices for (001)- and (111)-oriented thin films are given as follows:

$$T_{ij}^{(001)} = \begin{pmatrix} 1 & 0 & 0 \\ 0 & 1 & 0 \\ 0 & 0 & 1 \end{pmatrix}, \ T_{ij}^{(111)} = \begin{pmatrix} 0 & 1/\sqrt{2} & -1/\sqrt{2} \\ -2/\sqrt{6} & 1/\sqrt{6} & 1/\sqrt{6} \\ 1/\sqrt{3} & 1/\sqrt{3} & 1/\sqrt{3} \end{pmatrix}. \tag{9}$$

Similarly, elastic stiffness tensors, electrostrictive coefficient tensors, background dielectric constant tensors, and gradient energy coefficient tensors also need to be transformed from coordinate systems $\boldsymbol{x}$ to $\boldsymbol{x'}$ using transformation matrices via following relations:

$$c_{ijkl}^{'} = T_{im}T_{jn}T_{ks}T_{lt}c_{mnst} \ , \tag{10}$$

$$Q'_{ijkl} = T_{im}T_{jn}T_{ks}T_{lt}Q_{mnst}\,, \tag{11}$$

$$\kappa'_{ij} = T_{im}T_{jn}\kappa_{mn}\,, \tag{12}$$

$$G'_{ijkl} = T_{im}T_{jn}T_{ks}T_{lt}G_{mnst}\,. \tag{13}$$

Here the temporal evolution of domain structures can be obtained by numerically solving the TDGL equation using the semi-implicit Fourier spectral method with previously reported materials parameters. Discrete grid points of $256\Delta x \times 256\Delta y \times 40\Delta z$ with real grid space $\Delta x = \Delta y = \Delta z = 2$ nm are used to describe the film/substrate system, wherein the thickness of $PbZr_{0.2}Ti_{0.8}O_3$ is set as 48 nm with $h_{\text{film}} = 24\Delta z$ and the film/substrate mismatch strain $\overline{\varepsilon_{ij}}$ is set to be zero based on experimental observations. Using the superposition spectral method and short-circuit surface boundary conditions, the electrostatic equilibrium equation can be solved to obtain the energy evolution for polarization switching and domain structures in $PbZr_{0.2}Ti_{0.8}O_3$ films (Figs. 6.7 and 6.8).

Appendix E

Supplementary Structural Characterizations

E.1 X-ray structural analyses for (001)- and (111)-oriented heterostructures

The complete results and information of the structural analysis for (001)- and (111)-oriented heterostructures are provided in this Appendix. Detailed X-ray reciprocal space mapping measurements were performed about the 103- and 312-, 330-diffraction conditions as a function of film thickness for (001)- and (111)-oriented heterostructures, respectively. In (001)-oriented heterostructures, it is noted that the $PbZr_{0.2}Ti_{0.8}O_3$ 103-diffraction peak shifts towards higher Q_y values and lower Q_x values with increasing film thickness, suggesting continually relaxing strain conditions (Fig. E1). In (111)-oriented heterostructures, for film of thickness < 60 nm, three sub-peaks were observed about the 312-diffraction condition and two sub-peaks were observed about the 330-diffraction condition (Figs. E2 and E3). Such peak splitting is caused by the presence of three structural variants in the $PbZr_{0.2}Ti_{0.8}O_3$ films (two structural variants converge into one peak in the 330-diffraction condition). In films of thickness > 60 nm, the additional peak splitting was observed due to the onset of a tilt of the unit cell which contributes another set of peaks. In order to characterize the tilt of unit cells, 3D synchrotron X-ray studies were performed about the 222-diffraction conditions (Fig. E4). In *HK* mapping, clear three-fold peak splitting was observed in

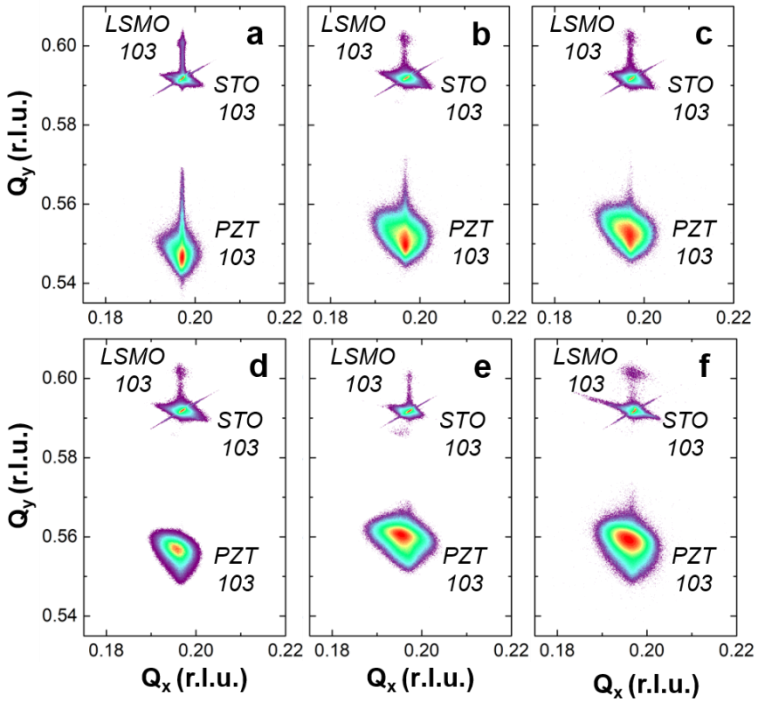

Fig. E1: X-ray RSM studies about the 103-diffraction conditions of the films and substrate for (001)-oriented $PbZr_{0.2}Ti_{0.8}O_3$ heterostructures of thickness a) 20 nm, b) 40 nm, c) 60 nm, d) 95 nm, e) 165 nm, and f) 230 nm.

films of thickness > 60 nm suggesting the presence of tilted cells in thick films (Fig. E5). Furthermore, the tilting direction can be extracted from the *KL* mapping wherein the peak

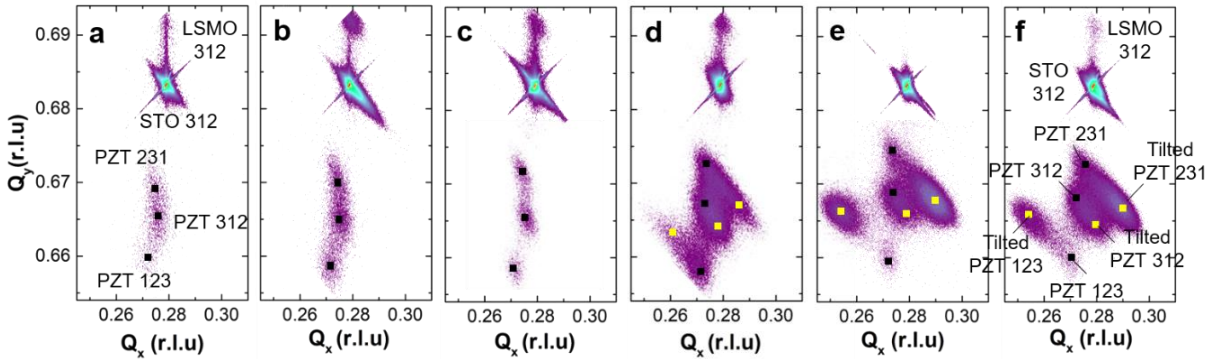

Fig. E2: X-ray RSM studies about the 312-diffraction condition of the films and substrate for (111)-oriented $PbZr_{0.2}Ti_{0.8}O_3$ heterostructures of thickness a) 20 nm, b) 40 nm, c) 60 nm, d) 95 nm, e) 165 nm, and f) 230 nm.

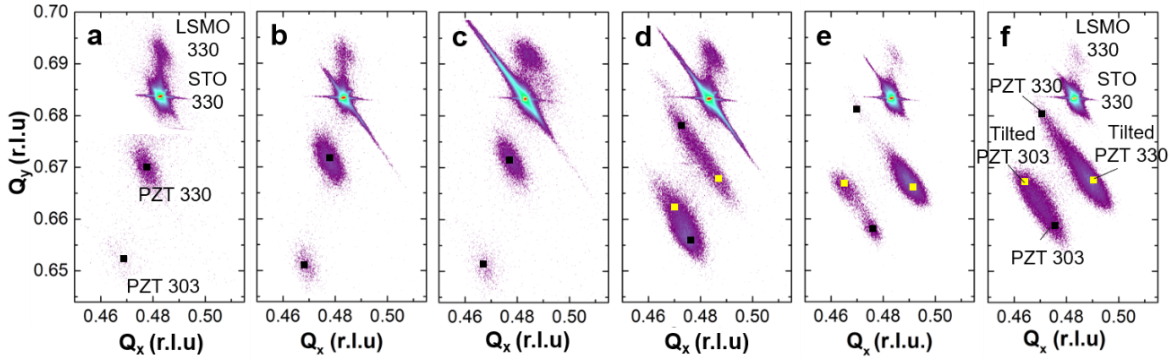

Fig. E3: X-ray RSM studies about the 330-diffraction condition of the films and substrate for (111)-oriented $PbZr_{0.2}Ti_{0.8}O_3$ heterostructures of thickness a) 20 nm, b) 40 nm, c) 60 nm, d) 95 nm, e) 165 nm, and f) 230 nm.

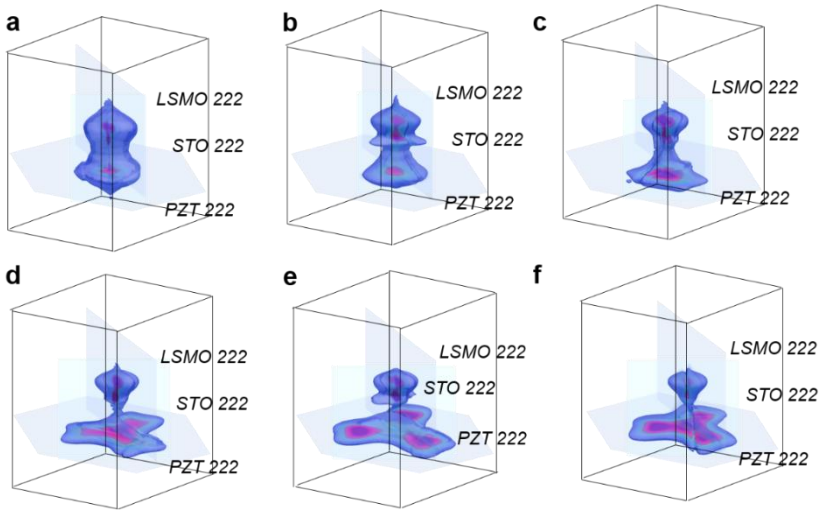

Fig. E4: 3D synchrotron-based X-ray RSM studies about the 222-diffraction conditions of (111)-oriented $PbZr_{0.2}Ti_{0.8}O_3$ heterostructures of thickness a) 20 nm, b) 40 nm, c) 60 nm, d) 95 nm, e) 165 nm, and f) 230 nm.

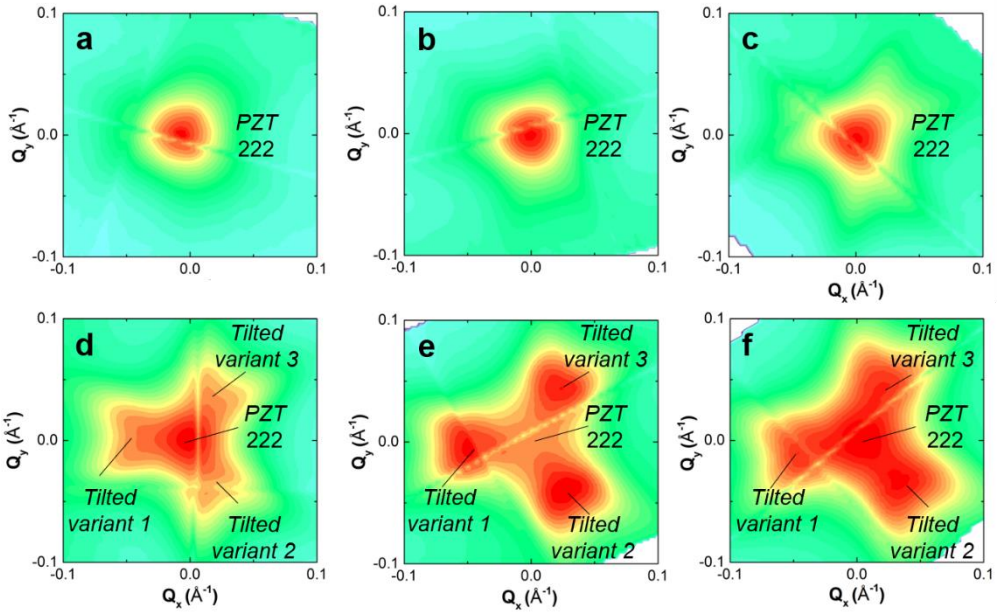

Fig. E5: *HK* mapping extracted from the 3D, synchrotron-based RSM studies about the 222-diffraction conditions for (111)-oriented $PbZr_{0.2}Ti_{0.8}O_3$ heterostructures of thickness a) 20 nm, b) 40 nm, c) 60 nm, d) 95 nm, e) 165 nm, and f) 230 nm.

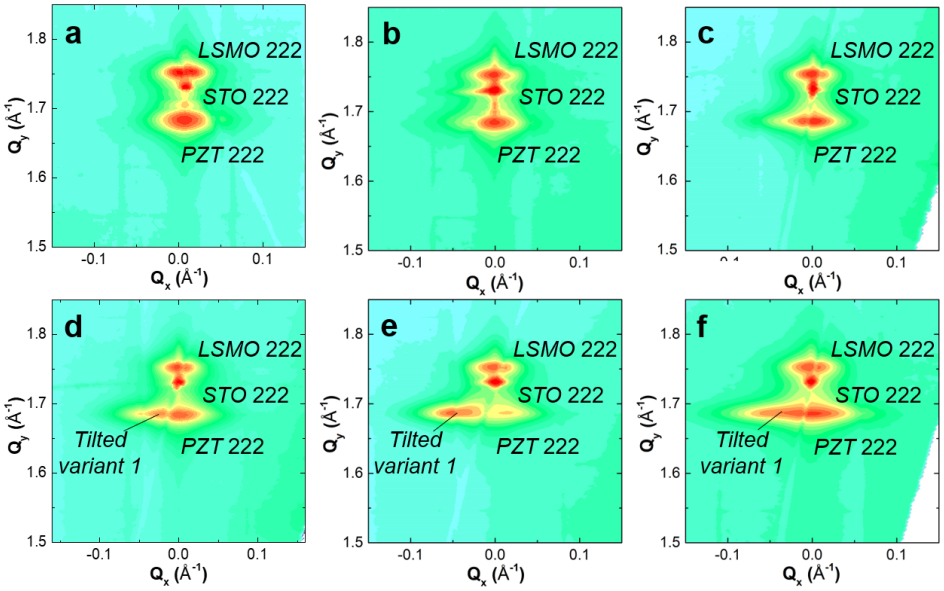

Fig. E6: *KL* mapping extracted from the 3D, synchrotron-based RSM studies about the 222-diffraction conditions for (111)-oriented $PbZr_{0.2}Ti_{0.8}O_3$ heterostructures of thickness a) 20 nm, b) 40 nm, c) 60 nm, d) 95 nm, e) 165 nm, and f) 230 nm.

elongates along the $\langle 11\bar{2} \rangle$ indicating the cells are titled towards the $\langle 11\bar{2} \rangle$ (Fig. E6).

E.2 The calculation of the average strain in (111)-oriented heterostructures

The measured lattice parameters of the cubic cell can be converted into the hexagonal lattice parameters along the ⟨110⟩. Here, I use a = 3.94 Å and c = 4.12 Å to calculate the bulk lattice parameters. The detailed calculation process and results can be found as follows (Table E1 and Fig. E7):

$a_1' = \sqrt{a^2 + a^2 - 2a \cdot a \cdot \cos(\gamma)}$;

$a_2' = \sqrt{a^2 + c^2 - 2a \cdot c \cdot \cos(\alpha)}$;

$a_1^{bulk} = \sqrt{3.94^2 + 3.94^2 - 2 \times 3.94 \times 3.94 \times \cos(90°)} = 5.5698$ Å;

$a_2^{bulk} = \sqrt{3.94^2 + 4.12^2 - 2 \times 3.94 \times 4.12 \times \cos(90°)} = 5.6984$ Å ;

Strain along a_1': $\epsilon_1' = \frac{a_1' - a_1^{bulk}}{a_1^{bulk}}$;

Strain along a_2': $\epsilon_2' = \frac{a_2' - a_2^{bulk}}{a_2^{bulk}}$;

Average strain: $\overline{\epsilon'} = \frac{\epsilon_1' + \epsilon_2'}{2}$.

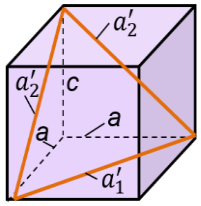

Fig. E7: Schematic of the lattice parameters.

Table E1: Calculation of average strain in (111)-oriented heterostructures.

Thickness (nm)	a (Å)	c (Å)	α (°)	γ (°)	a_1' (Å)	ϵ_1'	a_2' (Å)	ϵ_2'	$\overline{\epsilon'}$
20	3.970	3.993	87.24	89.44	5.584	0.00271	5.491	-0.03638	-0.01684
40	3.962	3.989	87.41	89.91	5.597	0.00488	5.492	-0.03627	-0.01569
60	3.947	4.014	88.88	90.02	5.581	0.00196	5.572	-0.02223	-0.01014
95	3.950	4.060	89.47	90.06	5.587	0.00309	5.636	-0.01094	-0.00393
165	3.946	4.100	89.82	90.04	5.580	0.00186	5.679	-0.0034	-7.69E-4
230	3.946	4.100	89.82	90.04	5.580	0.00186	5.679	-0.0034	-7.69E-4

Appendix F

First-Principles Density Functional Calculations

Details of first-principles density functional calculations are provided in this Appendix. This work is performed in collaboration with Dr. Sebastian Lillo and Prof. Jeffrey Neaton from University of California, Berkeley. To elucidate the effect of epitaxial strain on the properties of $PbZr_{0.2}Ti_{0.8}O_3$, first-principles DFT simulations were performed on the model system $PbTiO_3$. The energy gain, lattice parameters, *c/a* ratio, and polarization for polar structures of $PbTiO_3$ obtained by off-centring the Ti atom along different directions in the cubic unit cell are provided (Table F1). LDA lattice parameters underestimate experimental $PbTiO_3$ lattice parameters (a = 3.969 Å for $Pm\bar{3}m$; a = 3.902 Å, c = 4.156 Å for $P4mm$) by ~2-3%, as is typical for LDA.

In the case of (001)-strain, the *P*4*mm* structure is found to be the ground state structure of $PbTiO_3$, where the relaxed in-plane lattice parameter of the *P*4*mm* structure (a_{001} = 3.865 Å) is used as the reference point to calculate the (001)-strain. Here, the in-plane lattice parameter a is modified to fit the matching plane, while the out-of-plane lattice parameter c is allowed to relax. In the case of (111)-strain, *P*4*mm* lowers its symmetry to *Cm*. The in-plane hexagonal lattice vectors $\boldsymbol{a}_1$ and $\boldsymbol{a}_2$ are modified to fit the matching plane, while the out-of-plane lattice vector $\boldsymbol{a}_3$ is allowed to relax. The large in-plane polarization component of the *Cm* structure (63.5 μC/cm^2) induces a large anisotropic mismatch of the in-plane hexagonal lattice vectors $\boldsymbol{a}_1$ and $\boldsymbol{a}_2$ of 0% and 2.1%, respectively, with respect to the ideal lattice vectors (a_{001} = 3.865 Å). The average in-plane lattice parameter a_{111} = 3.906 Å is used as the reference point to calculate the (111)-strain. In addition, the macroscopic polarization (in Cartesian coordinates) is computed as **P** = (0, 0, 77.2) μC/cm^2 for the *P*4*mm* structure and **P** = (0.2, 63.5, 45.0) μC/cm^2 for the *Cm* structure (|**P**| = 77.9 μC/cm^2), which is in good agreement with the measured out-of-plane polarization (~80 μC/cm^2 for (001)-strain and ~50 μC/cm^2 for (111)-strain) (Fig. 7.3).

Table F1: Computed energy gain (meV/f.u.) with respect to cubic $PbTiO_3$, lattice parameters, *c/a* ratio, and polarization (μC/cm^2) for polar structures of $PbTiO_3$.

Phase	**Energy gain (meV/f.u.)**	**Latt. param. (Å)**	***c/a* ratio**	**Polarization (μC/cm^2)**
Pm-3*m*	0	a = 3.888	1.000	0
*R*3*m*	41	a = 3.908	1.000	66.2
*Amm*2	44	a = 3.932 c = 3.868	0.984	68.7
*P*4*mm*	53	a = 3.865 c = 4.026	1.042	77.2

Bibliography

1. Valasek, J. Piezo-electric and allied phenomena in Rochelle salt. *Phys. Rev.* **17,** 475–481 (1921).
2. Chanthbouala, a *et al.* A ferroelectric memristor. *Nat. Mater.* **11,** 860–864 (2012).
3. Guo, R. *et al.* Non-volatile memory based on the ferroelectric photovoltaic effect. *Nat. Commun.* **4,** 1–5 (2013).
4. Whyte, J. R. & Gregg, J. M. A diode for ferroelectric domain-wall motion. *Nat. Commun.* **6,** 7361 (2015).
5. Mcgilly, L. J., Yudin, P., Feigl, L., Tagantsev, a K. & Setter, N. Controlling domain wall motion in ferroelectric thin fi lms. *Nat. Nanotechnol.* **10,** 1–6 (2015).
6. Bhaskar, U. K. *et al.* A flexoelectric microelectromechanical system on silicon. *Nat. Nanotechnol.* **11,** 263–266 (2016).
7. Pandya, S. *et al.* Pyroelectric energy conversion with large energy and power density in relaxor ferroelectric thin films. *Nat. Mater.* **xx,** xx–xx (2018).
8. Rabe, K. M., Ahn, C. H. & Triscone, J.-M. *Physics of Ferroelectrics A Modern Perspective*. (Springer-Verlag Berlin Heidelberg, 2007).
9. Bader, R. F. W. An interpretation of potential interaction constants in terms of low-lying excited states. *Mol. Phys.* **3,** 137–151 (1960).
10. Halasyamani, P. S. & Poeppelmeier, K. R. Noncentrosymmetric Oxides. *Chem. Mater.* **10,** 2753–2769 (1998).
11. Cohen, R. E. Origin of ferroelectricty in perovskite oxides. *Nature* **358,** 136–138 (1992).
12. Waser, R., Bottger, U. & Tiedke, S. *Polar Oxides: Properties, Characterization, and Imaging*. (Wiley-VCH Verlag GmbH & Co. KGaA, Weinheim, 2005).
13. Cross, E. Lead-free at last. *Nucl. Med. Commun.* **32,** 666–668 (2011).
14. Koukhar, V. G., Pertsev, N. A. & Waser, R. Thermodynamic theory of epitaxial ferroelectric thin films with dense domain structures. *Phys. Rev. B* **64,** 214103 (2001).
15. Tagantsev, A. K. & Gerra, G. Interface-induced phenomena in polarization response of ferroelectric thin films. *J. Appl. Phys.* **100,** 051607 (2006).
16. Känzig, W. Space charge layer near the surface of a ferroelectric. *Phys. Rev.* **98,** 549–550 (1955).
17. Kittel, C. Theory of the structure of ferromagnetic domains in films and small particles. *Phys. Rev.* **70,** 965–971 (1946).
18. Janovec, V. On the theory of the coercive field of single-domain crystals of BaTiO3. *Czechosl. Journ. Phys.* **8,** 3–15 (1958).

19. Kay, H. F. & Dunn, J. W. Thickness dependence of the nucleation field of triglycine sulphate. *Philos. Mag.* **7,** 2027–2034 (1962).

20. Newnham, R. E. *Properties of Materials*. (Oxford University Press Inc., New York, 2005).

21. Nye, J. F. *Physical Properties of Crystals*. (Oxford University Press, 1957).

22. Bain, A. K. & Chand, P. *Ferroelectrics*. (Wiley-VCH Verlag GmbH & Co. KGaA, 2017).

23. Zhang, Q. M., Wang, H., Kim, N. & Cross, L. E. Direct evaluation of domain-wall and intrinsic contributions to the dielectric and piezoelectric response and their temperature dependence on lead zirconate-titanate ceramics. *J. Appl. Phys.* **75,** 454–459 (1994).

24. Taylor, D. V. & Damjanovic, D. Evidence of domain wall contribution to the dielectric permittivity in PZT thin films at sub-switching fields. *J. Appl. Phys.* **82,** 1973–1975 (1997).

25. Randall, C. a, Kim, N., Kucera, J.-P., Cao, W. & Shrout, T. R. Intrinsic and Extrinsic Size Effects in Fine-Grained Morphotropic-Phase-Boundary Lead Zirconate Titanate Ceramics. *J. Am. Ceram. Soc.* **81,** 677–688 (1998).

26. Hall, D. A. & Stevenson, P. J. High field dielectric behaviour of ferroelectric ceramics. *Ferroelectrics* **228,** 139–158 (1999).

27. Fousek, J. The contribution of domain walls to the small-signal complex permittivity of BaTiO3. *Czech J. Phys.* **15,** 412–417 (1965).

28. Nettleton, R. E. Switching resonance in crystallites of barium titanate. *J. Phys. Soc. Japan* **21,** 1633–1639 (1966).

29. Lawless, W. N. & Fousek, J. Small-Signal Permittivity of the Stationary (100)-180° Domain Wall in BaTiO3. *J. Phys. Soc. Japan* **28,** 419–424 (1970).

30. Lawless, W. 180° Domain-Wall Energies in BaTiO3. *Phys. Rev.* **175,** 619–624 (1968).

31. Morozovska, A. N., Eliseev, E. A., Varenyk, O. V. & Kalinin, S. V. Effective piezoelectric response of twin walls in ferroelectrics. *J. Appl. Phys.* **113,** 187222 (2013).

32. Waser, R. *Nanoelectronics and Information Technology*. (Wiley-VCH Verlag & Co. KGaA, 2012).

33. Meena, J. S., Sze, S. M., Chand, U. & Tseng, T. Y. Overview of emerging nonvolatile memory technologies. *Nanoscale Res. Lett.* **9,** 526 (2014).

34. Scott, J. F. *Ferroelectric Memories*. (Springer-Verlag Berlin Heidelberg, 2000).

35. Yang, S. M., Yoon, J. G. & Noh, T. W. Nanoscale studies of defect-mediated polarization switching dynamics in ferroelectric thin film capacitors. *Curr. Appl. Phys.* **11,** 1111–1125 (2011).

36. Landauer, R. Electrostatic considerations in BaTiO3 domain formation during polarization reversal. *J. Appl. Phys.* **28,** 227–234 (1957).

37. Jo, J. Y. *et al.* Nonlinear dynamics of domain-wall propagation in epitaxial ferroelectric thin films. *Phys. Rev. Lett.* **102,** 045701 (2009).

38. Merz, W. J. Domain formation and domain wall motions in ferroelectric BaTiO3 single crystals. *Phys. Rev.* **95,** 690–698 (1954).

39. Avrami, M. Kinetics of phase change. II Transformation-time relations for random distribution of nuclei. *J. Chem. Phys.* **8,** 212–224 (1940).

40. Ishibashi, Y. A Model of Polarization in Ferroelectrics. *Journal of the Physical Society of Japan* **59,** 4148–4154 (1990).

41. Ishibashi, Y. & Takagi, Y. Note on ferroelectric domain switching. *Journal of the Physical Society of Japan* **31,** 506–510 (1971).

42. Tagantsev, A., Stolichnov, I., Setter, N., Cross, J. & Tsukada, M. Non-Kolmogorov-Avrami switching kinetics in ferroelectric thin films. *Phys. Rev. B* **66,** 214109 (2002).

43. Gao, P. *et al.* Atomic-scale mechanisms of ferroelastic domain-wall-mediated ferroelectric switching. *Nat. Commun.* **4,** 2791 (2013).

44. Gao, P. *et al.* Revealing the role of defects in ferroelectric switching with atomic resolution. *Nat. Commun.* **2,** 591 (2011).

45. Gao, P. *et al.* Ferroelastic domain switching dynamics under electrical and mechanical excitations. *Nat. Commun.* **5,** 3801 (2014).

46. Nelson, C. T. *et al.* Electrochemical ferroelectric switching. *Science* **334,** 968–971 (2011).

47. Martin, L. W., Chu, Y. H. & Ramesh, R. Advances in the growth and characterization of magnetic, ferroelectric, and multiferroic oxide thin films. *Mater. Sci. Eng. R Reports* **68,** 89–133 (2010).

48. Martin, L. W. & Schlom, D. G. Advanced synthesis techniques and routes to new single-phase multiferroics. *Curr. Opin. Solid State Mater. Sci.* **16,** 199–215 (2012).

49. Smith, D. L. *Thin-Film Deposition Principles & Practice*. (Mc-Graw-Hill, Inc., 1995).

50. Alpay, S. P. & Roytburd, A. L. Thermodynamics of polydomain heterostructures. III. Domain stability map. *J. Appl. Phys.* **83,** 4714–4723 (1998).

51. Speck, J. S. & Pompe, W. Domain configurations due to multiple misfit relaxation mechanisms in epitaxial ferroelectric thin films. I. Theory. *J. Appl. Phys.* **76,** 466–476 (1994).

52. Speck, J. S., Daykin, A. C., Seifert, A., Romanov, A. E. & Pompe, W. Domain configurations due to multiple misfit relaxation mechanisms in epitaxial ferroelectric thin films. III. Interfacial defects and domain misorientations. *J. Appl. Phys.* **78,** 1696–1706 (1995).

53. Waser, R. *Nanoelectronics and Information Technology, 3rd Edition*. (Wiley-VCH, 2012).

54. Chrisey, D. B. & Hubler, G. K. *Pulsed Laser Deposition of Thin Films*. (Wiley-Interscience, 1994).

55. Ashfold, M. N. R., Claeyssens, F., Fuge, G. M. & Henley, S. J. Pulsed laser ablation and deposition of thin films. *Chem. Soc. Rev.* **33,** 23–31 (2004).

56. Birkholz, M. *Thin Film Analysis by X-Ray Scattering*. (Wiley-VCH Verlag GmbH & Co. KGaA, Weinheim, 2006).

57. Voigtlander, B. *Scanning Probe Microscopy - Atomic Force Microscopy and Scanning Tunneling Microscopy*. (Springer-Verlag Berlin Heidelberg, 2015).

58. Moler, K. A. Imaging quantum materials. *Nat. Mater.* **16,** 1049–1052 (2017).

59. Kalinin, S. V. & Gruverman, A. *Scanning Probe Microscopy - Electrical and Electromechanical Phenomena at the Nanoscale Volume II*. (Springer Science + Business Media, LLC, 2007).

60. Bassiri-Gharb, N. *et al.* Domain wall contributions to the properties of piezoelectric thin films. *J. Electroceramics* **19,** 47–65 (2007).

61. Waser, R. *Polar Oxides: Properties, Characterization, and Imaging*. (Wiley-VCH Verlag GmbH & Co. KGaA, 2005).

62. Pertsev, N. A., Zembilgotov, A. G. & Tagantsev, A. K. Effect of Mechanical Boundary Conditions on Phase Diagrams of Epitaxial Ferroelectric Thin Films. *Phys. Rev. Lett.* **80,** 1988–1991 (1998).

63. Kukhar, V. G., Pertsev, N. A., Kohlstedt, H. & Waser, R. Polarization states of polydomain epitaxial Pb (Zr1-x Tix) O3 thin films and their dielectric properties. *Phys. Rev. B* **73,** 214103 (2006).

64. Chen, L.-Q. *Landau Free-Energy Coefficients, Physics of Ferroelectrics: A Modern Perspective*. (Springer-Verlag, Berlin, 2007).

65. Zhang, J. X. *et al.* Computer simulation of ferroelectric domain structures in epitaxial BiFe O3 thin films. *J. Appl. Phys.* **103,** 094111 (2008).

66. Ban, Z. G. & Alpay, S. P. Dependence of the pyroelectric response on internal stresses in ferroelectric thin films. *Appl. Phys. Lett.* **82,** 3499–3501 (2003).

67. Schlom, D. G. *et al.* Strain Tuning of Ferroelectric Thin Films. *Annu. Rev. Mater. Res.* **37,** 589–626 (2007).

68. Saito, K., Kurosawa, T., Akai, T., Oikawa, T. & Funakubo, H. Structural characterization and 90° domain contribution to ferroelectricity of epitaxial Pb(Zr0.35,Ti0.65)O3thin films. *J. Appl. Phys.* **93,** 545–550 (2003).

69. Ouyang, J. *et al.* Engineering of self-assembled domain architectures with ultra-high piezoelectric response in epitaxial ferroelectric films. *Adv. Funct. Mater.* **17,** 2094–2100 (2007).

70. Chu, Y. H. *et al.* Domain control in multiferroic BiFeO3 through substrate vicinality. *Adv.*

Mater. **19,** 2662–2666 (2007).

71. Xu, R., Karthik, J., Damodaran, A. R. & Martin, L. W. Stationary domain wall contribution to enhanced ferroelectric susceptibility. *Nat. Commun.* **5,** 3120 (2014).

72. Xu, R. *et al.* Ferroelectric polarization reversal via successive ferroelastic transitions. *Nat. Mater.* **14,** 79–86 (2015).

73. Wada, S., Yako, K., Kakemoto, H., Tsurumi, T. & Kiguchi, T. Enhanced piezoelectric properties of barium titanate single crystals with different engineered-domain sizes. *J. Appl. Phys.* **98,** 014109 (2005).

74. Bernal, A., Zhang, S. & Bassiri-Gharb, N. Effects of orientation and composition on the extrinsic contributions to the dielectric response of relaxor-ferroelectric single crystals. *Appl. Phys. Lett.* **95,** 142911 (2009).

75. Sluka, T., Tagantsev, A. K., Damjanovic, D., Gureev, M. & Setter, N. Enhanced electromechanical response of ferroelectrics due to charged domain walls. *Nat. Commun.* **3,** 747–748 (2012).

76. Hlinka, J., Ondrejkovic, P. & Marton, P. The piezoelectric response of nanotwinned BaTiO3. *Nanotechnology* **20,** 105709 (2009).

77. Pertsev, N. A., Kukhar, V. G., Kohlstedt, H. & Waser, R. Phase diagrams and physical properties of single-domain epitaxial Pb(Zr1-xTix)O3 thin films. *Phys. Rev. B* **67,** 054107 (2003).

78. Pálová, L., Chandra, P. & Rabe, K. M. Modeling the dependence of properties of ferroelectric thin film on thickness. 1–12 (2007).

79. Sheng, G. *et al.* Phase-field simulations of thickness-dependent domain stability in PbTiO3 thin films. *Acta Mater.* **60,** 3296–3301 (2012).

80. Glinchuk, M. D., Morozovska, A. N. & Eliseev, E. A. Ferroelectric thin films phase diagrams with self-polarized phase and electret state. *J. Appl. Phys.* **99,** 114102 (2006).

81. Tagantsev, A. K., Pertsev, N. A., Muralt, P. & Setter, N. Strain-induced diffuse dielectric anomaly and critical point in perovskite ferroelectric thin films. *Phys. Rev. B* **65,** 121041–121044 (2002).

82. Oja, R., Johnston, K., Frantti, J. & Nieminen, R. M. Computational study of (111) epitaxially strained ferroelectric perovskites BaTiO3 and PbTiO3. *Phys. Rev. B* - **78,** 094102 (2008).

83. Angsten, T., Martin, L. W. & Asta, M. Orientation-dependent properties of epitaxially strained perovskite oxide thin films: Insights from first-principles calculations. *Phys. Rev. B* **95,** 1–14 (2017).

84. Gui, Z., Prosandeev, S. & Bellaiche, L. Properties of epitaxial (110) BaTiO 3 films from first principles. *Phys. Rev. B* **84,** 214112 (2011).

85. Xu, R., Zhang, J., Chen, Z. & Martin, L. W. Orientation-dependent structural phase

diagrams and dielectric properties of PbZr1-xTixO3 polydomain thin films. *Phys. Rev. B* **91,** 144106 (2015).

86. Yan, L., Li, J., Cao, H. & Viehland, D. Low symmetry phase in Pb(Zr0.52Ti0.48)O3 epitaxial thin films with enhanced ferroelectric properties. *Appl. Phys. Lett.* **89,** 262905 (2006).

87. Ray, S. C. *et al.* Loycal atomic and electronic structures and ferroelectric properties of PbZr0.52Ti0.48O3: An x-ray absorption study. *Appl. Phys. Lett.* **99,** 109–112 (2011).

88. Karthik, J., Damodaran, A. R. & Martin, L. W. Effect of 90° domain walls on the low-field permittivity of PbZr 0.2Ti 0.8O 3 thin films. *Phys. Rev. Lett.* **108,** 167601 (2012).

89. Liu, S. & Cohen, R. E. Origin of stationary domain wall enhanced ferroelectric susceptibility. **95,** 094102 (2017).

90. Du, X., Belegundu, U. & Uchino, K. Crystal Orientation Dependence of Piezoelectric Properties in Lead Zirconate Titanate: Theoretical Expectation for Thin Films. *Jpn. J. Appl. Phys.* **36,** 5580–5587 (1997).

91. Du, X., Zheng, J., Belegundu, U. & Uchino, K. Crystal orientation dependence of piezoelectric properties of lead zirconate titanate near the morphotropic phase boundary. *Appl. Phys. Lett.* **72,** 2421–2423 (1998).

92. Chanthbouala, A. *et al.* Solid-state memories based on ferroelectric tunnel junctions. *Nat. Nanotechnol.* **7,** 101–104 (2012).

93. Hoffman, J. *et al.* Ferroelectric field effect transistors for memory applications. *Adv. Mater.* **22,** 2957–2961 (2010).

94. Muralt, P. & Muralt, P. Ferroelectric thin films for micro-sensors and actuators: a review. *J. Micromechanics Microengineering* **10,** 136 (2000).

95. Eom, C. B. & Trolier-McKinstry, S. Thin-film piezoelectric MEMS. *MRS Bull.* **37,** 1007–1017 (2012).

96. Lang, S. B. Pyroelectricity: From ancient curiosity to modern imaging tool. *Phys. Today* **58,** 31–36 (2005).

97. Karthik, J. & Martin, L. W. Pyroelectric properties of polydomain epitaxial Pb(Zr1-x,Tix)O3 thin films. *Phys. Rev. B* **84,** 024102 (2011).

98. Pertsev, N. A. & Koukhar, V. G. Polarization instability in polydomain ferroelectric epitaxial thin films and the formation of heterophase structures. *Phys. Rev. Lett.* **84,** 3722–3725 (2000).

99. Wada, S., Yako, K., Yokoo, K., Kakemoto, H. & Tsurumi, T. Domain wall engineering in barium titanate single crystals for enhanced piezoelectric properties. *Ferroelectrics* **334,** 17–27 (2006).

100. Wada, S. *et al.* Domain wall engineering in lead-free piezoelectric crystals. *Ferroelectrics* **355,** 37–49 (2007).

101. Nagarajan, V. *et al.* Thickness dependence of structural and electrical properties in epitaxial lead zirconate titanate films. *J. Appl. Phys.* **86,** 595–602 (1999).

102. Pertsev, N. A. & Zembilgotov, A. G. Domain populations in epitaxial ferroelectric thin films: Theoretical calculations and comparison with experiment. *J. Appl. Phys.* **80,** 6401–6406 (1996).

103. Romanov, A. E., Vojta, A., Pompe, W., Lefevre, M. J. & Speck, J. S. Domain patterns in (111) oriented tetragonal ferroelectric films. *Phys. Status Solidi Appl. Res.* **172,** 225–253 (1999).

104. Floquet, N. & Valot, C. Ferroelectric domain walls in $BaTiO_3$: Structural wall model interpreting fingerprints in XRPD diagrams. *Ferroelectrics* **234,** 107–122 (1999).

105. Tsai, F., Khiznichenko, V. & Cowley, J. M. High-resolution electron microscopy of 90 ° ferroelectric domain boundaries in BaTiO3 and Pb(Zr0.52Ti0.48)O3. *Ultramicroscopy* **45,** 55–63 (1992).

106. Dennis, M. D. Thickness of 90° ferroelectric domain walls in (Ba,Pb)TiO3 single crystals. *J. Appl. Phys.* **45,** 1931–1933 (1974).

107. Tanaka, M. & Honjo, G. Electron Optical Studies of Barium Titanate Single Crystal Films. *J. Phys. Soc. Jpn.* **19,** 954–970 (1964).

108. Venkatesan, S., Kooi, B. J., De Hosson, J. T. M., Vlooswijk, A. H. G. & Noheda, B. Substrate influence on the shape of domains in epitaxial PbTiO3 thin films. *J. Appl. Phys.* **102,** 104105 (2007).

109. Kurosawa, K. S., Oikawa, T. A. & Funakubo, H. Structural characterization and 90° domain contribution to ferroelectricity of epitaxial thin films Structural characterization and 90° domain contribution to ferroelectricity. *J. Appl. Phys.* **545,** (2017).

110. Hlinka, J. & Márton, P. Phenomenological model of a 90° domain wall in BaTiO3 -type ferroelectrics. *Phys. Rev. B* **74,** 104104 (2006).

111. Scrymgeour, D. A. & Gopalan, V. Nanoscale piezoelectric response across a single antiparallel ferroelectric domain wall. *Phys. Rev. B* **72,** 024103 (2005).

112. Morozovska, A. N., Eliseev, E. A., Bravina, S. L. & Kalinin, S. V. Resolution-function theory in piezoresponse force microscopy: Wall imaging, spectroscopy, and lateral resolution. *Phys. Rev. B - Condens. Matter Mater. Phys.* **75,** 174109 (2007).

113. Scott, J. F. Applications of Modern Ferroelectrics. *Science* **315,** 954–959 (2007).

114. Dawber, M., Rabe, K. M. & Scott, J. F. Physics of thin-film ferroelectric oxides. *Rev. Mod. Phys.* **77,** 1083–1130 (2005).

115. Li, Y. L., Hu, S. Y., Liu, Z. K. & Chen, L. Q. Effect of electrical boundary conditions on ferroelectric domain structures in thin films. *Appl. Phys. Lett.* **81,** 427–429 (2002).

116. Pertsev, N. A., Arlt, G. & Zembilgotov, A. G. Domain-wall and intrinsic contributions to the dielectric response of epitaxial ferroelectric films. *Microelectron. Eng.* **29,** 135–140

(1995).

117. Xu, F. *et al.* Domain wall motion and its contribution to the dielectric and piezoelectric properties of lead zirconate titanate films. *J. Appl. Phys.* **89,** 1336–1348 (2001).

118. Kim, D.-J., Maria, J.-P., Kingon, A. I. & Streiffer, S. K. Evaluation of intrinsic and extrinsic contributions to the piezoelectric properties of Pb(Zr1−xTix)O3 thin films as a function of composition. *J. Appl. Phys.* **93,** 5568–5575 (2003).

119. Bruchhaus, R., Pitzer, D., Schreiter, M. & Wersing, W. Optimized PZT thin films for pyroelectric IR detector arrays. *J. Electroceramics* **3,** 151–162 (1999).

120. Oikawa, T., Aratani, M., Funakubo, H., Saito, K. & Mizuhira, M. Composition and orientation dependence of electrical properties of epitaxial Pb(ZrxTi1-x)O3 thin films grown using metalorganic chemical vapor deposition. *J. Appl. Phys.* **95,** 3111–3115 (2004).

121. Grigoriev, A. *et al.* Nanosecond domain wall dynamics in ferroelectric Pb(Zr,Ti)O3 thin films. *Phys. Rev. Lett.* **96,** 1–4 (2006).

122. Jo, J. Y. *et al.* Nanosecond dynamics of ferroelectric/dielectric superlattices. *Phys. Rev. Lett.* **107,** 1–4 (2011).

123. Zubko, P., Stucki, N., Lichtensteiger, C. & Triscone, J. M. X-ray diffraction studies of 180° ferroelectric domains in PbTiO3/SrTiO3 superlattices under an applied electric field. *Phys. Rev. Lett.* **104,** 1–4 (2010).

124. Kalinin, S. V. *et al.* Defect-mediated polarization switching in ferroelectrics and related materials: From mesoscopic mechanisms to atomistic control. *Adv. Mater.* **22,** 314–322 (2010).

125. Gruverman, A. & Kholkin, A. Nanoscale ferroelectrics: Processing, characterization and future trends. *Reports Prog. Phys.* **69,** 2443–2474 (2006).

126. Gruverman, A. *et al.* Direct studies of domain switching dynamics in thin film ferroelectric capacitors. *Appl. Phys. Lett.* **87,** 1–4 (2005).

127. Nelson, C. T. *et al.* Electrochemical ferroelectric switching. *Science* **334,** 968–971 (2011).

128. Winkler, C. R., Damodaran, A. R., Karthik, J., Martin, L. W. & Taheri, M. L. Direct observation of ferroelectric domain switching in varying electric field regimes using in situ TEM. *Micron* **43,** 1121–1126 (2012).

129. Chang, H. *et al.* Watching domains grow: In-situ studies of polarization switching by combined scanning probe and scanning transmission electron microscopy. *J. Appl. Phys.* **110,** (2011).

130. Sepliarsky, M., Phillpot, S. R., Stachiotti, M. G., Wolf, D. & Migoni, R. L. Atomic-level simulation of ferroelectricity in perovskttes. *Integr. Ferroelectr.* **38,** 81–90 (2001).

131. Liu, S., Grinberg, I., Takenaka, H. & Rappe, A. M. Reinterpretation of the bond-valence model with bond-order formalism: An improved bond-valence-based interatomic potential

for PbTiO3. *Phys. Rev. B - Condens. Matter Mater. Phys.* **88,** 1–7 (2013).

132. Liu, S., Grinberg, I. & Rappe, A. M. Development of a bond-valence based interatomic potential for BiFeO 3 for accurate molecular dynamics simulations. *J. Phys. Condens. Matter* **25,** (2013).

133. Sepliarsky, M., Stachiotti, M. G. & Migoni, R. L. Surface and substrate effects on the ferroelectric properties of PbTiO 3 ultrathin films. *Ferroelectrics* **335,** 3–12 (2006).

134. Takenaka, H., Grinberg, I. & Rappe, A. M. Anisotropic local correlations and dynamics in a relaxor ferroelectric. *Phys. Rev. Lett.* **110,** 1–5 (2013).

135. Shin, Y.-H., Grinberg, I., Chen, I.-W. & Rappe, A. M. Nucleation and growth mechanism of ferroelectric domain-wall motion. *Nature* **449,** 881–884 (2007).

136. Roitburd, A. L. Equilibrium Structure of Epitaxial Layers. **329,** 329–339 (1976).

137. Karthik, J., Damodaran, A. R. & Martin, L. W. Epitaxial ferroelectric heterostructures fabricated by selective area epitaxy of SrRuO 3 using an MgO mask. *Adv. Mater.* **24,** 1610–1615 (2012).

138. Kamel, T. M. & De With, G. Double-peak switching current in soft ferroelectric lead zirconate titanate. *J. Appl. Phys.* **102,** 0–5 (2007).

139. Yin, J. & Cao, W. Polarization reversal study using ultrasound. *Appl. Phys. Lett.* **79,** 4556–4558 (2001).

140. Daniels, J. E. *et al.* Neutron diffraction study of the polarization reversal mechanism in [111]c-oriented Pb (Zn1/3Nb2/3) O3-x PbTiO3. *J. Appl. Phys.* **101,** (2007).

141. Pramanick, A., Prewitt, A. D., Forrester, J. S. & Jones, J. L. Domains, domain walls and defects in perovskite ferroelectric oxides: A review of present understanding and recent contributions. *Crit. Rev. Solid State Mater. Sci.* **37,** 243–275 (2012).

142. Nagarajan, V. *et al.* Dynamics of ferroelastic domains in ferroelectric thin films. *Nat. Mater.* **2,** 43–47 (2003).

143. Anbusathaiah, V. *et al.* Labile ferroelastic nanodomains in bilayered ferroelectric thin films. *Adv. Mater.* **21,** 3497–3502 (2009).

144. Meyer, B. & Vanderbilt, D. Ab initio study of ferroelectric domain walls in PbTiO3. *Phys. Rev. B* **65,** 104111 (2002).

145. Martin, L. W. & Rappe, A. M. Thin-film ferroelectric materials and their applications. *Nat. Rev. Mater.* **2,** (2016).

146. Setter, N. *et al.* Ferroelectric thin films: Review of materials, properties, and applications. *J. Appl. Phys.* **100,** 1–46 (2006).

147. Waser, R. & Rüdiger, A. Ferroelectrics: Pushing towards the digital storage limit. *Nat. Mater.* **3,** 81–82 (2004).

148. Alexe, M., Harnagea, C., Hesse, D. & Gösele, U. Polarization imprint and size effects in

mesoscopic ferroelectric structures. *Appl. Phys. Lett.* **79,** 242–244 (2001).

149. Ha, S. D. & Ramanathan, S. Adaptive oxide electronics: A review. *J. Appl. Phys.* **110,** 071101 (2011).

150. Kuzum, D., Yu, S. & Philip Wong, H.-S. Synaptic electronics: materials, devices and applications. *Nanotechnology* **24,** 382001 (2013).

151. Jeong, D. S., Kim, K. M., Kim, S., Choi, B. J. & Hwang, C. S. Memristors for Energy-Efficient New Computing Paradigms. *Adv. Electron. Mater.* **2,** 1600090 (2016).

152. Lee, D. *et al.* Active control of ferroelectric switching using defect-dipole engineering. *Adv. Mater.* **24,** 6490–6495 (2012).

153. Ghosh, A., Koster, G. & Rijnders, G. Multistability in Bistable Ferroelectric Materials toward Adaptive Applications. *Adv. Funct. Mater.* **26,** 5748–5756 (2016).

154. Park, M. H. *et al.* Tristate memory using ferroelectric-insulator-semiconductor heterojunctions for 50% increased data storage. *Adv. Funct. Mater.* **21,** 4305–4313 (2011).

155. Park, C. & Chadi, D. Microscopic study of oxygen-vacancy defects in ferroelectric perovskites. *Phys. Rev. B* **57,** R13961–R13964 (1998).

156. Pöykkö, S. & Chadi, D. J. Dipolar defect model for fatigue in ferroelectric perovskites. *Phys. Rev. Lett.* **83,** 1231–1234 (1999).

157. Scott, J. F. & Dawber, M. Oxygen-vacancy ordering as a fatigue mechanism in perovskite ferroelectrics. *Appl. Phys. Lett.* **76,** 3801–3803 (2000).

158. Warren, W. L., Dimos, D. & Waser, R. M. Degradation mechanisms in ferroelectric and perovskites. **3,** 40–45 (1996).

159. Boni, G. A. *et al.* Multiple polarization states in symmetric ferroelectric heterostructures for multi-bit non-volatile memories. *Nanoscale* **9,** 19271–19278 (2017).

160. Chew, K. H., Ong, L. H., Osman, J. & Tilley, D. R. Hysteresis loops of ferroelectric bilayers and superlattices. *Appl. Phys. Lett.* **77,** 2755–2757 (2000).

161. Baudry, L., Lukyanchuk, I. & Vinokur, V. M. Ferroelectric symmetry-protected multibit memory cell. *Sci. Rep.* **7,** 42196 (2017).

162. Lee, J. H., Chu, K., Kim, K.-E., Seidel, J. & Yang, C.-H. Out-of-plane three-stable-state ferroelectric switching: Finding the missing middle states. *Phys. Rev. B* **93,** 115142 (2016).

163. Damodaran, A. R. *et al.* Three-State Ferroelastic Switching and Large Electromechanical Responses in PbTiO3Thin Films. *Adv. Mater.* **29,** 1–9 (2017).

164. Tripathi, A. K. *et al.* Multilevel information storage in ferroelectric polymer memories. *Adv. Mater.* **23,** 4146–4151 (2011).

165. Tybell, T., Paruch, P., Giamarchi, T. & Triscone, J. Domain Wall Creep in Epitaxial Ferroelectric Pb(Zr0.2Ti0.8)O3 Thin Films. *Phys. Rev. Lett.* **89,** 8–11 (2002).

166. Paruch, P., Giamarchi, T. & Triscone, J. M. Domain wall roughness in epitaxial ferroelectric PbZr0.2Ti0.8O3 thin films. *Phys. Rev. Lett.* **94,** 3–6 (2005).

167. Qi, T., Shin, Y. H., Yeh, K. Lo, Nelson, K. A. & Rappe, A. M. Collective coherent control: Synchronization of polarization in ferroelectric PbTiO3 by shaped THz fields. *Phys. Rev. Lett.* **102,** 1–4 (2009).

168. Liu, S., Grinberg, I. & Rappe, A. M. Intrinsic ferroelectric switching from first principles. *Nature* **534,** 360–363 (2016).

169. Jo, S. H. *et al.* Nanoscale memristor device as synapse in neuromorphic systems. *Nano Lett.* **10,** 1297–1301 (2010).

170. Matzen, S. *et al.* Super switching and control of in-plane ferroelectric nanodomains in strained thin films. *Nat. Commun.* **5,** 1–8 (2014).

171. Bell, R. P. The Theory of reactions involving proton transfers. *Proc. R. Soc. A Math. Phys. Eng. Sci.* **143,** 414–429 (1935).

172. Polanyi, M. E. Further considerations on the thermodynamics of chemical equilibria and reaction rates. *Proc. Roy. Soc. A* 1333–1360 (1936).

173. Garcia, V. *et al.* Giant tunnel electroresistance for non-destructive readout of ferroelectric states. *Nature* **460,** 81–84 (2009).

174. Tomas, J., Bellaiche, L. & Bibes, M. Learning through ferroelectric domain dynamics in solid-state synapses. **8,** 14736 (2017).

175. Ma, T. P. & Han, J. P. Why is nonvolatile ferroelectric memory field-effect transistor still elusive? *IEEE Electron Device Lett.* **23,** 386–388 (2002).

176. Kimura, H. *et al.* Complementary ferroelectric-capacitor logic for low-power logic-in-memory VLSI. *IEEE J. Solid-State Circuits* **39,** 919–926 (2004).

177. Moazzami, R. Ferroelectric thin film technology for semiconductor memory. *Semicond. Sci. Technol.* **10,** 375–390 (1995).

178. Hu, Z., Tian, M., Nysten, B. & Jonas, A. M. Regular arrays of highly ordered ferroelectric polymer nanostructures for non-volatile low-voltage memories. *Nat. Mater.* **8,** 62–67 (2009).

179. Ihlefeld, J. F., Harris, D. T., Jacob, K., Maria, L. J. J. & Trolier-mckinstry, S. Scaling Effects in Perovskite Ferroelectrics: Fundamental Limits and Process-Structure-Property Relations. **2557,** 6–9 (2016).

180. Nagarajan, V. *et al.* Scaling of structure and electrical properties in ultrathin epitaxial ferroelectric heterostructures. *J. Appl. Phys.* **100,** 1–10 (2006).

181. Huang, C. W., Chen, Z. H. & Chen, L. Thickness-dependent evolutions of domain configuration and size in ferroelectric and ferroelectric-ferroelastic films. *J. Appl. Phys.* **113,** 094101 (2013).

182. Lee, H. N. *et al.* Suppressed dependence of polarization on epitaxial strain in highly polar

ferroelectrics. *Phys. Rev. Lett.* **98,** 98–101 (2007).

183. Fong, D. D. *et al.* Ferroelectricity in Ultrathin Perovskite Films. **304,** 1650–1654 (2004).

184. Pertsev, N. A. *et al.* Coercive field of ultrathin epitaxial films. *Appl. Phys. Lett.* **3356,** 3356–3358 (2015).

185. Yoo, I. K. & Desu, S. B. Mechanism of Fatigue in Ferroelectric Thin Films. *Phys. Status Solidi* **133,** 565–573 (1992).

186. Tagantsev, A. K., Landivar, M., Colla, E. & Setter, N. Identification of passive layer in ferroelectric thin films from their switching parameters. *J. Appl. Phys.* **78,** 2623–2630 (1995).

187. Larsen, P. K., Dormans, G. J. M., Taylor, D. J. & van Veldhoven, P. J. Ferroelectric properties and fatigue of $PbZr_{0.51}Ti_{0.49}O_3$ thin films of varying thickness: Blocking layer model. *J. Appl. Phys.* **76,** 2405–2413 (1994).

188. Chandra, P., Dawber, M., Littlewood, P. B. & Scott, J. F. Scaling of the Coercive Field with Thickness in Thin-Film Ferroelectrics. *Ferroelectrics* **313,** 7–13 (2004).

189. Bune, A. V. a. V. *et al.* Two-dimensional ferroelectric films. *Nature* **391,** 874–877 (1998).

190. Ducharme, S. *et al.* Intrinsic Ferroelectric Coercive Field. *Phys. Rev. Lett.* **84,** 175–178 (2000).

191. Jo, J. Y., Kim, Y. S., Noh, T. W., Yoon, J. G. & Song, T. K. Coercive fields in ultrathin BaTiO3 capacitors. *Appl. Phys. Lett.* **89,** 89–92 (2006).

192. Dawber, M., Chandra, P., Littlewood, P. B. & Scott, J. F. Depolarization corrections to the coercive field in thin-film ferroelectrics. *J. Phys. Condens. Matter* **15,** L393–L398 (2003).

193. Liu, G. & Nan, C. W. Thickness dependence of polarization in ferroelectric perovskite thin films. *J. Phys. D. Appl. Phys.* **38,** 584–589 (2005).

194. Budimir, M., Damjanovic, D. & Setter, N. Piezoelectric response and free-energy instability in the perovskite crystals BaTiO3, PbTiO3, and Pb (Zr,Ti)O3. *Phys. Rev. B* **73,** 174106 (2006).

195. Wang, J. J., Wang, Y., Ihlefeld, J. F., Hopkins, P. E. & Chen, L. Q. Tunable thermal conductivity via domain structure engineering in ferroelectric thin films: A phase-field simulation. *Acta Mater.* **111,** 220–231 (2016).

196. Li, Y. L., Hu, S. Y. & Chen, L. Q. Ferroelectric domain morphologies of (001) PbZr1-xTixO3 epitaxial thin films. *J. Appl. Phys.* **97,** 1–7 (2005).

197. Khachaturyan, A. G. *Theory of Structural Transformations in Solids*. (Wiley, New York, NY, 1983).

198. Wang, J. J., Ma, X. Q., Li, Q., Britson, J. & Chen, L. Q. Phase transitions and domain structures of ferroelectric nanoparticles: Phase field model incorporating strong elastic and dielectric inhomogeneity. *Acta Mater.* **61,** 7591–7603 (2013).

199. Jo, J. Y. *et al.* Polarization switching dynamics governed by the thermodynamic nucleation process in ultrathin ferroelectric films. *Phys. Rev. Lett.* **97,** 247602 (2006).